Supercritical Fluids as Antisolvents and Transport Media



By

S. Adam O'Neil (MSci)

Thesis submitted to The University of Nottingham for the degree of Doctor of Philosophy, February 2003

Table of Contents

Table of Contents ..... **i**

Abstract ..... **v**

Acknowledgements ..... **vii**

Publications List ..... **viii**

Abbreviations ..... **ix**

Variables ..... **xi**

Chapter 1 Introduction **1**

An Introduction to Supercritical Fluids 2

Supercritical Fluid Behaviour as a Solvent 13

Supercritical Fluid Behaviour as an Antisolvent 14

PCA 19

GAS 24

Chapter 2 C_{60}(Gas) Intercalation Via the PCA and GAS Techniques **26**

C_{60} and C_{60}-Intercalation Chemistry 26

PCA 31

$C_{60}(C_2H_4)$ 36

$C_{60}(C_2H_6)$ 39

$C_{60}(C_3H_6)$ 41

$C_{60}(C_3H_8)$ 43

GAS 46

$C_{60}(C_2H_4)$ 54

$C_{60}(C_2H_6)$ 58

$C_{60}(C_3H_6)$ 62

$C_{60}(C_3H_8)$ 66

Conclusion 73

Chapter 3 Single Crystals of C_{60}(Gas) **75**

Conventional Crystallisation 76
Nucleation 76
Crystal Growth 86
Diffusion Driven Precipitation 95
$C_{60}(C_2H_4)$ 105
$C_{60}(C_2H_6)$ 110
$C_{60}(C_3H_6)$ 114
$C_{60}(C_3H_8)$ 117
$C_{60}(CO_2)$ 119
Continuous Diffusion Driven Precipitation 120
C_{70} Intercalate Crystals 122
Discussion 125
Conclusion 130
Chapter 4 Nano-Peapods 131
Introduction to Nanotubes 131
Filling of Nanotubes with C_{60} Using SCF 134
Conclusion 139
Chapter 5 Mesoporous Silica Impregnation 140
An Introduction to Mesoporous Silica 140
Silica Impregnation with Aluminium 146
Initial Investigation of $scCO_2$ Acting on Silica 150
Supercritical CO_2 and Propane Impregnation 151
Liquid Propane Impregnation 155
Effect of Impregnation Time 157
Increased Aluminium Content 160
Repeated Steaming 162
Alternative Sources of Aluminium 164
Discussion 167
Conclusion 169
Chapter 6 Mesoporous Silica Extraction 170
Extraction of Dodecylamine: Design 1 171

Extraction of Dodecylamine: Design 2 179
Assessment of the Two Designs 187
Conclusion 189
Chapter 7 Conclusion 190
Chapter 8 References 192
Appendix I Equipment 216
Gas Supply 218
Pumping Methods 218
Gilson Pump 218
Pickel Pump 219
Vessels 220
32 ml and 10 ml Keystone Extraction Vessels 220
Sapphire Tube View Cell 221
60 ml Stirred Autoclave 221
60 ml Unstirred Autoclave 222
Large Sapphire View Cell 223
Back Pressure Regulators 223
Tescom 223
Jasco 224
Appendix II Analytical Equipment 225
X-Ray Diffraction XRD 225
Powder X-Ray Diffraction 225
MAS ^{13}C NMR 225
Scanning Electron Microscopy 226
Infra Red Spectroscopy 226
Differential Scanning Calorimetry 226
Thermal Gravimetric Analysis 226
MAS ^{27}Al NMR 227
N_2 Adsorption 227
Acidity Testing 227
Appendix III Safety Issues 229

250 bar L Limit.....229
Combined Use of High Temperature and Pressure 229
Flammable and Non Flammable Gas Supply.....230
Pressure Rating Formulae 230
Seal Types and Suitability.....231

Abstract

This thesis contains details of experiments involving the use of supercritical fluids (SCF) and high pressure liquids acting as antisolvents and transport media. The thesis is divided into six Chapters, each detailing different aspects of SCF technology.

Chapter 1: Provides the reader with general information concerning the properties of supercritical fluids. Information is given concerning the use of SCFs as solvents and antisolvents. Reviews of the PCA and GAS processes are also provided.

Chapter 2: Describes the initial study of the preparation of C_{60}(gas) intercalation compounds. PCA generates compounds of C_2H_4, C_2H_6, C_3H_6 and C_3H_8, which were characterised by IR. A novel GAS technique is used to allow collection of PXD, SEM and MAS ^{13}C NMR data of these compounds.

Chapter 3: Details a novel supercritical antisolvent technique which allows the generation of macroscopic crystals of intercalate species $C_{60}(C_2H_4)$ and $C_{60}(C_2H_6)$. Crystallographic data on these compounds is presented. Datasets for the intercalates $C_{60}(CO_2)$, $C_{70}(C_2H_6)$ and $C_{70}(CO_2)$ were also collected.

Chapter 4 Contains preliminary information on the formation of 'nano-peapods', that is, carbon nanotubes filled with C_{60}. A new route to the formation of these materials at room temperature is shown.

Chapter 5: Describes the impregnation of mesoporous silica with aluminium containing species using SCF as a solvent. Materials display unprecedented stability to steaming with high retention of structural ordering and surface area.

Chapter 6: Describes the extraction of template molecules from mesoporous silica. The possibility of complete removal of surfactant using a SCF is shown. The effect of temperature and pressure effects are also measured.

Appendices are available at the back of the thesis to describe the equipment, analytical techniques and some safety principles for use of SCF.

To Rose

Acknowledgements

I offer very grateful thanks to my supervisor Prof. Martyn Poliakoff. Martyn has always been available to turn me in the right direction when I have lost my way. His speed in returning document drafts is remarkable and his advice on IR spectroscopy I found to be invaluable. Mainly though I would like to give thanks for his unerring faith in me, the support of which has allowed me to complete this thesis. I would also like to thank greatly the EPSRC and ICI for providing the funds to allow me to carry out this research and Derek Graham, my supervisor at ICI, in particular. I wish to also give great thanks to Dr. Claire Wilson for her work in solving the structures of the C_{60} compounds. Her dedication to collection of X-ray diffraction data and struggles when no solution seemed evident is very gratefully appreciated. Many thanks are also deserved by Dr. Robert Mokaya, who introduced me to silica grafting and has patiently helped me understand the study of mesoporous silica in more detail. I would also like to thank my collaborators both in Nottingham and further away. Drs. Jez Webster and Christian Field I must thank immediately for beginning the work on C_{60} and for leaving it with so many potential avenues for me to explore. In this regard I must also thank Drs. Jeremy Titman, Duncan Gregory Jason Hyde, Ed Lester and Frank Allison for their valuable assistance with MAS ^{13}C NMR, PXD, SEM, TGA and DSC respectively. The help I received from them enabled me to characterise the C_{60} compounds more adequately. I would like to thank Dr. Andrei Khlobystov of the University of Oxford for his help and collaboration with the nano-peapod experiments and TEM. Hopefully this collaboration will prove very fruitful in the future and also lead to continued collaboration in synthesising crystals of new and precious fullerenes. My thanks also go to Drs. Andrea Watson and Duncan Macquarie at the University of York for their collaboration during the silica extraction experiments, for supplying the test silica, and analysis using TGA. I also thank my friends and colleagues, who I have worked with over the past 3 years, Helen Kirke, Dan Carter, Pete Licence, Steve Barlow, Nicky Meehan, Eleni Venardou, Lucinda Dudd, Eduardo Verdugo and Edward Evans and Jia Wei Wang. I would also like to thank Mark Guyler, Keith Stanley, Pete Fields and Richard Wilson for technical support. Finally, I would like to thank my wife, Rose, whose love and support throughout the last 3 years made this all possible.

Publications List

1. O'Neil, A.; Wilson, C.; Webster, J. M.; Allison, F. J.; Howard, J. A. K.; Poliakoff, M. "The Supercritical Fluid Anti-Solvent Synthesis of $C_{60}(C_2H_x)$ (x = 4 or 6); The Crystal Structures of Two Materials Which Were Thought Unlikely to Exist." *Angew. Chem. Int. Ed. Eng.;* 2002, 41, 20, 3796.

2. O'Neil, A. S.; Mokaya R. M.; Poliakoff, M. "Supercritical Fluid Mediated Alumination of Mesoporous Silica and its Beneficial Effect on Hydrothermal Stability." *J. Am. Chem. Soc.*; 2002, *124,* 36, 10636.

3. O'Neil, A. S.; Webster, J. M.; Wilson, C.; Blake, A. J.; Poliakoff, M. "Fullerene (gas) Intercalates: A New Approach to Growing Single Crystals using Supercritical Anti-Solvents." *Proceedings of the 8th Meeting on Supercritical Fluids*; Bernard, M., Cansell, F., Eds.; ISASF: Bordeaux, 2002, pp 63.

4. O'Neil, A. S.; Hamley, P. A.; Poliakoff, M. "Supercritical Fluids: Clean Solvents for Extraction, Reaction and Crystallisation" *Proceedings of the International Solvent Extraction Conference ISEC;* Sole, K. C., Cole, P. M., Preston, J. S., Robinson, D. J., Eds.; South African Institute of Mining and Metallurgy, Johannesburg, 2002.

Abbreviations

AOT	Sodium Bis(2-ethylhexyl) Sulfosuccinate
BPR	Back Pressure Regulator
CTAB	Cetyl trimethyl ammonium bromide
DCB	1,2-Dichlorobenzene
DDP	Diffusion Driven Precipitation
DSC	Differential Scanning Calorimetry
EOS	Equation of State
FCC	Face Centred Cubic
GAS	Gas Antisolvent
HCP	Hexagonal Close Packing
HIP	Hot Isostatic Pressing
IR	Infra Red
LLV	Liquid Liquid Vapour
MAS ^{13}C NMR	Magic Angle Spinning ^{13}C Nuclear Magnetic Resonance
MCM	Mobil Composition of Matter (Zeolite)
PCA	Precipitation Using a Compressed Antisolvent
PEG	Poly (Ethylene Glycol)
PLA	Poly (Lactic Acid)
PND	Powder Neutron Diffraction
ppm	Parts Per Million
PXD	Powder X-Ray Diffraction
RESS	Rapid Expansion of Supercritical Solution
SAS	Supercritical Antisolvent
SC	Simple Cubic
sc	Supercritical
SCF	Supercritical Fluid
SEDS	Solution Enhanced Dispersion with Supercritical Fluid
SEM	Scanning Electron Microscopy
SFC	Supercritical Fluid Chromatography

SFE	Supercritical Fluid Extraction
SH	Simple Hexagonal
TEM	Transmission Electron Microscopy
TEOS	Tetraethyl Orthosilicate
TGA	Thermal Gravimetric Analysis
UTS	Ultimate Tensile Strength
UV-Vis	UV Visible
XRD	X-Ray Diffraction

Variables

a	Van der Waal's Attraction Parameter
A	Cluster Surface Area
A_{cc}	Concentration to Generate Critical Cluster
b	Van der Waal's Repulsion Parameter
B	A Constant
B_J	Nucleation Constant
c	Concentration
c_1	Critical Point of Substance 1
c_2	Critical Point of Substance 2
c_∞	Concentration of Bulk Solution
c_{eq}	Equilibrium Concentration
c_i	Concentration at Surface Interface
c_{sat}	Saturation Concentration
D	Jet Diameter
Da	Damköhler Number
D_{AB}	Mass Diffusivity
E_{sl}	Energy per Surface Molecule
E_{ss}	Lattice Energy
g_b	Free Energy of Bulk Molecules
g_s	Free Energy of Surface Molecules
g_z	Free Energy of Cluster Size z
J	Rate of Nucleation
k_{CG}	Growth constant
k_d	Mass Transfer Coefficient
k_J	Nucleation Constant
k_r	Growth Rate Constant
k_{SN}	Surface Nucleation Growth Rate
n	Moles
N_{Re}	Reynolds Number
N_{Sc}	Schmidt Number

N_{We}	Webber Number
P	Pressure
p^b	Bulk Crystal Pressure
P_c	Critical Pressure
p^f	Fluid Pressure
P_r	Reduced Pressure
Q	Probability of a Crystal which has Reached Critical Concentration will Nucleate
R	Gas Constant
r	Radius of Cluster
R_G	Overall Mass Growth Rate
S	Supersaturation Ratio
T	Temperature
T_c	Critical Temperature
T_r	Reduced Temperature
u	Relative Velocity
V	Volume
V_c	Critical Volume
V_m	Molar Volume
V_r	Reduced Volume
w	Growth Parameter (usually between1 and 2)
x	Composition
x_{eq}	Molecules at Equilibrium
x_i	Composition at Interface
x_{ss}	Molecules at Supersaturation
z_b	Number of Molecules in Bulk
z_{bn}	Number of Nearest Neighbours of a Bulk Molecule
z_{cc}	Critical Cluster Size
z_s	Number of Molecules in Surface
z_{sn}	Number of Nearest Neighbours of a Surface Molecule
α	Crystal Growth Factor
β	Cluster Shape Factor
γ	Surface Tension

ΔE	Energy Change
ΔE_d	Activation Energy of Diffusion
ΔE_r	Activation Energy of Growth
ΔG	Gibbs Free Energy Change
ΔG_b	Bulk Gibbs Free Energy
ΔH	Enthalpy Change
ΔH_f	Enthalpy Change of Fusion
η	Viscosity
η_i	Effectiveness of Integration into the Crystal Surface
μ	Chemical Potential
μ_{eq}	Chemical Potential at Equilibrium
μ_{ss}	Chemical Potential at Supersaturation
ξ	Crystallographic Factor
ρ	Density
ρ_A	Antisolvent Density
ρ_c	Critical Density
σ	Supersaturation
υ	Crystal Growth Rate
υ_c	Molar Volume of Crystal
ω	Acentric Factor

Chapter 1 Introduction

The use of supercritical fluids (SCFs) for chemical processing offers a wealth of opportunities to the materials chemist. This has prompted several excellent texts and reviews on the subject.[1-5] This thesis documents examples of both conventional and novel uses of supercritical fluids and high pressure liquids to make and process materials in ways apparently superior to those used conventionally. This Chapter explains the properties of SCFs which are important to the processes described and details which effects are prominent in specific cases. Later Chapters will describe the synthesis of C_{60}(gas) intercalation compounds which have so far proved impossible to synthesise by any conventional techniques. The extraction and impregnation of mesoporous silica will also be discussed with description as to why this technique leads to synthesis of a superior product. A brief Chapter is devoted to preliminary results on the production of nano-peapods, carbon nanotubes filled with C_{60}. This offers the first low temperature synthesis of these compounds and could have a considerable impact on nanotechnology research.

The 'green' benefits of using supercritical fluids are due to the elimination of organic solvents and replacement with non toxic gases, most commonly CO_2. The use of compressed gases also allows more facile separation thus minimising processing and waste.[6,7] These 'green' benefits will not be emphasised further during this thesis, because advantages of the work are related to the specific properties of the fluids and their interactions with materials to which they are exposed.[6] This Chapter begins with a description of the nature of a supercritical fluid. It is deliberately abridged as many similar reports of supercritical nature are easily obtainable, an excellent starting point would be the thesis by Ke Jie who describes phase behaviour and mixing in much greater detail than will be mentioned here.[8] Limited information on the uses of supercritical fluids is given as a brief overview, again this can be found in greater detail in other locations[5,9-12] and is included only out of completeness. Introduction to each of the specific topics mentioned in this thesis will be made at the beginning of each Chapter.

An Introduction to Supercritical Fluids

Supercritical fluids possess several properties which are to the advantage of the process chemist. These have allowed uses of SCF to include extraction, particle fractionation and use as a reaction medium.[1-3] As a generalisation, supercritical fluids can be visualised as existing in a state between liquid and gas. For example they may possess the ability to dissolve materials in a manner similar to a liquid and then mix that material through mass transport similar to a gas.

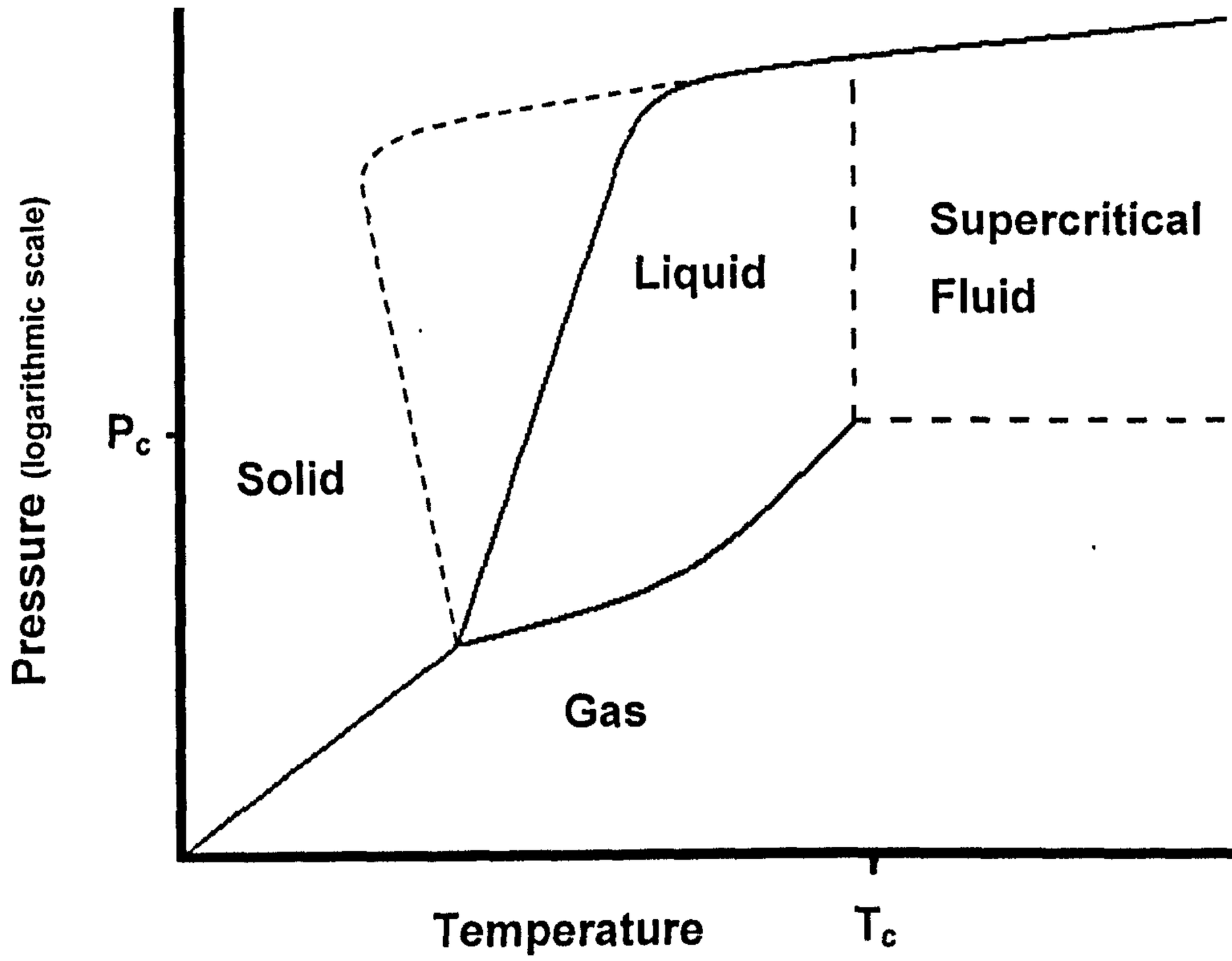


Figure 1-1: The phase diagram for a pure substance.[1]

In Figure 1-1 we see the phase diagram most associated with supercritical fluids. This diagram displays the phase changes of a pure substance and is similar for all pure systems. The only significant difference is the gradient of the solid/liquid line which can be positive or negative depending on the substance. Commonly this gradient is positive with increased pressure promoting formation of solid. In a few cases, for example that of water, the gradient is negative and increased pressure

promotes liquefaction, and thus provides the basis for ice skating. The region around the critical point is the most relevant to the work within this thesis. This, perhaps appropriately, proves the hardest region to model. Formally, as the pressure and temperature are raised and a material becomes 'supercritical', this region represents a removal of the boundaries between liquid and gas. An official definition of this point is given in Figure 1-2 where isothermal lines of varying pressure and molar volume offer a point of inflection where there is no longer any specific transition between the liquids and gaseous states.[13,14] This is given in Equation 1-1.

$$\left(\frac{\partial^2 P}{\partial V^2}\right)_T = \left(\frac{\partial P}{\partial V}\right)_T = 0$$

Equation 1-1: The mathematical representation of the critical point shows a point of inflection where an infinite change in volume causes no change in pressure, effectively the material becomes infinitely compressible.

Once the critical temperature, T_c has been exceeded, the fluid will never liquefy, regardless of applied pressure. This statement collapses at enormously high pressures when the fluid can be forced to solidify by the physical placement of molecules in close proximity to one another. This is, however, far beyond the practical limitations of the equipment used in this thesis. The fluid also will formally never become a "perfect gas" although density will drop until this point becomes moot. A simple example being nitrogen inside a cylinder at room temperature, which exceeds the critical parameters (T_c = -146.96 °C, P_c = 33.96 bar)[15] and is therefore supercritical but so far exceeds T_c, that it is effectively gaseous. To remove this confusion reduced variables are often used. These are defined in Equation 1-2 and, remarkably, analysis has shown that materials at the same reduced conditions will behave very similarly if not identically.[1] The reduced variables relate the actual conditions of a system with the critical parameters in question and so help to identify how a given material will behave in a given system. For example when discussing a supercritical fluid it is normal for $T_c < T < 2T_r$ and $P_c < P < 4P_r$, this isolates a region in which the useful properties of supercritical fluids are best utilised.

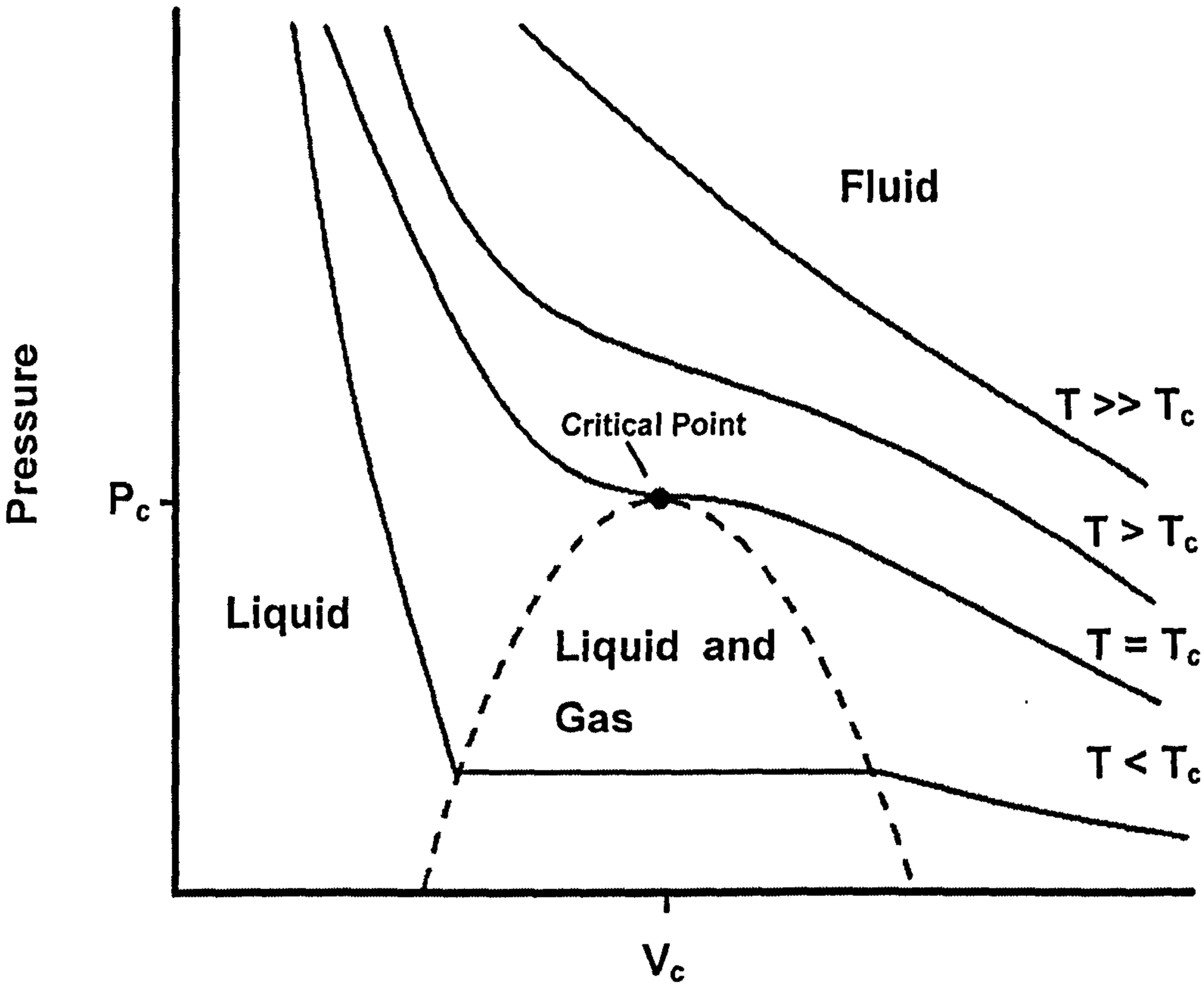


Figure 1-2: An alternative view of the phase diagram of a pure substance, plotting Molar Volume against Pressure. At the critical temperature and pressure a point of inflection exists, this offers mathematical information of the state of matter, Equation 1-1.

$$P_r = \frac{P}{P_c}, T_r = \frac{T}{T_c}, V_r = \frac{V}{V_c}$$

Equation 1-2: The reduced parameters of a material.

In Table 1-1 details are given of commonly quoted figures comparing the physical properties of supercritical fluids with liquids and gases. The table contains information for supercritical fluids under two separate conditions, these conditions being under different pressures. The higher pressure example ($P_r = 4$) demonstrates a situation where the fluid is behaving more like a liquid, while the lower pressure conditions ($P_r = 1$) shows behaviour closer to a gas. These figures give examples of

how the fluid properties can be tuned so as to create different conditions. This could be in separate experiments or changing conditions, and hence properties, during the same experiment. It should be noted that if we follow our example a supercritical fluid will be a poorer solvent than when in its liquid state and have reduced mixing ability than when in its gaseous state. The specific properties will be discussed in greater detail later in this Chapter.

Table 1-1: Some common physical properties of supercritical fluids, as compared to liquids and gases. The SCF data is given in two sections to provide information on the tuneable properties.[2,15-17]

Property	Liquid	SCF $T_r = 1$ $P_r = 4$	SCF $T_r = 1$ $P_r = 1$	Gas
Density (kgm^{-3})	800-1500	400-1000	200-500	1-10
Mass Diffusivity (m^2s^{-1})	$0.2\text{-}2\times10^{-9}$	1×10^{-8}	7×10^{-8}	$1\text{-}3\times10^{-5}$
Compressibility (MPa^{-1})	$1\text{-}5\times10^{-3}$	0.1-10	$\rightarrow \infty$	Very High
Viscosity (Pa s)	$0.2\text{-}3\times10^{-3}$	$3\text{-}9\times10^{-5}$	$1\text{-}3\times10^{-5}$	$0.1\text{-}2\times10^{-5}$
Thermal Diffusivity (m^2s^{-1})	$1\text{-}2\times10^{-7}$	$1\text{-}2\times10^{-6}$	$\rightarrow 0$	5×10^{-4}
Thermal Conductivity ($Wm^{-1}K^{-1}$)	0.1-0.5	0.07-0.1	0.04-0.07	0.03-0.04

Much work has been carried out in the attempt to predict the behaviour of gases. The most basic is given by the ideal gas equation, Equation 1-3. This rearranges to Equation 1-4 if we consider molar volume as in Figure 1-2.

$$PV = nRT$$

Equation 1-3: The ideal gas equation.

$$P = \frac{RT}{V_m}$$

Equation 1-4: Modified ideal gas equation with molar volume.

Equation 1-4 provides only limited information on gas phase interactions and does not contain real information on the repulsive and attractive interactions between molecules; it also assumes that molecules possess zero volume. It is only of real value when dealing with non-associating gases at low pressures. Obviously this is of extremely limited use for supercritical fluids which are neither. The van der Waal's Equation, Equation 1-5, introduces two parameters, a and b to represent the attractive and repulsive forces respectively. As we can see the attractive force a is reduced with respect to V_m^2 as the attractive forces have less influence as the volume increases. The repulsive forces are represented by the term (V_m-b) which represents the molecules having hard shells which reduces the volume available for the molecules to move. This term (V_m-b) is often referred to as the accessible or free volume.[18]

$$P = \frac{RT}{(V_m - b)} - \frac{a}{V_m^2}$$

Equation 1-5: The van der Waal's Equation

Since we know that, at the critical point, there is a point of inflection where Equation 1-1 holds true, it is possible to calculate the a and b parameters approximately from knowledge of the critical parameters of a material, Equation 1-6a,b. V_c is the critical volume, the maximum molar volume capable of generating P_c on heating to T_c.

$$a = 3P_cV_c^2 \qquad b = \frac{V_c}{3}$$

Equation 1-6a,b: The a and b constants can be calculated from a knowledge of the critical parameters.

These values can be returned to the van der Waal's Equation and give rise to the reduced equation of state, which compares all substances with respect to their reduced variables.[14]

$$\left(\frac{P}{P_c}+3\frac{V_c^2}{V^2}\right)\left(3\frac{V}{V_c}-1\right)=8\frac{T}{T_c}$$

Equation 1-7: The reduced equation of state.[14]

Table 1-2: Critical parameters of some commonly used substances.[1,2,14,15]

Substance	T_c(°C)	P_c(bar)	ρ_c(kg m^{-3})
Acetic Acid	321.6	57.2	351
Acetone	235.0	47	268
Ammonia	132.4	111.5	235
Carbon dioxide	31.1	73.8	468
Ethane	32.1	48.8	210
Ethanol	243.1	63.1	275
Ethene	9.7	50.9	220
Isopropanol	235.2	47.6	271
Methanol	240	81	272
Propane	96.7	42.5	220
Propene	91.9	46.2	223
Toluene	320.6	41.6	292
Water	374.0	217.7	322
Xenon	16.6	58.2	1155

The use of the Van der Waal's Equation is a good basis for calculations. However, it is insufficiently close to experimentally observed values to be used quantitatively. The equation was modified by Peng and Robinson in 1976 to include a cubic term in the attractive forces to define better the influence of the physical volume assumed by the molecules themselves and how this affects the attractive term, *a*.[19] The Peng-Robinson Equation of State (EOS) has been widely adopted for work with supercritical fluids and is given in Equation 1-8. This was one of a family of cubic equations which also includes the Redlich-Kwong and Soave equations.[20,21]

$$P = \frac{RT}{(V-b)} - \frac{a}{V^2 + 2Vb - b^2}$$

Equation 1-8: Peng-Robinson EOS, includes cubic term for the Van der Waal's *a* parameter.

With this equation it is possible to evaluate the *a* and *b* parameters as with the Van der Waal's Equation and values obtained are given in Equation 1-9a,b.

$$a = 0.45724\frac{R^2T_c^2}{P_c} \qquad b = 0.07780\frac{RT_c}{P_c}$$

Equation 1-9a,b: The *a* and *b* parameters as calculated from the Peng-Robinson EOS.

This has still been found wanting as a true representation of the conditions with results for V_c and Z_c (compressibility) still 11% out compared to the experimental results determined for CO_2. The cause of the inaccuracy was determined to be the absence of any representation of the non-spherical nature of most of the molecules studied and the subsequent rotation thereof. This acentric term, devised by Pitzer is given in Equation 1-10.[22]

$$\omega = -\log P_r(T_r = 0.7) - 1$$

Equation 1-10: The acentric factor as defined by Pitzer.[22]

This factor allows modelling of this behaviour inside the EOS. It was modified by Peng and Robinson in 1976 to include experimental information, see Equation 1-11.

$$a(T) = a(T_c)\{1 + (0.37464 + 1.54226\omega - 0.26992\omega^2)(1 - T_r^{1/2})\}^2$$

Equation 1-11: The acentric factor is introduced into the Peng-Robinson EOS.

This can then be used to express the Peng-Robinson EOS in terms of its reduced variables, Equation 1-12, and hence to show that the equation obeys the law of corresponding states.

$$P_r = \frac{3.2529T_r}{V_r - 0.25308} - \frac{4.83825\{1 + (0.37464 + 1.54226\omega - 0.26992\omega^2)(1 - T_r^{1/2})\}^2}{V_r^2 + 0.5062V_r - 0.06405}$$

Equation 1-12: The Peng-Robinson EOS including the acentric factor in reduced terms.[2]

The temperature dependence of the *a* parameter allowed Soave to perform quantitative calculations on pure compounds and mixtures.[21]

Table 1-1 compares the properties of a supercritical fluid to those of either liquid or gas. As already stated, supercritical fluids exhibit properties between those of a liquid and a gas. This is directly related to their usefulness as media. Diffusion in a fluid, for example, is one aspect where supercritical fluids have a real advantage over liquid media. The interaction at a phase boundary will be superior to that of a liquid. The effect of this can be viewed as the result of the lower density of the fluid allowing longer mean free paths of molecules. Often, mass transport numbers are quoted as Schmidt numbers, Equation 1-13, which suggests that supercritical fluids are poorer at transferring mass than conventional solvents. This is due to the lower solubility of materials in the fluid affecting the rate of movement. Although this is an important effect in terms of reaction dynamics, in the work contained in this thesis, the effect is less important as the rate of movement of material is largely governed by the experimental conditions rather than relative solubilities.

$$N_{Sc} = \frac{\eta}{\rho D_{AB}}$$

Equation 1-13: Schmidt equation, where η is the viscosity, ρ is the density and D_{AB} is the mass diffusivity.

Another important factor which influences supercritical fluid properties, particularly solvation, is the presence of local areas of greater density.[23-25] This gives rise to the fluid's ability to dissolve more material than would otherwise be expected in a homogeneous fluid of a given density. The local density augmentation is related to the bulk properties and is observable even below the critical point so is not a true critical phenomenon. The presence of a co-solvent which has a greater affinity for the solute than the fluid can cause local densities to be up to 10 times higher than that of the bulk fluid, as measured by fluorescence spectroscopy.[26-28] Density augmentation is more pronounced at lower densities,[24] which is why the effect is larger in supercritical fluids than in conventional solvents.

The viscosity of a fluid is also important in understanding the physical conditions of a given process, particularly when a pressure drop through a restricted opening is involved, as in the RESS process described below.[13] The viscosity of a fluid does not, however, change linearly with density, it is instead often referred to as the kinematic viscosity, η/ρ, which can be plotted as a function of pressure. Under isothermal, conditions a pressure increase will drop the kinematic viscosity from high levels at low pressure, reach a minimum at the critical point then rise slightly above the critical point.[16,29,30]

The thermal conductivity of a fluid is important, particularly when dealing with reaction chemistries because one of the roles of a solvent is to give an even and controlled distribution of heat throughout a reaction mixture. In the case of supercritical fluids, the thermal conductivity is always lower than that of a corresponding liquid, Table 1-1. This means that care should be taken to ensure that heat is distributed evenly throughout a reactor. Thermal conductivity varies approximately linearly with density but shows a positive deviation at the critical point.

The study of supercritical fluids requires a detailed knowledge of phase behaviour and accompanying this, the understanding of the phase diagrams which are commonly used to describe the possible phases. The simplest system to examine is a binary mixture. It has been shown that there are 6 different possible phase diagrams for a binary mixture; these are given in Figure 1-3.[1]

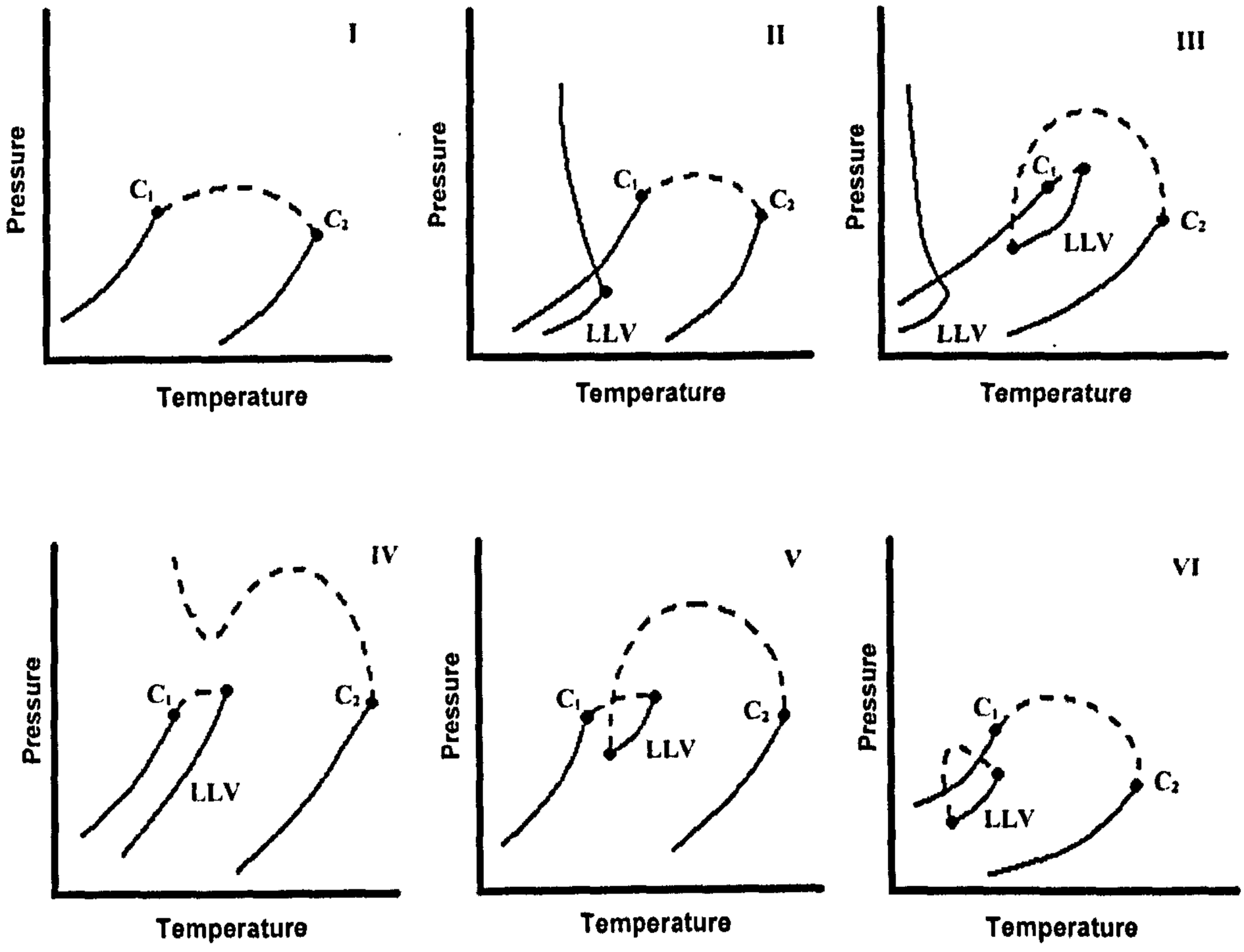


Figure 1-3: The six types of critical phase interfaces as shown by a pressure vs. temperature plot, as classified by Scott, van Konynenburg and Street.[31-33]

These six phase diagrams can be further split into two subgroups. Class I (Diagrams 1,2 and 6) represent mixtures with similar molar masses and critical temperatures. Class II (Diagrams 3,4 and 5) describe mixtures containing one light fluid and one much heavier, involatile component. This will become important when discussing

the antisolvent work on C_{60} in Chapter 2 and Chapter 3. The simplest form of the diagram is Type I and is shown with the example of CO_2 + Toluene, Figure 1-4.

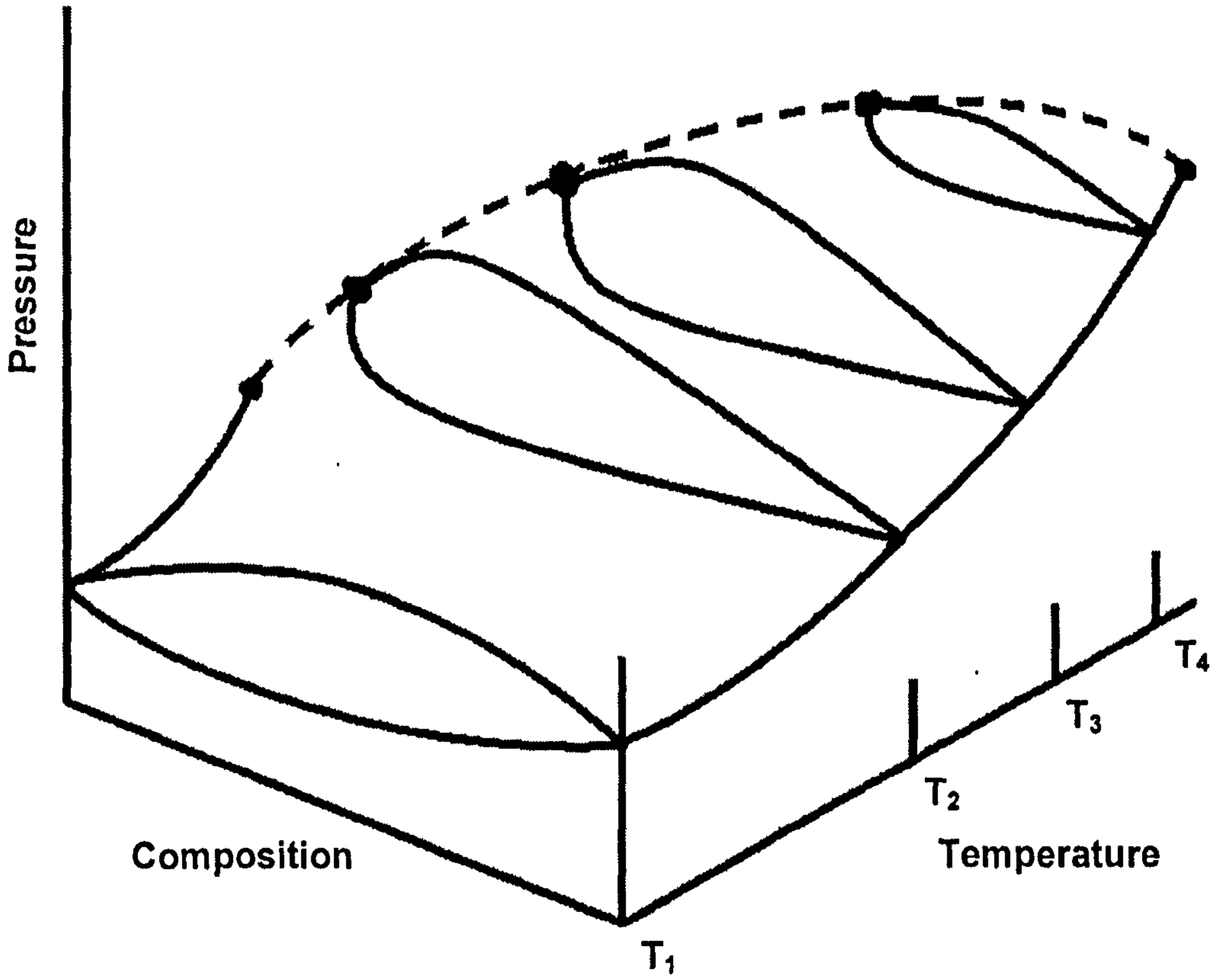


Figure 1-4: The P,T,x diagram for a CO_2 + toluene mixture close to the critical point. The two phase region shrinks as the temperature is increased. Above this region the components are miscible.

The phase behaviour of many systems are known and literature reviews are available to cover published systems up to 1999.[34-38]

Supercritical Fluid Behaviour as a Solvent

Use of supercritical fluids as solvents has taken a number of forms, including extraction, chromatography, reaction medium and particle formation through rapid expansion of supercritical solution (RESS). The topic with least relevance to this thesis, the use of supercritical fluids as a reaction medium will not be discussed further although there are several excellent references to the topic.[4,12,39-43] The use of supercritical fluid for extraction (SFE) is undoubtedly the area of the science which has received the most attention from industry.[1] The extraction of caffeine from coffee, Figure 1-5, is an often quoted example of SFE with much of the world's coffee being decaffeinated with CO_2. The extraction of natural products using supercritical fluids is also a large and increasing industry.[44-46] A real benefit of SFE being the fact that CO_2 is designated as a harmless solvent by government bodies; so it can be used without further processing requirements. The coupled effect of a liquid-like solubility and increased diffusivity allows supercritical fluids to be highly penetrating while able to still dissolve significantly large quantities of solute for removal. The use of supercritical fluids for extraction is extensively published in the literature and will be discussed in Chapter 6 on mesoporous silica template extraction.

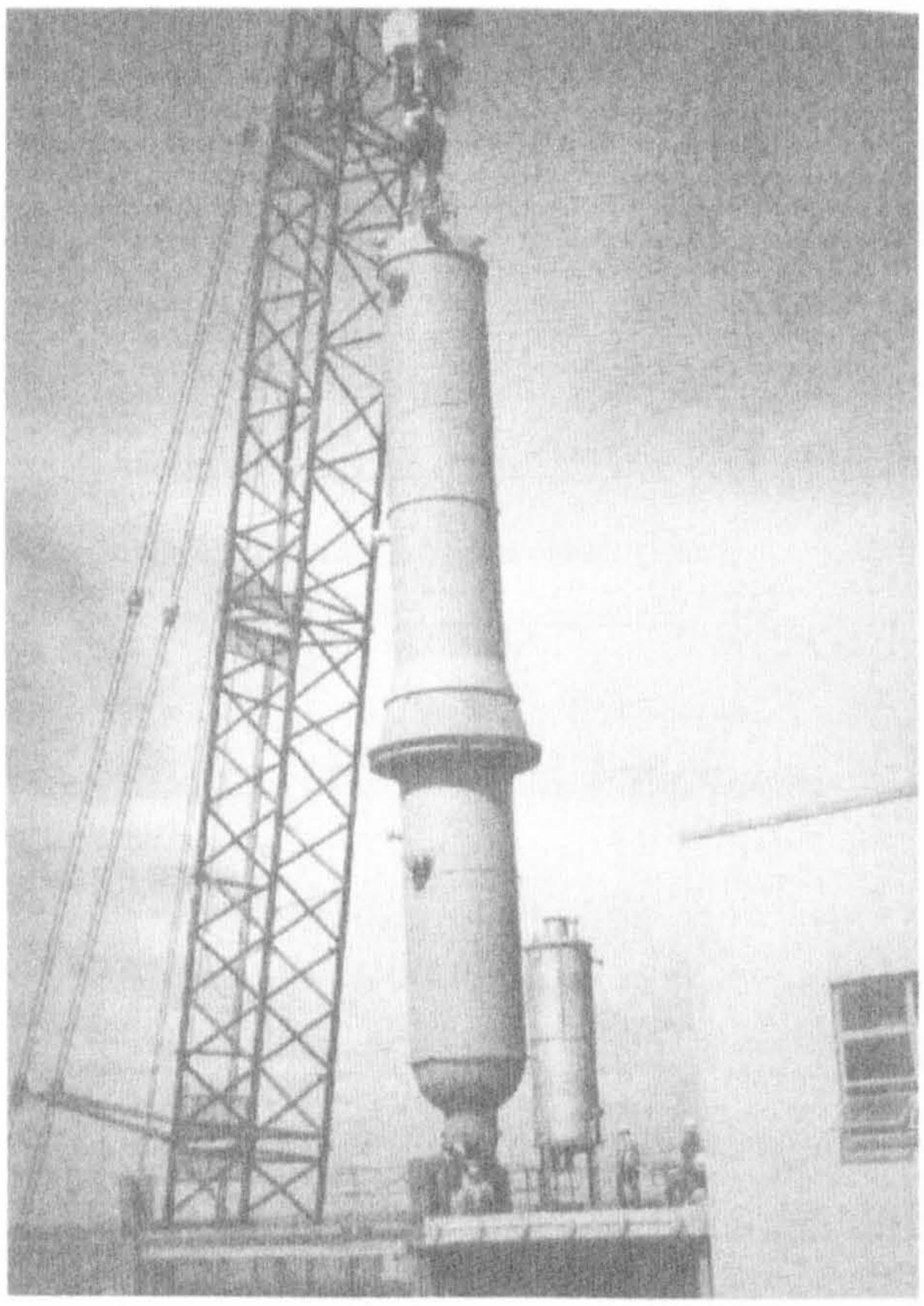


Figure 1-5: Maxwell House Coffee Company decaffeination plant in Houston Texas.[1]

Another use of supercritical fluids which relies on the solvent abilities and the diffusivity is the use in chromatography (SFC).[47,48] Supercritical fluids provide a good compromise between the low solubility of involatile compounds in gas chromatography and the low diffusion coefficients which can result in broad peaks in liquid chromatography.[49]

The final use of SCFs which is relevant to this thesis in the sense that it provides a method for generating nano- and micro-particles is the rapid expansion of a supercritical solution (RESS). RESS provides an example of one of the first recorded experiments using supercritical fluid solutions by Hannay and Hogarth in 1879, who observed crystal forming on rapid depressurisation during their investigation of the solubility of solids in gases.[50] This work, in practice, was very similar to the RESS process used today, which involves the dissolution of a solute in a supercritical fluid and then spraying that solution through a nozzle into a vessel at lower pressure. The technique was first introduced in its present form by Smith[51] and was used initially in a number of instances to provides microfine pharmaceutical particles[52,53] and ceramic precursors.[54] The obvious problem with RESS is that the solute must be soluble in the supercritical fluid and, although much work has involved the use of modifiers and surfactants,[55,56] the poor solubility of most materials in SCFs remains the biggest obstacle to this technique.

Supercritical Fluid Behaviour as an Antisolvent

The use of supercritical fluids as an antisolvent is a good way of overcoming the low solubility of materials in the most commonly used supercritical fluids as the processes make use of this very property. It has been known for many years that a supercritical fluid can be used as an antisolvent.[57-61] Initial interest stemmed from research by the pharmaceutical industry.[62-65] The particular advantage of the use of SCFs in this field was possibility of processing materials and leaving them completely free of solvent. Research has also been made into the preparation of superconductor precursors[60,66-68] and on the processing of polymers.[69-71]

The initial investigation of what is now termed the "GAS process" was started in 1984 by Krukonis.[57] This was followed by Gallagher in 1989[72] who demonstrated the first use of what was later named the "PCA process" by Dixon.[73] Several other abbreviated terms exist, including aerosol solvent extraction system (ASES), solution enhanced dispersion with supercritical fluid (SEDS) and supercritical antisolvent (SAS). For the purpose of this thesis, however, PCA will be used to describe a system where solution is added to antisolvent and GAS to describe where antisolvent is added to a solution.

The antisolvent techniques capitalise on the rapid interaction between supercritical fluids and conventional solvents and the insolubility of most organic materials in supercritical fluids. The techniques themselves rely on the miscibility of the supercritical fluids with the organic solvent which allows rapid mixing while reducing the solvent power of the organic solvent by increasing interaction between the solute and the SCF and by reducing the overall density of the solution. The techniques provide a very neat route to materials of a controlled particle size, completely free of solvent. By varying the conditions of the precipitation, it is possible to create particles of highly interesting morphology including spheres, balloons and "partial" balloons. The morphology is controlled by the way in which the solvent and antisolvent interact and gives clues as to what is happening inside the precipitation vessel. Many attempts have been made to predict the morphology of particles which are produced, sometimes with contradictory results.[74-77] Papers by Werling recently attempted to make sense of part of the process by examining the mass transfer in droplets. [78,79] This remains only one of several factors which must be taken into account, including the thermodynamics, hydrodynamics and nucleation kinetics. These have been dealt with by separate researchers as independent influencing factors but a model for the whole process still does not yet exist. Thus the process of supercritical antisolvent precipitation remains an experimentally driven technique.

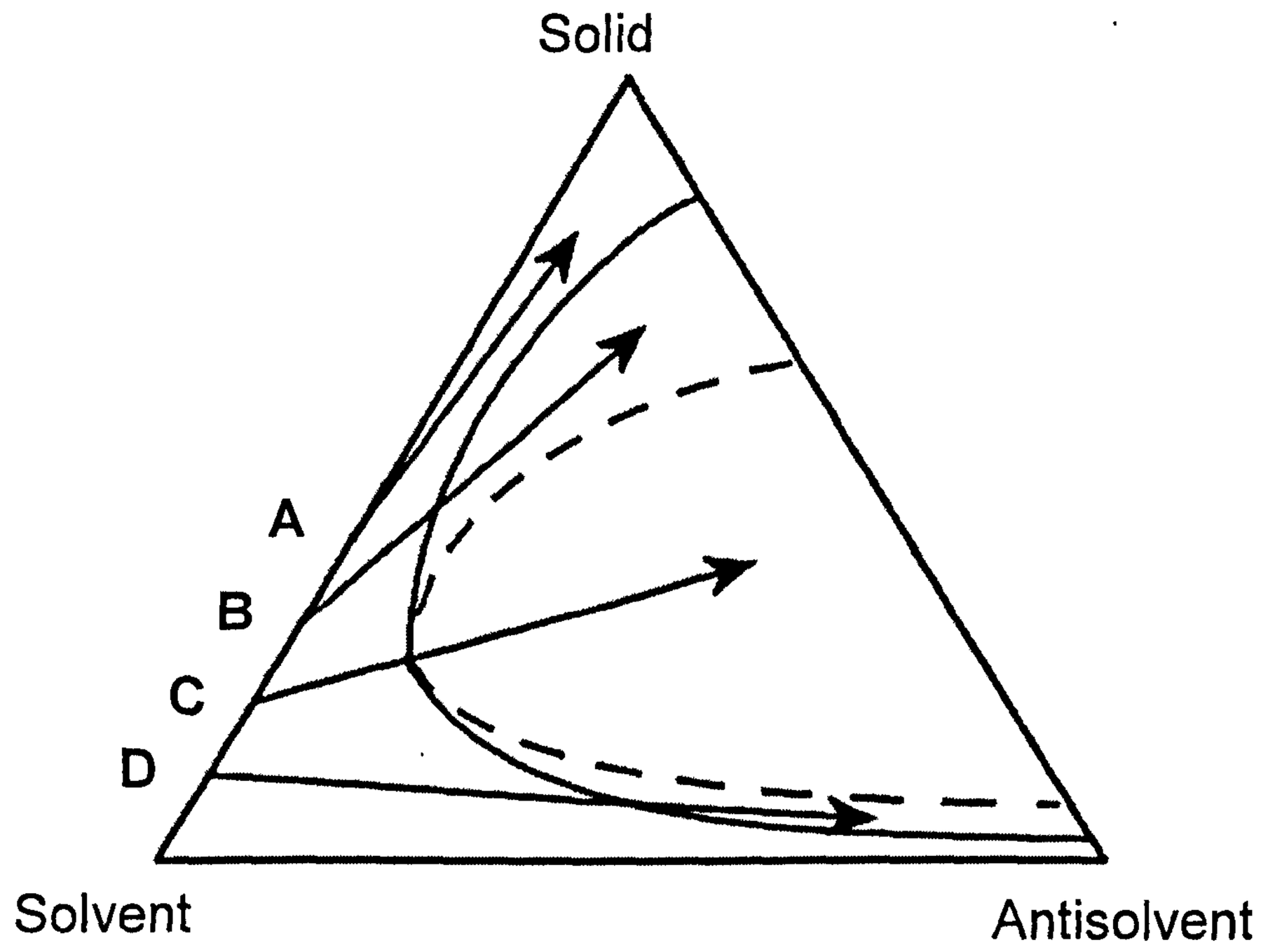


Figure 1-6: Diagram of potential mass transfer pathways during antisolvent precipitation as suggested by Dixon[73] and updated by Werling.[78] The solid line represents the binodal curve and the dotted line the spinodal curve.

Figure 1-6 shows the possible ways in which mass transfer can occur as the antisolvent process takes place in a polymer system. The diagram was first produced by Dixon[73] and was originally created to rationalise the production of polystyrene particles from a toluene solution but the concept is universally applicable.

To interpret Figure 1-6,[73,79,80] a droplet of solution should be considered, with analysis of how the introduction of the antisolvent affects it. The binodal and spinodal curves divide the diagram. These represent the boundaries between an ordinary solution, a metastable region and a supersaturation region. A metastable region is one which has exceeded the maximum concentration of the solution yet there is no direct system within the solution to initiate precipitation, while a supersaturated solution is one where spontaneous precipitation can occur. This will be discussed in much greater detail in Chapter 3. For now it is sufficient to examine the paths of the solution in different situations. In path A, the mass transfer is mainly out of the droplet; the solvent evaporates into the fluid with little inward movement of antisolvent. This results in the precipitation of a dense particle for each droplet,

Figure 1-7a.[81] In path B, the system crosses the binodal curve on the solvent side. Antisolvent diffuses into the droplet as the solvent is evaporating, ensuring that, when the solute nucleates, there is gas inside the solid which creates holes inside the structure. The result is the production of a solid particle which is porous, Figure 1-7b.[82] If even more antisolvent dissolves into the droplet the spinodal curve can be breached, path C, and the precipitation occurs through spinodal decomposition. This is direct precipitation through supersaturation of the solution. This is the route in which fine structure is observed in the product rather than discrete particles. There are a number of examples of different types of specific fine structure for specific systems. In general the common fine structure observed includes needles, balloons and burst balloons. The example of a burst balloon is given in Figure 1-7c.[60] The final path to antisolvent action is the crossing of the binodal curve on the antisolvent side. In this path the antisolvent diffuses very rapidly into the droplet and initiates nucleation by mechanical forces of the highly turbulent conditions, producing the smallest discrete molecules, Figure 1-7d.[66]

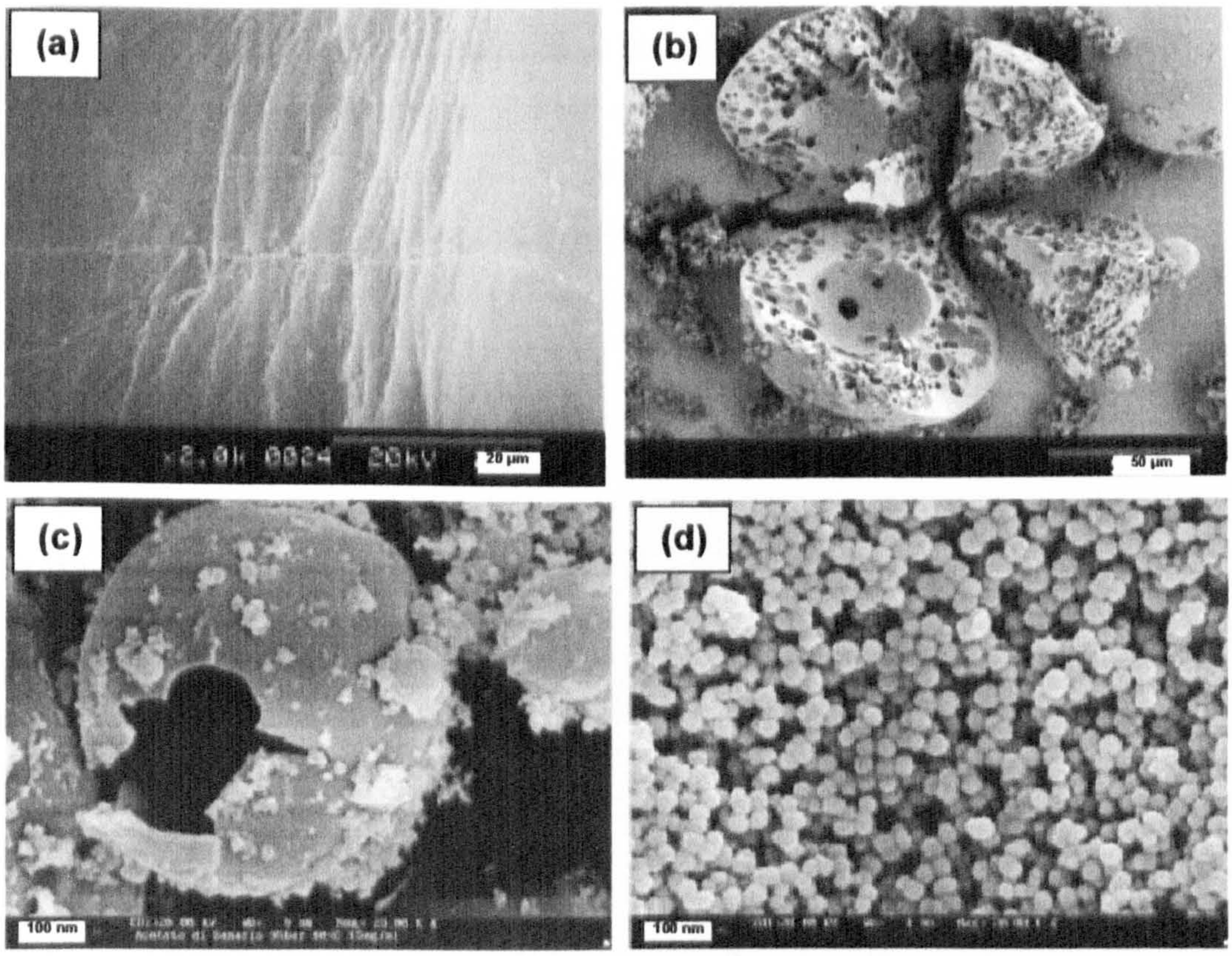


Figure 1-7a-d: The different types of phase separation products as dictated by Figure 1-6. (a) provides an example of very weak interaction between the solvent and antisolvent. In this case Tan[81] uses HFC 143a as the antisolvent with a toluene solution, the miscibility of the system is so low that a dense solid is produced. (b) shows the precipitation of a relatively concentrated sample of copper indomethacin with CO_2 by Warwick.[82] The influx of solution is slow and large, porous structures are created. (c) is a samarium acetate balloon, as prepared by Reverchon.[60] Finally the even distribution of discrete particles (d) is shown. This time small, discrete particles of actinium acetate are observed, by Reverchon.[66]

A recent review by Jung[83] lists the literature and patents on all forms of supercritical antisolvent precipitation published up to late 2000. A more detailed review of specifically GAS and PCA as understood up to 2000 can be found in the thesis by Webster which excellently describes the most important examples of the use of supercritical antisolvents.[16] The exact arrangement of apparatus varies between

research groups and will not be discussed in detail here. Instead an overview of the precipitation using a compressed antisolvent (PCA) and the gas antisolvent (GAS) process are described in their most basic forms. Examples are given to bring the reader up to date on recent work. For information pre-2000, the reader is directed to the review of Jung.[83] Several general review papers have been written recently, mostly aimed at the pharmaceutical industy.[84-93] For more general information, the papers by DeSimone[93] and Thiering[91] are recommend.

PCA

The PCA process is shown schematically in Figure 1-8. A solution is injected into the vessel which is filled with the chosen antisolvent. Nucleation occurs rapidly and nano-particles of the solute precipitate. These nano-particles can then be washed with more antisolvent to ensure that the final product is completely free of solvent.

One measure of supercritical mixing which is often quoted it conjunction with antisolvent processes is the Webber number (N_{We}). This is the ratio of inertial forces to the tension forces in a system. It is used to predict the size of the droplets in a spray.

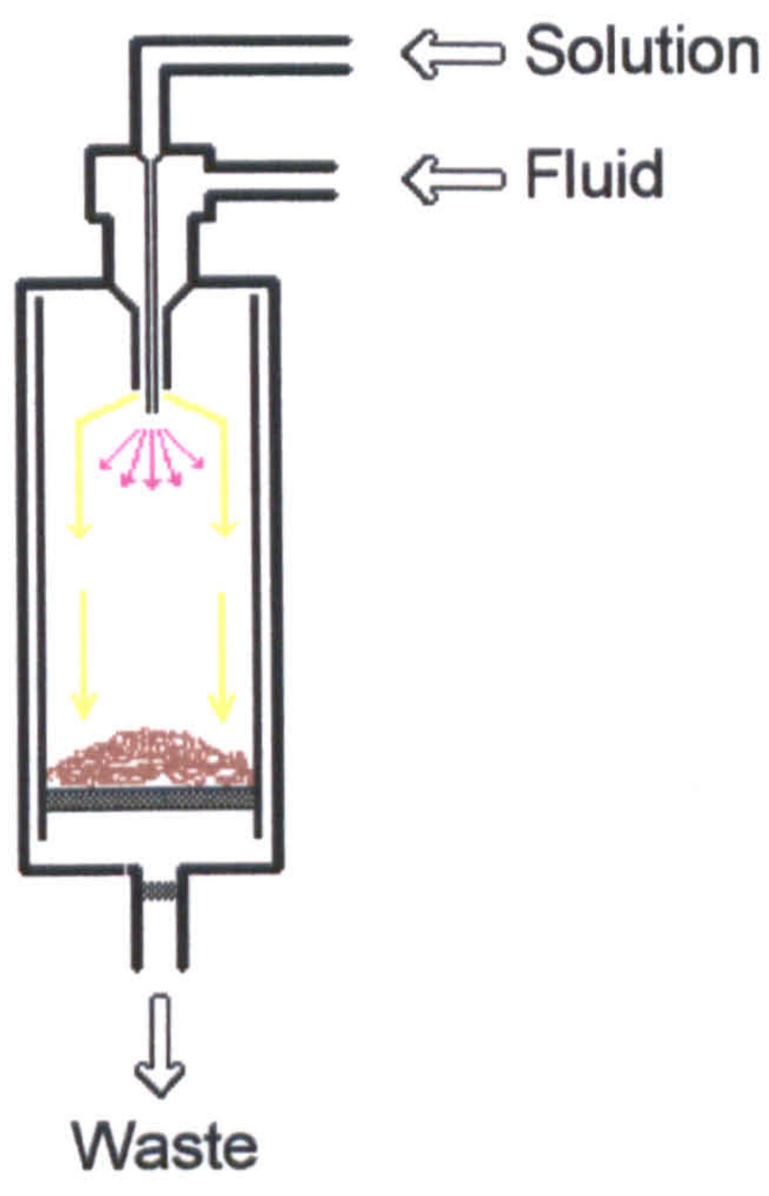


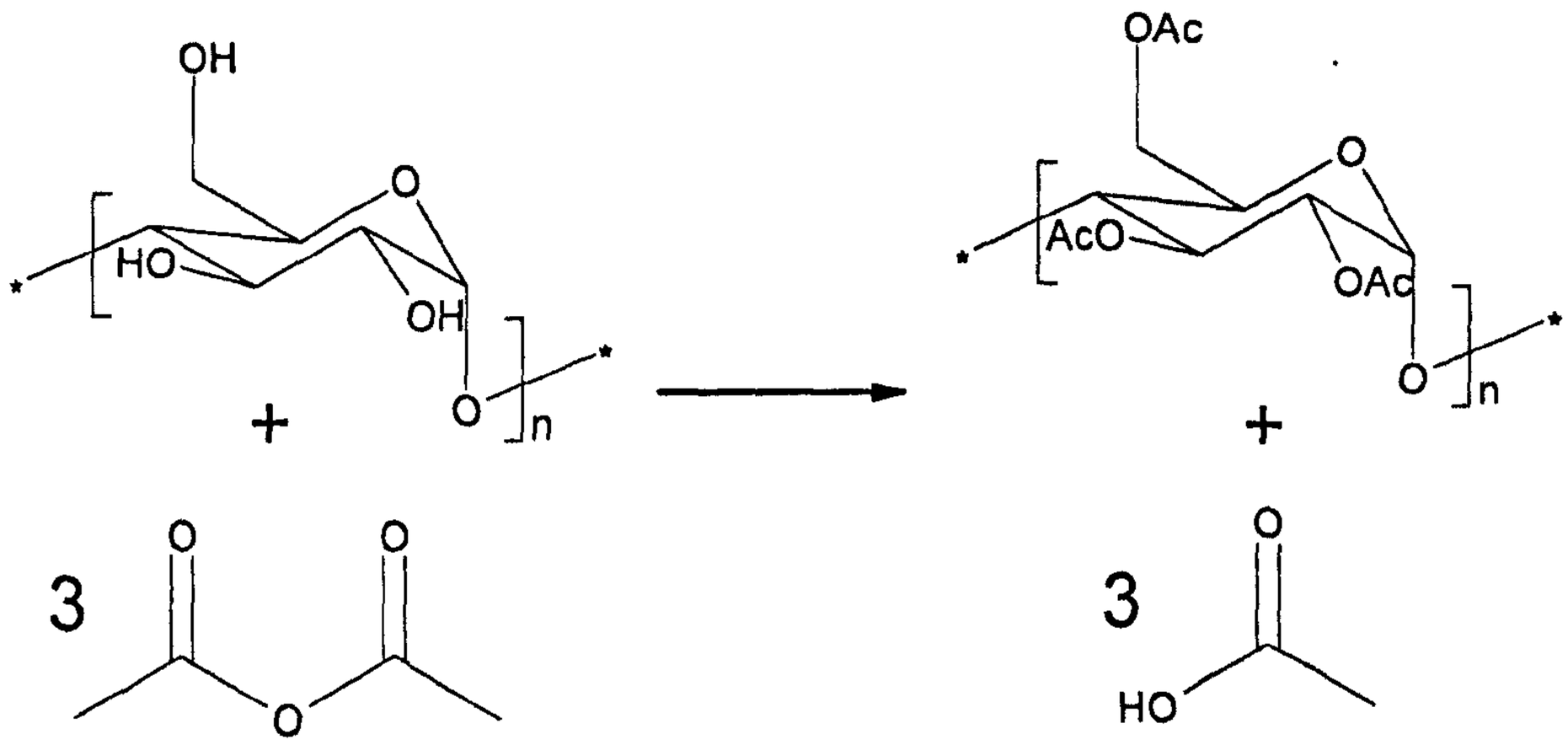
Figure 1-8: The PCA process for generation of nanoparticles. Solution is sprayed into a vessel containing antisolvent gas. The rapid mixing of the solvent and gas generates high supersaturation ratios and precipitates the solute as nanoparticles.

$$N_{We} = \frac{\rho_A u^2 D}{\gamma}$$

Equation 1-14: The Webber number for predicting jet break-up.

where ρ_A is the antisolvent density, u is the relative velocity, γ is the surface tension and D is the jet diameter. The surface tension between a supercritical fluid and a liquid under miscible conditions is zero, and under highly soluble conditions is very low. Also, the fact that during the antisolvent process the density and the jet velocity are relatively high, leads to a large Webber number and so indicates there will be many droplets as the spray will be broken up very rapidly. It should be noted, however, that although this equation is often mentioned, it only provides a semi-quantitative measurement of the jet break-up since the actual surface tension is not known, theoretically becoming zero at the critical point but in practice having a very low but finite quantity.

Initially, the goal of my doctorate was to investigate the potential modification of starch in supercritical CO_2, thus providing an essentially 'green' route to a biodegradable polymers. Over time, this proved not to be fruitful but one of the experiments performed during this initial study illustrates the PCA technique well. The precipitation of starch acetate was performed using PCA. Investigation at ICI research laboratories in Wilton had produced acetylated starch by treatment of starch with acetic anhydride and CO_2, see Equation 1-15.[94]



Equation 1-15: The formation of acetylated starch by application of acetic anhydride.

The specific results of these experiments were disappointing and produced brown material, indicating cleavage on starch chains and opening of the end glycosides through caramelisation. Precipitation using a compressed antisolvent was performed to process the material after reaction. The progress of these experiments are shown in Figure 1-9. The initial white powdered starch (a) was reacted under supercritical conditions and produced the brown porous solid (b) of starch acetate. This was then dissolved in chloroform (c) and filtered (d) before the use of PCA (e). The resultant powder is shown as (f) and was very similar in appearance to the starting starch. In this example the technique produced a powdered polymer which would be potentially suitable for injection moulding. This would be impossible for the brown cake which was retrieved from the original reactor. The use of PCA as a technique is tremendously expensive for material processing, however, and so is only worth performing on very valuable products, hence the interest with pharmaceuticals and superconductor precursors. For this reason the precipitation of starch acetates has very little future, the main advantage of which is its cheapness. This experiment does, however provide a very graphic example of what PCA can achieve.

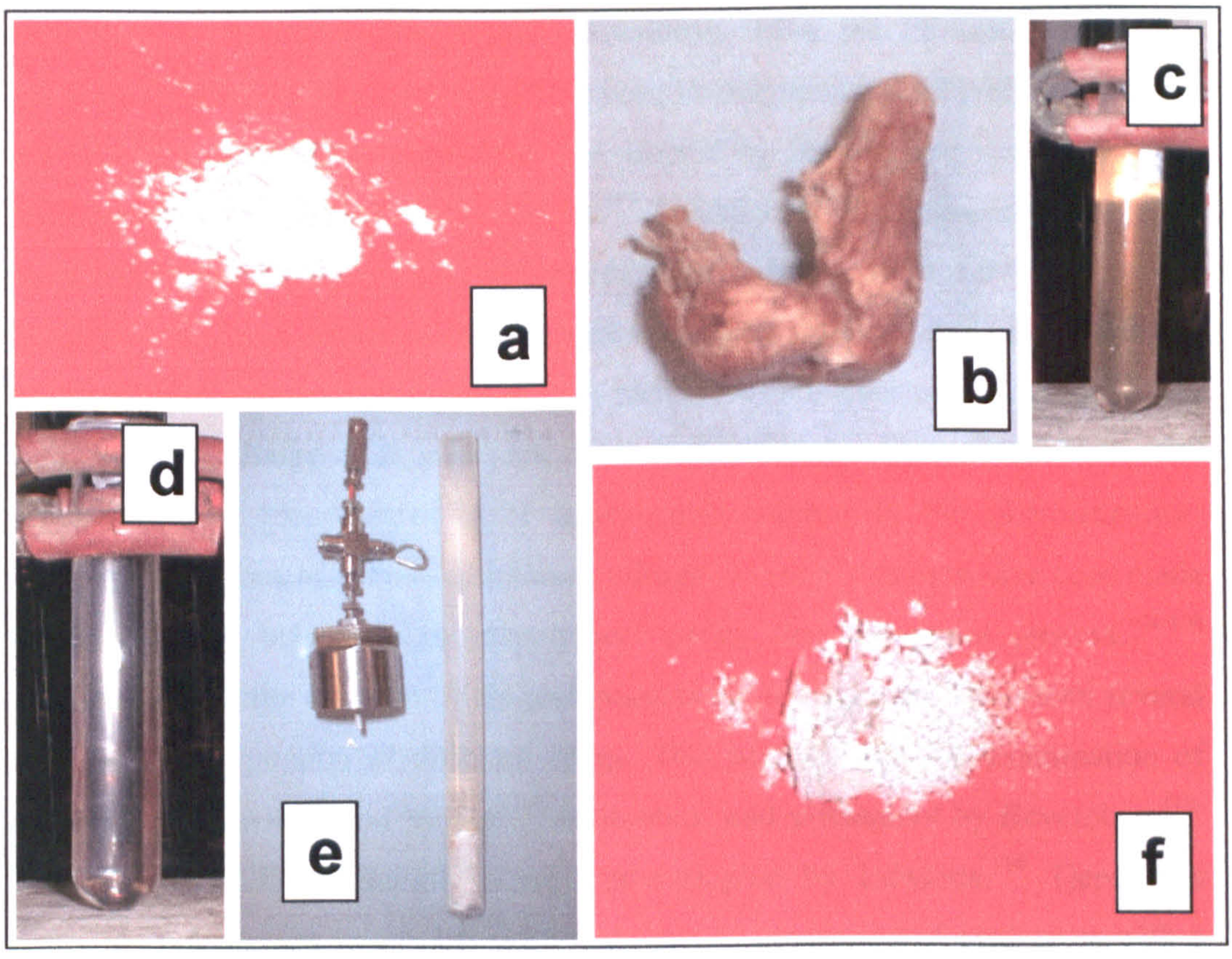


Figure 1-9: Starch (a) was reacted with acetic anhydride under supercritical CO_2 (b), dissolved in chloroform (c), filtered (d) and precipitated using CO_2 (e) to leave white powder similar to the starting material (f).

The ability to manipulate physical size and morphology has permitted the production of particles tailored for a specific purpose. Bradford Particle Design, who performs this technique commercially, currently own patent rights to it.[95]

The majority of recent work involving supercritical antisolvents has centred around PCA or one of its derivatives. The only new feature of the technique has been introduced by Chattopadhyay who added ultrasonic vibrations to the tip of the injection nozzle. By doing this he improved the micronisation of the solution and achieved smaller nanoparticles. This allowed particles to be generated which were consistently lower than 300 nm in size. He has precipitated biologically active compounds including proteins,[96] antibiotics[97] and griseofulvin,[98] an anti fungal agent. During his research into griseofulvin, he co-precipitated this compound with poly-lactic acid (PLA) in an attempt to generate a controlled release system. He

performed a similar co-precipitation experiment using the ultrasonic nozzle to generate nanoparticles of magnetically responsive polymers loaded with magnetite.[99] The concept of an ultrasonic nozzle was adopted by Snavely and used during his work with precipitation of human insulin.[100] The concept of micro-encapsulation of materials in polymers by co-precipitation of polymer and active agent was also used by Elvassore who precipitated microcapsules of insulin inside PLA.[101] This is similar to the work of Taki who precipitated PLA blended with the herbicide, Diuron[102] and Tu, who precipitated PLA with lysozyme and parahydroxybenzoic acid.[103] The precipitation of biopolymers is of considerable interest to the pharmaceutical industry as a means of controlled release of drugs. As such, attempts have been made to describe the behaviour of biopolymers during the antisolvent process.[104-108] Continuing with the example of the pharmaceutical industry there have been several studies on precipitation of different drugs. This has included the examination of steroids by Warwick[82] and Velaga,[109] antibiotics and salbutamol by Reverchon,[110-112] paracetamol by Shekunov[113] and Carbmazepine by Edwards.[114] Tiepel has returned to one of the original uses of PCA, that of processing of explosives with a suggestion for manipulation on a pilot plant scale.[115] Reverchon has also continued his work on superconductor precursors with a study of the precipitation of europium and gadolinium acetate.[67] Investigation of tartaric and nicotinic acids were made by Krober[116] and Rehmann[117] respectively. Soy lecithin precipitation was examined by Magnan[106] and Bardens,[118] Bronze red pigment particles by Hong, [119] and a cycloolefin copolymer was precipitated with HFC-134a by Hsu.[120] Inorganic precipitations have been made by Yeo examining crystals of $BaCl_2$[121] and by Hutchings and Lopez-Sanchez have continued the work on vanadium phosphate started as a collaboration with Webster.[122-124] Studies to gain a better understanding of the antisolvent process were made by Kordikowski who examined the effect of precipitation on polymorphism of sulfathiazole[125] and by Subra who prepared information to help the design of future precipitation systems. [126] A general review of the technique was also prepared by Reverchon.[127]

GAS

The GAS process is also a technique which has been available for several years and typically involves mixing of antisolvent gases with miscible solutions. The solution is held inside a steel vessel and the antisolvent gas is rapidly pumped in. Mixing takes place immediately, often with the help of stirring, and the solute is precipitated in an even manner which often exhibits very controlled size distribution. A diagram of this basic apparatus is shown in Figure 1-10. This technique is widely used as an analogue of PCA experiments. The mixing is not as constant or as fast as with the PCA process, however, and so a greater range of particle sizes is usually observed. It is possible to process a greater amount of material using this technique and so this technique is less expensive to perform than PCA. It is therefore viable to use it on materials which have a lower added value than with PCA. Compared with conventional synthetic routes, however, it remains expensive. As mentioned above the GAS process was explored in great detail in the review by Jung[83] and the thesis by Webster.[16] Below are details of experiments which have been carried out since the publication of these sources.

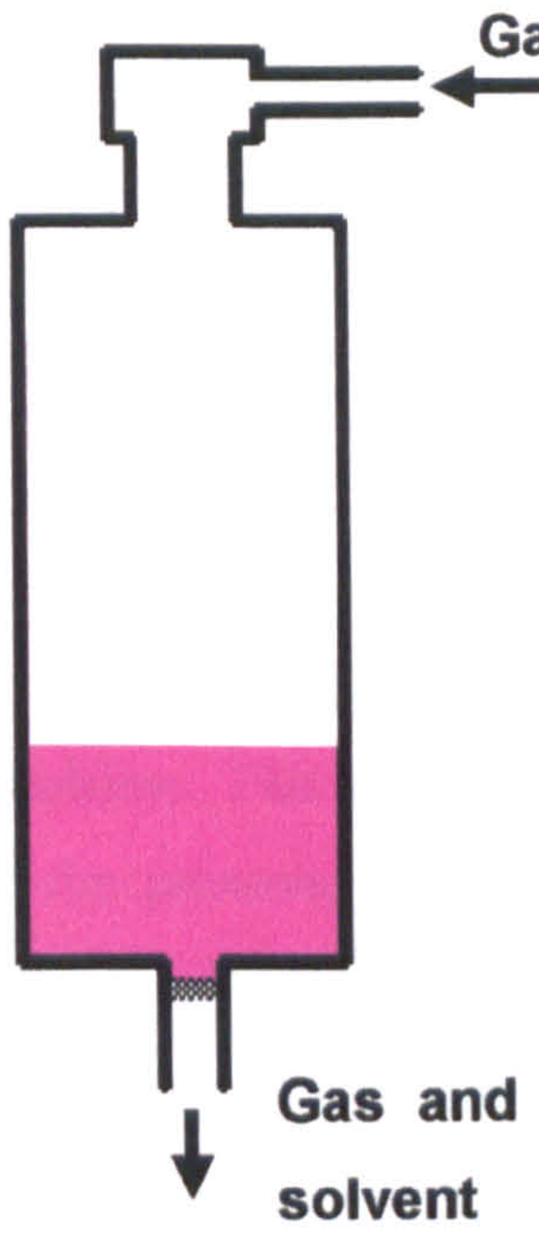


Figure 1-10: A (GAS) experiment involves the rapid introduction of a supercritical antisolvent to a solution held in a batch vessel.

Fewer specific precipitations have been carried out over the last 2 years using the GAS compared to the PCA technique. Work with the GAS technique has involved study of the actual process with attempts to model the process by Muhrer[128] and advice is given on the volumetric expansion by Elvassore[129] and Badilla.[130] Ke offers advice on the solvent to use[131] and Bristow explains the effect of supersaturation on the process.[132]

Compounds which have been examined using the technique have included the precipitation of β-carotene by Cocero,[133] hydrocortisone by Corrigan [134] and HMX by Cai.[135] Thiering has provided information on the effect of experimental conditions on the precipitation of the model proteins lysozyme, insulin and myoglobin.[136,137] The precipitation of a non steroidal anti-inflammatory drug, copper indomethacin was shown by Warwick[82,138] Similar to the PCA review, work on the encapsulation of drugs with polymers was performed with research on the co-precipitation of insulin and PLA by Elvassore[139] and carbamazepine and poly-ethylene glycol (PEG) by Moneghini.[140]

A new technique which has recently been developed by Han's group in China involves the GAS precipitation of a reverse micro-emulsion. This uses water suspended inside isooctane (2,2,4-trimethyl pentane) by the presence of sodium bis(2-ethylhexyl) sulfosuccinate (AOT). The aqueous phase contains the material to be precipitated. This precipitation occurs when CO_2 is introduced to the system. Han's group has so far precipitated nanoparticles of bovine serum albumin (BSA),[141,142] lysozyme,[143] ZnS[144] and silver[145] using this technique. The method performs well at precipitating material which is water soluble and would be more difficult to generate nanoparticles of by conventional means. The use of the micro-emulsion, however, only allows very small quantities of material to be made per experiment.

Chapter 2 C_{60}(Gas) Intercalation Via the PCA and GAS Techniques

In this Chapter the production of C_{60}(gas) intercalation compounds using the PCA and GAS techniques are discussed. The Chapter begins with a description of C_{60} and fullerenes and explains the previous work which has been carried out on the preparation of C_{60}(gas) intercalates. This begins with the initial discovery of the ability of C_{60} to hold gas molecules and progresses to the use of supercritical antisolvents for their generation. Information is then given on the use of the PCA technique to generate new intercalation compounds and the beginning of characterisation of those compounds. This is followed by a novel GAS experiment to gain further insight into these compounds. This Chapter represents the initial investigation into the synthesis if C_{60}(gas) intercalation compounds. Supercritical fluids are used as antisolvents in a conventional manner. Problems created during the synthesis are discussed and lead to suggestions for a better route to these materials, which is described in Chapter 3.

C_{60} and C_{60}-Intercalation Chemistry

C_{60} was discovered by Kroto *et al.* in 1985 during experiments designed to simulate carbon nucleation inside red giant stars. Unintentionally, yet spectacularly, they provided evidence to the existence of a third allotrope of carbon.[146] Due to its truncated icosahedral shape, it was named after the architect Buckminster Fuller, famous for the design of buildings containing geodesic domes.[147] Work on C_{60} was limited to mass spectra until 1990 when Krätschmer *et al.* devised a technique to generate fullerenes on a much larger scale using an arc discharge between two graphite rods.[148] C_{60} proved to be only the most obvious member of a new family of

compounds, which have been named the fullerenes. The structure of fullerenes was shown to be closed cages of carbon, the most easily elucidated of which being the truncated icosahedron of C_{60}. The next most obvious fullerene is C_{70} which can be imagined as a C_{60} molecule cut in two with a ring of 10 carbon atoms placed between the two hemispheres, see Figure 2-1.[149] Many more fullerene structures both larger and smaller than C_{60} are known, often with several isomers (*eg* C_{80} possesses 7 possible structures).[150] While the price of C_{60} and C_{70} has fallen dramatically the price of higher fullerenes remains prohibitively high for many groups. This has meant that the bulk of current research has centred around C_{60}.[151]

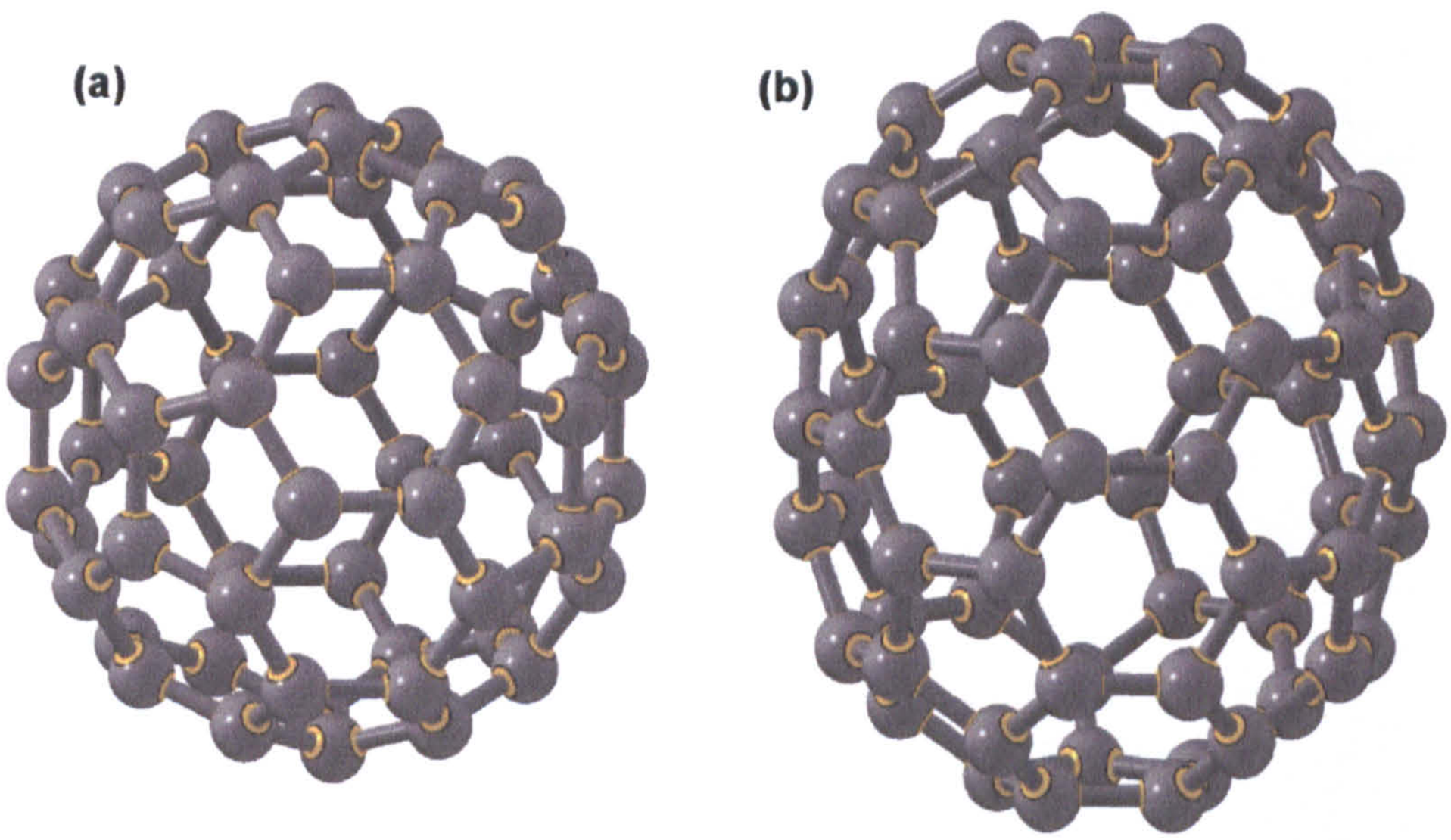


Figure 2-1: Diagrams of the structures of (a) C_{60} and (b) C_{70}.

The largest of the known fullerenes are nanotubes of carbon which are identical in structure to a graphite sheet wrapped round into a tube with the ends capped with smaller fullerene-like hemispheres. These hemispheres can be removed to give hollow tubes by treatment with oxidant[152-154] or, more recently, supercritical water.[155] The structure, synthesis and properties of these nanotubes will be dealt with in greater detail in Chapter 4.

The discovery of fullerenes prompted unprecedented interest with research carried out from every conceivable angle on this completely new and seemingly

revolutionary material. Research into uses of C_{60} and fullerenes suggested applications as diverse as HIV inhibitors,[156-160] solar cells[161] and superconductors.[162-169] The vast quantity of research performed on fullerenes, which even includes research on the quantity and background of fullerene research itself[151] will not be discussed further except in specific sections in respect to the properties relevant to the work in question.

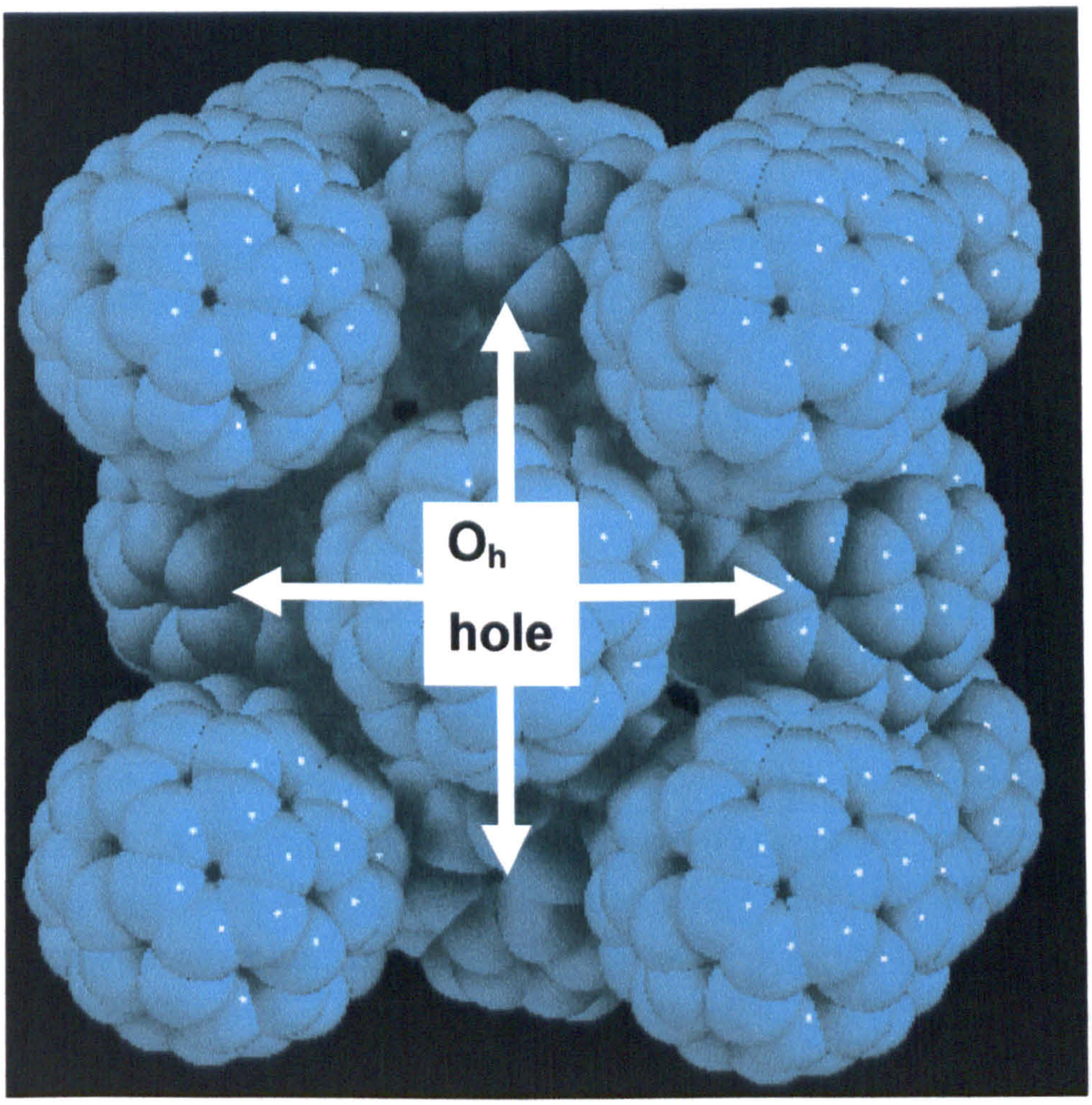


Figure 2-2: Face centred cubic lattice of C_{60}. Large octahedral holes between the C_{60} spheres are indicated.

The solubility of fullerenes in most solvents is generally poor compared to common organic compounds. Kroto isolated the C_{60} by dissolution into toluene. Later many solvents were reported to dissolve fullerenes and several were shown to be superior to toluene. Information on the solubility of C_{60} is available[170-173] and is a useful reference point when trying to choose a new solvent for work with fullerenes. One interesting feature of fullerene solubility is that maximum solubility is reached at 7

°C, as reported by Ruoff *et al.*[174] This was ascribed to the influence of a phase change in the solid. The solid lattice structure of pure C_{60} is a face centred cube at room temperature, see Figure 2-2,[149] with a lattice constant of 14.16 Å.[175] This is known to revert to a simple cubic lattice at 260 K with reported ΔH values by DSC for this change of 6.6 and 7.0 kJ mol^{-1}.[176,177]

One feature of fullerenes is the ability to hold a significant pressure of gas within its solid structure by van der Waal's forces. This ability is due to the large octahedral holes in the solid structure, these are visible in Figure 2-2. This discovery led to the suggestion that C_{60} might be used as a gas storage medium.[178] The species would be capable of holding *ca.* 40 bar of intercalated gas at atmospheric pressure which could be released in a controlled manner through diffusion at room temperature or on heating.

Assink reported the first instance of intercalation into a C_{60} lattice with his work on the intercalation of molecular oxygen.[179] This was further analysed by Belahmer in 1993.[180] This property was only a curiosity until Schirber found intercalation of He and Ne but failed to intercalate Ar during C_{60} lattice compressibility studies.[181] The field was extended by Gadd, who introduced heating of the sample to high temperatures to open the fullerene structure sufficiently to facilitate diffusion. This hot isostatic pressing technique (HIP) typically involved pressures in excess of 1.5 GPa and temperatures over 500 °C. Several publications, mainly by Gadd, Holleman and Schirber detail the expansion of the field with the preparation and characterisation of C_{60} intercalates of He,[182] Ne,[183,184] Ar,[185-188] Kr,[189] Xe,[190] O_2,[179,180,191-194] N_2,[194] H_2,[179,195] CO,[192,193,196-198] CH_4,[199] CO_2[200,201] and N_2O.[202] Details of the behaviour of molecules in the C_{60} holes is available for CO[192,193,196-198] and CH_4[199] studies on intercalation of C_{70} has also been carried out.[203] Experimentation was, however, always limited by the ability of solid fullerenes to accept gaseous matter physically forced into it and the stability of the materials to these high temperature conditions.

Work on fullerene(gas) intercalates culminated with publication of a review[178] by Gadd in 1999 detailing gas intercalate species published up to that date. Schirber has

been credited as the originator of the intercalation phenomenon even though the absorption of CO_2 into C_{60} solid was noted by Nagano as early as 1994 in his studies using supercritical CO_2.[204] Nagano's work predates the HIP research performed by Gadd and suggests that the extreme pressures required by this technique were not actually necessary for the successful intercalation of molecular species to C_{60}. Gadd also failed to mention the initial research performed on oxygen absorption[179] and research performed on the methane intercalate prepared by Morosin.[199] His review did include attempts to intercalate the largest species to that date, namely CF_4, SF_6 and C_2H_6. Evidence of the intercalation of CF_4 was presented but the other compounds failed. Gadd claimed that the conditions necessary to achieve intercalation using the HIP technique (typically 1.7 GPa and > 500 °C) were causing polymerisation of the substrates. This placed the intercalation of larger, more complex gas molecules out of the reach of the HIP technique. The review also contained detailed calculations of the lattice-hole sizes in the fullerenes and indicated that intercalation of hydrocarbons larger than CH_4 was unlikely.

Preparation of fullerene(solvent) intercalation compounds of a wide range of systems are known. These are similar to the gas species although generally are easier to prepare and result in intercalation of several solvent molecules per C_{60} molecule and a major rearrangement of the crystal lattice. These compounds are usually formed either by conventional antisolvent precipitation by placing a layer of antisolvent on top of a C_{60} solution, by simply evaporating a solution to dryness or by vapour deposition. Dyachenko discusses these in detail in his review.[205] The study of these solvate complexes is a whole topic in itself and is not covered in detail here.

The physical limitations of the intercalation techniques left a gap containing a series of compounds too large and thermally unstable to be intercalated as a gas but with too low a boiling point and solubility for C_{60} to be as a solvent intercalate. A novel approach to this problem came with the use of supercritical CO_2 as an antisolvent for precipitation of $C_{60}(CO_2)$.[206] This intercalate was already known at the time, although the precipitation route provided a method for production of a superior product (maximum intercalation level 0.95 instead of 0.90). The new supercritical route was also useful in the ease of preparation, requiring only moderate pressures and mild temperatures. This represented a major step forward in the production of

these intercalation compounds. It was believed that instead of CO_2, small hydrocarbon gases could be used as the antisolvent. It was possible to build the intercalates on a molecular level by controlled reduction of the solvating power of solutions of C_{60}. Soon after, Chattopadhyay published a similar synthesis of C_{60} nanoparticles, however, no reference was given to the existence of a CO_2 intercalate.[207] The nanoparticles produced were an order of magnitude smaller than those prepared by Field, however, and this could explain why CO_2 was not detected.

The experimental conditions used during Field's investigation were much less forcing than the HIP technique, as an order of magnitude lower temperature and two orders of magnitude lower pressures were required. These conditions were much less likely to damage the materials or produce the problems associated with polymerisation, encountered by Gadd.

PCA

PCA experiments were performed to acquire particles of the new compounds. The initial investigation in to these materials was begun by Webster.[16] He and Field, having very successfully synthesised and characterised $C_{60}(CO_2)$,[206] progressed into the intercalation of novel species, namely N_2O, C_2H_4 and C_2H_6. Webster collected small quantities of these intercalation compounds with some assistance from the author. This research provided a new route to the N_2O intercalate and the first evidence of the hydrocarbon compounds. It is these hydrocarbon intercalates that we are interested in. Webster collected IR for both of these intercalates, and MAS ^{13}C NMR and some PXD data for the $C_{60}(C_2H_4)$ compound. At this time the techniques detailed by Field were still being employed.[206] These techniques were a standard PCA experiment performed in the sapphire tube view cell (see Appendix I) and a 'slow grow' experiment where a dish of solution was agitated lightly in a larger view cell, see Appendix I. These techniques will be discussed more in the section on the GAS process. Webster's techniques provided a reasonably small quantity of the PCA material (*ca.* 100 mg per experiment) and a very small quantity of the larger 'slow grow' product (*ca.* 50 mg per experiment). These quantities were enough to obtain

reliable IR data, although MAS ^{13}C NMR and PXD was be less reliable as will be discussed later.

The starting point for this investigation was to recreate the PCA experiments to obtain the two intercalates as carried out by Webster. Investigation was also made into the possibility of synthesis of the new intercalates of $C_{60}(C_3H_6)$ and $C_{60}(C_3H_8)$. The experiments were performed in a larger vessel, similar to the work done on $C_{60}(CO_2)$. This was the Keystone extraction vessel using a 75 μm capillary tube as the inside of a coaxial nozzle, Figure 2-3, to maximise jet break-up and dispersion of solute material, as suggested by Mawson.[208] The details of the apparatus are given in Figure 2-4 and in Appendix I.

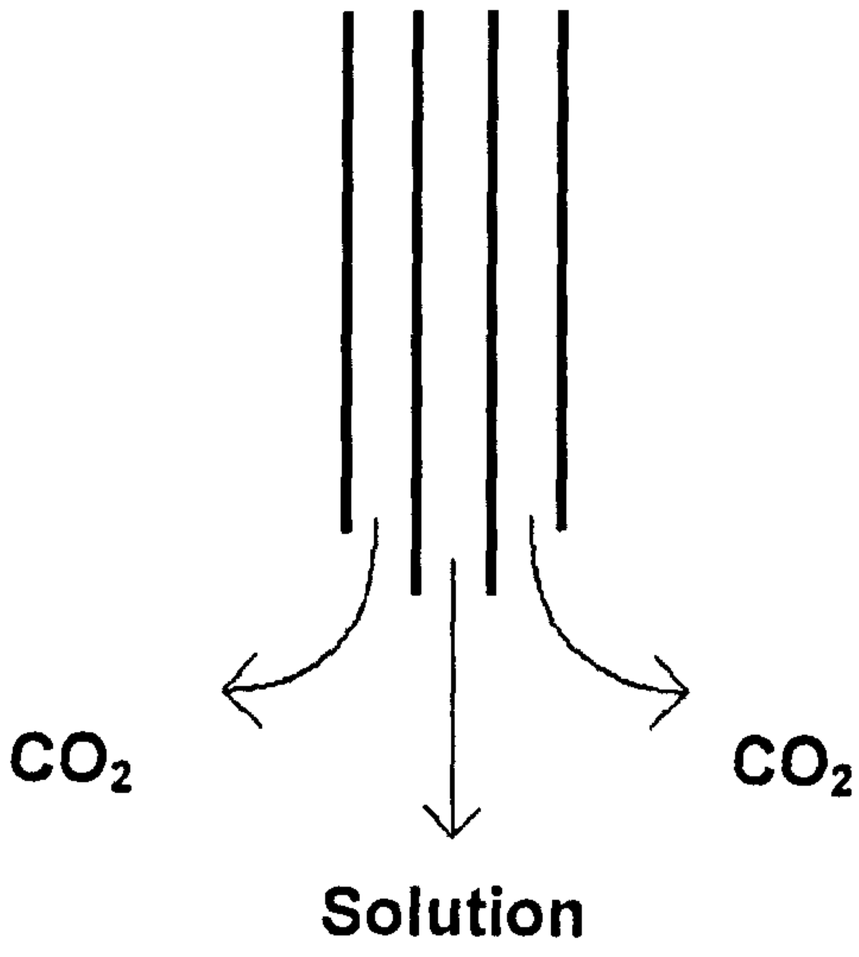


Figure 2-3: The simplest form of coaxial nozzle to maximise jet break-up. CO_2 flows down the outside of the tube while the solution to be precipitated flows down the centre through a capillary tube. Rapid mixing occurs at the point at which the two mix and nanoparticles of material are produced.

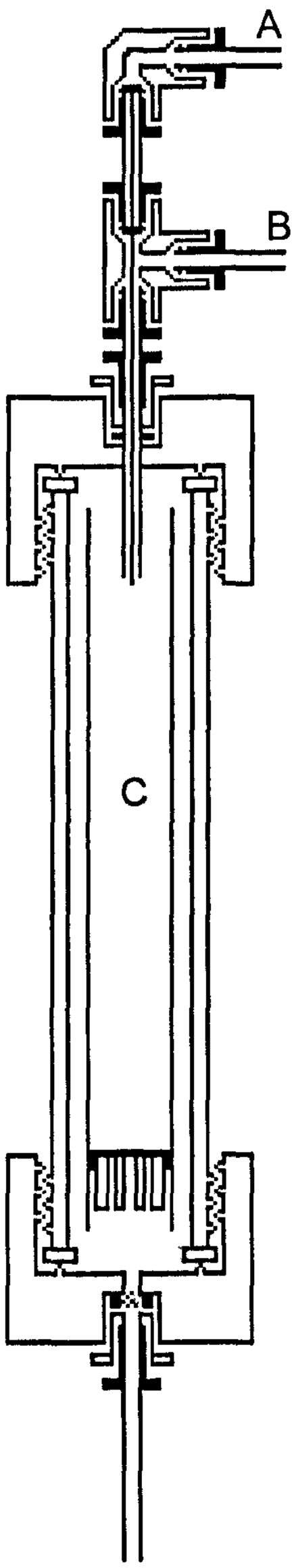


Figure 2-4: PCA apparatus used in this work. A hole was drilled through the nut and a new Teflon seal was made to accept a piece of 1/16" tubing. This tubing was fitted with a length of GC capillary tubing in an arrangement to allow flow of two separate materials which will not mix until the tip of the capillary tubing. The capillary tubing was held in place using a plastic tube which was attached using Valco fittings. A glass tube fitted with a filter paper and a perforated Teflon bung was used inside the steel vessel to catch the precipitate as it was formed.

The vessel was pressurised using the antisolvent gas and a flow of 10 ml min^{-1} was established for 5 min using a Pickel pump. Gas progressed along the inside of the 1/16" tubing but outside of the capillary tubing, introduced from point A on Figure 2-4. This flow was stabilised and the entire system checked for leaks under pressure. A feed of pure solvent was fed down the centre of the capillary tubing at a rate of 0.1 ml min^{-1} from point B. The general mixing flow was established and the pure solvent was then replaced with a solution of C_{60}. This flow was continued until it was believed that there had been sufficient precipitation to ensure a reasonable sample had been collected. The flow was then switched back to pure solvent for 5 min, the

solvent flow was then stopped and the gas flow continued for a time sufficient to ensure removal of any residual solvents. The vessel was then depressurised slowly through the base of the vessel over 10 min and the glass tube removed to collect the sample precipitate from point C. The experimental setup is shown in Figure 2-5.

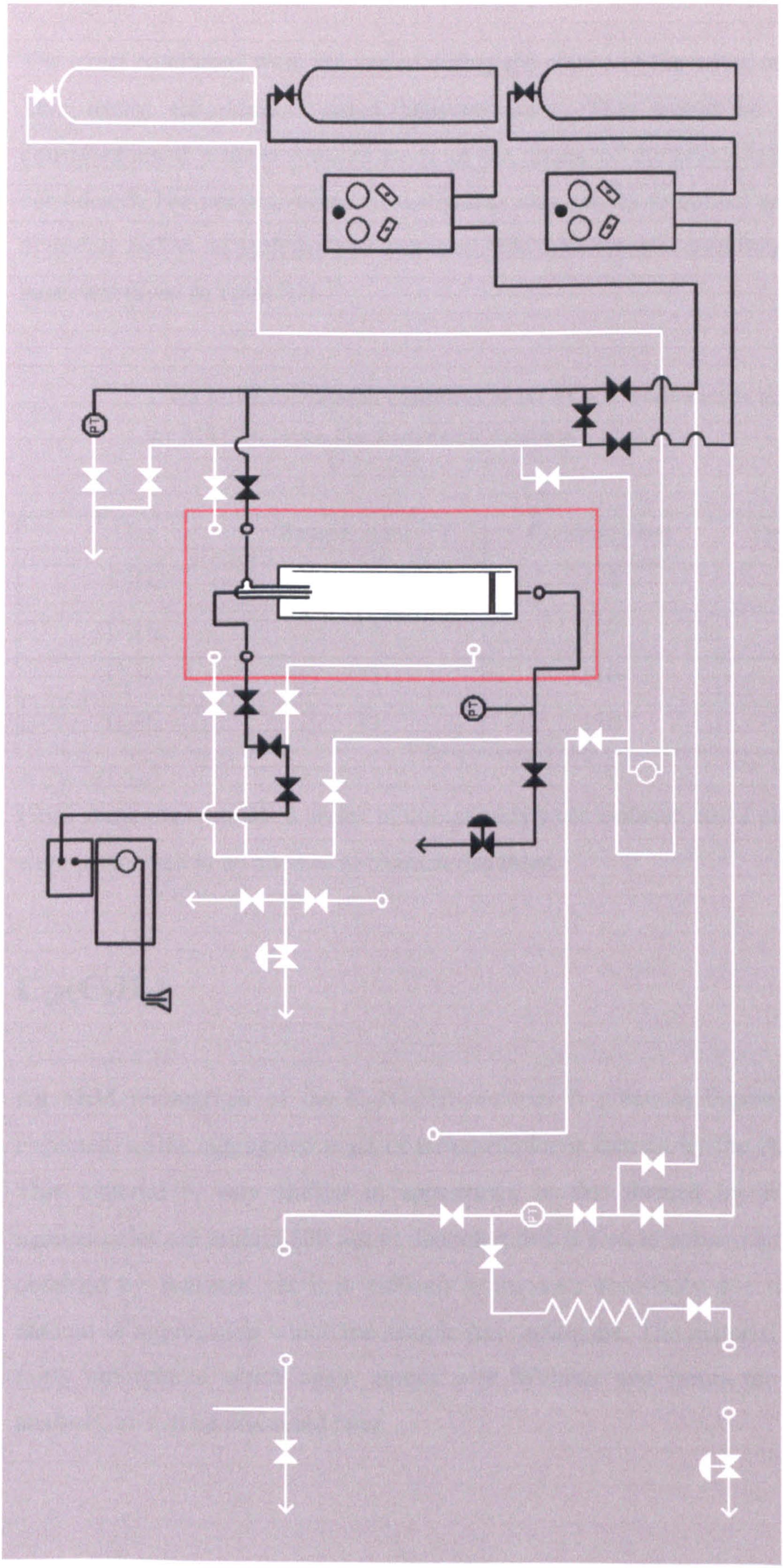


Figure 2-5: The PCA equipment inside the general experimental design.

The exact conditions were not varied during the course of the series of experiments. This meant the density varied between gases. This would be an important consideration if a more detailed study of the nature of the precipitation was to be considered. The purpose of this investigation was simply to collect and analyse the materials and so no such method was used. The experimental conditions for the four gases are given in Table 2-1.[15]

Table 2-1: Experimental conditions of the PCA Experiments as from the NIST Webbook thermodynamic database.[15]

Gas	Temperature / °C	Pressure / bar	Density / gcm^{-3}
C_2H_4	35	110	0.31
C_2H_6	35	110	0.37
C_3H_6	35	110	0.52
C_3H_8	35	110	0.50

From these experiments a series of compounds were isolated. SEM and IR analysis were performed in an attempt to characterise them.

$C_{60}(C_2H_4)$

An SEM photograph of the $C_{60}(C_2H_4)$ material is given in Figure 2-6. As was expected, a fine aggregated mass of nanoparticles is formed by the PCA technique. This material is very similar in appearance to that formed by Webster.[16] The nanoparticles are around 500 nm in diameter; this is also in agreement with the data obtained by Webster, yet it is difficult to measure accurately due to the extreme amount of aggregation which the sample has undergone. The material appears to be fairly amorphous which again agrees with Webster and limits the use of PXD analysis, as will be discussed later.

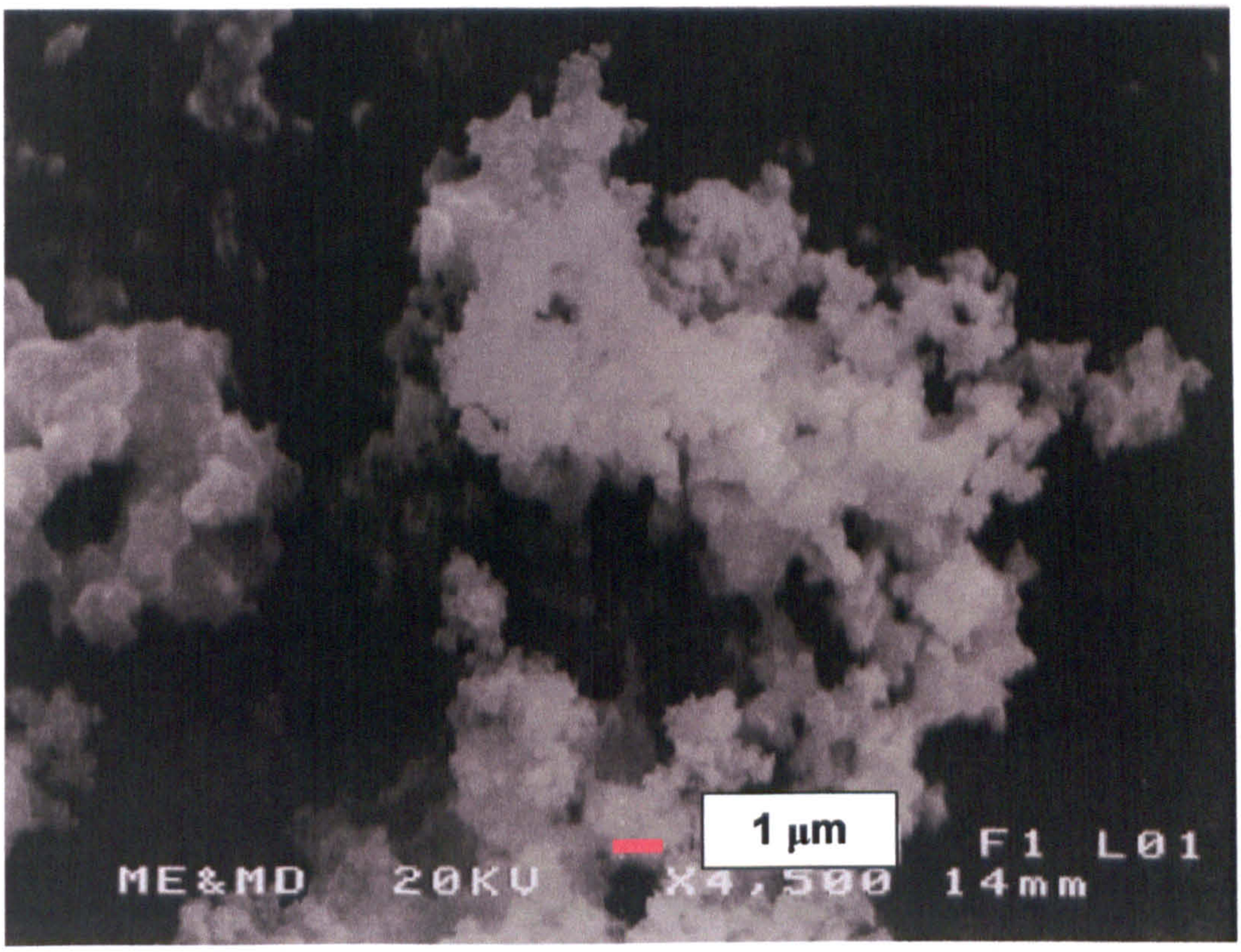


Figure 2-6: SEM photographs of $C_{60}(C_2H_4)$ shown relatively small particles of amporphous nature.

The IR spectrum of $C_{60}(C_2H_4)$ is presented in Figure 2-7. A summary table with the relevant band assignments is also provided, Table 2-2. Data on gas phase ethene[209] and pure C_{60} are included. C_{60} only has four allowed bands which are visible at room temperature,[210-212] two of these were beyond the range of the equipment. However, C_{60} has several combination bands in the region of 2000 to 2700 cm^{-1}.[213,214]

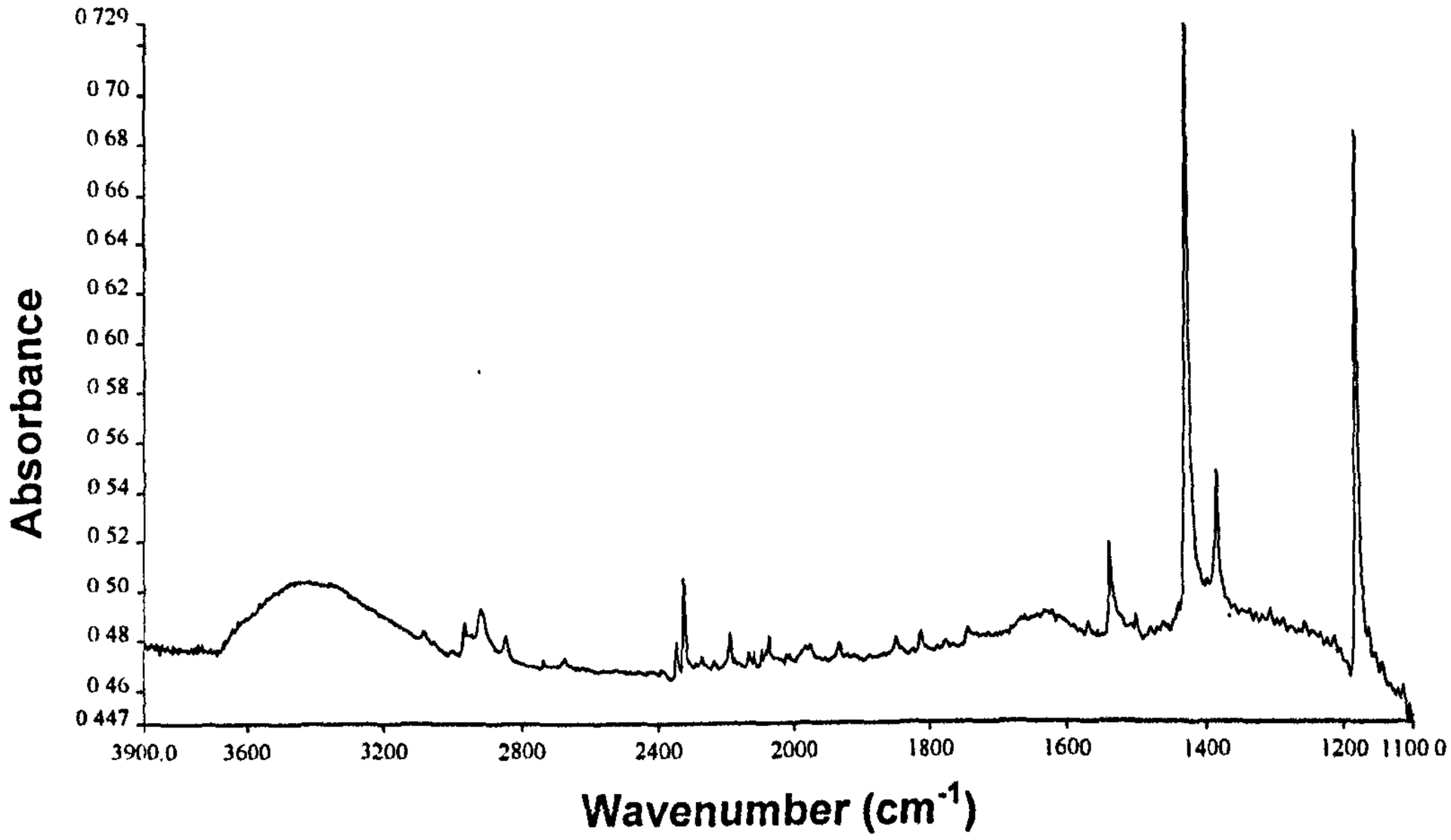


Figure 2-7: IR Spectrum of $C_{60}(C_2H_4)$ taken as a KBr disk.

Table 2-2: IR bands of $C_{60}(C_2H_4)$ with comparison to the bands observed in pure ethene and C_{60}. Extra peaks indicated that not all of the toluene was removed during the washing phase of the experiment.

Observed Band cm^{-1}	Ethene Gas cm^{-1}	C_{60} cm^{-1}	Shift	Assignment
3084	3105		-21	CH_2 stretching
2969	2989		-20	CH_2 stretching
2920				toluene
2847				toluene
2674		2677		C_{60} combination
2348		2348		C_{60} combination
2191		2191		C_{60} combination
2135		2136		C_{60} combination
2075		2076		C_{60} combination
1538		1538		C_{60} combination
1440	1443		+3	CH_2 scissor
1429		1427		C=C stretch
1182		1181		C-C-C bend

$C_{60}(C_2H_6)$

The SEM of $C_{60}(C_2H_6)$, Figure 2-8, also shows a highly aggregated mass of nanoparticles, this time, however the identification of individual nanoparticles is more obvious. Again the nanoparticles are around 500 nm in diameter, which agrees with the results by Webster. IR evidence is presented in Figure 2-9 and Table 2-3.

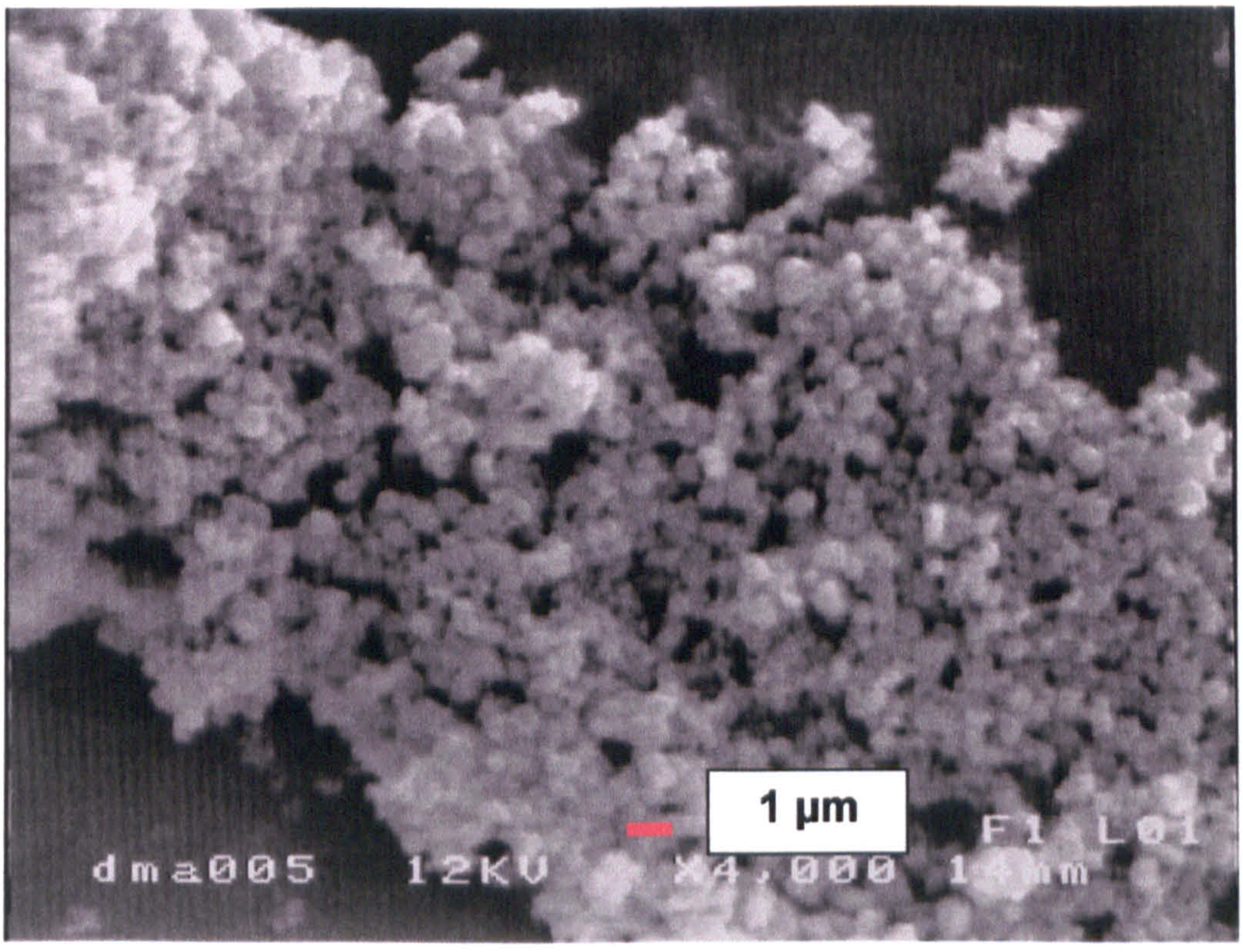


Figure 2-8: SEM photograph of $C_{60}(C_2H_6)$ as grown by PCA.

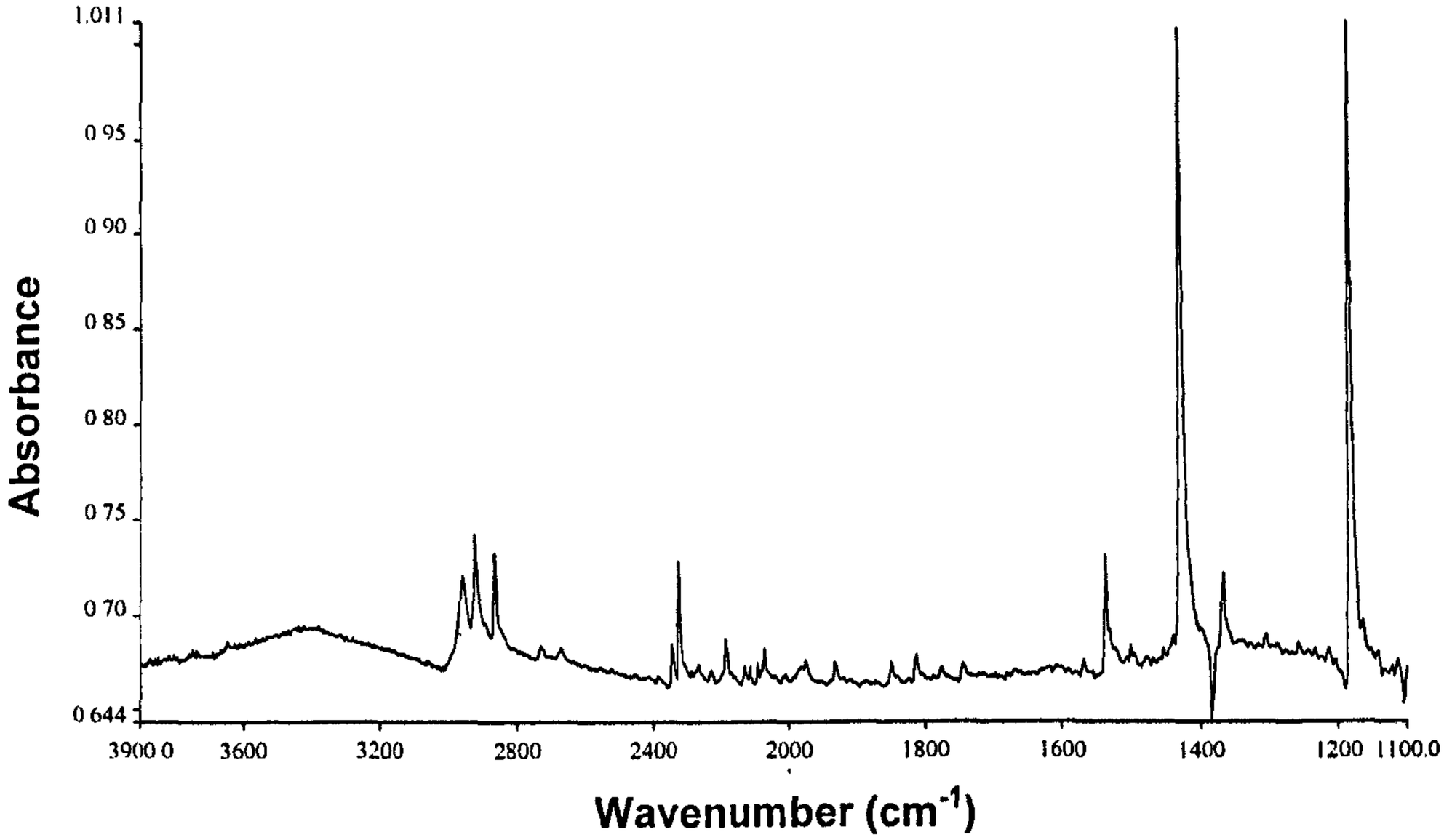


Figure 2-9: IR spectrum of $C_{60}(C_2H_6)$ taken as a KBr disk.

Table 2-3: IR bands of $C_{60}(C_2H_6)$ as compared to ethane gas and pure C_{60}.

Observed Band cm^{-1}	Ethane Gas cm^{-1}	C_{60} cm^{-1}	Shift cm^{-1}	Assignment
2963	2994		-31	CH_3 stretching
2924	2954		-30	CH stretching
2866	2894		-28	CH_3 stretching
2730	2753		-23	C_2H_6 combination
2675		2677		C_{60} combination
2346		2348		C_{60} combination
2325		2328		C_{60} combination
2189		2191		C_{60} combination
2133		2136		C_{60} combination
2075		2076		C_{60} combination
1537		1538		C_{60} combination
1426		1427		C=C stretching
1365	1379		-14	CH_3 scissor
1179		1179		C-C-C bend

$C_{60}(C_3H_6)$

An SEM photograph of $C_{60}(C_3H_6)$ is given in Figure 2-10. This shows a more needle-like morphology than has been seen for the smaller intercalates. There is also a greater range in particle size than in the previous samples, although there appears to be a similar amount of agglomeration. Particles appear, on average, to be slightly larger than for the smaller intercalates, although some of the larger crystal in this sample are considerably bigger than the previous examples.

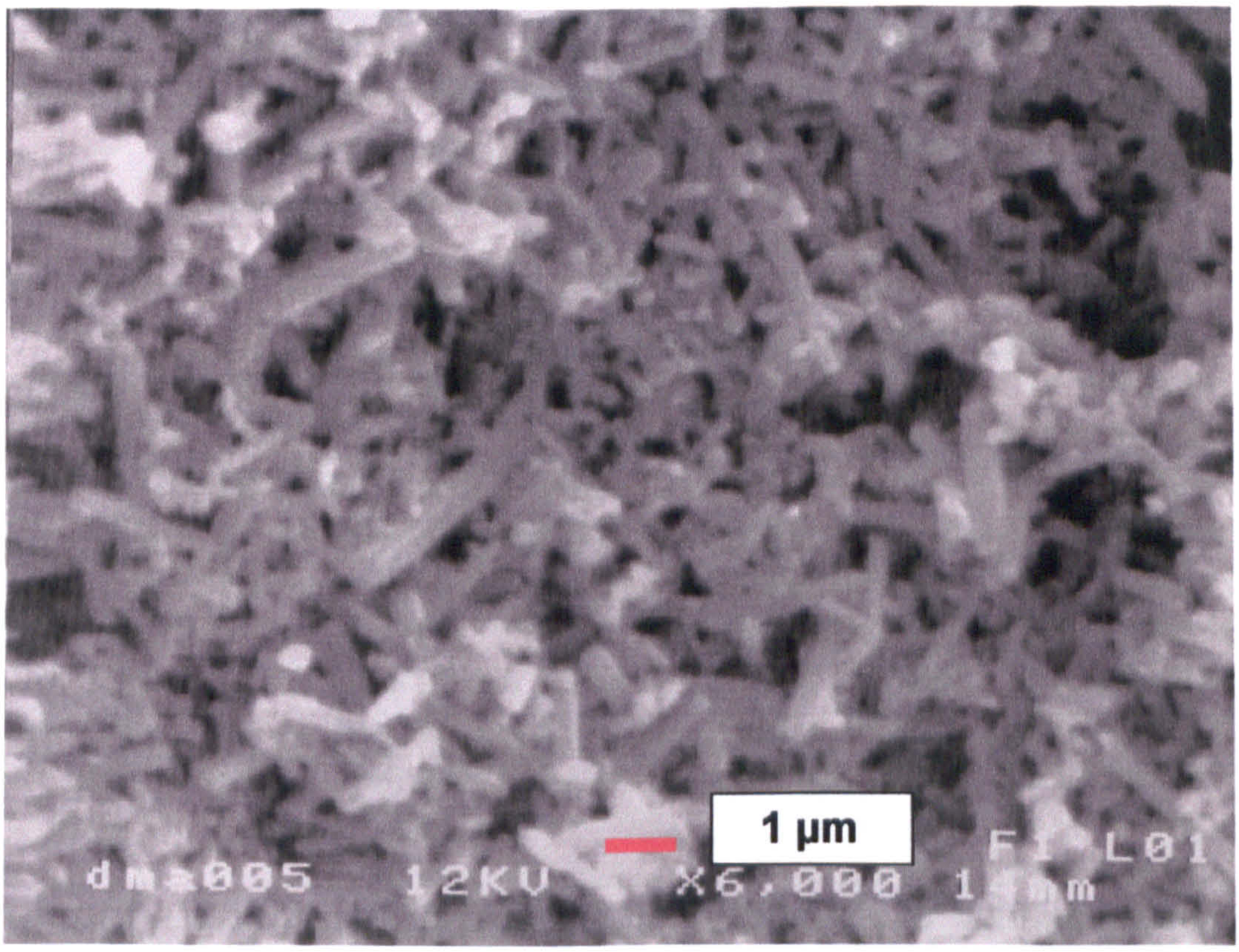


Figure 2-10: SEM photograph of $C_{60}(C_3H_6)$.

An IR spectrum of the new compound with data is given in Figure 2-11. This shows a set of (C-H) stretching bands which are clearly not from the C_{60}. Data on peak positions and assignments are given in Table 2-4.

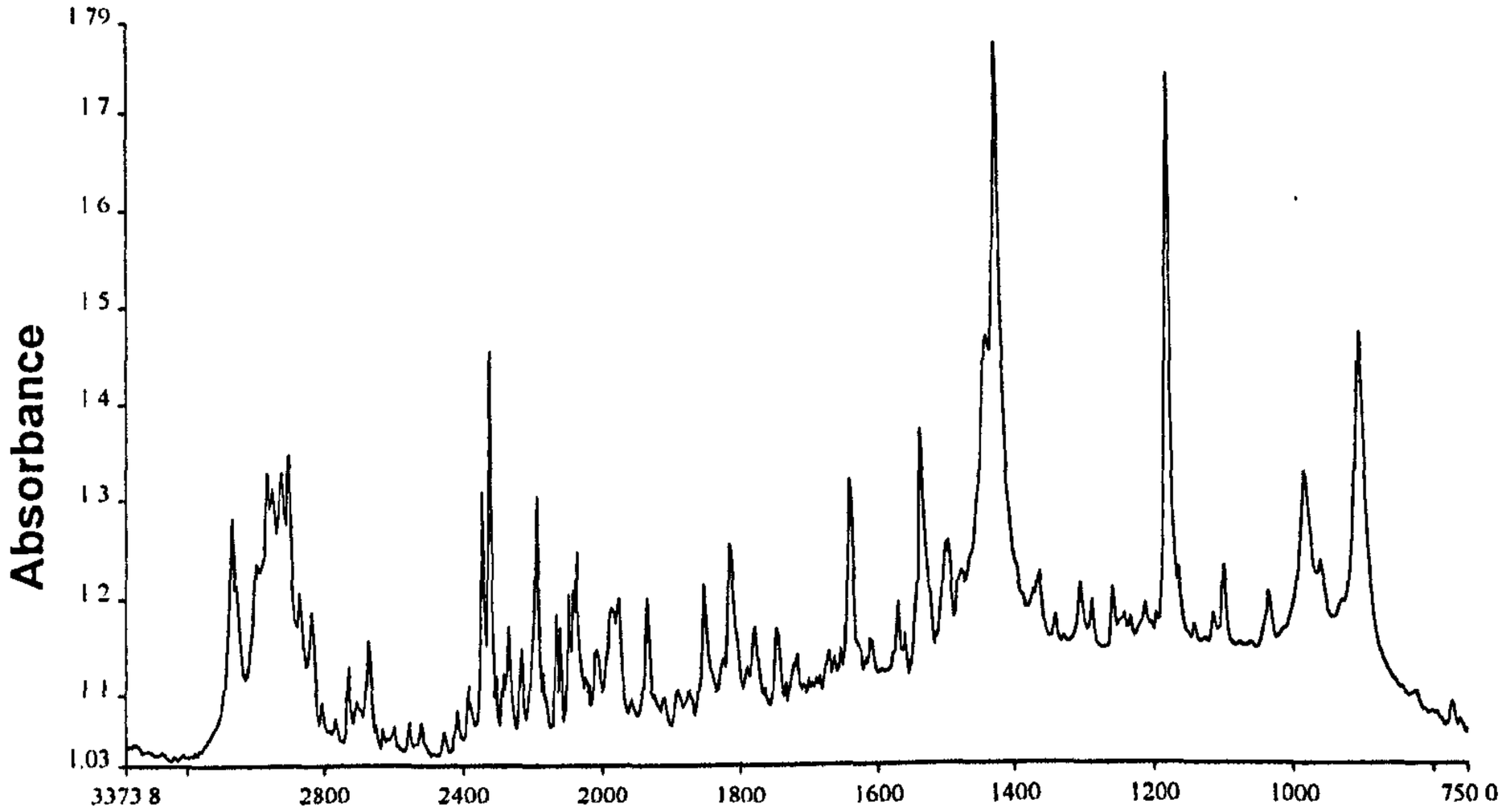


Figure 2-11: IR spectrum of $C_{60}(C_3H_6)$ taken using a transmission IR microscope on fullerene crystals.

Table 2-4: IR bands of $C_{60}(C_3H_6)$ as compared to pure propene and pure C_{60}.

Observed Band cm^{-1}	Propene Gas cm^{-1}	C_{60} cm^{-1}	Shift cm^{-1}	Assignment
3070	3081		-11	CH_2 asym stretching
3057	3067		-10	C_3H_6 combination
3001	3012		-11	CH stretching
2971	2979		-8	CH_2 sym stretching
2954	2960		-6	CH_3 asym stretching
2927	2942		-15	CH_3 asym stretching
2907	2916		-11	CH_3 asym stretching
2875	2884		-9	CH_3 sym stretching
2842	2852		-10	CH_3 sym stretching
2677		2677		C_{60} combination
2561	2574		-13	unassigned
2347		2348		C_{60} combination
2328		2328		C_{60} combination
2192		2191		C_{60} combination
2136		2136		C_{60} combination
2076		2076		C_{60} combination
2019	2035		-16	C_3H_6 combination
1815	1830		-15	unassigned
1719	1718		+1	unassigned
1640	1647		-	C=C stretching
1538		1538		C_{60} combination
1444	1448		-4	CH_3 asym deformation

Observed Band cm^{-1}	Propene Gas cm^{-1}	C_{60} cm^{-1}	Shift cm^{-1}	Assignment
1428		1427		C=C stretching
1307	1317		-10	CH bending
1181		1179		C-C-C bend
1165	1166		-1	CH_2 rocking
1035	1043		-8	CH_3 rocking
983	996		-13	C-C stretching
904	919		-15	C=C stretching

$C_{60}(C_3H_8)$

The SEM photographs (Figure 2-12) shows a more amorphous-looking sample to that of $C_{60}(C_3H_6)$. Some evidence of column-like crystals, similar to the previous intercalate are noticed. The sample appears aggregated as before and a mix in particle sizes is observed to be similar to the propene intercalate.

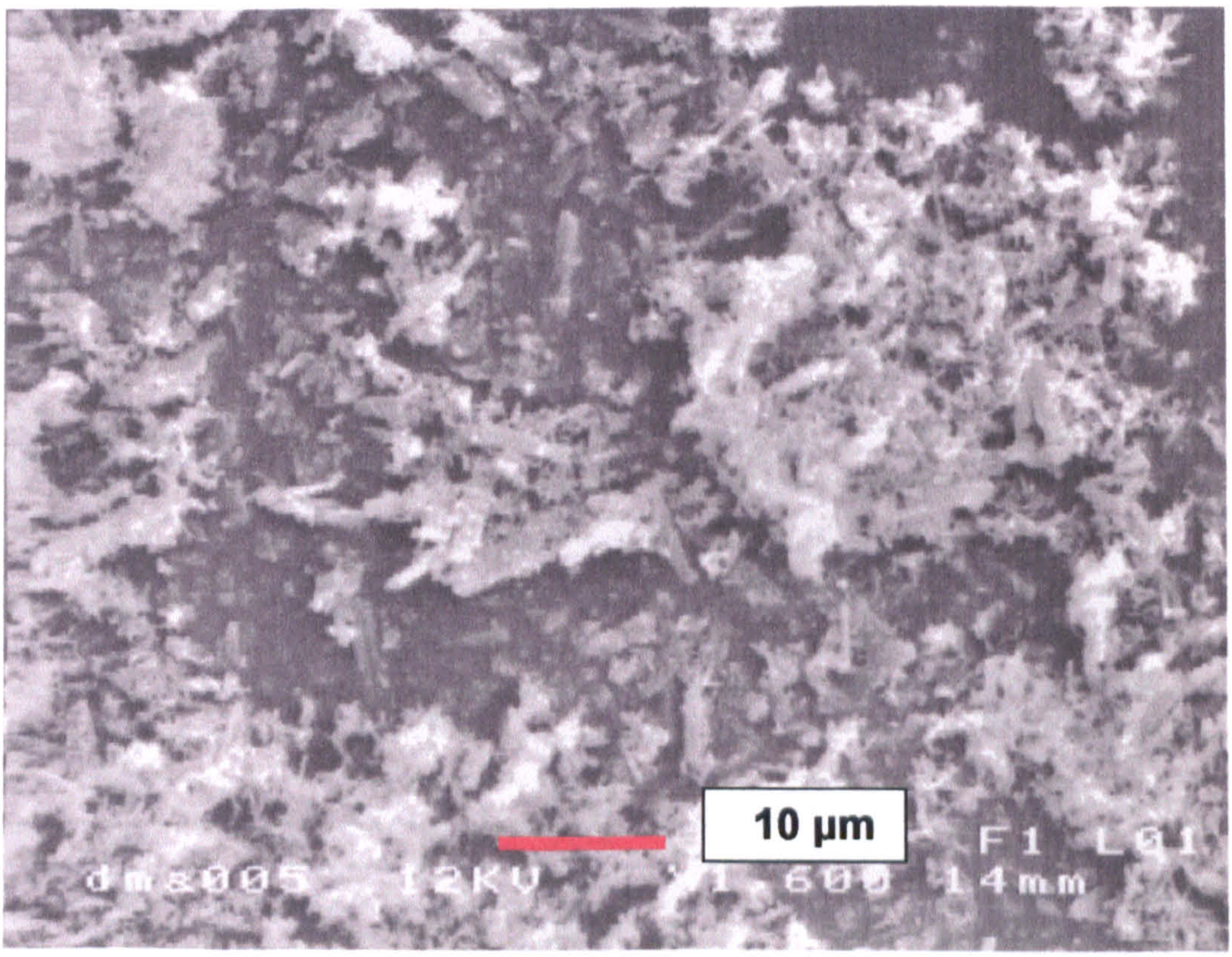


Figure 2-12: SEM photograph of $C_{60}(C_3H_8)$.

The IR spectrum of $C_{60}(C_3H_8)$ shows the C-H stretching bands at 3000 cm^{-1} as we would expect. A list of the peaks is given in Table 2-5.

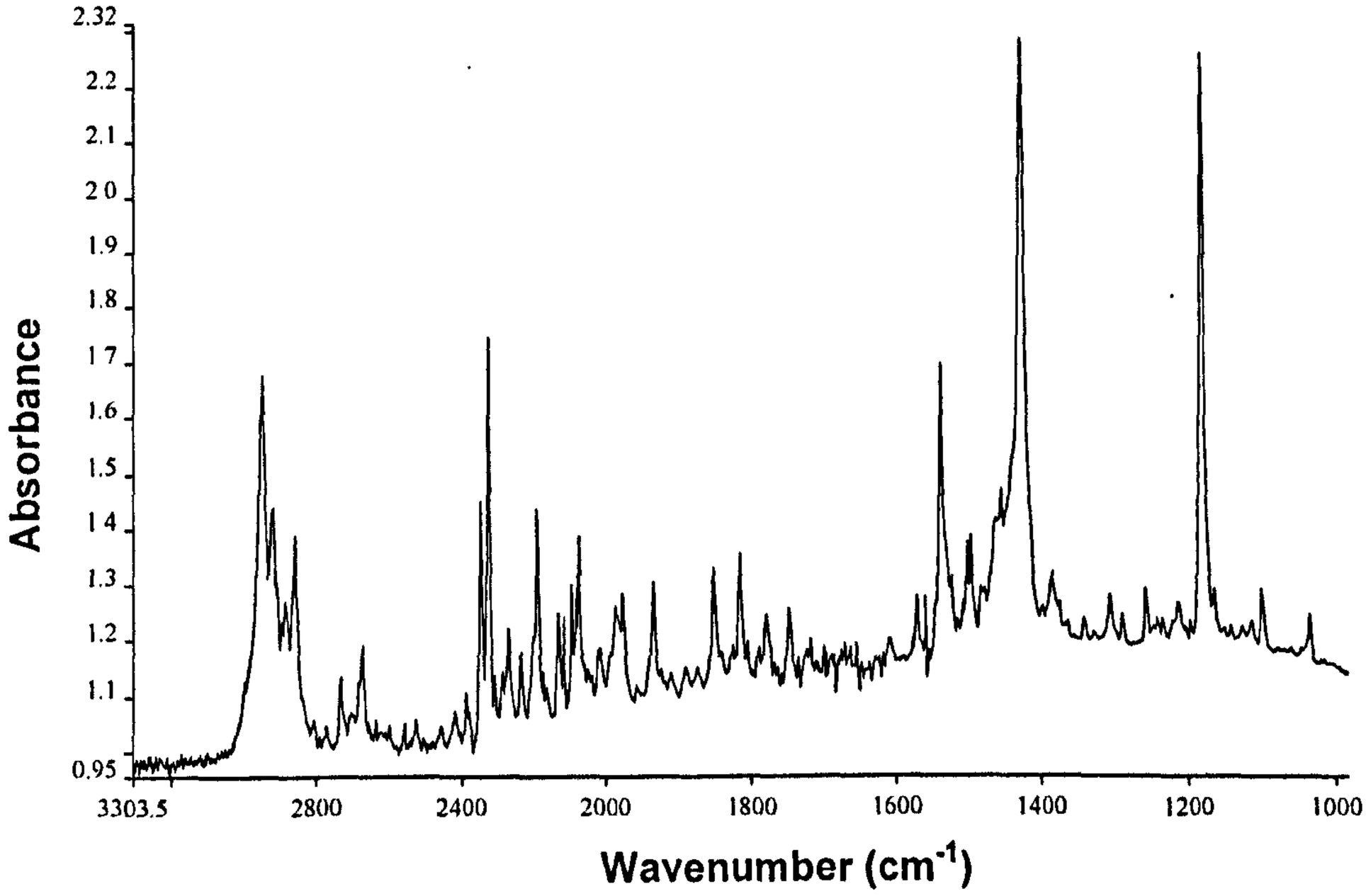


Figure 2-13: IR spectrum of $C_{60}(C_3H_8)$ taken with fullerene powder using and IR microscope.

Table 2-5: IR bands of $C_{60}(C_3H_8)$ including bands of propane and pure C_{60}.

Observed Band cm^{-1}	Propane Gas cm^{-1}	C_{60} cm^{-1}	Shift cm^{-1}	Assignment
2948	2968		-20	CH stretching
2925	2946 Raman		-21	CH stretching
2890	2903 Raman		-13	CH stretching
2863	2885		-22	CH stretching
2735	2725 Raman		+10	unassigned
2678		2677		C_{60} combination
2349		2348		C_{60} combination
2328		2328		C_{60} combination
2191		2191		C_{60} combination
2136		2136		C_{60} combination
2076		2076		C_{60} combination
1977				unassigned
1935	1936		+1	unassigned
1853				unassigned
1817				unassigned

Observed Band cm^{-1}	Propane Gas cm^{-1}	C_{60} cm^{-1}	Shift cm^{-1}	Assignment
1781				unassigned
1748	1730		-18	unassigned
1539		1538		C_{60} combination
1429		1427		C=C stretching
1182		1179		C-C-C bending
1100				unassigned
1035	1053		-18	unassigned

Ideally, the new fullerene compounds should be characterised using NMR and powder XRD as was performed on the $C_{60}(CO_2)$ by Field. Powder X-ray diffraction was attempted on the new intercalate species. This, however, yielded very poor patterns. Little useful, and no reliable, data could be extracted from the pattern due to the poor intensity and sloping baseline, although it did possess a similar shape to the expected pattern. The pattern fails to index, however, and so it must be assumed that the structure is the same Fm3m space group as $C_{60}(CO_2)$. This seems likely but there is no evidence for this. The pattern does provide information, however, as to what the problems with the sample are. The broadness of the peaks indicated that the individual crystallites are too small to diffract properly. Also the general weakness of the signals indicates that the sample is at least partially amorphous. These are not unreasonable findings as the PCA technique used is designed to produce very small particles and in the case of fullerenes these have been shown to have an amorphous character.[206] It was for this reason that a separate technique was initially used by Webster to collect material of a larger size and more crystalline morphology. This technique was based on a conventional GAS synthesis as detailed in the Introduction.

GAS

The first GAS technique used by Webster involved a pressurised tube of C_{60} solution with antisolvent supplied by a capillary tube hanging above it, see Figure 2-14a. This was carried out on a very small scale inside the sapphire tube view cell so observation of the experiment was possible. The technique relied on the solvent being miscible with the antisolvent gas. The vessel was brought to the working pressure and precipitation was initiated. The flow of antisolvent was continued and the capillary used to ensure the sample was free of solvent. This technique was only able to produce a tiny amount of sample due to the fact that a miscible solvent, toluene, was used.

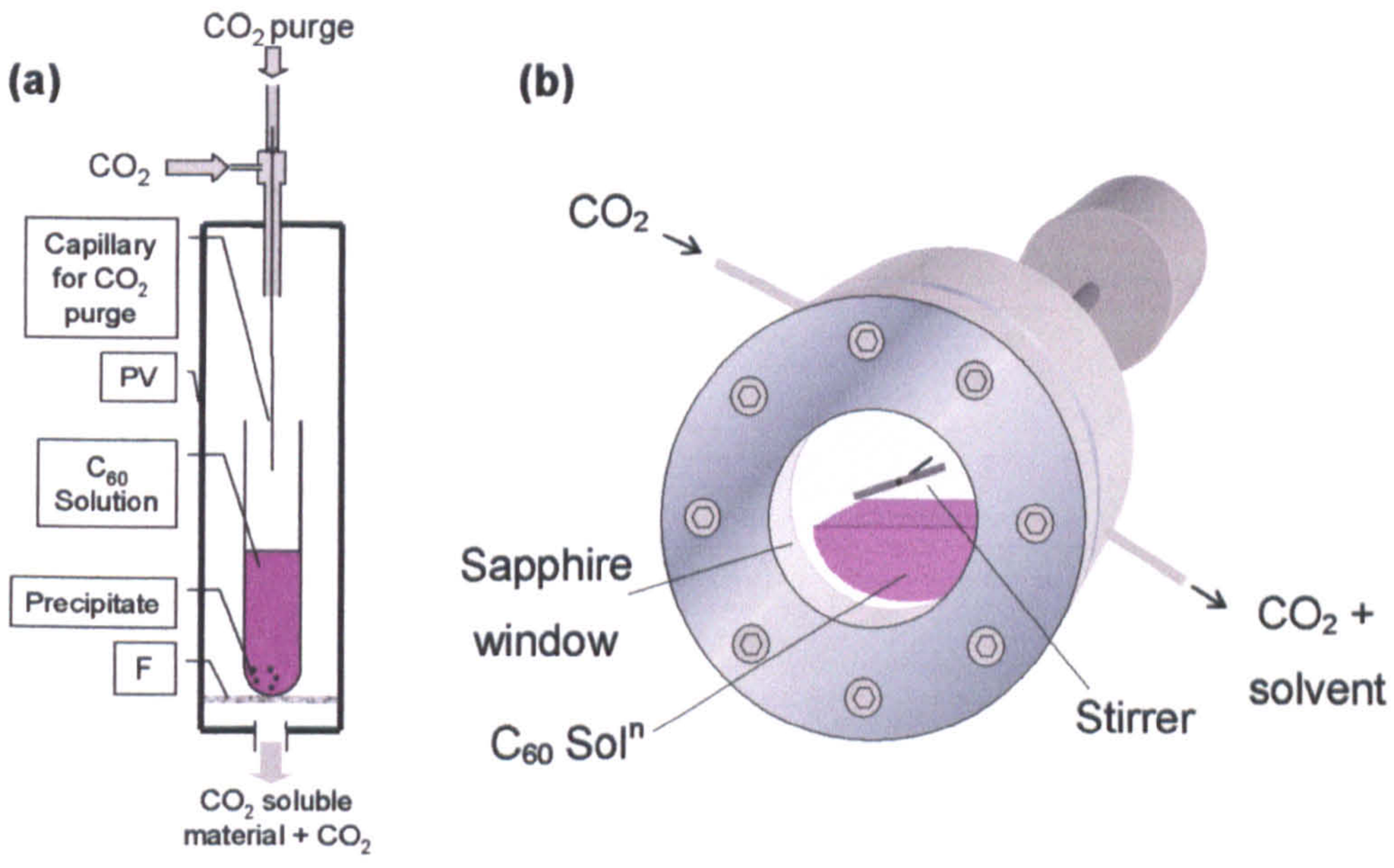


Figure 2-14a and b: The two GAS methods used by Webster and Field to grow larger crystals of C_{60} intercalate.

The second technique employed by Webster was to place a dish of solution inside a Sapphire view cell. This is shown in Figure 2-14b. A solution of 1,2 dichlorobenzene

was used; this allowed up to 10 times as much C_{60} to be dissolved and so, on precipitation, much more sample was available. Unfortunately as dichlorobenzene is a much denser solvent than toluene its phase behaviour when interacting with antisolvent gas is different to that of toluene. This was discussed in Supercritical Fluids section of the Introduction in the section on binary phase behaviour. The result of this is that under experimental conditions it was not possible to achieve a miscible environment. The antisolvent was still observed to induce precipitation in the experiments, yet the solvent became much harder to remove. In this way the antisolvent is partially soluble in the DCB rather than being miscible with it. The answer employed by Webster and Field was to equip the view cell with a small stirrer blade capable of removing the solvent physically under a situation of continuous gas flow. Care had to be taken to ensure that all solvent had been removed as damage to crystals was clearly visible in SEM photographs when the solvent removal was inadequate. This is shown in Figure 2-15 which is reproduced from Webster's thesis.[16] The technique resulted in superior product yet still was only capable of producing relatively small quantities of material each experiment. For example to acquire sufficient material to gain MAS ^{13}C NMR it was necessary to perform the experiment several times and group the products together. Also as already mentioned great care was needed to ensure that all solvent had been removed.

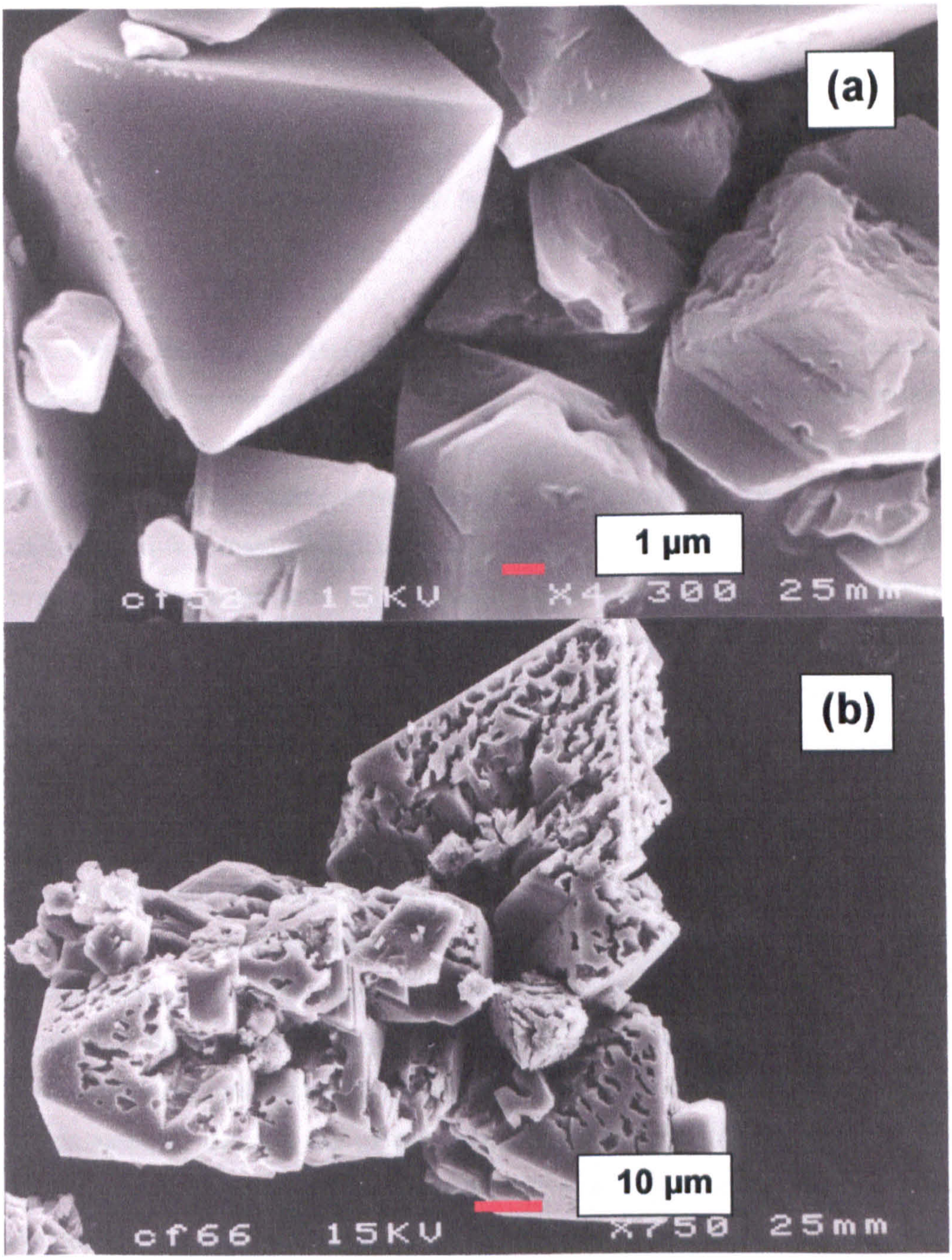


Figure 2-15: Two examples of $C_{60}(CO_2)$ grown from 1,2 dichlorobenzene by Field and Webster after (a) complete and (b) incomplete removal of solvent.[16]

Both of these techniques share the need to contain the C_{60} sample. A conventional GAS technique relies on a filter to stop the removal of material from the vessel. Often material is simply removed from the surface of the filter when the experiment

is over. This is not possible in the case of C_{60}, as the particles formed smear very easily on rough contact with surfaces. This would damage the specific morphology of the particles and, more importantly, create a significant safety risk due to a blockage almost certainly being created at the filter. There would also be expected to be a significant amount of loss of material which would be intolerable both scientifically and financially.

The above techniques have been shown to work effectively in generating $C_{60}(CO_2)$.[206] What was known about the hydrocarbon molecules, however, was that even the smallest, ethene, was larger than CO_2.[178] Since the ethene intercalate had only been tentatively characterised previously, no information on its stability was known. Also it seemed reasonable to assume that the stability would decrease for larger molecules in the same way that it had already been shown for the instability of the noble gas intercalates.[189] For this reason, it was not desirable to rely on the cumulative products of several runs of an experiment to produce enough sample to analyse. The sample should also be examined as soon after preparation as possible.

As mentioned in the Introduction, the traditional use of GAS produces slightly larger particles than with PCA by injection of gas into solution under miscible conditions. The use of 1,2 dichlorobenzene was seen as a necessary starting point to generate enough product material. Since the use of an immiscible solvent has not been reported in the literature, because the purpose of SCF antisolvent techniques has been to achieve rapid mixing, this raises questions as to how the system will behave. It was assumed that the use of the immiscible 1,2 dichlorobenzene will produce larger crystals than would be generated by other techniques because of slower interactions. In this case, as it is the material we are interested in, this is not important except in the sense that special consideration must be given to the removal of the solvent at the end of the precipitation.

A new series of experiments was started to try to maximise the amount of sample available. Moving from miscible to immiscible conditions created several problems.

1. Care was needed to ensure that the solution was not removed before precipitation had taken place.

2. A method for separation of the precipitated material from the solvent/antisolvent mix was needed.
3. It was necessary to remove the solvent on completion of the experiment in a more vigorous way.

These difficulties were compounded by the additional problem that to produce enough material a larger steel vessel had to be used. This would mean that on-line observation was impossible. Also the difficulty in handling finely precipitated C_{60} meant that precipitation onto the walls of a vessel would result in the waste of relatively large amounts of material.

A brief description of the chosen solution to these problems is given in the list below:

1. The use of the Keystone Extraction Vessel to provide a container large enough to precipitate sufficient material for the analysis.
2. The presence of a long tube running to the base of the solution. This allowed the solution to be agitated to initiate precipitation and also to provide a solvent purge at the end of the experiment.
3. The use of a second inlet to allow the vessel to be brought to working pressure with minimal agitation to the solution.
4. Use of a Gilson pump to supply the antisolvent gas. This allowed the careful control of the flow during the experiment, with slow flow to initiate precipitation and rapid flow to remove solvent.
5. The containment of the solution inside the vessel with a glass tube. This would create a situation where the solution could be contained away from the vessel. If this could be continued after the precipitation had taken place then the precipitated material would be easily removed from the vessel with no loss.
6. The presence of an outlet at the bottom of the vessel. This allowed the solution removal to be aided by gravity, its density being much greater than the antisolvent gas.

The purpose of this examination was to generate the set of apparatus as shown in Figure 2-16.

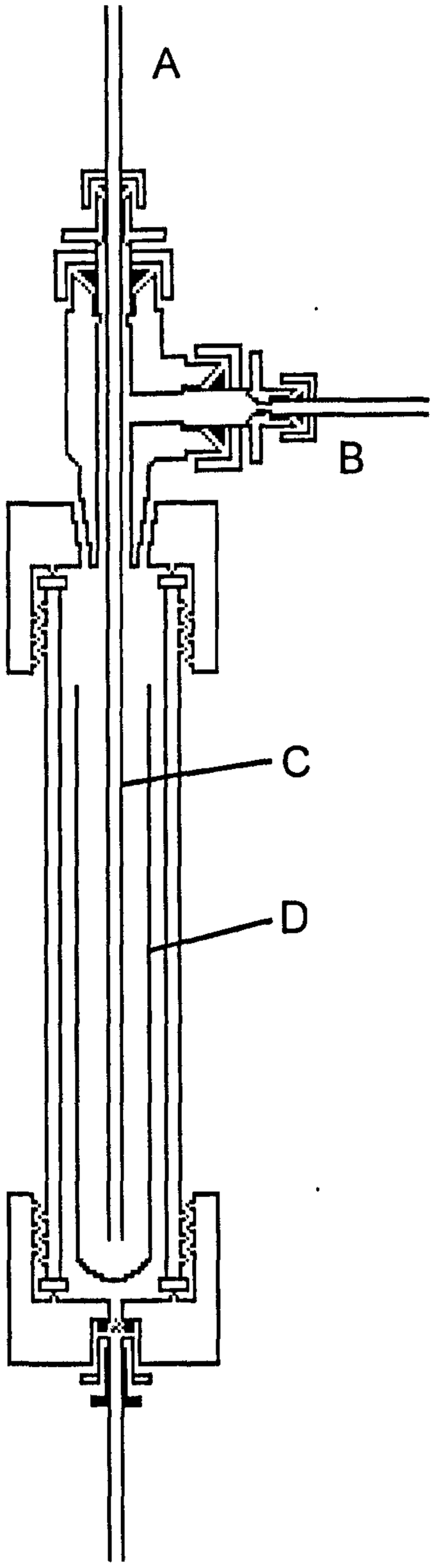


Figure 2-16: Diagram of the GAS apparatus. The apparatus is based on a Keystone extraction vessel. The top end nut is drilled out and re-threaded to accept a male ¼" NPT T-piece. The other ports of this T-piece are Swagelok and are reduced down to 1/16" fittings using two Swagelok Reducers. These provide a purging inlet (A) and a main filling inlet (B). The uppermost Reducer is bored through to accept a long piece of 1/16" steel tubing (C) which runs to the bottom of the vessel. A glass tube (D) is placed inside the vessel so that the base of the tube rests near to the end of the long internal tubing. The vessel is otherwise unchanged from that used for the PCA experiments and is discussed in more detail in Appendix I.

The apparatus itself fitted into the overall experimental scheme as shown in Figure 2-17.

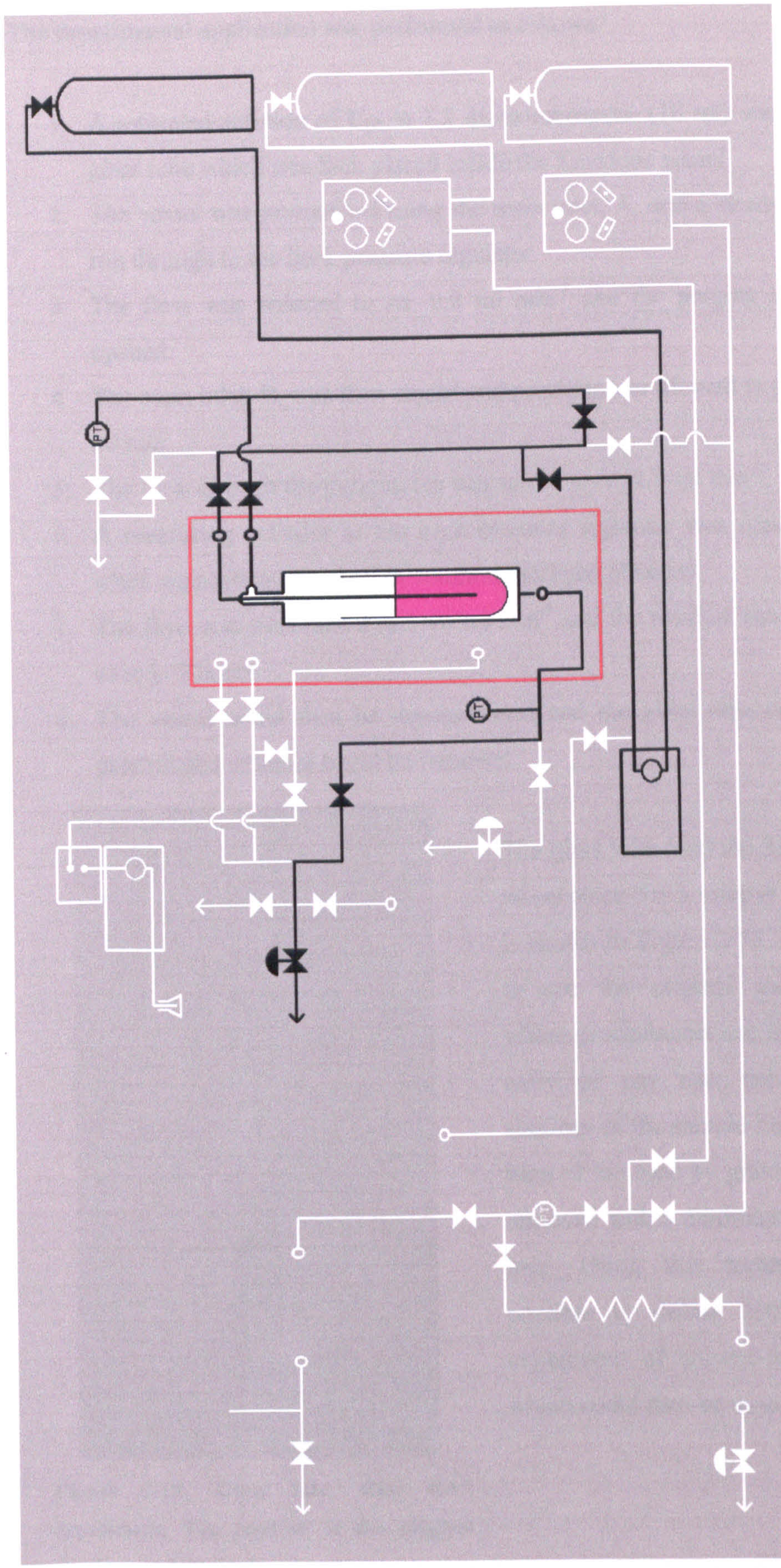


Figure 2-17: The GAS apparatus fitted into the general experimental scheme thus.

The experimental application was performed as follows:

1. A saturated solution of C_{60} in 1,2 dichlorobenzene (10 ml) was placed in a glass tube which was then placed inside the Keystone vessel.
2. The vessel was pressurised using the main inlet, A, and a steady flow of gas run through to the back pressure regulator.
3. The flow was reduced to *ca.* 0.2 ml min^{-1} and the purging inlet, B, was opened.
4. The main inlet, B, was then closed and precipitation allowed to progress over 30 min.
5. The flow through the purging tap was raised to *ca.* 1.0 ml min^{-1}.
6. A measuring cylinder at the back pressure regulator was used to measure when approximately 10 ml of solution had been obtained.
7. The flow was then raised to 5-10 ml min^{-1} and the residual solvent removed over 1- 2 hours.
8. The vessel could then be depressurised and the glass tube containing the precipitated material could be removed.

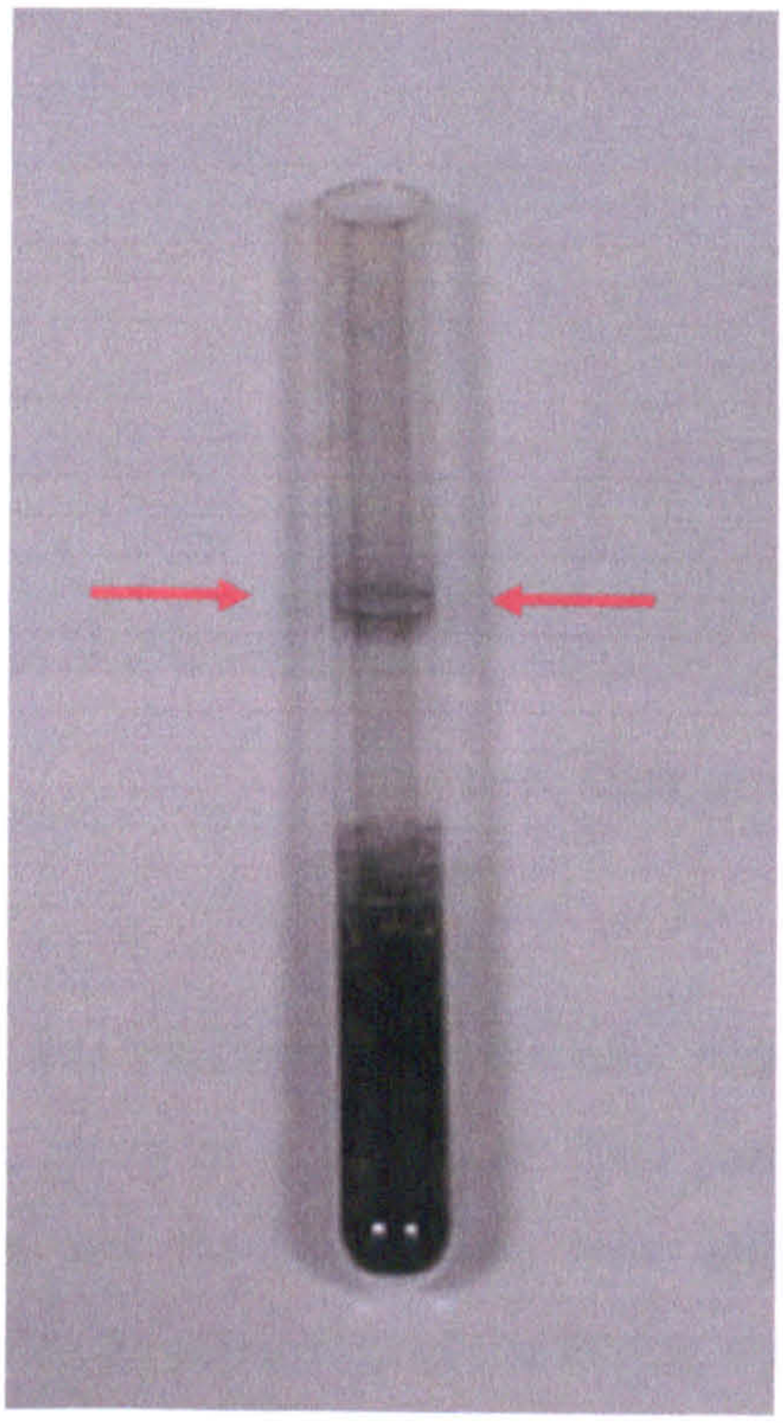


Figure 2-18: Glass tube after GAS experiment. The position of the original meniscus is indicated.

The glass tube after the experiment has taken place for a sample of $C_{60}(C_2H_6)$ is shown in Figure 2-18. In is possible to see the original meniscus level where precipitation was initiated by the entry of gas into the vessel. The majority of the sample has fallen to the base of the tube by gravity and can be removed with a minimum of effort and loss. Using this technique it was possible to isolate 200-250 mg per experiment of solvent-less intercalate which could then be used for analysis.

$C_{60}(C_2H_4)$

The first intercalate to be attempted was C_{60} with ethene. A representative example SEM photograph is given in Figure 2-19. This indicates that the morphology is much more crystalline and also the particle size is much larger than in Figure 2-6. This suggests that the technique has been successful in improving the quality of product. The material appears highly aggregated; however this should not affect the analysis.

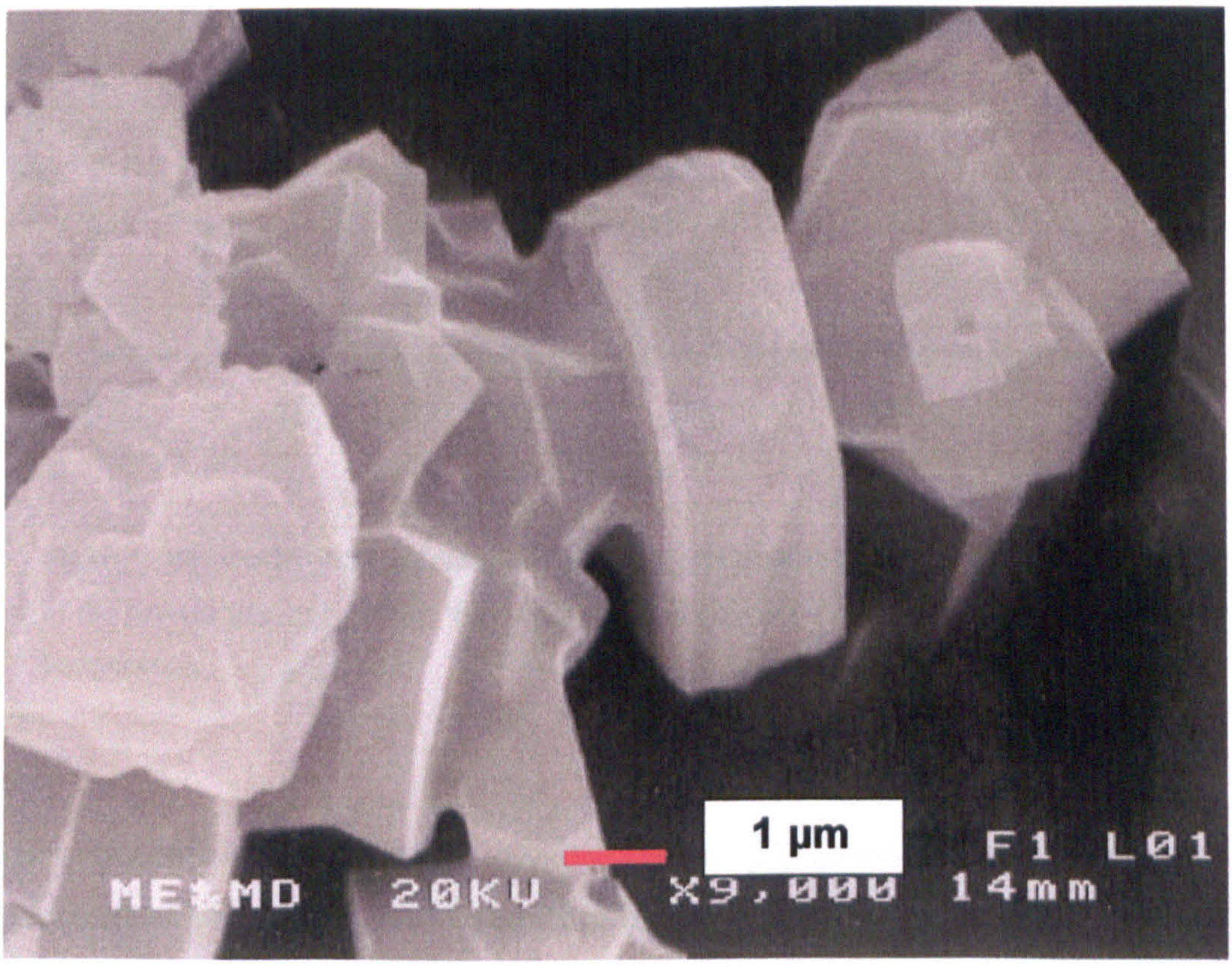


Figure 2-19: SEM of $C_{60}(C_2H_4)$ as grown by the new GAS technique.

PXD was performed on the new sample and provided a much more satisfactory result, given in Figure 2-20. This pattern is very similar to that given by pure C_{60} except that the peaks have been slightly shifted in position and intensity. This indicates an expansion of the lattice, a new 200 peak has also emerged to indicate the presence of an intercalated species. The pattern is almost identical to the pattern generated by $C_{60}(CO_2)$ only this time with a further expanded lattice.

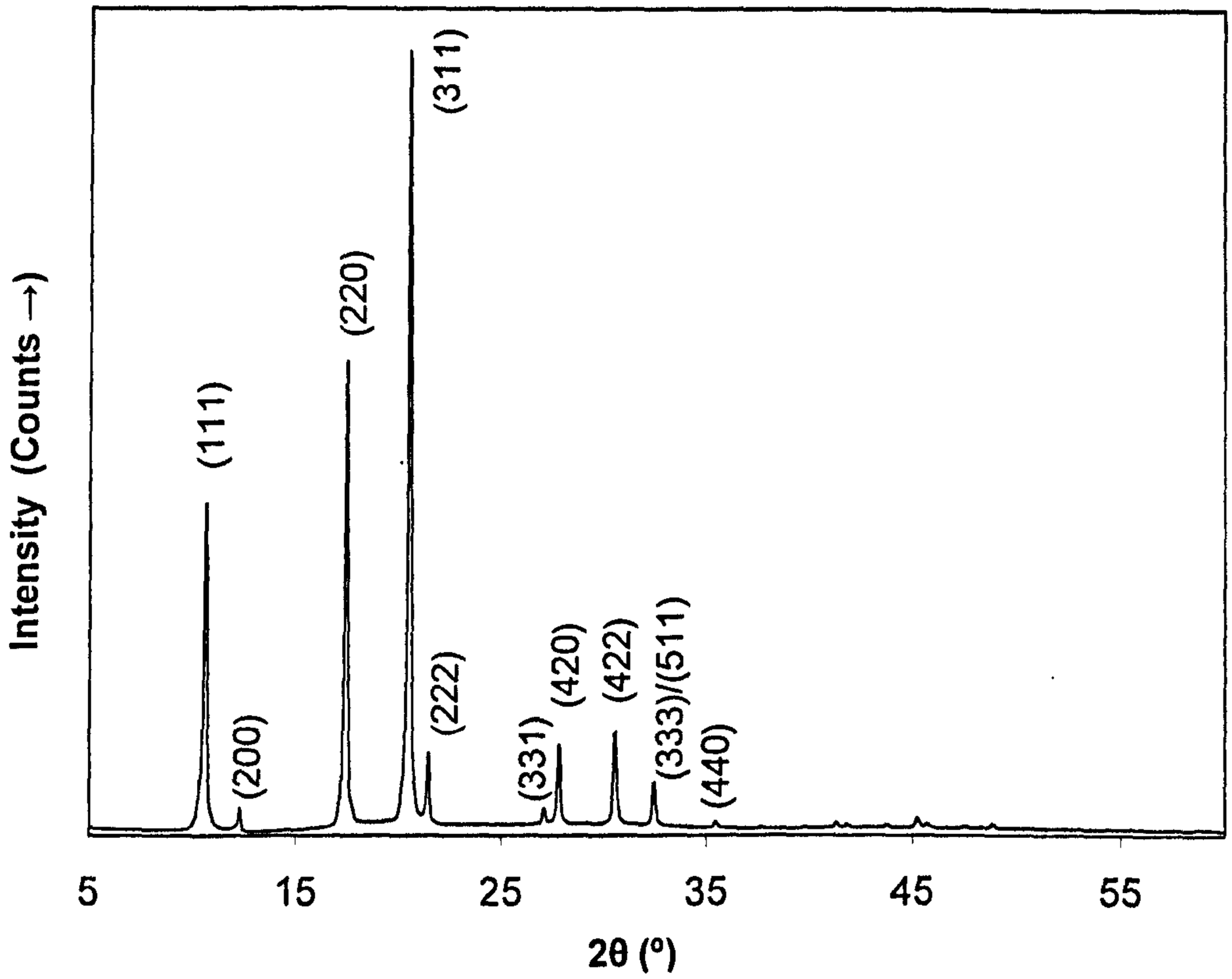


Figure 2-20: Powder diffractogram of $C_{60}(C_2H_4)$. Sharp peaks indicate crystalline sample of the correct size. No defined high angle peaks are visible as would be expected at room temperature.

The lattice indexes using the DICVOL programme[215] to give a cubic lattice with an a parameter of 14.337(4) Å at room temperature. This indexing has a figure of merit of 26.3 using 10 peaks. Relatively few peaks were available to index as the constant rotation of the C_{60} at room temperature removes the possibility of studying higher angle peaks. This is a common feature of all C_{60} compounds and is not unique to this species. Low temperature work has been able to gather high angle data for PXD and PND[178] although this was not possible due to equipment availability in Nottingham. The powder data gives definite evidence of the intercalated species in the C_{60} lattice. The lattice expansion represents the largest expansion of the C_{60} lattice by an intercalating species without the initiation of a phase change *c.f.* $C_{60}(CO_2)$ a = 14.243(3)Å and C_{60}(Xe) a = 14.247(2) Å.[189,206]

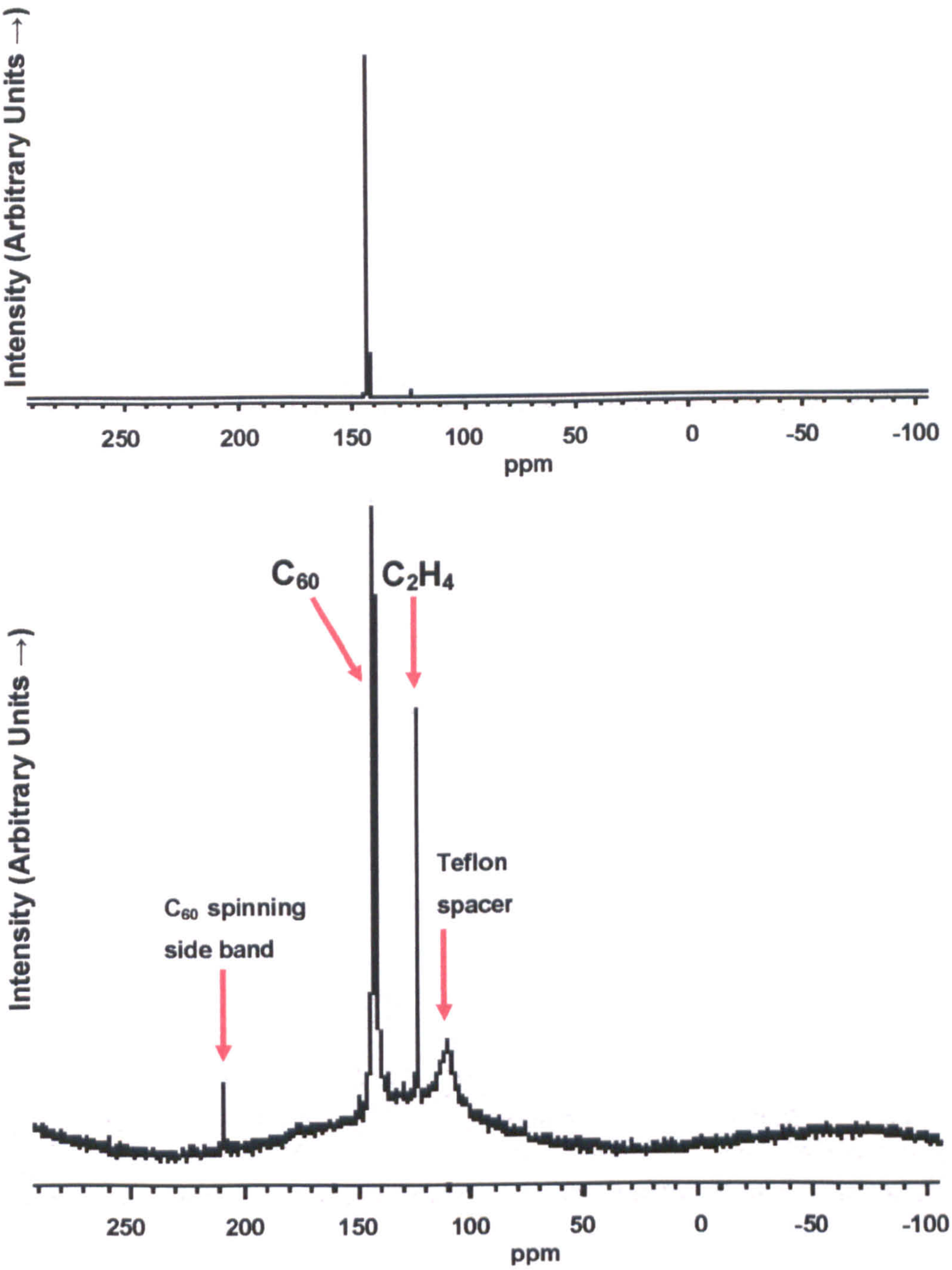


Figure 2-21: The MAS ^{13}C NMR of $C_{60}(C_2H_4)$ allows calculation of the quantity of ethene trapped inside the C_{60} lattice.

These data reinforce the data collected by Webster. The pattern has the same form as he described, although in this case the peaks are sharper and better defined. Webster was able to estimate the lattice constant by examination of the (111) peak. His sample contained significant quantities of HCP material and so he was not able to

carry out indexing of the pattern. This therefore represents the most conclusive evidence of the C_2H_4 intercalate at present. This was further supported by NMR examination.

MAS ^{13}C NMR was performed on the new sample directly as the new technique allowed production of enough material to offer a strong signal. The spectrum is shown in Figure 2-21. The spectrum reveals a large C_{60} peak at 142 ppm with a spinning side band at 208 ppm. The ethene peak is visible at 125.3 ppm and the large, broad peak at 110 ppm is the Teflon spacer used to mount the sample. From relative peak integration of 32±2 : 1 it is possible to estimate the loading of the lattice at 95 % ± 5 %. This agrees with the value of 91 % calculated by Webster.

The ethene intercalate was also subjected to TGA analysis, as were all of the other intercalates produced by this technique. The results are presented at the end of this section so as to compare the relative amounts of gas loss.

$C_{60}(C_2H_6)$

The next material to be investigated by the new GAS technique was the ethane intercalate of C_{60}. This was to prove more interesting in terms of its internal structure. The intercalate itself was produced as previously detailed. An example of the particle size can be viewed by the SEM photograph given in Figure 2-22.

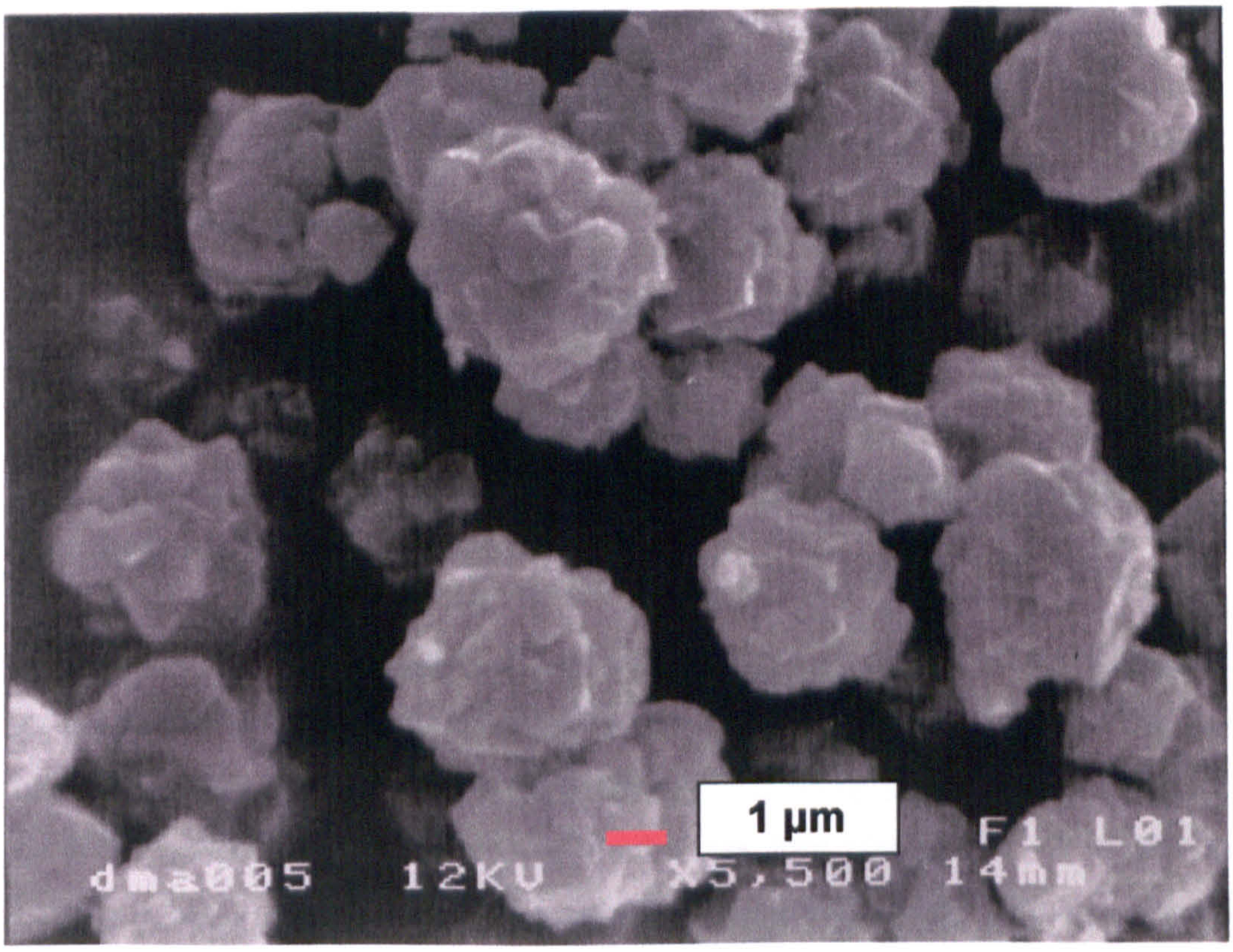


Figure 2-22: SEM of $C_{60}(C_2H_6)$ as grown by the new GAS technique.

The SEM photograph of $C_{60}(C_2H_6)$ shows aggregated crystals of material approximately 5 µm in diameter. This result is similar to the C_2H_4 intercalate in terms of size, the crystals themselves exhibit a much greater surface roughness. The crystals do, however, show multiple clear faces and so it was likely that the sample would provide sharp PXD data. This was indeed shown to be the case and this is given in Figure 2-23.

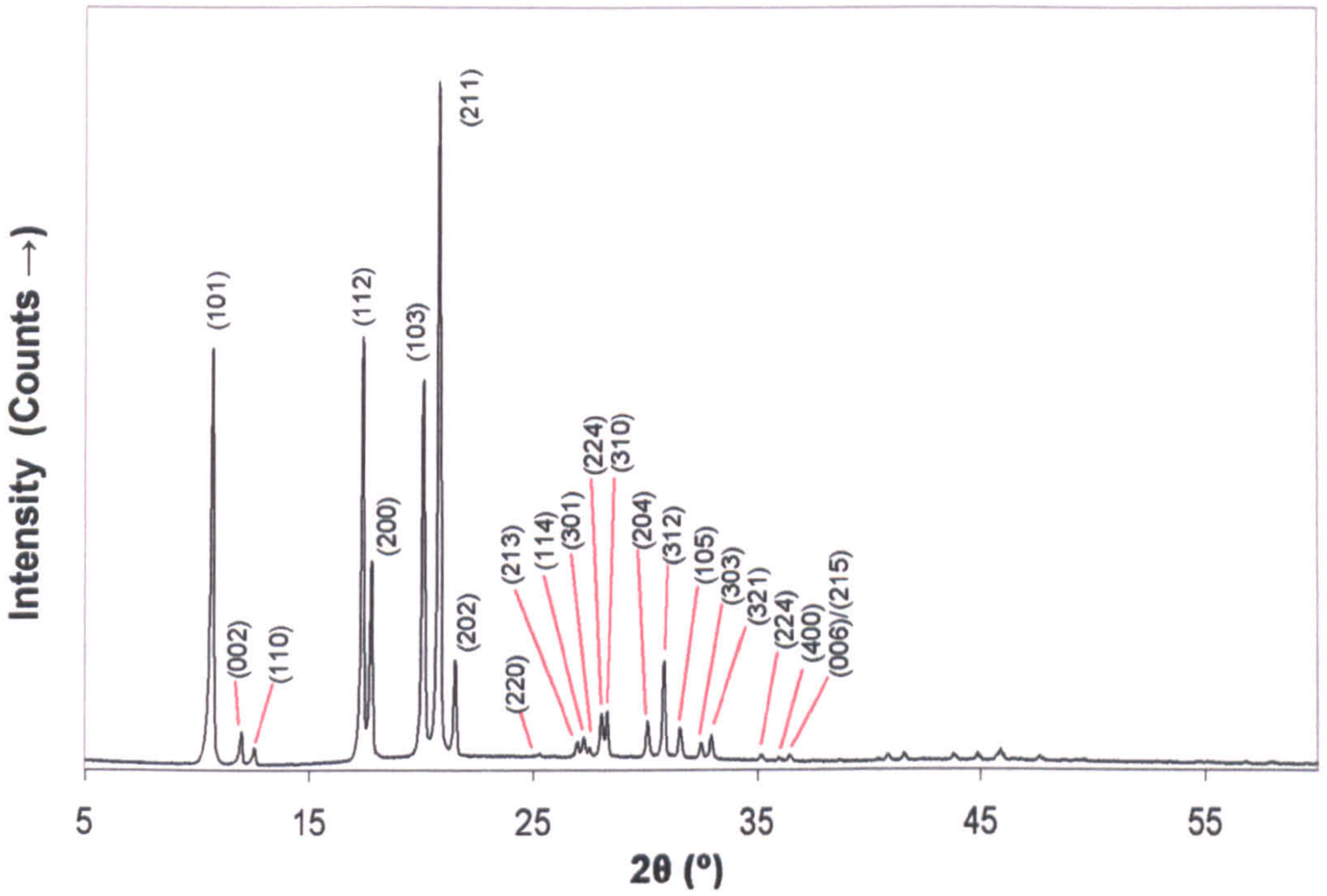


Figure 2-23: The PXD data collected for the ethane intercalate of C_{60}. The pattern indicates a change from a cubic to a tetragonal lattice.

The above pattern clearly suggested that the material had changed phase. Several of the peaks had split into two indicating a change to a tetragonal lattice. This was further supported by investigation using the DICVOL program,[215] which showed the phase change from cubic to tetragonal. Lattice constants were now a = 9.97026(98) Å and c = 14.77170(206) Å and the internal volume 1468.40 $Å^3$. The data offered very good agreement to this phase, even when using very small peaks above 2θ 35°. In total 26 peaks were used and the figure of merit was given as 35.4, indicating that the data were likely to be reliable. Webster was unable to present any powder data on the ethane intercalate, although he did believe that it possessed a similar structure to the ethene intercalate with a lattice parameter of 14.27 Å.

MAS ^{13}C NMR was carried out on the sample and the spectrum integrated to calculate an intercalation level. The resulting spectrum is given in Figure 2-24. The NMR spectrum of the ethane intercalate again shows the spinning sideband and broad Teflon spacer peaks. The up-field peak of ethane is seen at 8.7 ppm. This is again dwarfed by the C_{60} peak but integrates to 29.9±2 : 1 this equates to 100 % ± 5

% intercalation. Webster failed to collect NMR data on this compound therefore no data exist as a comparison.

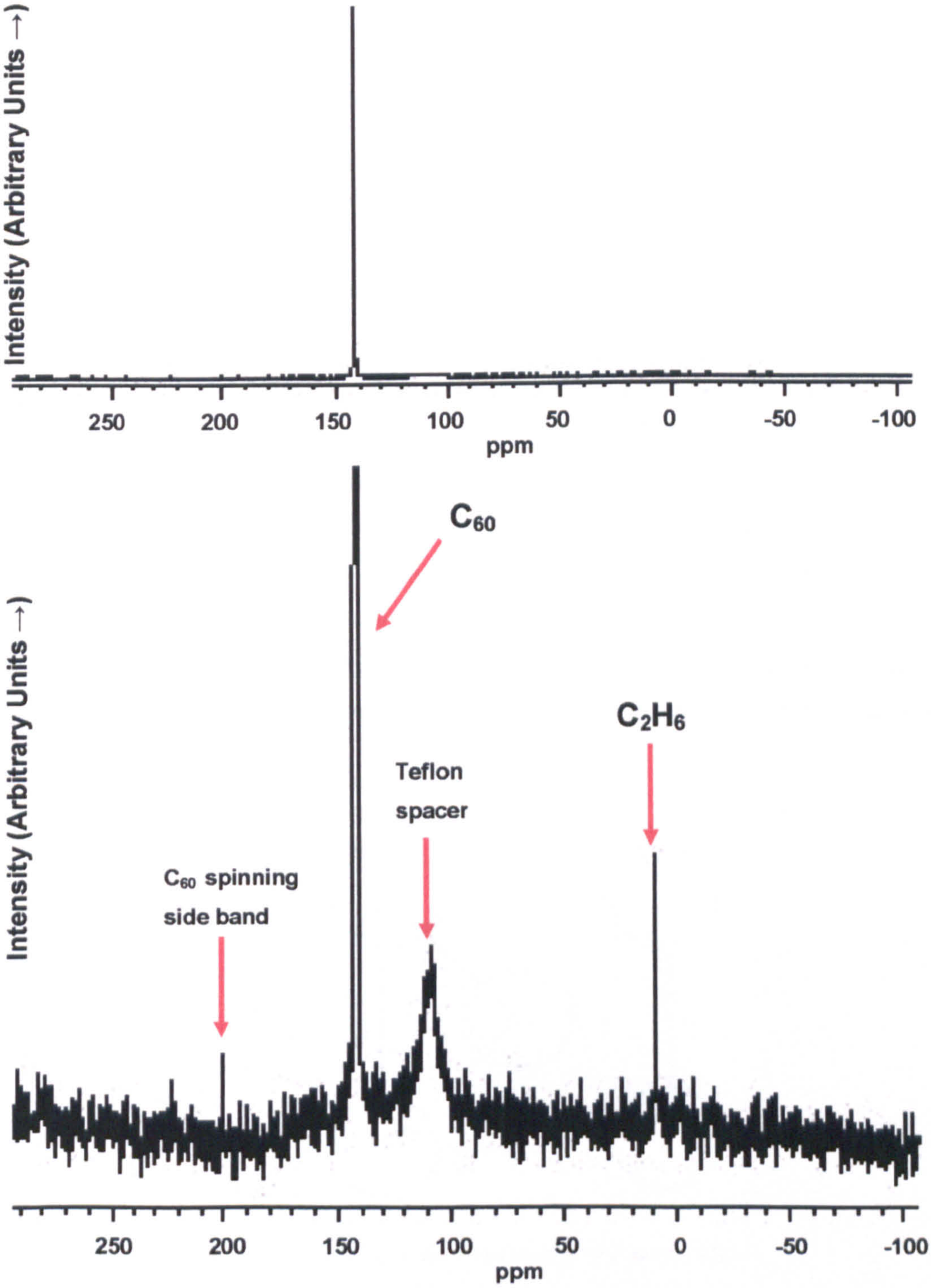


Figure 2-24: MAS ^{13}C NMR spectrum of the ethane intercalate of C_{60}.

The phase change as shown by the powder diffractogram is highly significant as it is the first reported instance when an intercalating gas is able to alter the C_{60} lattice at room temperature. It is also significant that, although there is a change, it is only relatively small. As can be seen in Figure 2-24, there is still approximately 1:1 C_{60}:gas. Normally when a phase change is initiated on crystallisation of a fullerene there are several molecules of co-crystallite per C_{60} and the lattice is completely restructured.[205] Here we only observe a slight 1D expansion due to the large, cylindrical nature of the ethane molecule. The phase change, when examined more thoroughly is not as extreme as first appears. The shift to a tetragonal lattice is believed to be similar to the one reported by Gadd during studies of $C_{60}(CO_2)$ at low temperatures. Gadd used Rietveld analysis to show a low temperature monoclinic structure ($P2_1/n$, a=9.7438(9) Å, b=9.7473(9) Å, c=14.6121(11) Å, β=90.390(6)°, at 5 K) This is close to the observed structure and is explained by the use of Figure 2-25. We are simply looking at a different part of the face centred arrangement. Some simple trigonometry allows us to see that the corresponding a value for the face centred arrangement is 14.10 Å. This shows contraction in the lattice but is explained by the elongation along the c axis. We are not able to make any further deductions on the basis of Gadd's study, however, as both temperature and material were different from our case. More definite conclusions will be presented in Chapter 3.

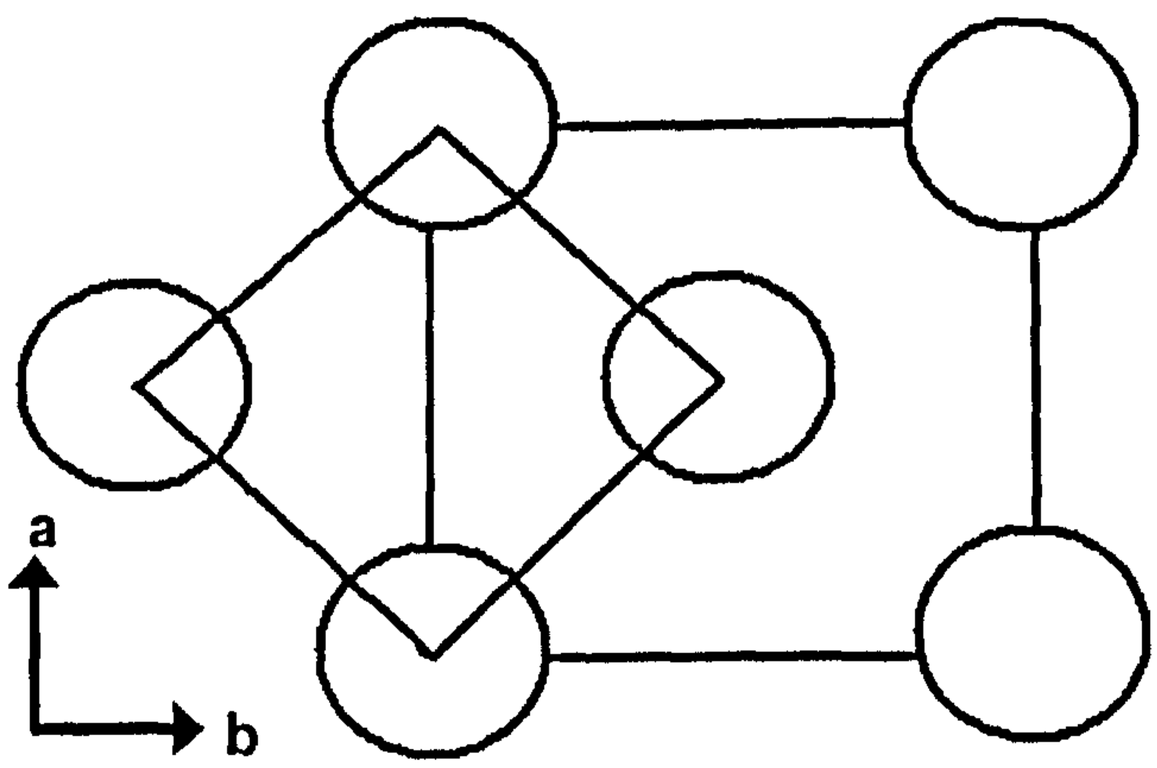


Figure 2-25: Illustration of the large change in a and b values on the transformation form a cubic to a tetragonal lattice.

$C_{60}(C_3H_6)$

IR evidence for the propene intercalate of C_{60} was shown earlier in this Chapter, but no other evidence for this intercalate existed. The experiments were not attempted by Webster and other research groups had already failed to intercalate smaller hydrocarbons. The GAS technique was used as for the ethene and ethane intercalates. This would have an impact on the precipitation as in this case liquefied rather than supercritical fluid was used. This was due to the relatively high critical temperature of propene, $T_c = 91.9$ °C (and propane, $T_c = 96.7$ °C). This should not be important in the synthesis of the compounds and their composition but it would seem likely that the liquid/liquid interaction would be slower and so material would have a longer crystal growth period and hence produce larger crystals, see Chapter 3. This supposition is supported by the SEM photographs of the new intercalate species. This is shown in Figure 2-26, which demonstrates the largest crystals to date. Interestingly, the crystal morphology has changed as well. Now the crystals are needles with a highly crystalline appearance and dimensions of approximately 1 μm by 10 μm.

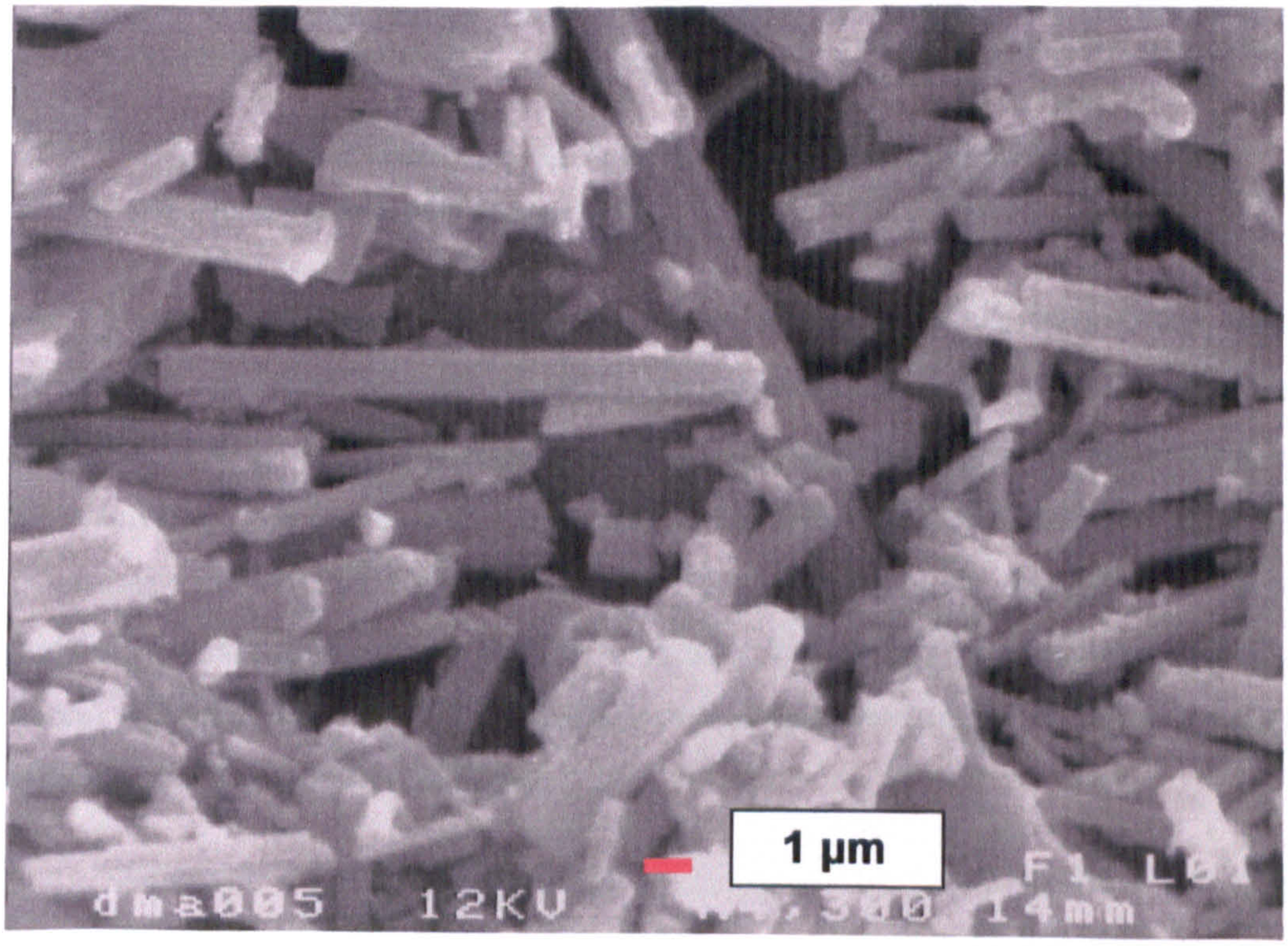


Figure 2-26: SEM of $C_{60}(C_3H_6)$ as grown by the new GAS technique.

From the highly crystalline appearance in Figure 2-26 it might be assumed that the powder pattern would be very detailed, however, as Figure 2-27 shows this is not the case.

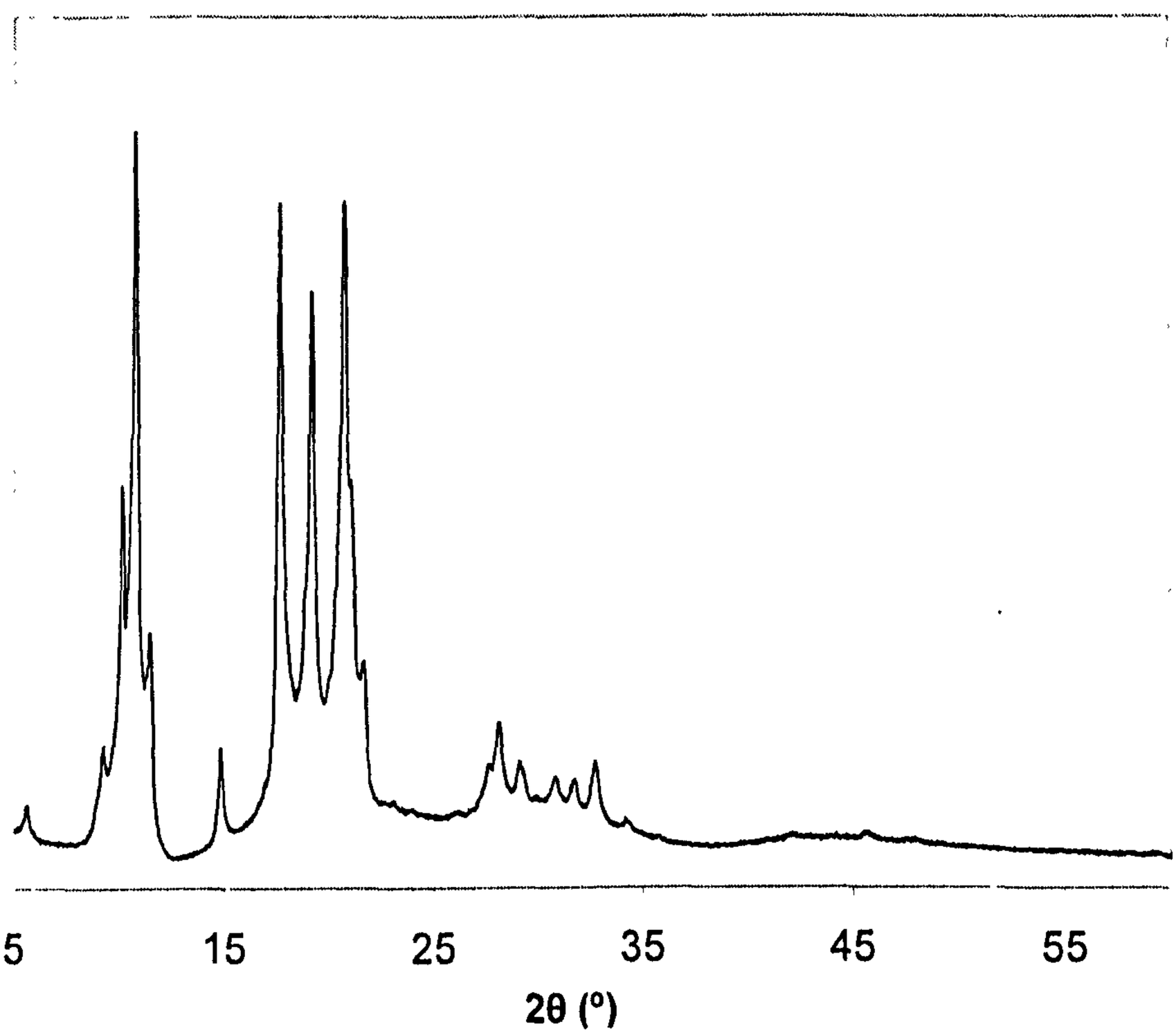


Figure 2-27: Powder data for $C_{60}(C_3H_6)$ shows lack of pure crystallinity despite promising SEM photographs.

The powder pattern for $C_{60}(C_3H_6)$ showed a poor diffraction pattern peaks were broad and a mixture of phases appeared to be present. The pattern itself did not index using DICVOL to any lattice and on examination of the quality of the pattern this is not surprising. The intensities of the peaks were also much lower than the previous intercalates and so this suggested that the samples were more amorphous. It was evident, however, that the precipitation technique had altered the structure of the C_{60} system and so MAS ^{13}C NMR was performed on it to attempt to judge the level of intercalation. This is given in Figure 2-28.

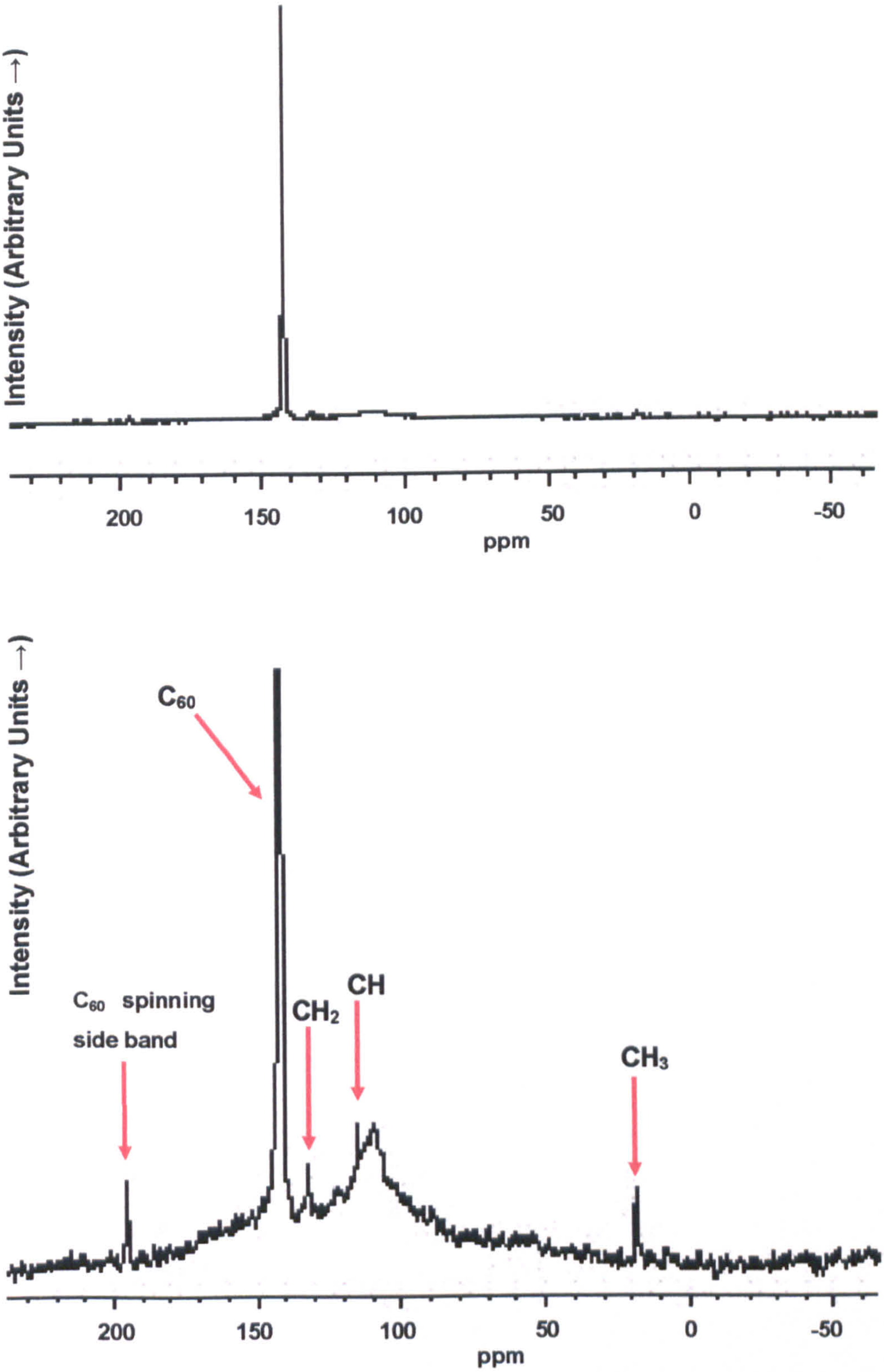


Figure 2-28: MAS ^{13}C NMR data clearly showing the three peaks of propene.

The NMR spectrum clearly shows the existence of the three extra peaks that we would expect form the presence of propene. The peaks lie at 18.1, 114.7 and 132.6 ppm. The integration of the peaks with respect to the large C_{60} peak gives a intercalation level of 61 % ± 5 % due to a ratio of 98±2 : 1. This level of intercalation could explain the poor powder pattern as with incomplete filling, or a structure too unstable to maintain complete filling, some area will contain propene and some areas will be pure C_{60}. Later observation by IR analysis of a 3 month old sample of the propene intercalate completely failed to show any trace of the hydrocarbon. This suggests that the propene is lost over time under atmospheric conditions. For this reason the NMR analysis was carried out as soon after sample preparation as possible, typically within a few hours. There is likely to be some loss of propene during this time and so an exact intercalation level at time of synthesis is not known. We therefore propose the NMR data as a proof of existence of the intercalate, rather than an accurate characterisation. Little more information can be gained, however, on the structure due to the presumed mixture of lattices present.

$C_{60}(C_3H_8)$

The investigation into $C_{60}(C_3H_8)$ proceeded in a very similar manner to that of $C_{60}(C_3H_6)$. Again this intercalate was one which had not been shown previously and was not thought likely to exist. Particles of the intercalated material were produced. SEM images of the particles revealed long needles of material, Figure 2-29, which are heavily twinned and relatively wide size distribution. The particles have well defined edges and faces and appear to be highly crystalline.

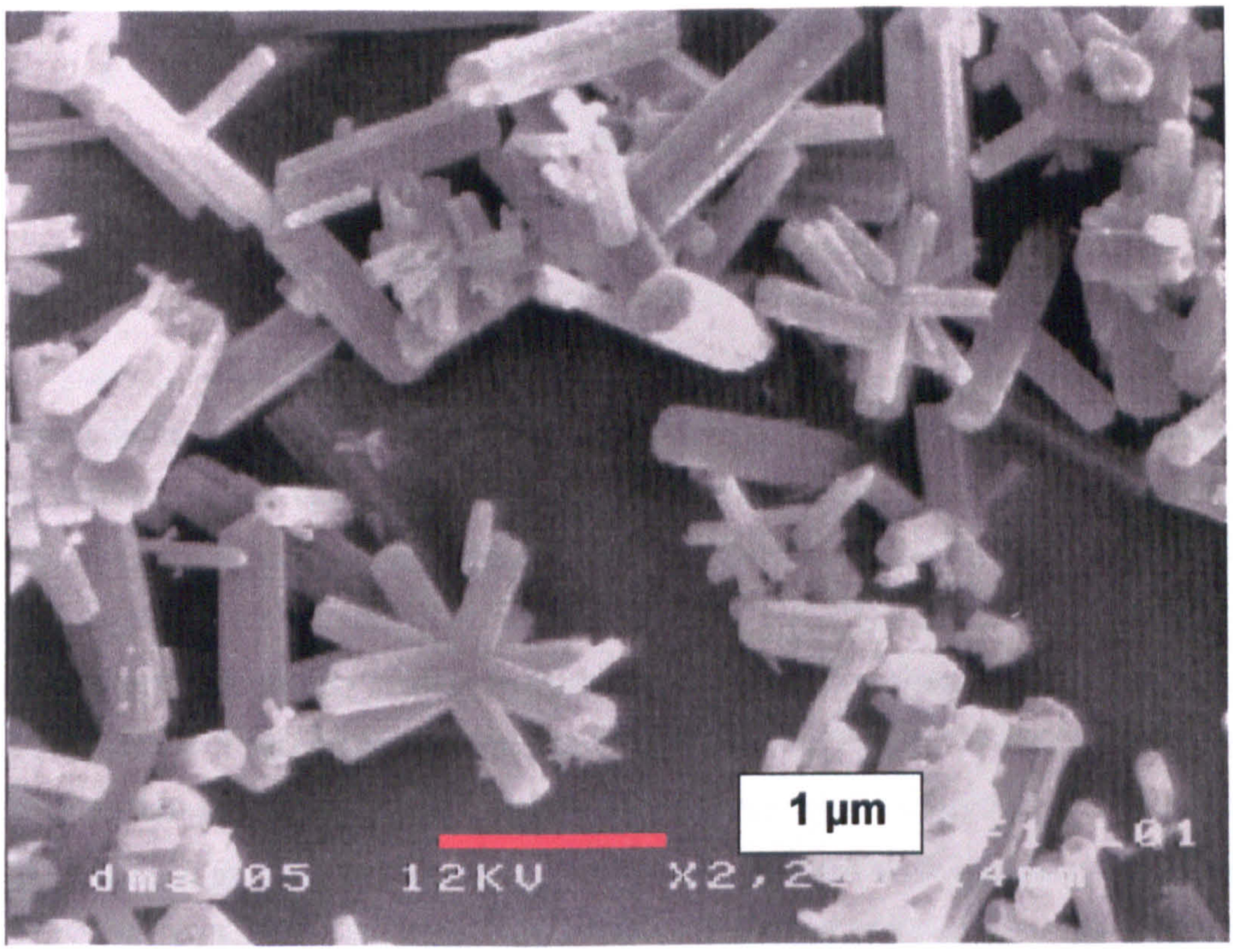


Figure 2-29: SEM of $C_{60}(C_3H_8)$.

The PXD analysis gives a similar pattern to $C_{60}(C_3H_6)$ with very broad peaks which do not index. The pattern is shown in Figure 2-30. Again, as with the propene intercalation, there appears to be a mixture of phases present in the pattern. Also, as with the propene intercalate, the intensity is relatively low, suggesting the sample is partly amorphous.

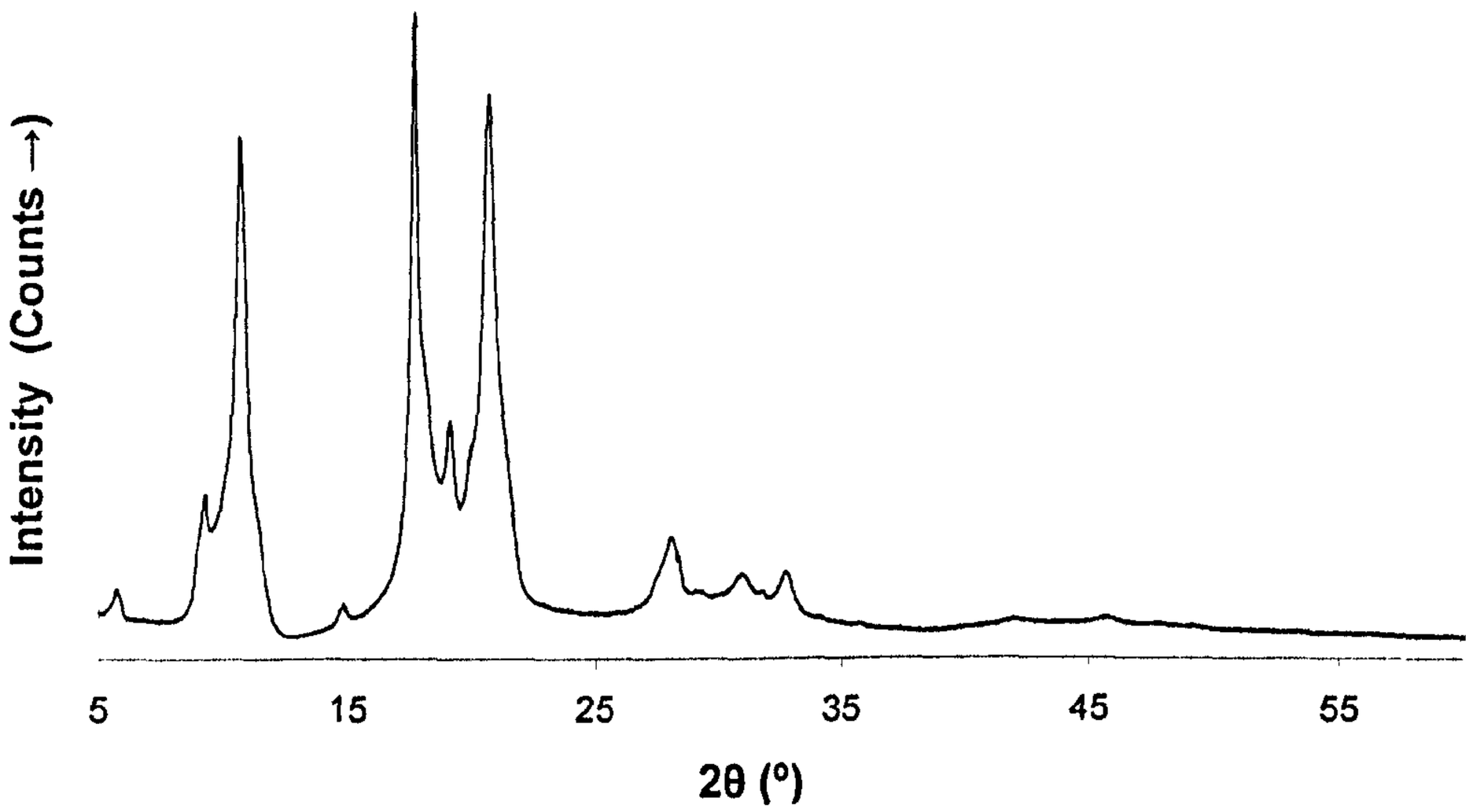


Figure 2-30: Powder diffraction pattern of $C_{60}(C_3I_8)$. The pattern appears similar to that for $C_{60}(C_3I_6)$ as a mixture of phases.

Again since little information can be gathered from the powder pattern NMR must be used to attempt view the system. This is shown in Figure 2-32. Here we see the typical C_{60} peak, the spinning sideband and the Teflon spacer. For C_3H_8 we would also expect to see two peaks to represent the CH_3 and CH_2 carbons in a 2:1 ratio. This is not immediately evident from the spectrum but, on closer inspection Figure 2-32, we see a second peak as a shoulder on the main peak. The peaks have an integral ratio of 1 : 0.569 which is close to what we would expect for the CH_3 and CH_2 peaks in propane. With a second integration peak, the total integration gives an intercalation of 59±2 : 3, which correspond to a level of 34 % ± 15 %. As with the propene sample the precision of these results are questionable due to the suspected loss of gas from the sample from the point when the pressure vessel was depressurised. This led to interest in the thermal stability of the samples and so a series of TGA experiments were devised.

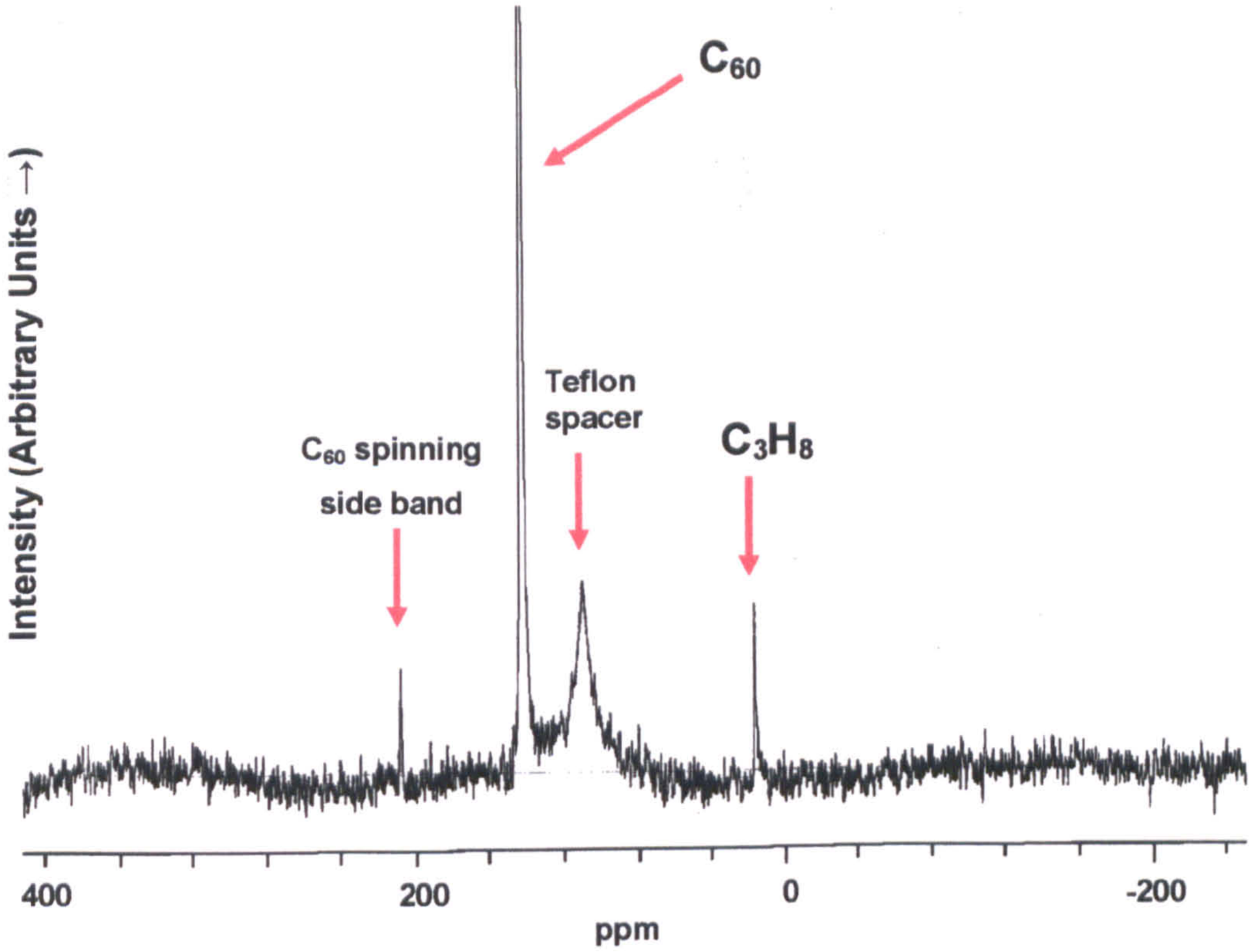


Figure 2-32: MAS ^{13}C NMR of propane intercalate. Only one alkane peak is visible

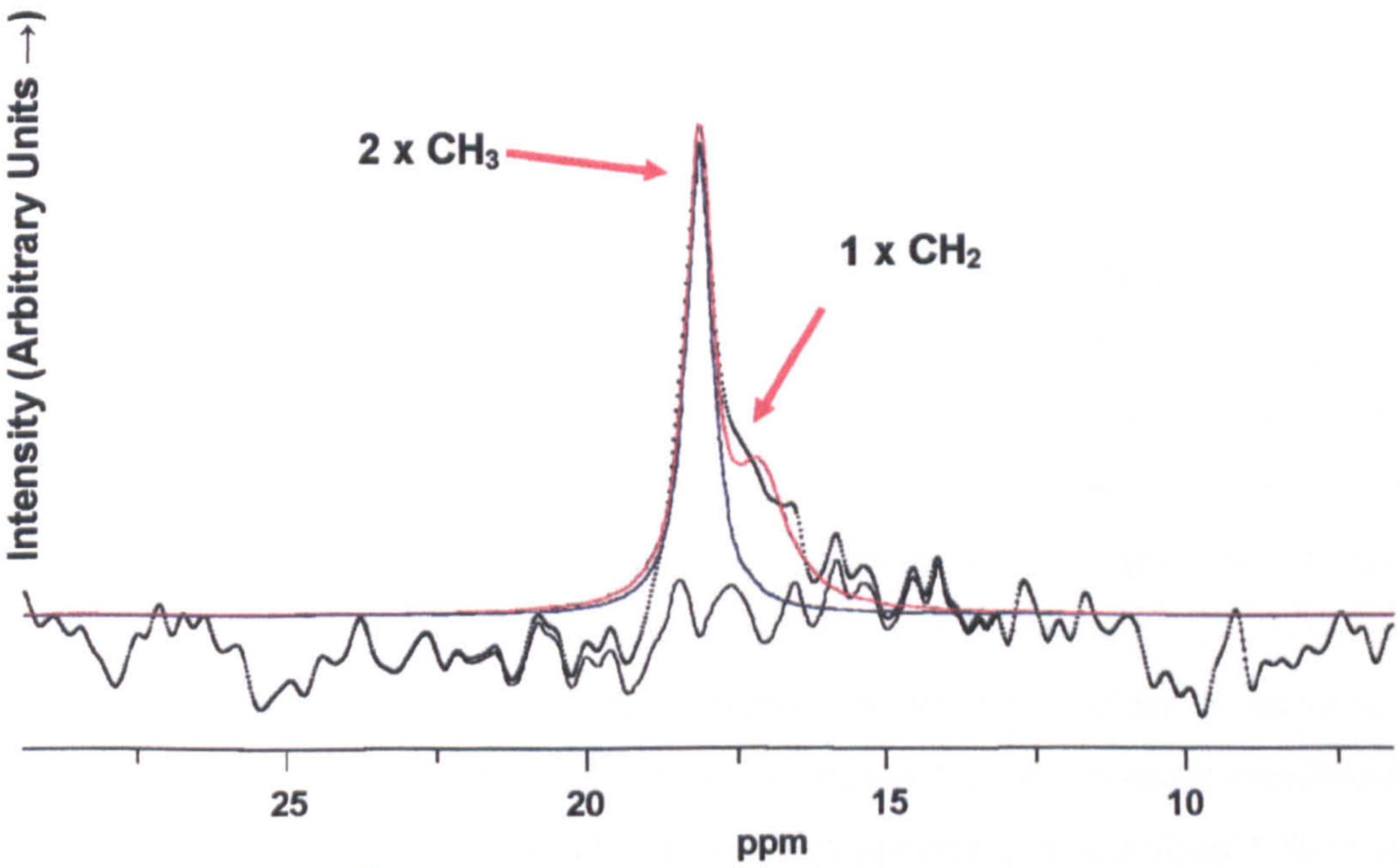


Figure 2-32: MAS ^{13}C NMR spectrum highlighting the propane peak. The blue line represents the first integration peak and the red line the combination two integration peaks. The black line at the base is a calculation of the baseline once the integration peaks have been remove and shows an acceptable convergence with the standard baseline

All four intercalates were subjected to TGA analysis. $C_{60}(CO_2)$ was also examined as this had not been attempted by Webster. A sample of material was heated at a rate of 10 degrees per minute for 90 minutes and the weight loss recorded over time. A graph records the resultant loss in Figure 2-33. An air flow of 30 ml min^{-1} was maintained throughout the experiment.

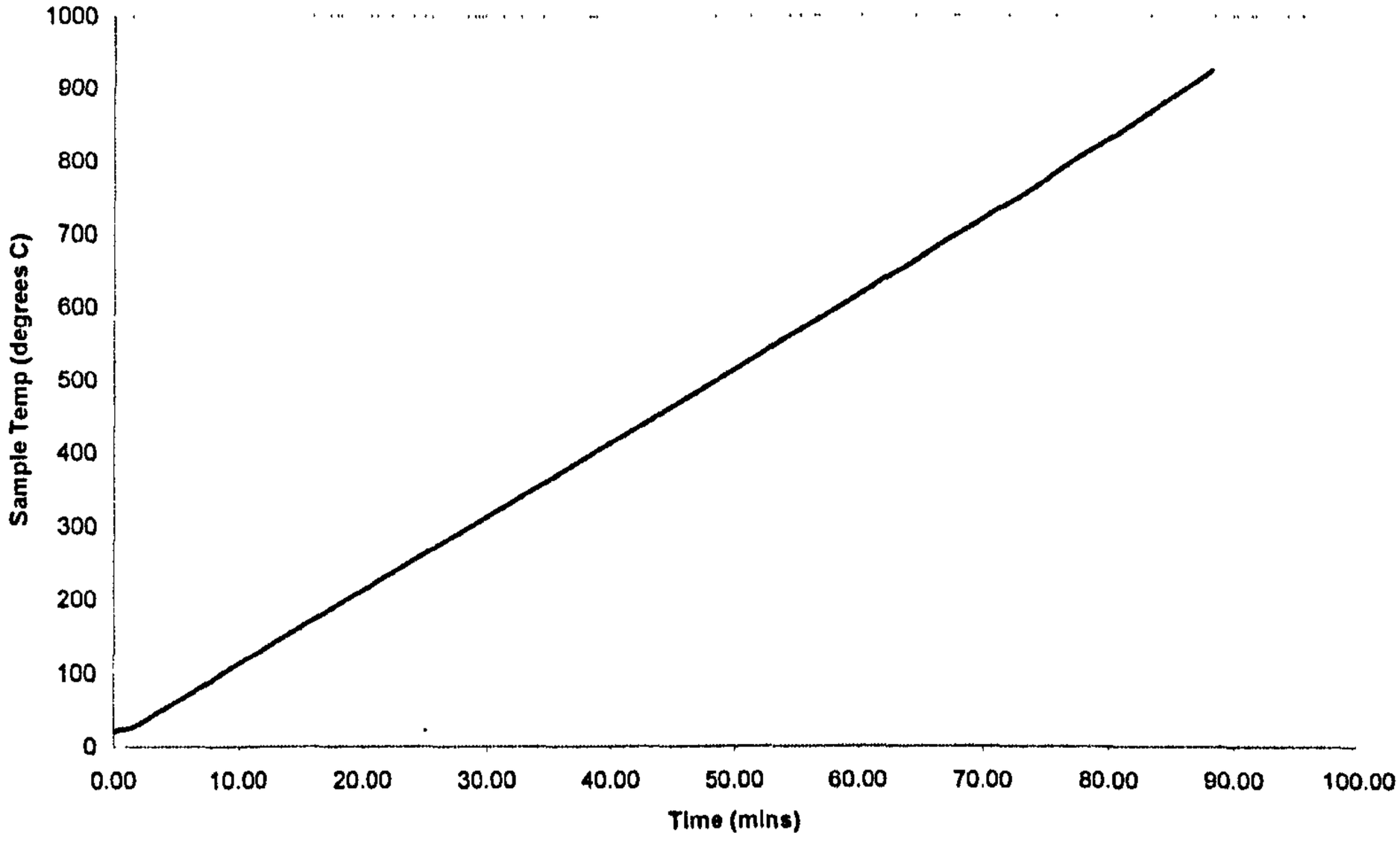


Figure 2-33: Heating profile of the fullerene intercalates during TGA analysis.

A graph containing all TGA data on the C_{60} intercalates is given in Figure 2-34. This chart gives us an idea of the relative stability of the compounds. The results are consistent with what would be expected. All intercalates are relatively stable with respect to temperature over this heating period. Initial weight losses can be shown to be due to loss of moisture, methane and oxygen, see Figure 2-35, Figure 2-37, Figure 2-38, Figure 2-39 and Figure 2-40. Gases are detected by mass spectroscopy and methane and water are present from impurities in the gas. Oxygen is inevitably present in all fullerene experiments which are exposed to atmospheric conditions. The exception to this is the CO_2 intercalate which appears to lose around 5 % of its CO_2 at 100 °C, see Figure 2-35. This intercalate then behaves as the others. The escaping gas is detected as CO_2, in all cases.

The size of the intercalating species appears to be the most important factor influencing the loss of gas with the larger gases being more easily and completely

removed by the application of heat. Features similar to the initial loss of mass in the CO_2 sample around 200 °C were observed in the other cases although to a lesser extent. The lost gas was not detected in these cases, however. This could be due to the weakened effect in the case of the propene and propane intercalates and the incomplete oxidation to CO_2 due to low temperature in the ethene and ethane cases.

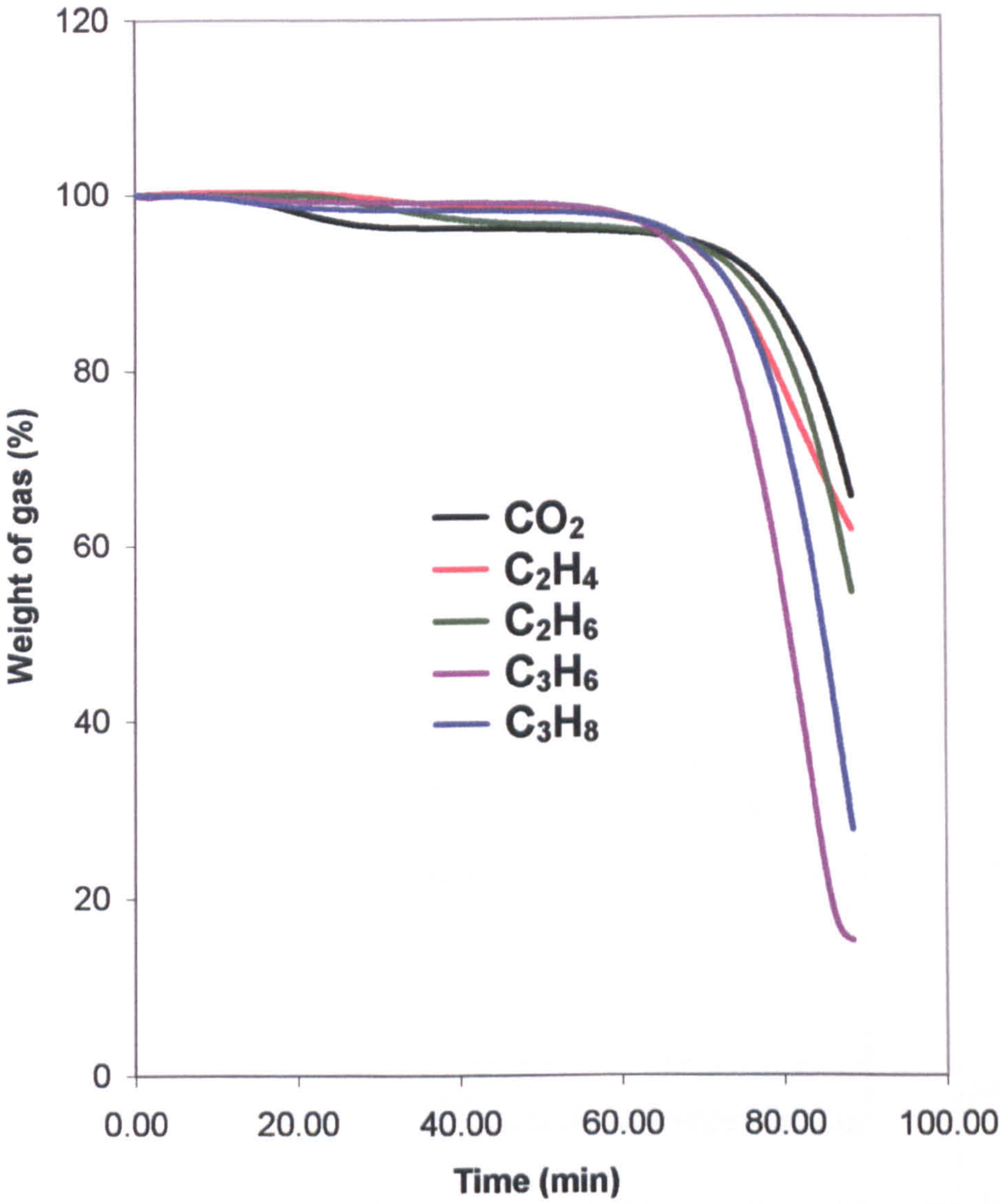


Figure 2-34: TGA plots of the percentage loss of gas over the course of the experiment.

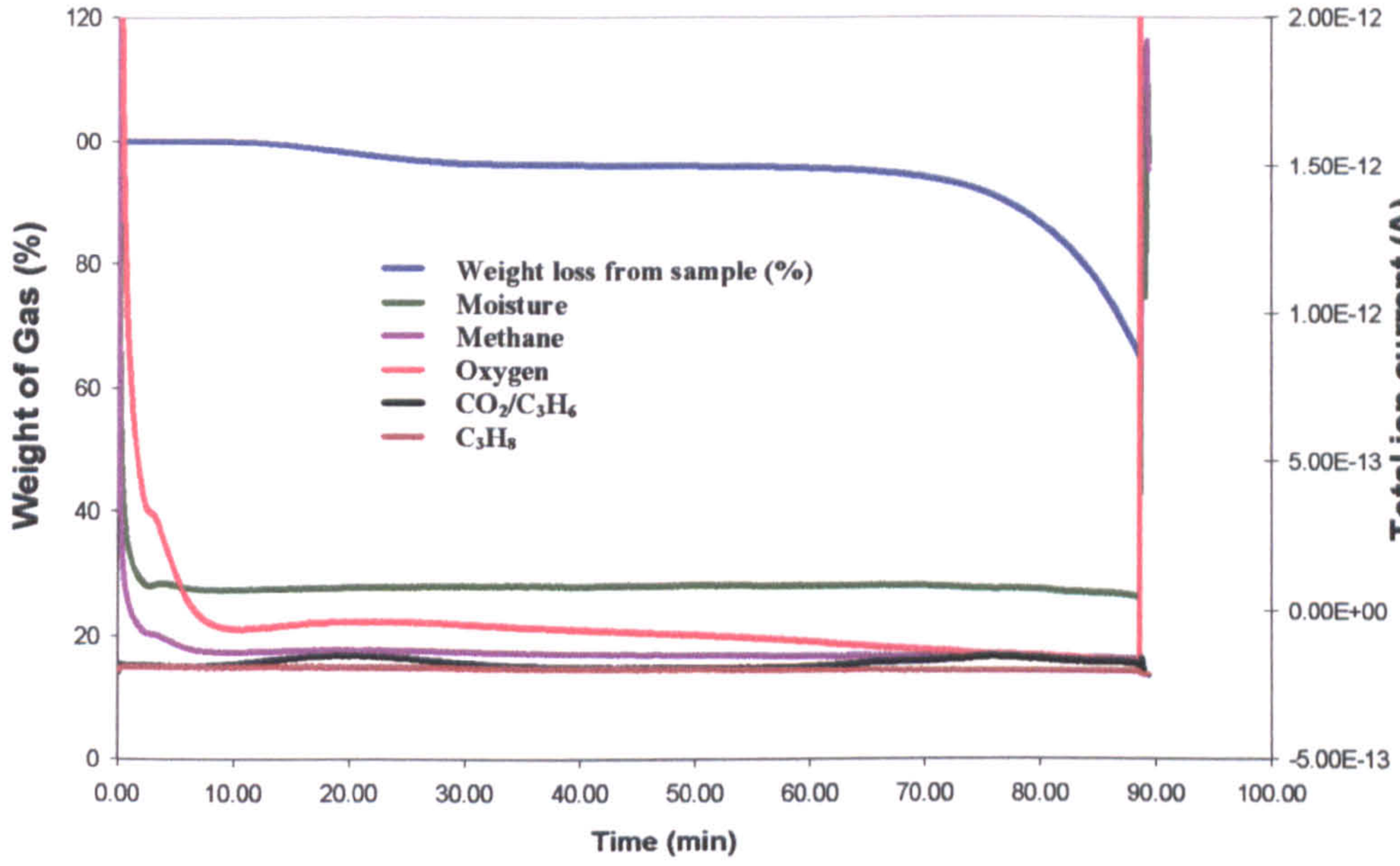


Figure 2-36: TGA plot of $C_{60}(CO_2)$ with gas loss measurements detected by mass spectroscopy. Note the loss of CO_2 at 20 min (200 °C) as well as 60-90 min (600-900 °C).

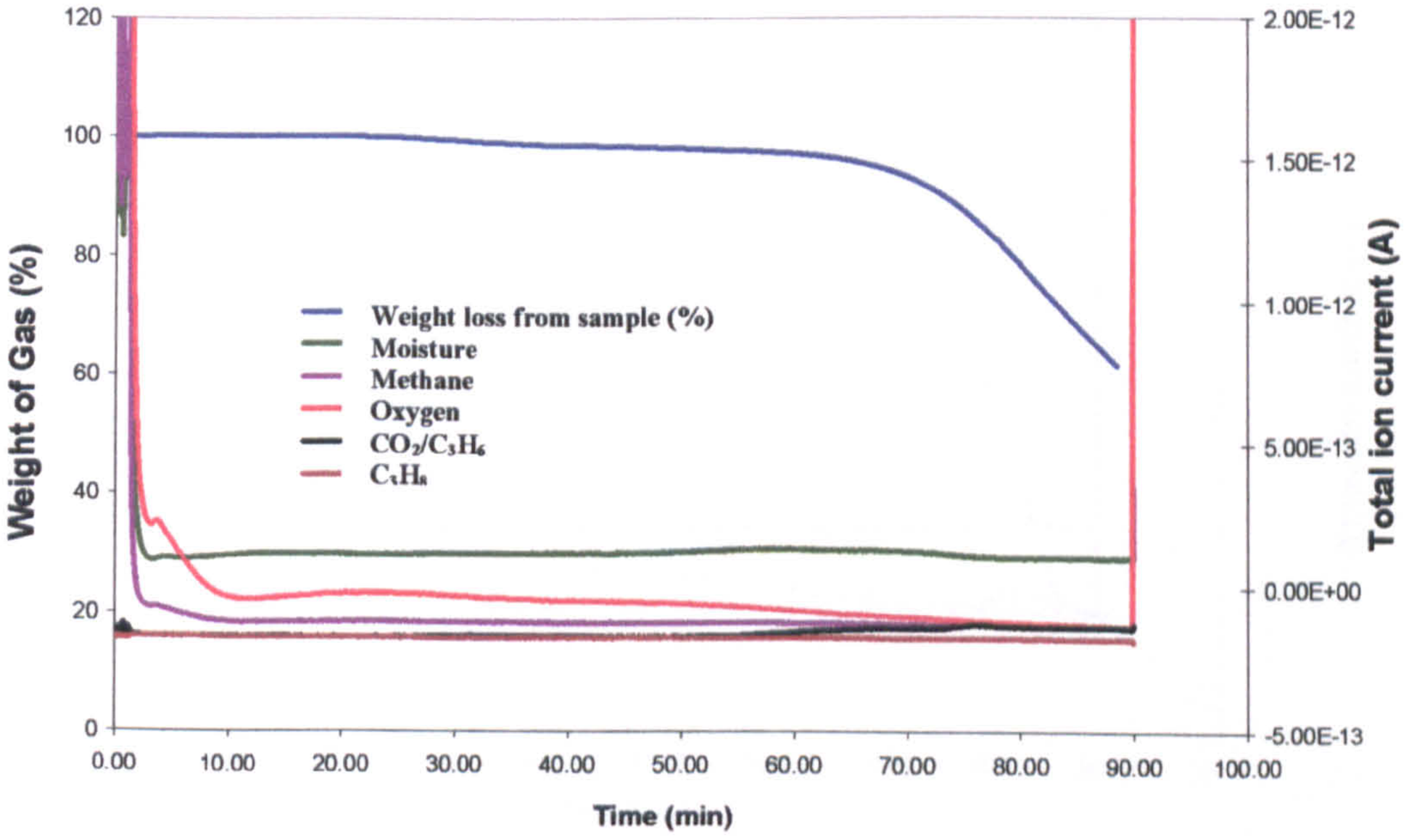


Figure 2-37: TGA of $C_{60}(C_2H_4)$, sample begins losing mass at 25 min (250 °C) but remains mainly stable until 70 min (700 °C).

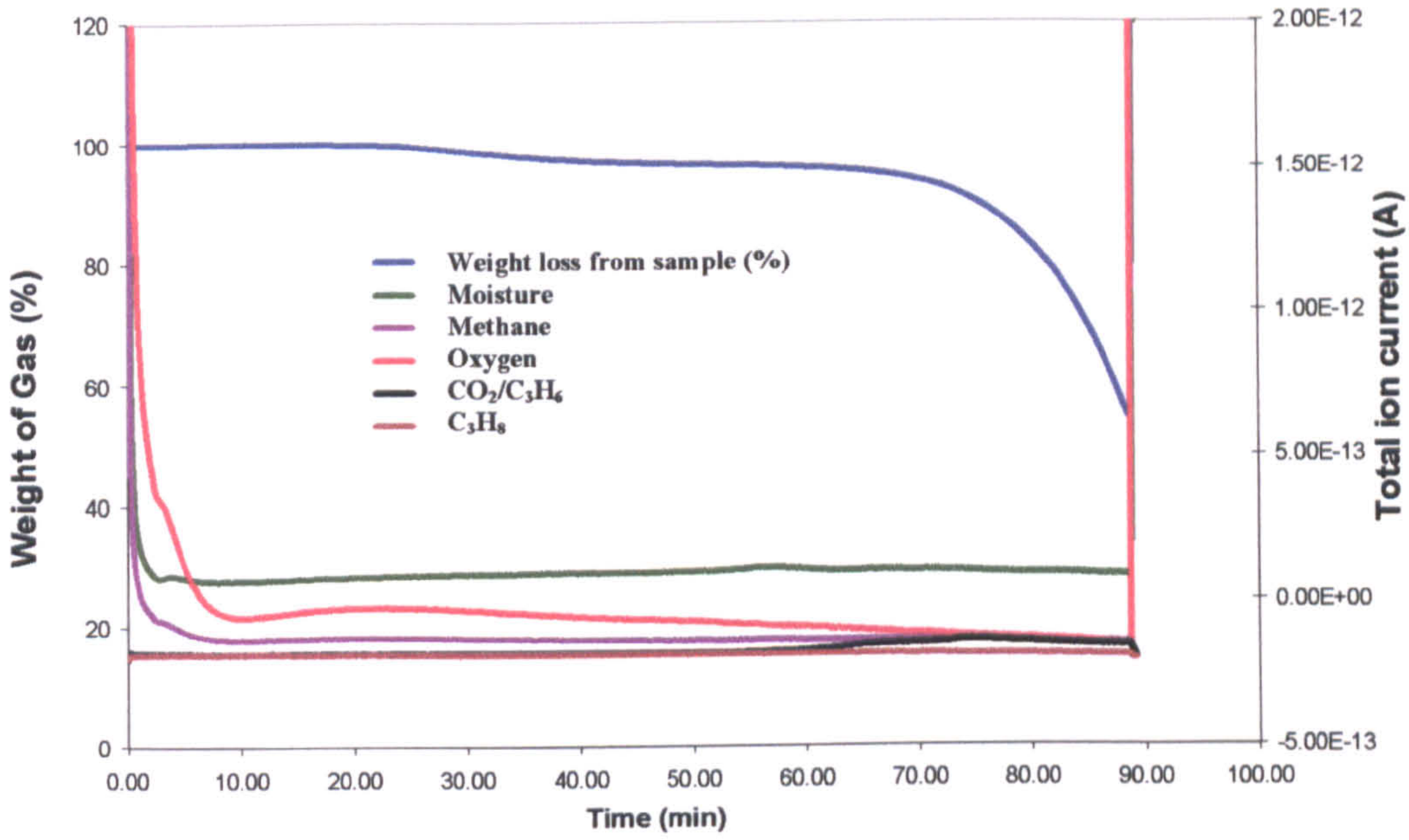


Figure 2-38: TGA plot of $C_{60}(C_2H_6)$, very similar to that of the ethene intercalate except the change at 25 min (250 °C) is slightly more pronounced and the larger loss around 70 min (700 °C) occurs slightly later.

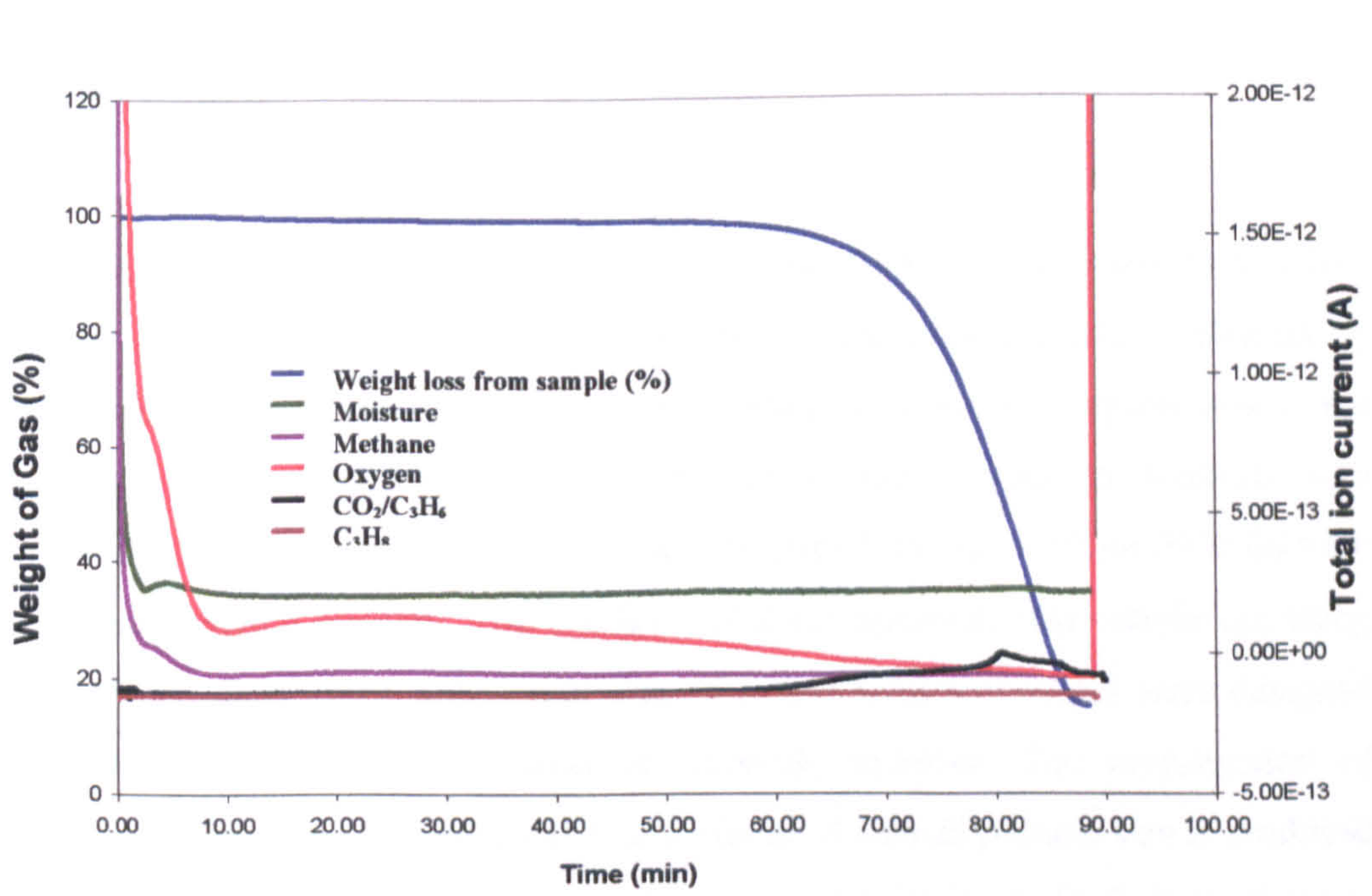


Figure 2-39: TGA plot of $C_{60}(C_3H_6)$ shows a less pronounced initial drop in mass initially but the final mass loss now occurs earlier 60 min (600 °C) and to a greater extent.

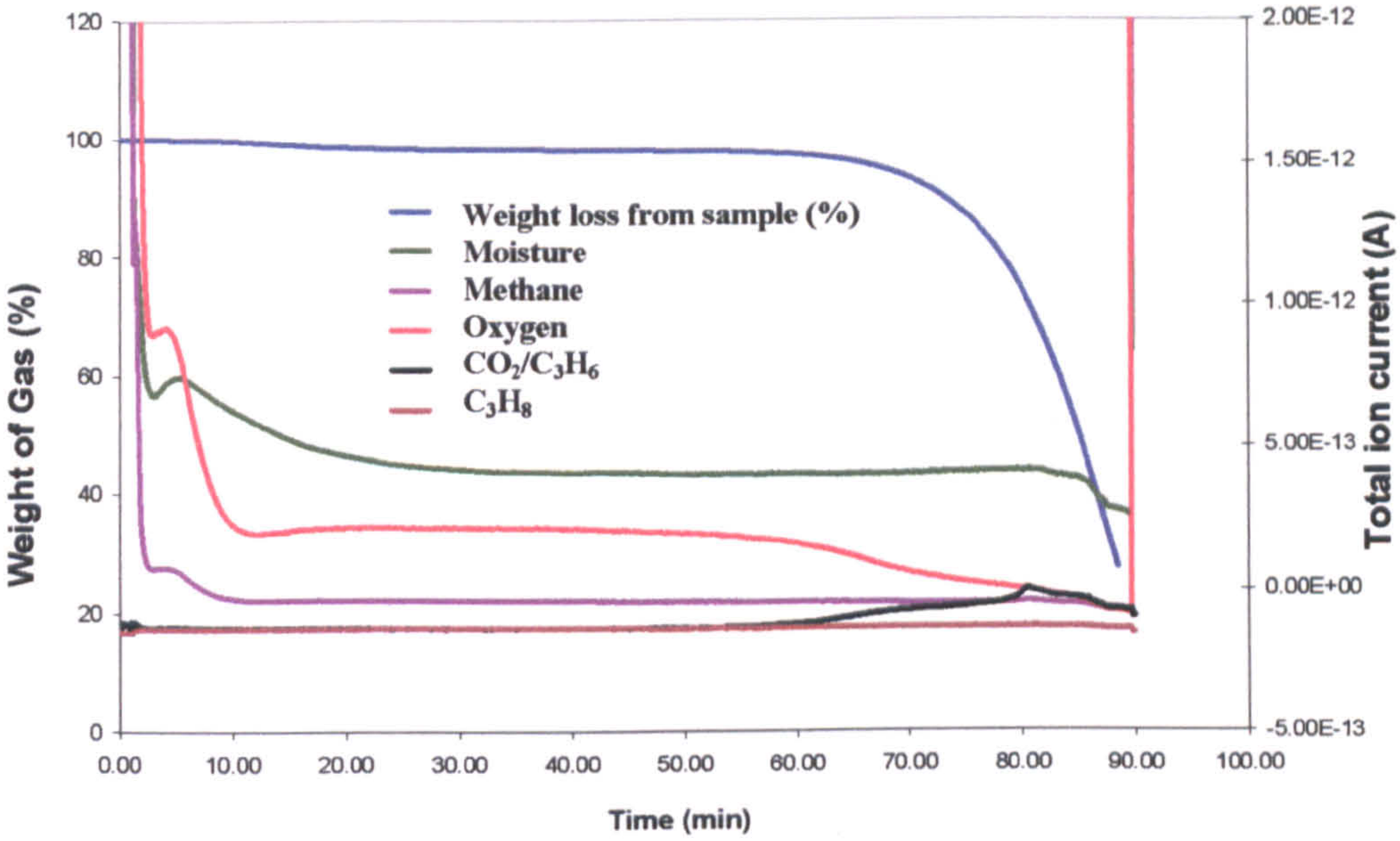


Figure 2-40: Final TGA plot showing the loss of gas from $C_{60}(C_3H_8)$. The initial loss is more pronounced than in the case of propene, occurring around 10 min (100 °C). The final gas loss begins similarly at 60 min (600 °C) and progresses rapidly.

Conclusion

To conclude this Chapter, the use of supercritical fluids has been shown to allow production of several new materials which have been impossible to synthesise by conventional means. The ethene and ethane intercalates are well characterised and Webster's initial results have been confirmed in these cases. In addition, new intercalates of propene and propane are also described, though without PXD data the structures remain a mystery. The synthesis of these materials was carried out using two different antisolvent techniques. The PCA and GAS techniques were designed originally to produce nanoparticles of material, however. The investigation of C_{60}(gas) is affected by this in-as-much as material of a small particle size is produced when, apart from for PXD analysis, this is not important. Indeed, it is counter-productive as it eliminates the possibility of characterisation by single crystal XRD. It would therefore be desirable to take the knowledge of the current techniques for

processing materials in supercritical fluids and create a new, simple technique which would allow us to produce crystalline samples of the fullerene intercalates. This will be discussed in the next Chapter with the goal of producing single, macroscopic crystals of these materials.

Chapter 3 Single Crystals of C_{60}(Gas)

In Chapter 2 it was shown that new C_{60} intercalation compounds could be made by using supercritical antisolvents. The techniques used were either directly or very closely related to techniques which have been previously used by other groups. It is known that "traditional" supercritical antisolvent precipitation acts to produce particles of a very small size. As was discussed in the Introduction, the important properties of these processes are a combination of mass transfer, nucleation kinetics, phase equilibria and hydrodynamics. It is clear that, in a given system at constant temperature and pressure, the rate of mass transfer should be constant. The speed at which gas moves into a droplet should only be dependent on the relative concentrations inside and outside of the droplet. This suggests that the larger the droplet the slower the attainment of equilibrium. This is not unreasonable from an understanding of conventional SCF antisolvent techniques. This Chapter uses this concept to suggest that, if to the greatest extent possible the hydrodynamic forces were removed, the crystals precipitated would be larger than in the previous techniques. If these principles were to be applied to the C_{60} intercalates, then it could be possible to grow these materials as single crystals large enough for X-Ray diffraction. If this were possible, it would be one of very few instances that these compounds could be characterised in this manner. To begin this Chapter, examination is made of how crystals grow in conventional systems. This will include experimental information on crystallisation systems and mathematical modelling of the nucleation and growth processes. This is followed by experimental details of several attempts to grow large crystals, of data collected from them and then a brief discussion on the influencing factors and the future of the project.

Crystal growth in fullerenes is of vital importance in allowing solid state measurements of the materials. Attempts have been made to grow materials from solution, although in all cases this results in a solvate complex being formed. These solvates have been reviewed by Dyachenko[205] and are generally made by

evaporation of the solvent to dryness, conventional antisolvent precipitation or vapour co-deposition. Indeed vapour deposition is by far the most effective way of growing large, pure fullerene crystals with reports of crystals as large as 6 mm by Tan.[216] Vapour deposition involves growth of crystals from vapour inside a vessel with a hot end and cold end. The vapour condenses at the cold end and, if the conditions are correct, crystals are grown. As relatively high temperatures are required for the sublimation process (*ca.* 550 °C) this cannot be used to intercalate heat sensitive materials. The process also requires relatively large quantities of fullerene and so is not ideal, particularly if crystals of rarer fullerenes are required.

Conventional Crystallisation

Crystallisation at atmospheric pressure has been studied and rationalised for decades.[217] The action of precipitation or any form of crystallisation involves two competing processes, that of nucleation and of crystal growth. The relative rates of the two processes govern the size of the crystals which are formed. In turn the external physical and chemical conditions influence the effectiveness of the two processes.

Nucleation

When crystallisation from a solution is to be achieved, the mass of solute dissolved in the solvent must be made greater than the quantity of solute the solution is theoretically capable of dissolving. Equation 3-1 is a simple equation, where c and c_{sat} refer to the concentration of solute in the solution and the concentration of solute at saturation respectively.[16] At first glance this appears to describe an unstable system; yet as far back as 1724, Fahrenheit was able to show that water could be cooled as low as -9.4 °C without freezing and, by 1813, Gay-Lussac had been able to demonstrate that supersaturated solutions which did not spontaneously nucleate were relatively common.[217] In fact these systems can be remarkably stable and it is generally reported that spontaneous nucleation will not occur until a supersaturation

ratio of approximately 4 is achieved. In practice, nucleation can be enhanced by some form of external force, such as a grain of dust or by scratching the sides of a beaker with a glass rod.

$$S = \frac{c}{c_{sat}}$$

Equation 3-1: The supersaturation ratio.[16]

The region where a solution becomes supersaturated but not spontaneously nucleating is given the term metastable, see Figure 3-1. In this example an understaturated solution of composition x_i can be made supersaturated by either lowering the temperature (a) or by increasing the concentration, *e.g.* by evaporation (b). Both these methods work to initiate the generation of crystals. The equilibrium concentration is shown as c_{eq} between the stable solution and the metastable region.

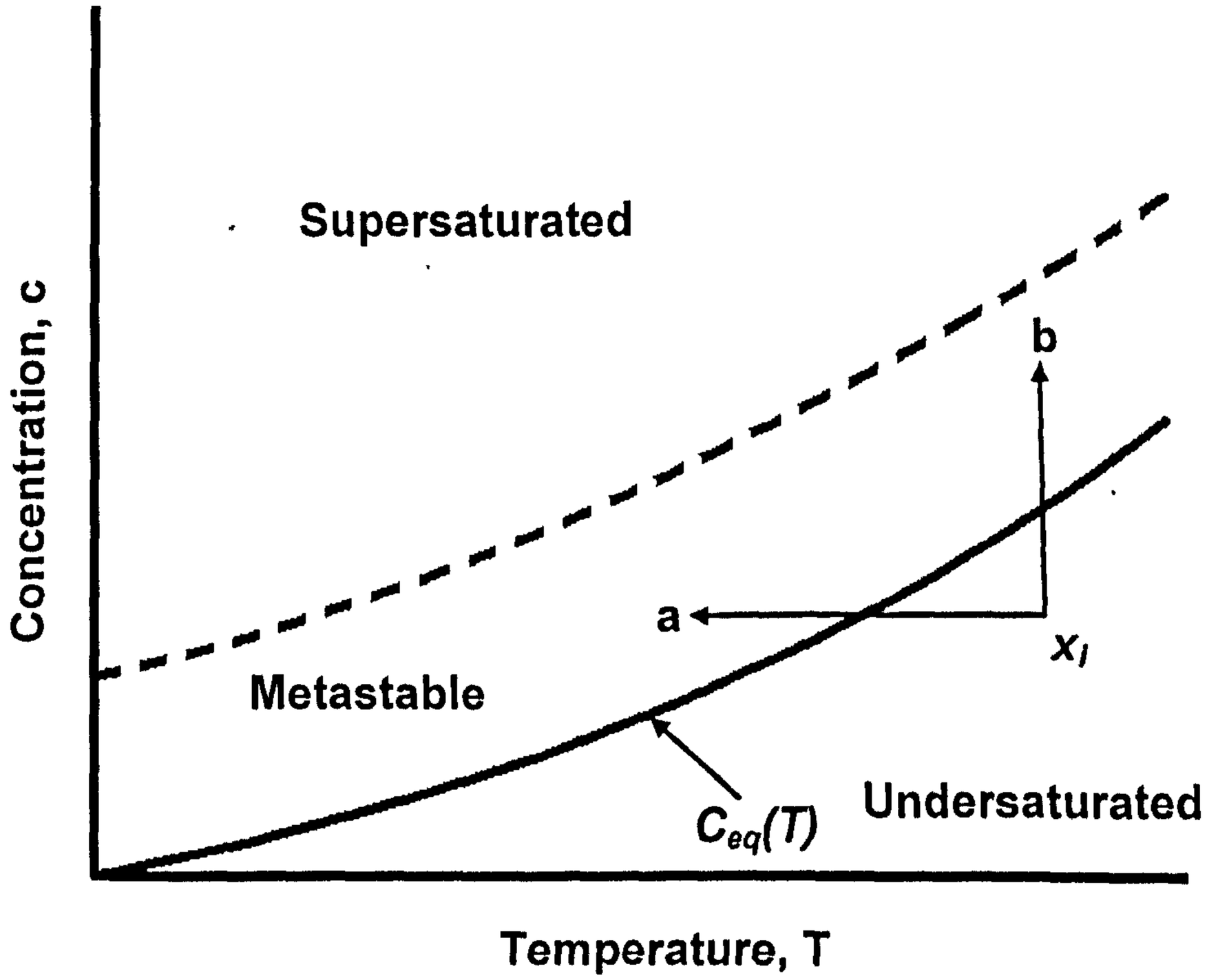


Figure 3-1: A solution will exist in a metastable state without spontaneously nucleating if there is no external influence.

The formal definition of a supersaturated state in thermodynamic terms is given in Equation 3-2,[217] where σ represents the dimensionless difference between the molecule in an equilibrium state, μ_{eq}, and the molecule in a supersaturated state, μ_{ss}.

$$\sigma = \frac{(\mu_{ss} - \mu_{eq})}{kT}$$

Equation 3-2: The formal definition of supersaturation.

For ideal solutions and using the Gibbs-Duhem equation, these chemical potentials can be described as in Equation 3-3.

$$\sigma = \ln\left(\frac{x_{ss}}{x_{eq}}\right)$$

Equation 3-3: The supersaturation in an ideal solution or in one which the activity coefficient is independent of temperature.

The process of nucleation itself is a much studied phenomenon and can be thought of as a chemical reaction requiring an activation process and possessing a transition state. This transition state is a forming cluster and, as in a chemical reaction, a cluster in its transition state can either return to its initial form or go on to its final form. The immediate difference being that, while a chemical reaction will generally involve only one, two or three molecules, a cluster will be made up of several tens of molecules. The initial investigation to the formation of this transition state begins with the assumption that, as solute begins to solidify, some solute atoms will be part of the bulk of the material while some will be on the surface. It is easy to suppose that the molecules in the bulk are in a more stable situation than those on the surface as we can see in Figure 3-2. In the example the atoms in the centre of the crystal are strongly bound on all sides while those on the surface are only bound to three other atoms.

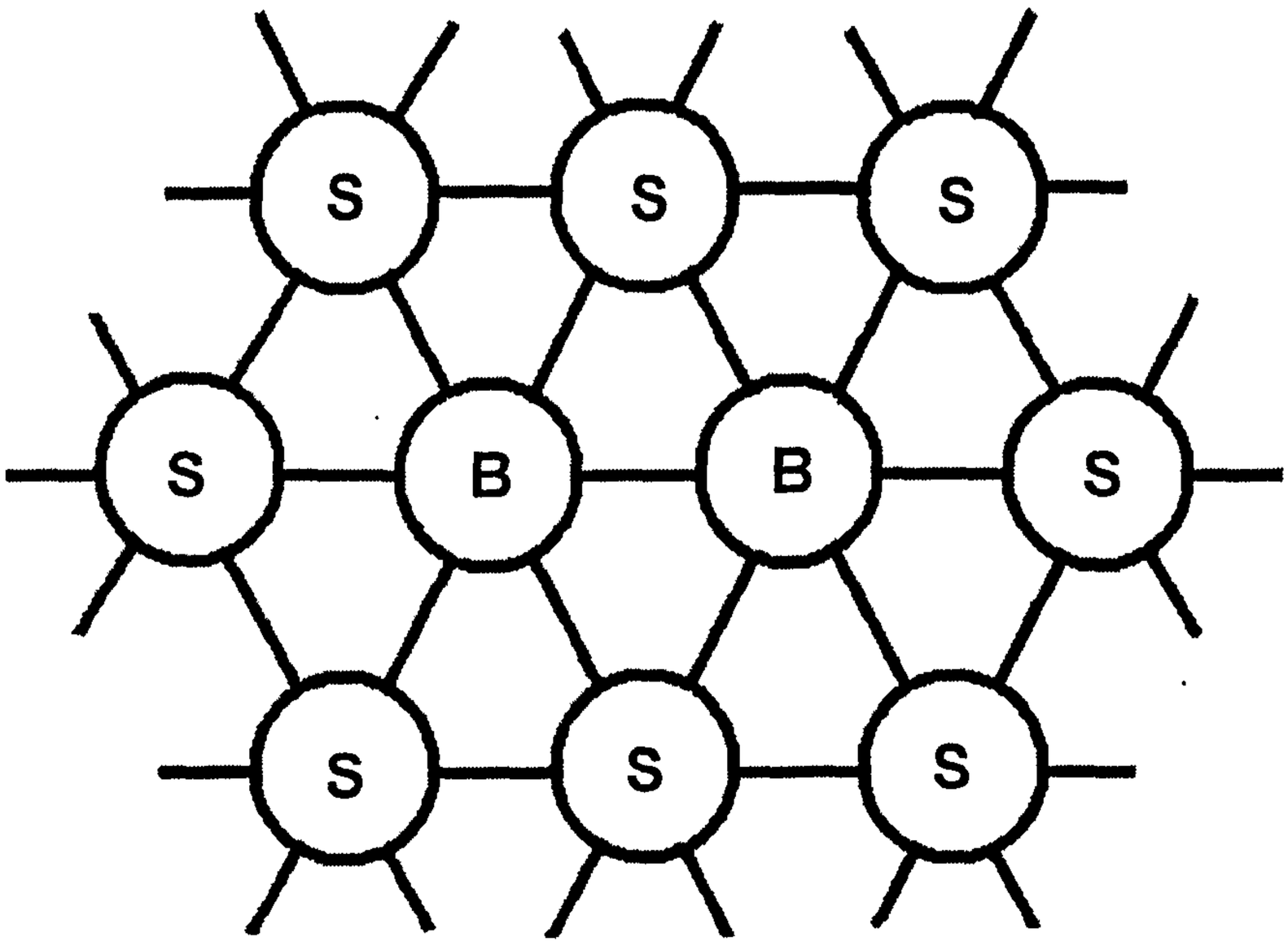


Figure 3-2: Schematic diagram of a forming crystallite, the atoms in the centre are in a more stable state than those on the surface. S represents a surface atom while B represents a bulk molecule.[218]

If a forming nucleus containing z molecules is considered, z_b molecules will be in the bulk of the material while z_s molecules will be on the surface. If the free energy of the cluster, g_z is considered, it can be said that, it is made up of the sum of the free energies of the molecules in the bulk, g_b, and the free energy of the molecules on the surface, g_s. This allows the formation of Equation 3-4 a and b.

$$g_z = z_b g_b + z_s g_s \qquad \text{so} \qquad g_z = (z_b + z_s) g_b + (g_s - g_b) z_s$$

Equation 3-4a and b: Considering the bulk and surface free energies.

If the interfacial tension between the cluster and the solution, γ, and the cluster surface area, A is considered, it can be said that:

$$\gamma = \frac{(g_s - g_b) z_s}{A}$$

Equation 3-5: The interfacial tension between the forming cluster and the solution.

and hence:

$$g_z = zg_b + \gamma A$$

Equation 3-6: The simple combination of Equation 3-4b and Equation 3-5.

If it is assumed that, as the clusters form, they are spherical it follows that $A \propto z^{2/3}$ and if the chemical potential, μ_b, is examined then Equation 3-6 can be transformed into Equation 3-7 where β is a factor which is influenced by the shape of the forming nucleus.

$$g_z = z\mu_b + \beta\gamma\ z^{2/3}$$

Equation 3-7: The free energy of the cluster in terms of the chemical potential and the interfacial tension.

Since at the time the process unfolds, the cluster is not irreversibly nucleated there exists a pseudo-equilibrium between the solute molecules in the cluster with the molecules in the supersaturated solution. The free energy change per mole of solute is $\Delta G = g_z - z\mu$ where μ is the chemical potential of individual solute molecules and is equal to $\mu^\circ + kT\ln x_{ss}$.

$$\Delta G = \left(z\mu_b + \beta\gamma.z^{2/3} \right) - z\left(\mu^\circ + kT\ln x_{ss}\right)$$

Equation 3-8: Free energy change of a nucleating species.

But for a saturated solution $x = x_{eq}$ and so $\mu_b = \mu^\circ + kT\ln x_{eq}$, this means that Equation 3-8 becomes Equation 3-9 where the free energy change in relation to the supersaturation ratio exists. This was defined earlier in Equation 3-3.

$$\Delta G = -zkT\ln\left(\frac{x_{ss}}{x_{eq}}\right) + \beta\gamma.z^{2/3}$$

Equation 3-9: the free energy relates to the supersaturation ratio of Equation 3-3.

Equation 3-9 shows the relationship between the size of the cluster, z, and the free energy, ΔG. If this is plotted for two supersaturation situations two curves beginning with a positive gradient which decreases and then becomes negative with increasing cluster size are seen. The effect of supersaturation is also noticed; under low supersaturation, the cluster must be larger before the free energy begins to decrease.

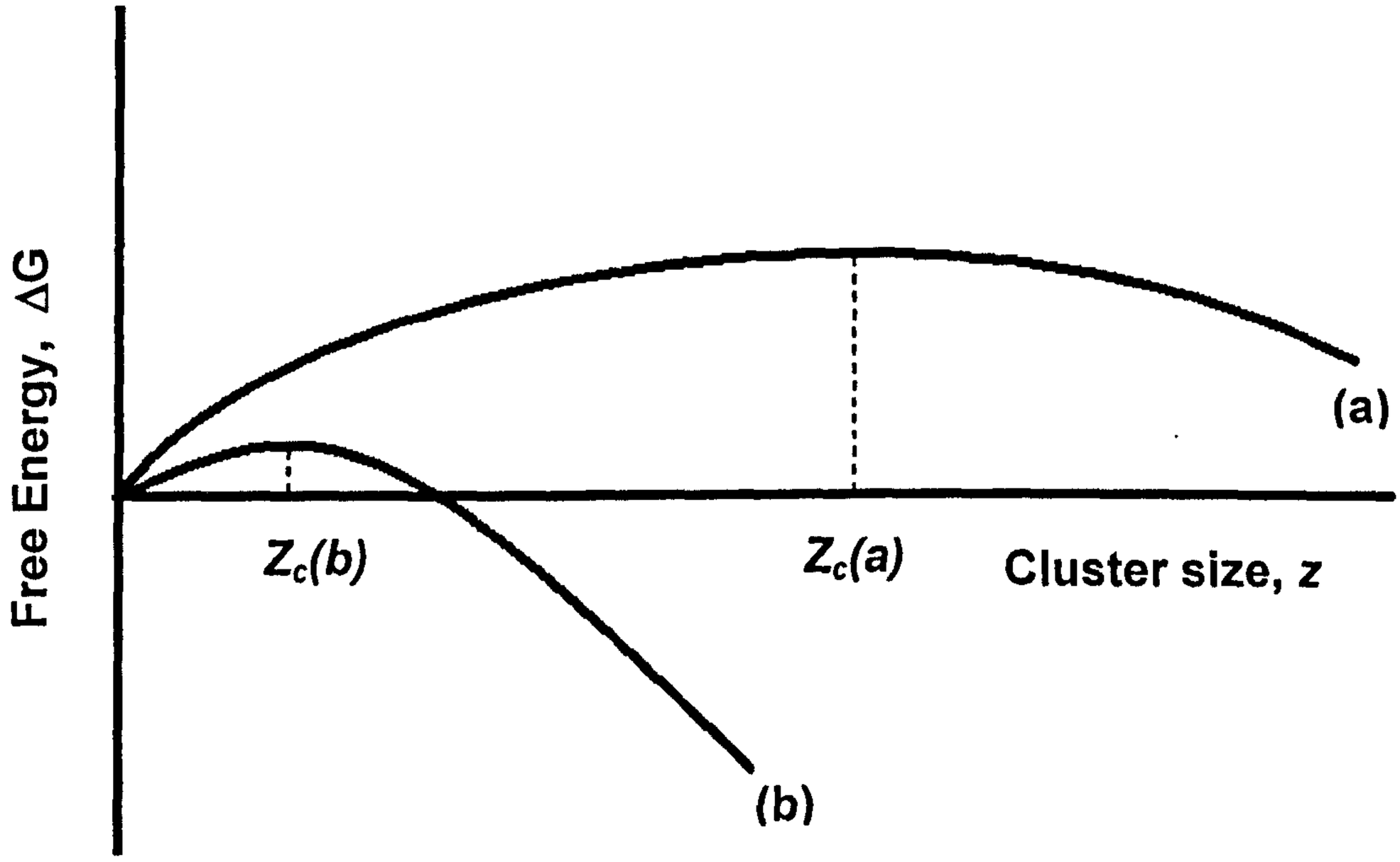


Figure 3-3: Free energy change as a function of cluster size and low supersaturation, (a) and high supersaturation, (b).[218]

Figure 3-3 shows the path of free energy during the formation of a cluster. The maximum value of ΔG can be seen as an activation energy to a chemical reaction. The value of z which correlates to this maximum is the critical crystal size and is the size beyond which clusters can go on to become crystals.

If the simplification shown in Figure 3-2 is extended and the molecules in the forming crystal are compared to those still in the fluid phase, it can be imagined that a skin of surface tension is formed over the surface of the forming crystal, this is exerting a force compression force on the bulk atoms in the crystallite. This means that the pressure that the bulk atoms are experiencing is slightly higher than in the fluid. This can be written mathematically as in Equation 3-10, where the difference

in bulk pressure, p^b, and fluid pressure, p^f, is related to surface tension and inversely to the crystal radius.

$$p^b - p^f = \frac{2\gamma}{r}$$

Equation 3-10: The difference in pressures is related to the surface tension and the radius.

Thus if the radius of the crystal is smaller the pressure exerted on the bulk is larger and hence the chemical potential, μ_b, is raised. It is known that at the equilibrium point the chemical potential in the crystal is equal to the chemical potential inside the crystal so it can be written:

$$\mu_b = \mu_{eq} = \mu^\circ + RT \ln x_{eq}(r)$$

Equation 3-11: When the chemical potential of the bulk crystal atoms equals the chemical potential at equilibrium we know that the change in free energy is zero.

It becomes clear that the solubility of the crystals becomes greater as the size decreases. This statement can be written formally as, Equation 3-12, where $\upsilon_{\text{crystal}}$ is the molar volume of the crystal.

$$\mu_b(T, p^b) = \mu_b(T, p^f) + (p^b - p^f)\upsilon_{crystal}$$

Equation 3-12: The chemical potentials of the solute atoms with regard to the relative pressure of the bulk and fluid.

By returning to Equation 3-10, Equation 3-12 can be converted into Equation 3-13.

$$\mu_b(T, p^b) = \mu_b(T, p^f) + \frac{2\upsilon_{crystal}\gamma}{r}$$

Equation 3-13: The chemical potentials related to the surface tension.

By taking Equation 3-13 and remembering that $\mu_b = \mu_{eq}$ Equation 3-14 can be written as:

$$\ln x_{eq}(r) = \ln x_{eq}(\infty) + \frac{2\upsilon_{crystal}\gamma}{rRT}$$

Equation 3-14: Converting Equation 3-13 into mole fractions.

Hence it is possible to rearrange into Equation 3-14 which is often referred to the Ostwald-Freundlich equation. This indicates that in a solution containing crystals with a large diversity of sizes the smaller crystals will re-dissolve and grow onto the larger ones, this is know as Ostwald ripening.

$$\frac{x_{eq}(r)}{x_{eq}(\infty)} = \exp\left(\frac{2\upsilon_{crystal}\gamma}{rRT}\right)$$

Equation 3-15: The Ostwald-Freundlich equation.

The rate of the nucleation is defined as the rate at which clusters pass this critical size and hence go on to become crystals. This rate can be expressed in an equation similar to a chemical reaction and so $z_{cc}A \rightarrow A_{cc}$ where z_{cc} molecules of A combine to form a cluster of critical size. The rate constant for this process is therefore:

$$K_z = \frac{[A]^{z_c}}{[A_{cc}]}$$

Equation 3-16: Rate constant for the formation of critical clusters.

This rate constant, Equation 3-16, can be simply equated to the free energy to yield Equation 3-17, where ΔG_{cc} is the free energy change at the critical cluster size.

$$\ln K_z = \frac{-\Delta G_{cc}}{RT}$$

Equation 3-17: The rate constant equates to the free energy of a system.

Now by combining Equation 3-16 and Equation 3-17, Equation 3-18 is generated.

$$[A_{cc}] = [A]^{z_c} \exp\left(\frac{-\Delta G_{cc}}{RT}\right)$$

Equation 3-18: The concentration of critical clusters in relation to the number initial solute concentration, the critical cluster size and the free energy change.

Thus the rate of nucleation, J, is this concentration when the radius, r_c, is the critical radius given by Equation 3-19.

$$\Delta G_{cc} = \left(\frac{4}{3}\pi r_{cc}^3\right)\Delta G_b + 4\pi r_{cc}^2 \gamma$$

Equation 3-19: ΔG expressed in terms of the radius and interfacial tension.

By remembering that when $r = r_{cc}$, $d\Delta G_{cc}/dr = 0$ it can be shown that the free energy for a molecule in the bulk is given by $\Delta G_b = -2\gamma/r_{cc}$. Equation 3-18 and Equation 3-19 can therefore be used to make Equation 3-20.

$$[A_{cc}] = [A]^{z_c} \exp\left(\frac{-8\pi\gamma\ r_{cc}^2}{3RT}\right)$$

Equation 3-20: Concentration of critical nuclei with the free energy replaced by the calculated value for $r = r_c$.

There still exists a probability term that the nuclei which grow to this radius, r_c, will go on to form crystals or will return to re-dissolve back into solution. This term, Q, is introduced in Equation 3-21.

$$J = Q[A_c] = Q[A]^{z_c} \exp\left(\frac{-16\gamma^3 \upsilon_c^2}{3R^3T^3\sigma^2}\right)$$

Equation 3-21: The rate of nucleation as controlled by the concentration of critical clusters multiplied by the probability they will progress to crystals.

Equation 3-21 can be simplified to Equation 3-22 where the surface tension, the supersaturation ratio and the temperature is examined.

$$J = K_J \exp\left(-\frac{B_J \gamma^3}{T^3 \sigma^2}\right)$$

Equation 3-22: Simplified equation for the rate of nucleation allows us to examine the important features of crystallisation at different temperatures.

In Equation 3-22 it is possible to gain some insight into the important features of crystallisation. For instance at low supersaturation the interfacial tension is significant and the free energy term becomes large and J tends to zero. The equation allows prediction of the metastable region which is observed in practice. The nucleation, J, remains very low until a critical supersaturation value is reached upon which the rate of nucleation begins to rise very rapidly. This is demonstrated in Figure 3-4. The temperature can be seen to have an important influence, although this can be important in conventional crystallisation where this is varied during the course of an experiment. PCA and GAS are also affected, where localised cooling caused by evaporation and spraying can influence precipitation.

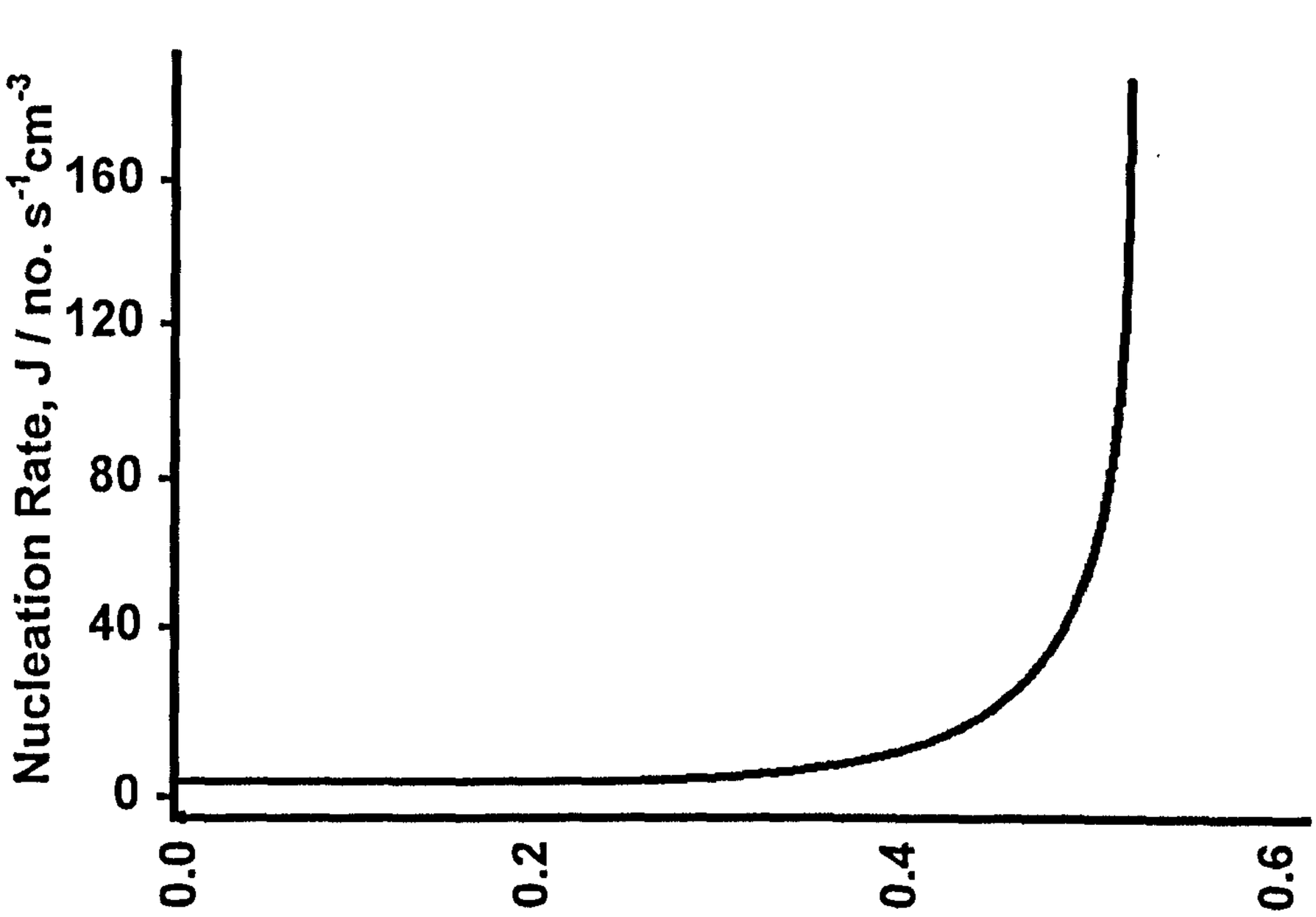


Figure 3-4: Rate of nucleation remains virtually zero until a supersaturation of approximately 0.4 is reached. At this point the nucleation rate grows very rapidly.

The action of an antisolvent, which is vital to the work presented here is modelled simply by a cubic equation, Equation 3-23. Here c_s and c_a are the concentrations of the solution and the antisolvent respectively. The x, y and z parameters are arbitrary variables for description of a given system.

$$c_s = xc_a^2 + yc_a + z$$

Equation 3-23: Cubic equation for explanation of antisolvent behaviour.

This equation is used for antisolvent crystallisation in conventional solvents, although is not tremendously helpful as the x, y and z parameters must be measured experimentally for a given system. Currently the facilities to do this for the SCF experiments are not available. This is not vitally important, however as the concept of the equation may still be used to describe what is occurring in the crystals.

Crystal Growth

The second factor in determining crystallisation is the rate of crystal growth. In investigating crystal growth, how a molecule arriving at a crystal surface will interact with it must be examined. A schematic diagram as used by Davey[217] is given in Figure 3-5. This illustrates the work of Hartnam and Perdock[218] that for a given system a newly arrived molecule will find the greatest resting stability if it fits into a *kinked* or K site where in this case there are three sides for the molecule to interact with. This is opposed to a *stepped* or S face where there are only two faces to interact with. Finally both these situations will be preferable the a *flat* of F face which has only one direct contact.

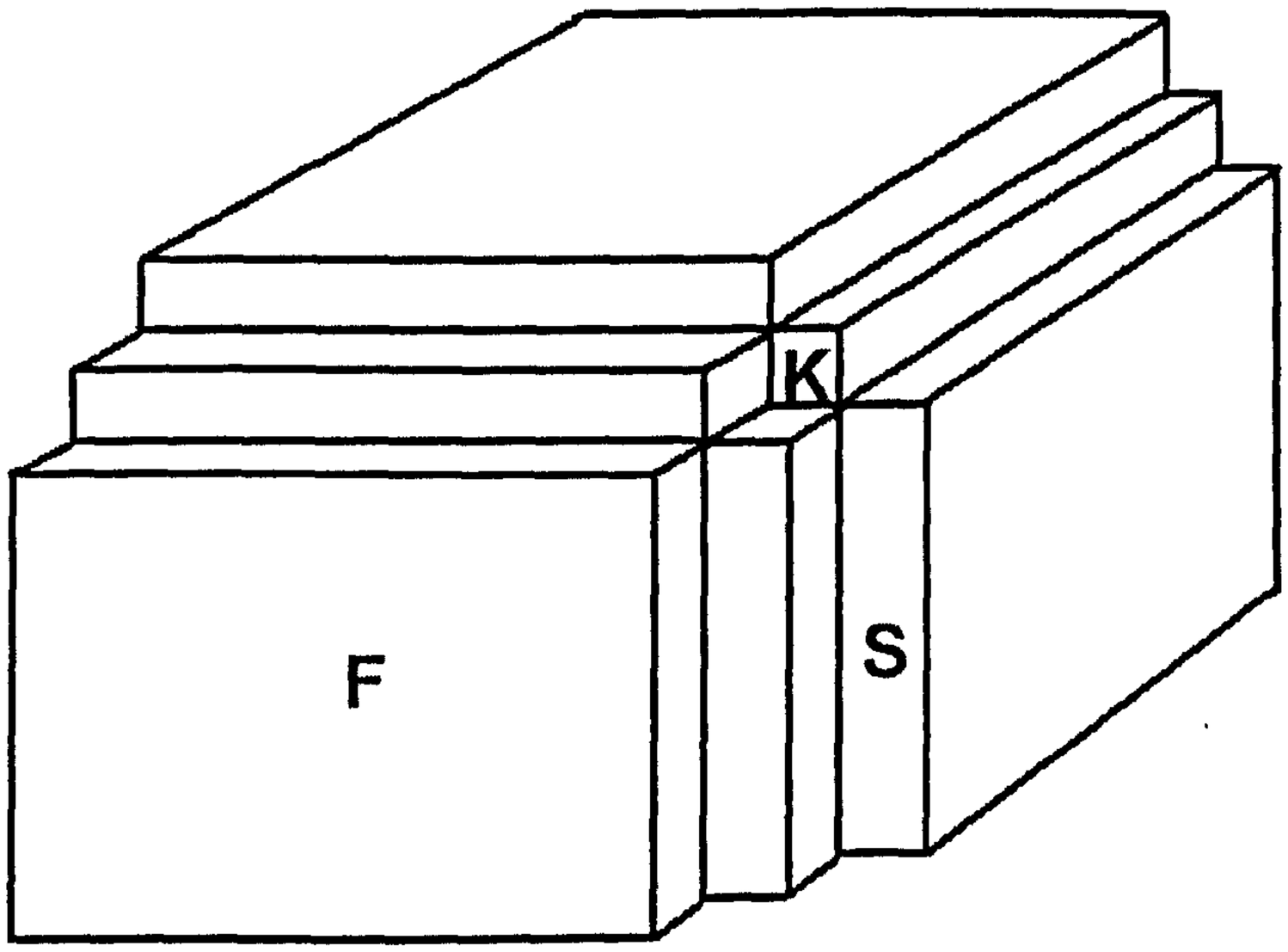


Figure 3-5: K, S and F faces in a forming crystal as suggested by Hartman and Perdock.

This suggests, not unreasonably, that a growing crystal will retain flat, F, surfaces where possible, which will minimise the energy of the system. Therefore, a way must be found, by which the growth occurs on the F faces if the crystal is to grow. A highly successful model for this process was suggested by Temkin.[219] This is where a solid and fluid are represented by squares, Figure 3-6.

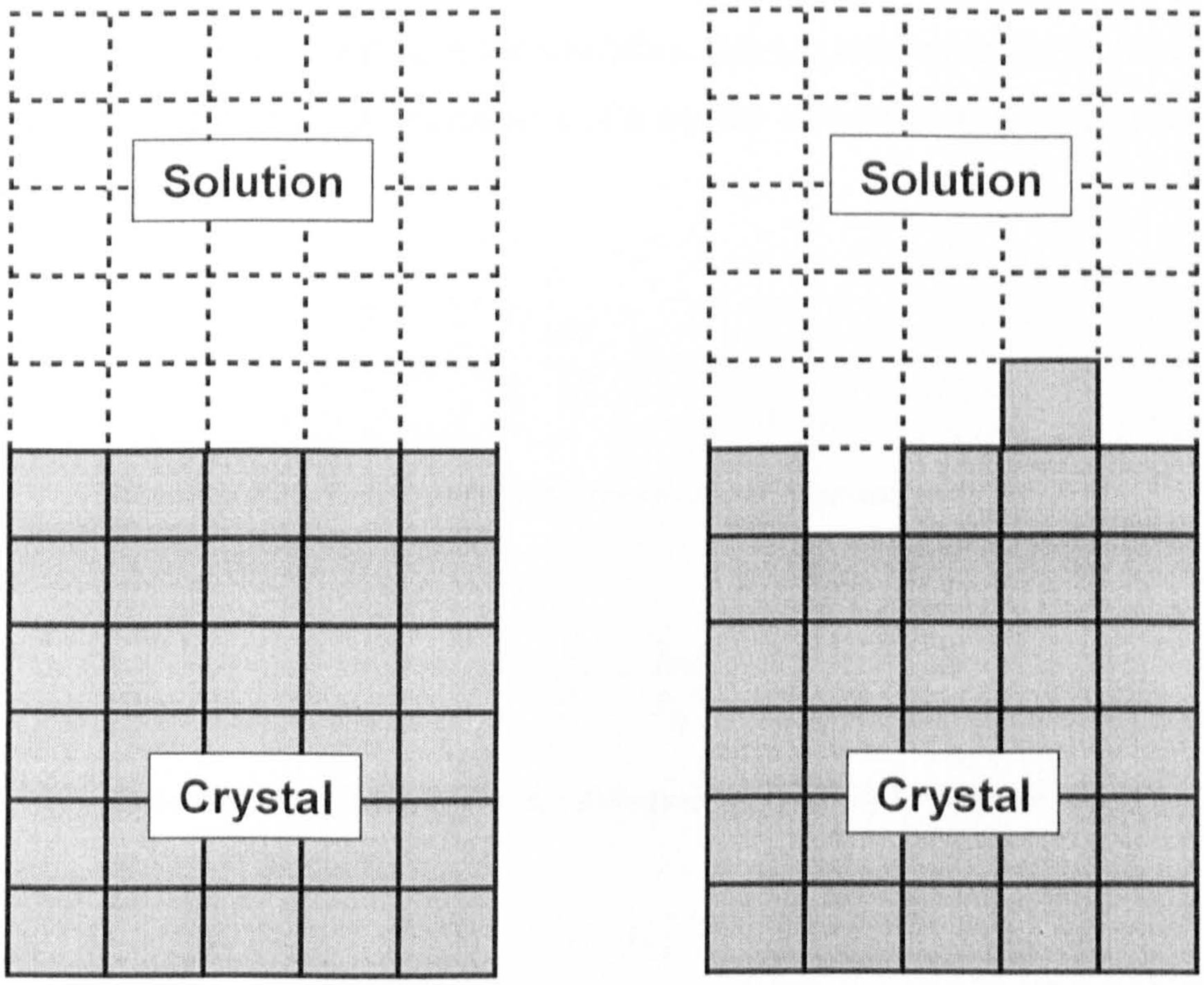


Figure 3-6: The Temkin model of crystal growth by the roughening of a crystal surface.

By removal of a molecule from the surface a K site and the beginning of a new S face is created. The energy required to remove a molecule from the face of the crystal and to deposit it on the surface is significant in determining the viability of the process. The ease at which a molecule of the crystal leaves to start a new layer also governs the roughness of the surface and is highly substrate specific. This allows an explanation of how the growth rates of different materials under the same conditions can vary greatly. This is said to generate an α-factor, given Equation 3-24.

$$\alpha = \frac{\Delta E}{kT}$$

Equation 3-24: The α-factor gives a measure of how easily new sites are created for crystal growth. Low numbers indicate a more rapid growth and a rougher surface texture.

In the case of a system growing from solution this equates to Equation 3-25, where ΔH_f is the heat of fusion and x_{eq} is the solubility. ξ is a crystallographic factor which describes the intermolecular interactions of a surface of interest and is described by Equation 3-26.

$$\alpha = \xi\left[\left(\frac{\Delta H_f}{RT}\right) - \ln x_{eq}\right]$$

Equation 3-25: Calculation of the growth factor from solution.

$$\xi = \frac{E_{sl}}{E_{ss}} \approx \frac{z_{sn}}{z_{bn}}$$

Equation 3-26: Relating the crystallographic factor ξ to number of nearest neighbours.

Where, E_{sl} is the total interaction energy per molecule in the surface layer and E_{ss} is the total lattice energy. The values z_{sn} and z_{bn} refer to the number of nearest neighbours of a molecule in the surface and the bulk respectively.

To understand how growth actually occurs, the mechanisms by which growth is believed to proceed must be examined. Three main routes to growth are suggested. Firstly, when the α-factor is low growth occurs spontaneously over the whole range of supersaturation. In this case, the growth rate follows a very simple formula, Equation 3-27, where υ is the growth rate normal to the surface, k_{CG} is the growth constant and σ is the supersaturation. This growth will dominate when α is less than three.

$$\upsilon = k_{(G)}\sigma$$

Equation 3-27: The equation for the spontaneous growth of a crystal.

A second method is that of secondary nucleation. This occurs when forming nuclei collide with a crystal and stick to it. This produces islands of material which grow

out in all directions. The velocity of this growth is related to the critical nuclei formed per unit time multiplied by the step height and step velocity. This results in the kinetic expression given in Equation 3-28. This type of growth is common when the value of α is between 3 and 5.

$$\upsilon = k_{SN}\sigma^{5/6}\exp\left\{\left(-\frac{\pi}{3\sigma}\right)\left(\frac{\gamma_e}{kT}\right)^2\right\}$$

Equation 3-28: The kinetic expression of the growth velocity.

Equation 3-28 can be simplified to Equation 3-29 and relates back to Equation 3-21 and Equation 3-22.

$$\upsilon = k_{SN}\sigma^{5/6}\exp\left(-\frac{B}{\sigma}\right)$$

Equation 3-29: Simplified version of Equation 3-28.

The third type of crystal growth occurs when α is greater than 5. In these systems the molecules are tightly bound to the surface and cannot break free in sufficient numbers to begin another surface. A mechanism was suggested by Frank to answer the question of how new layers can form.[220,221] This mechanism took the form of growth located in dislocations in the lattice. In these dislocations, spiral growth patterns are visible using AFM. The growth rate is controlled by the disorder within the sample, the more dislocations the greater the rate of growth. This allows crystals of identical material in the same solution to exhibit different growth rates.[222]

Determining which of the growth mechanisms are in control of a given crystallisation can be tricky. The easiest method involves measuring the growth of a specific crystal face with time under varying supersaturation conditions. This is demonstrated in Figure 3-7. Here it can be seen that the growth rate is highly influenced by the method of growth. This is measured by determining the increase in size of a specific face over time. The measurements must be done *in situ*. It would be

interesting to examine crystal growth under supercritical conditions but it would difficult to carry out.

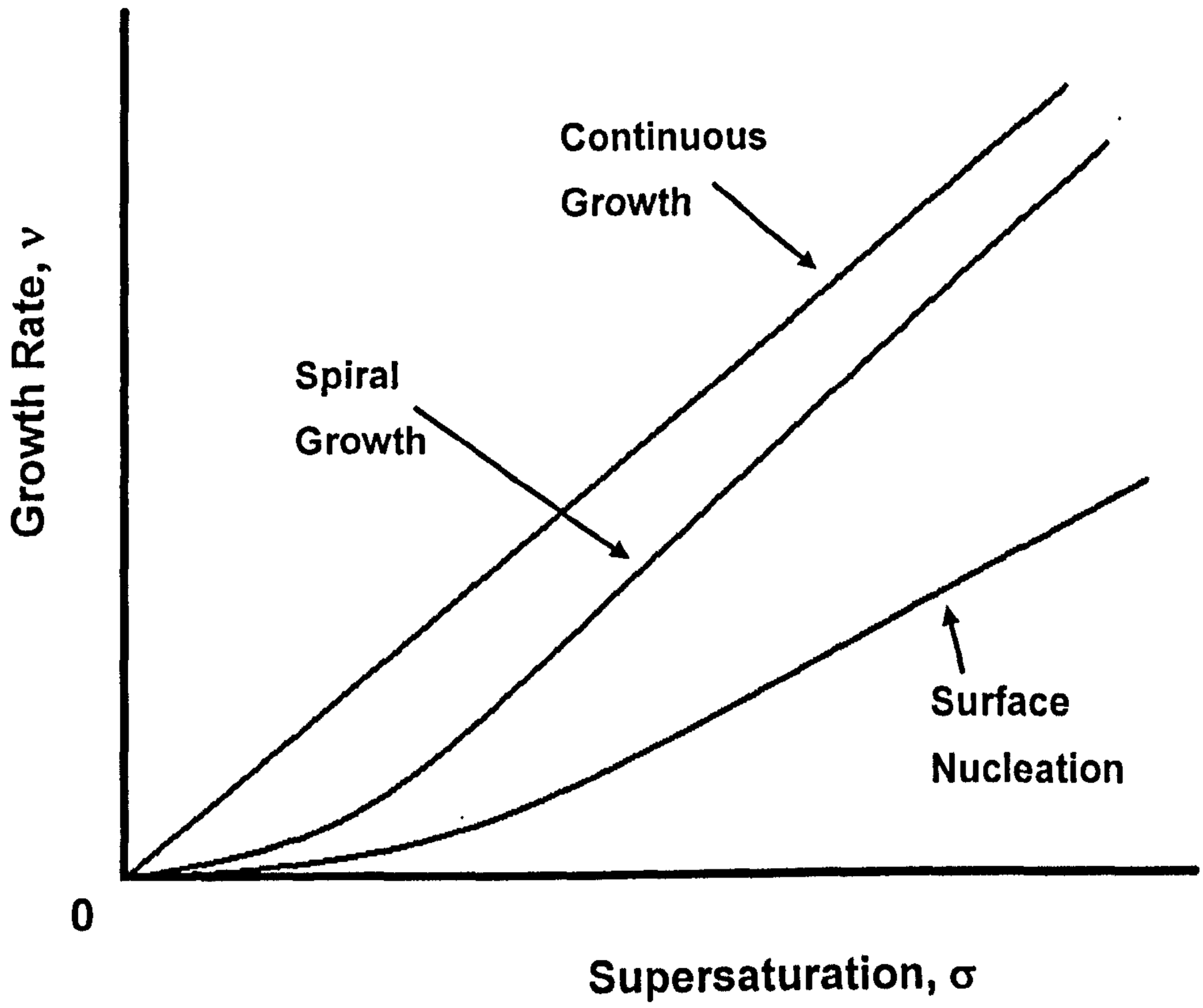


Figure 3-7: Graph of supersaturation vs growth rate to demonstrate the difference between different growth mechanisms.

Another important factor which influences the growth rate of a crystal is mass transport. Improved mass transport can often explain the effects observed when working with supercritical fluids. In terms of crystallisation, mass transport is important because insufficient material reaching the growing surface can slow the crystal growth down. The growth of a crystal is explained in Equation 3-30, where R_G is the overall mass growth rate, k_r, is the growth rate coefficient, c_i is the concentration at the interface, c_{eq} the equilibrium concentration and w is a number (usually between 1 and 2).

$$R_{G_i} = k_r \left(c_i - c_{eq}\right)^w$$

Equation 3-30: Simple view of crystal growth rate.

If instead the diffusion from the bulk to the crystal is examined, Equation 3-31 is obtained, where k_d is the mass transfer coefficient.

$$R_{G_i} = k_d \left(c_\infty - c_i\right)$$

Equation 3-31: The equation of diffusion of molecules from the bulk solution to the crystal face.

By combining Equation 3-30 and Equation 3-31, it is possible to eliminate the unknown interfacial concentration and produce Equation 3-32.

$$R_{G_i} = k_r \left[\left(c_\infty - c_{eq}\right) - R_{G_i}/k_d\right]^w$$

Equation 3-32: Combination of the Equation 3-30 and Equation 3-31 to eliminate the interfacial concentration.

If the surface integration is first order, then this equation simplifies to Equation 3-33.

$$R_{G_i} = k_{G_i} \left(c_\infty - c_{eq}\right)$$

Equation 3-33: Simplified version of Equation 3-32 for r = 1.

A new value for the overall growth rate coefficient, k_G, is created, which is related to k_r and k_d by: $1/k_{G_i} = 1/k_d + 1/k_r$.

This treatment is insufficient, however, as it assumes incorporation of all molecules which reach the surface. This is a specific case and is not always evident. To help explanation an extra term is used, that of the effectiveness factor, η_i.[223] This is given in Equation 3-34.

$$\eta_i = \frac{\textit{the actual growth of the crystal}}{\textit{the growth rate if the crystal was exposed to the bulk conditions}}$$

Equation 3-34: The effectiveness of the integration of molecules into the growing crystal.

The effectiveness has a maximum value of 1 where all growth is controlled by the integration step. When the process is diffusion controlled, the effectiveness $\rightarrow Da^{-1}$ where Da is the Damköhler number as defined in Equation 3-35. It represents the ratio of the pseudo-first-order rate coefficient at the bulk conditions to the mass transfer coefficient.

$$Da = \frac{k_r \left(c_\infty - c_{eq}\right)^{w-1}}{k_d}$$

Equation 3-35: The calculation of the Damköhler number.

This is related to the effectiveness by Equation 3-36.

$$\eta_i = \left(1 - \eta_i Da\right)^w$$

Equation 3-36: How the effectiveness relates to the Damköhler number, *Da*.

The Damköhler number, Da, itself indicates how the overall process proceeds. If $Da \gg 1$ then the process is controlled by mass transfer, and the concentration gradient would be expected to drive the transport. c_i would be expected to be close to the equilibrium concentration. If the two rates are comparable then $Da \approx 1$ and they will both be important in determining the rate of growth. Finally, if $Da \ll 1$, the process is integration dependent and we would expect c_i to be very close to c_∞.

This investigation will also allow the examination of the influence of temperature on crystal growth. If the two rates with activation energies as in Equation 3-37 and Equation 3-38, are examined, an understanding of the influence of temperature can be gained.

$$k_d = k_{do} \exp\left(-\frac{\Delta E_d}{RT}\right)$$

Equation 3-37: Activation energy of the diffusion process.

$$k_r = k_{r0} \exp\left(-\frac{\Delta E_r}{RT}\right)$$

Equation 3-38: Activation energy of the growth process.

Knowing that ΔE_d is typically 8 - 20 kJ mol^{-1} and that ΔE_r is typically 40 – 80 kJ mol^{-1}, we can see that the integration process increases with temperature more rapidly than the diffusion process. Thus, at lower temperatures, a higher effectiveness is obtained. This is relevant to supercritical applications as, with enhanced diffusion by using SCF, it may be interesting to investigate the influence of temperature on the systems.

In this section several aspects of the current understanding of crystallisation have been examined. This was done in an effort to better understand any observations made when using the new techniques detailed later in this Chapter.

Diffusion Driven Precipitation

The possibility of using diffusion driven precipitation for generation of larger crystals of C_{60}(gas) was first suggested during the application of the GAS experiments. The interaction of the solution and antisolvent was believed to behave as shown in Figure 3-8. This figure is taken from Webster's thesis and shows the volumetric expansion of a toluene solution of C_{60} when exposed to increasing pressures of CO_2. The pressure is increased from (a)-(e). The system becomes completely miscible at (e) (80 bar) and the meniscus disappears. What is observed is a volumetric expansion. This is a phenomenon described in most papers on precipitation and is assumed to be the case for all solvents. Indeed it is assumed to be the case for 1,2 dichlorobenzene although to a more modest extent during the experiments in Chapter 2.

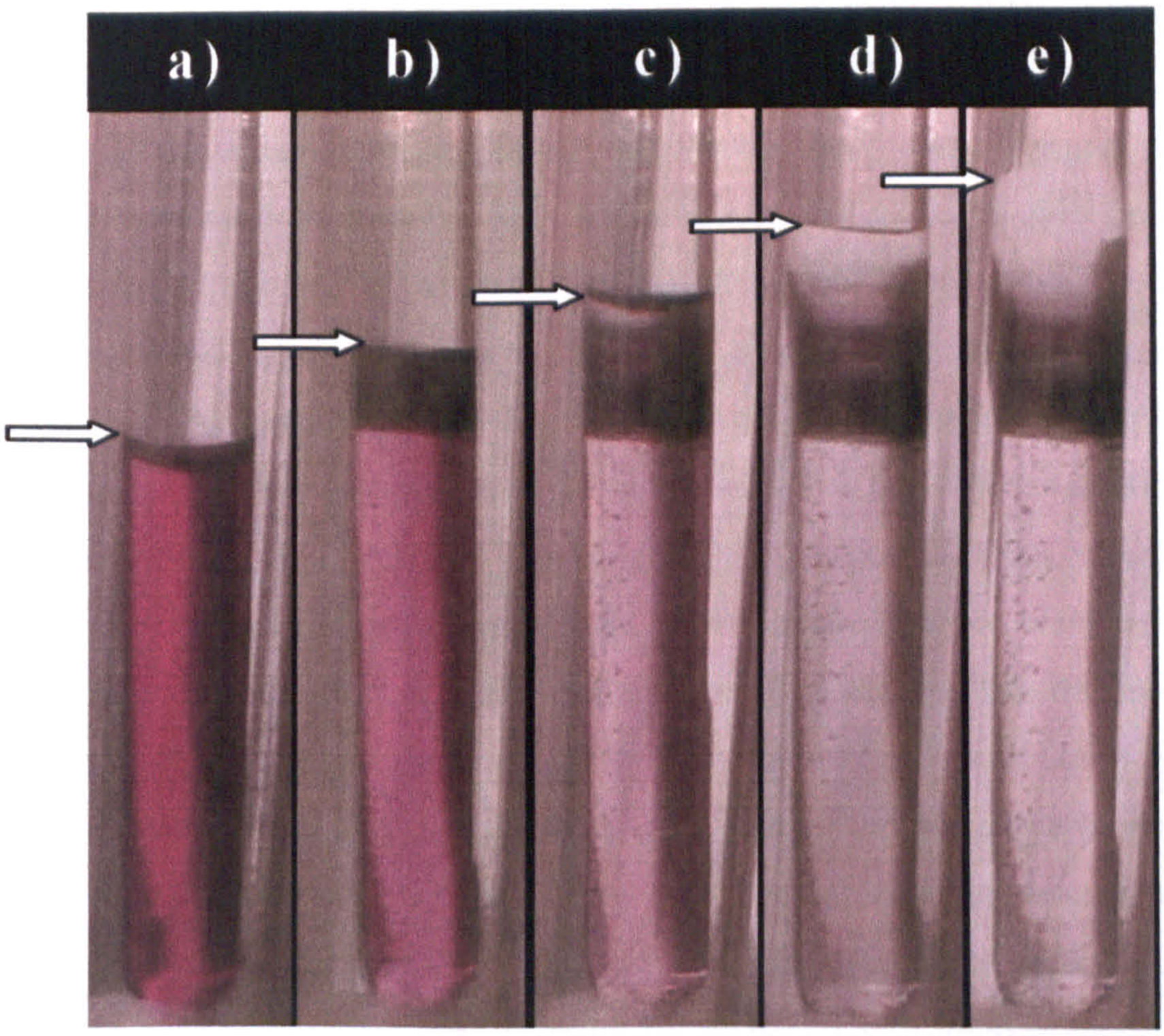


Figure 3-8: Observation of volumetric expansion of a toluene solution, reproduced from Webster's thesis. Pressure is raised and mixing occurs spontaneously. (a)-(d) show the pressure raised slowly, the meniscus is indicated. (e) shows the arrival of miscible conditions and all material is precipitated.[16]

It was decided to repeat Webster's experiments using 1,2-dichlorobenzene (DCB). The experiment was performed in the sapphire tube view cell as was done by Webster so that constant observation of the mixture was possible; a schematic diagram of the apparatus is given in Figure 3-9. A glass tube containing 1 ml of 5 mg ml^{-1} DCB solution was loaded into the sapphire tube view cell. This was then pressurised slowly to 200 bar with propene while monitoring anything which happened during the experiment. The initial observations were of the gas liquefying on top of the solution this slightly agitated the solution and caused a small amount of rapid precipitation. The growing layer of liquefied gas looked similar to a volumetric expansion of the solution and was initially misinterpreted as such. As the pressure was increased the liquefied gas level rose until the whole cell was filled with two liquid phases. The $C_{60,}$ which had been initially rapidly precipitated, began to re-dissolve and the gas started to dissolve into the solvent and was accompanied by a removal of the colouration of the solution from the top of the cell. No volumetric expansion was observed and the meniscus of the solvent was clearly visible at the beginning of the experiment and faded very slowly over several hours. As the antisolvent continued to dissolve into the solution very small, highly branched crystals were precipitated on the surface of the glass tube. These crystals reflected light very well and suggested that, if they could be isolated, then they might prove to be diffracting. The gas did not penetrate more than a centimetre into the sample (the sample was *ca.* 3 cm in height) and it was realised that the experiment was not reaching equilibrium. It was also noticed that the deeper into the sample the antisolvent progressed the larger the crystals were. At this time, however there was no way to remove the crystals form the cell and as soon as the pressure was released, any crystals that were present began to slowly dissolve back into the solution. By the time the tube could be removed and the solvent poured away no crystals were left. Droplets of DCB were also noticed on the inside of the sapphire tube indicating some dissolution of DCB into the antisolvent. A similar result was observed for a toluene solution when kept at low pressure (> 50 bar) These toluene experiments were abandoned in favour of DCB as the crystals produced in toluene were much smaller and of a poorer quality when compared to those grown from DCB solution. An example observation of this using $scCO_2$ as the antisolvent is shown in Figure

3-10. Here the slow progress of the gas is noted by decolourisation and individual crystals are seen to grow over time.

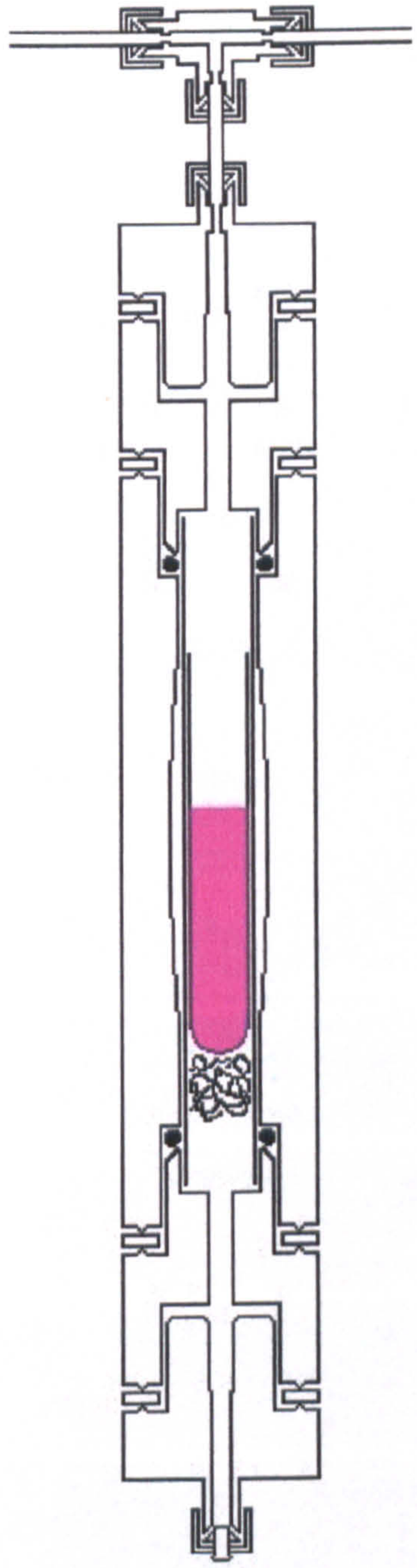


Figure 3-9: Diagram of the apparatus used for the diffusion driven precipitation experiments. A glass tube containing C_{60} in DCB sits inside a sapphire tube view cell.

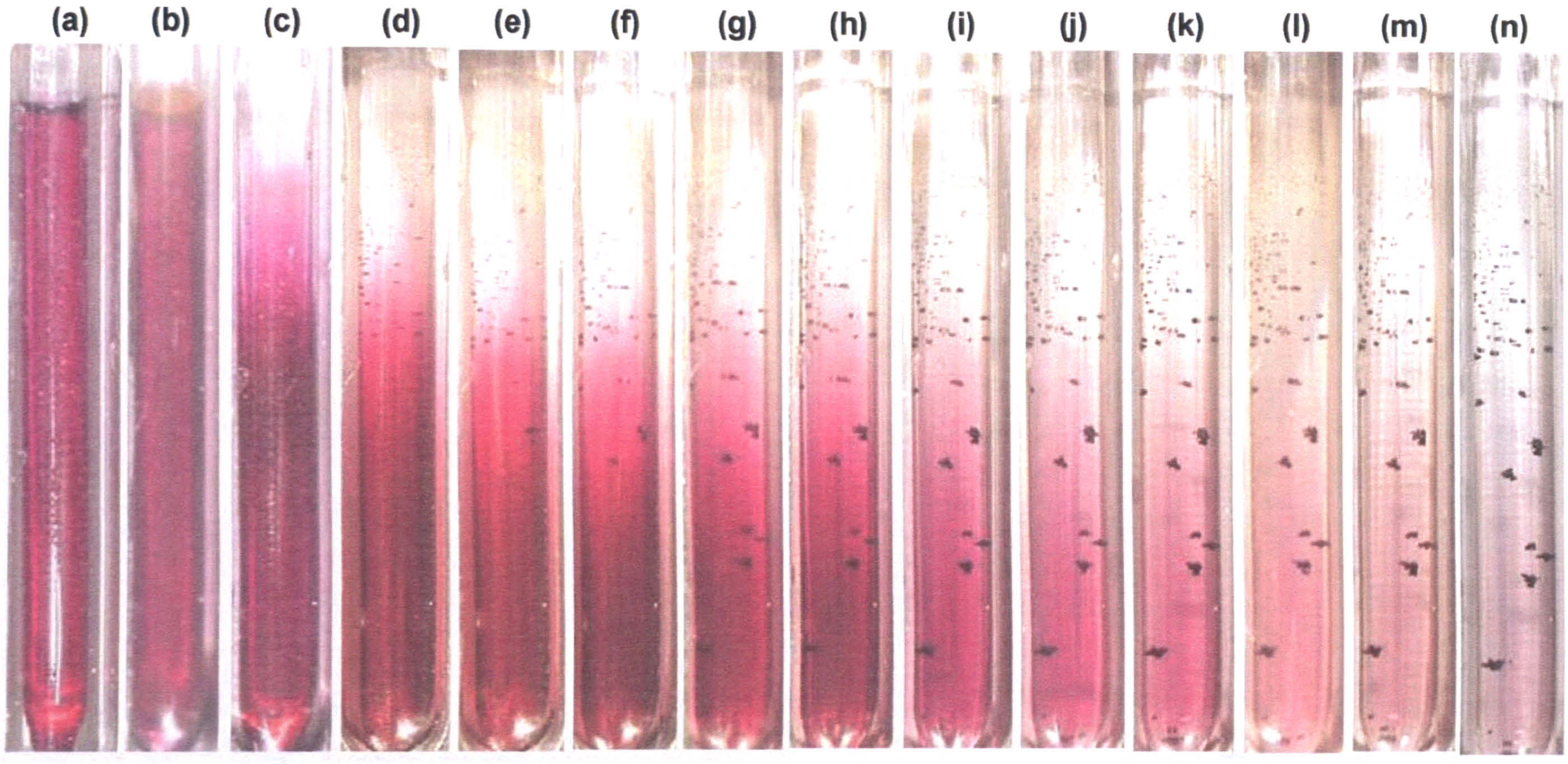


Figure 3-10: The diffusion driven crystallisation of C_{60} in DCB under a pressure of 150 bar of CO_2. The tube is setup (a) and antisolvent added (b) nanoparticulate C_{60} is observed to be precipitated (brown ring) after 1 day (c) this has mostly redissolved. On day 2 (d) larger crystals are visible and over the following days (one picture per day) the gas penetrates deeper into the solvent and causes more precipitation. Interestingly the overall height of the region where C_{60} is still dissolved does not change significantly after the first two days until the precipitation is complete. The solution does visibly lighten as time progresses, however.

This experiment provided a considerable amount of new information, not least that it was actually possible to grow crystals of these materials from solution, something which had not been achieved previously. The fact that any volumetric expansion was too small to measure easily or at least was compensated by DCB dissolving into the gas was also learned. This is known as the solvent meniscus was unchanged by the pressurisation and only disappeared very slowly over a period of hours. We learnt that the dissolution process would take longer than a few hours and so the apparatus would have to be left overnight. First, however, there needed to be a method for removing the solvent once the precipitation had taken place. This could be done by an arrangement similar to that in the GAS experiments, except the purging needle in the centre would be too large if it were steel and too brittle if it were capillary tube. This problem was solved in the simplest of ways. As the DCB is slightly soluble but not miscible with the antisolvent and much denser than the antisolvent, and since the crystals that do form are stuck to the sides of the glass, the vessel can simply be inverted and the solvent allowed to fall to the bottom and be washed away by the flow of the gas, see Figure 3-11.

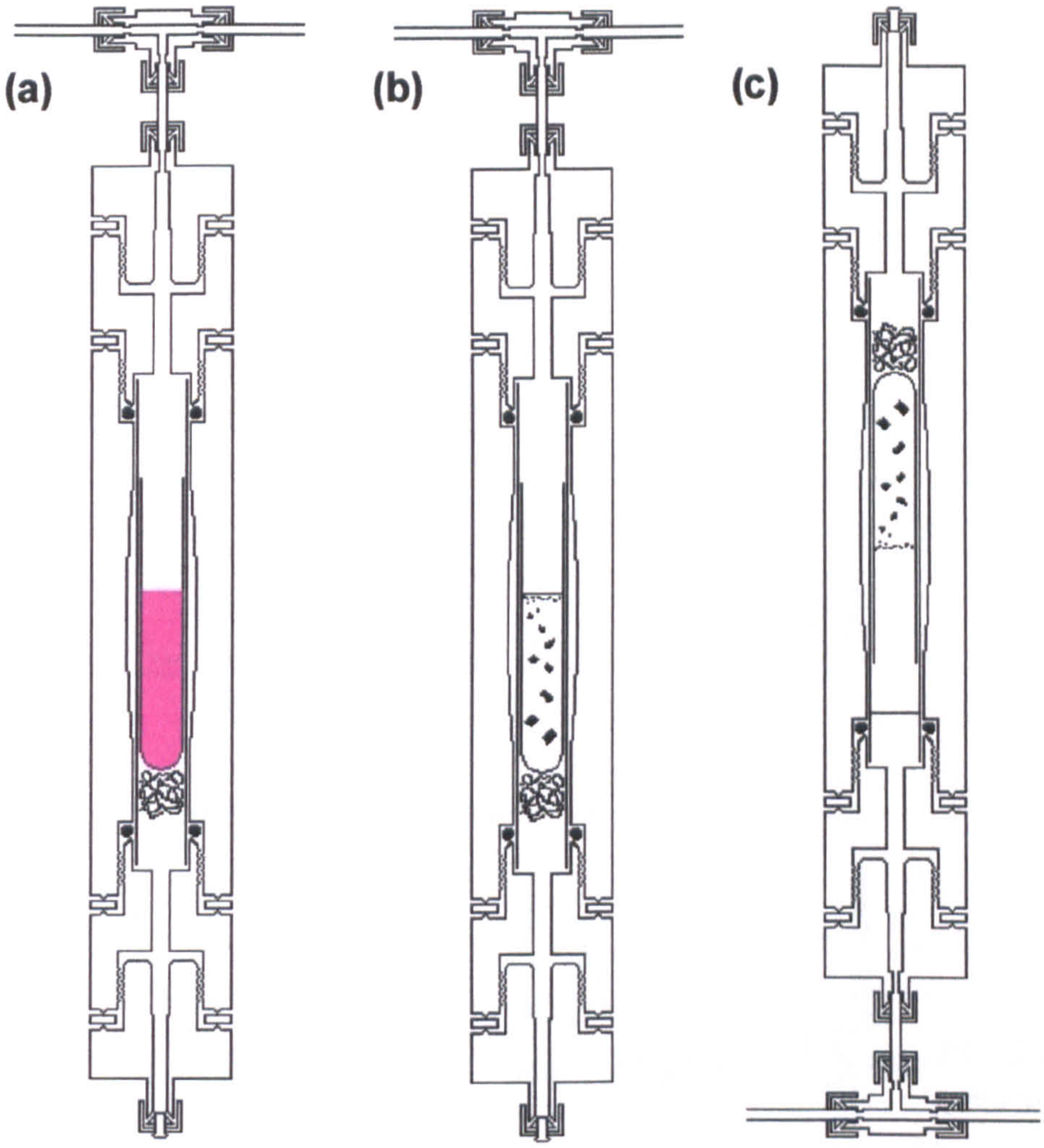


Figure 3-11: Schematic of diffusion driven precipitation. Once the crystallisation is complete (b) the tube is inverted (c), this allows the dichlorobenzene to fall to the exit pipe where it can be removed by restarting the flow of gas.

The following experimental procedure was adopted. Solution of the chosen concentration would be placed inside a glass tube (made by sealing a Pasteur pipette) and placed inside the sapphire tube vessel. The vessel was brought to a working pressure of 150 bar and then the system isolated. The tube was then left for several days until the colouration had almost completely been removed from the solution, although a check was made each day on the pressure and the gas was topped up if necessary. The gas flow was then re-started and the tube was inverted. The solvent fell to the base of the vessel and was transported out of the system by the flow of the gas. The pressure inside the vessel was then dropped to 130 bar and the pressure

cycled between 130 and 30 bar several times. This extra step was to ensure that absolutely all traces of solvent were removed from the system. The vessel was then depressurised completely and the sample collected. A schematic overview of this procedure is given in Figure 3-12. A temperature of 35 °C was maintained throughout the initial experiments although this was later observed to be unnecessary.

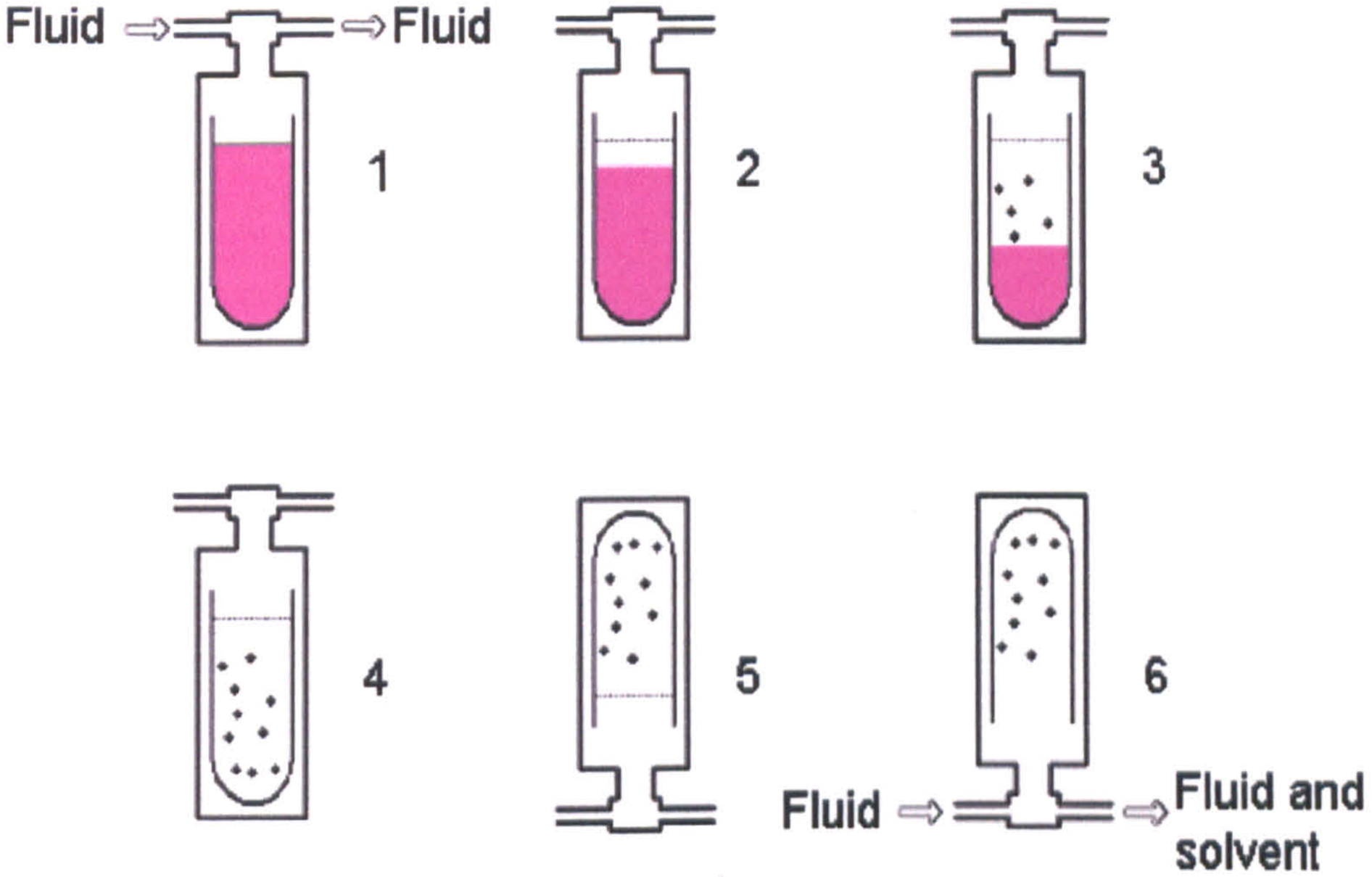


Figure 3-12: Schematic illustration of the supercritical technique for synthesising C_{60}(gas) intercalates. (1) A solution of C_{60} in 1,2-$C_6H_4Cl_2$ is placed in a glass tube inside a high-pressure view-cell; by placing the tube away from the direct path of incoming gas, the cell can be pressurised to 150 bar with the appropriate supercritical fluid at 35 °C with minimal disturbance of the solution. (2) The cell is sealed and the fluid is allowed to diffuse into the solution. Gas is added periodically to maintain the pressure at 150 bar. (3) Crystallisation takes place over a period of 3-5 days until the solution is completely colourless. (4) The view cell is then turned upside down and flowing supercritical fluid is used to flush out the solvent and dry the crystals. (5 & 6) The dry crystals can then be recovered from the tube.

Using the general experimental set-up it was possible to run these experiments singly or in parallel, see Figure 3-13 and Figure 3-14.

All of the intercalates investigated in Chapter 2 were crystallised by this technique. SEM photographs of the crystals produced are shown below. The crystals were submitted immediately for XRD and the results proved successful for ethene and ethane. Propene and propane, however, failed to diffract; this is discussed below.

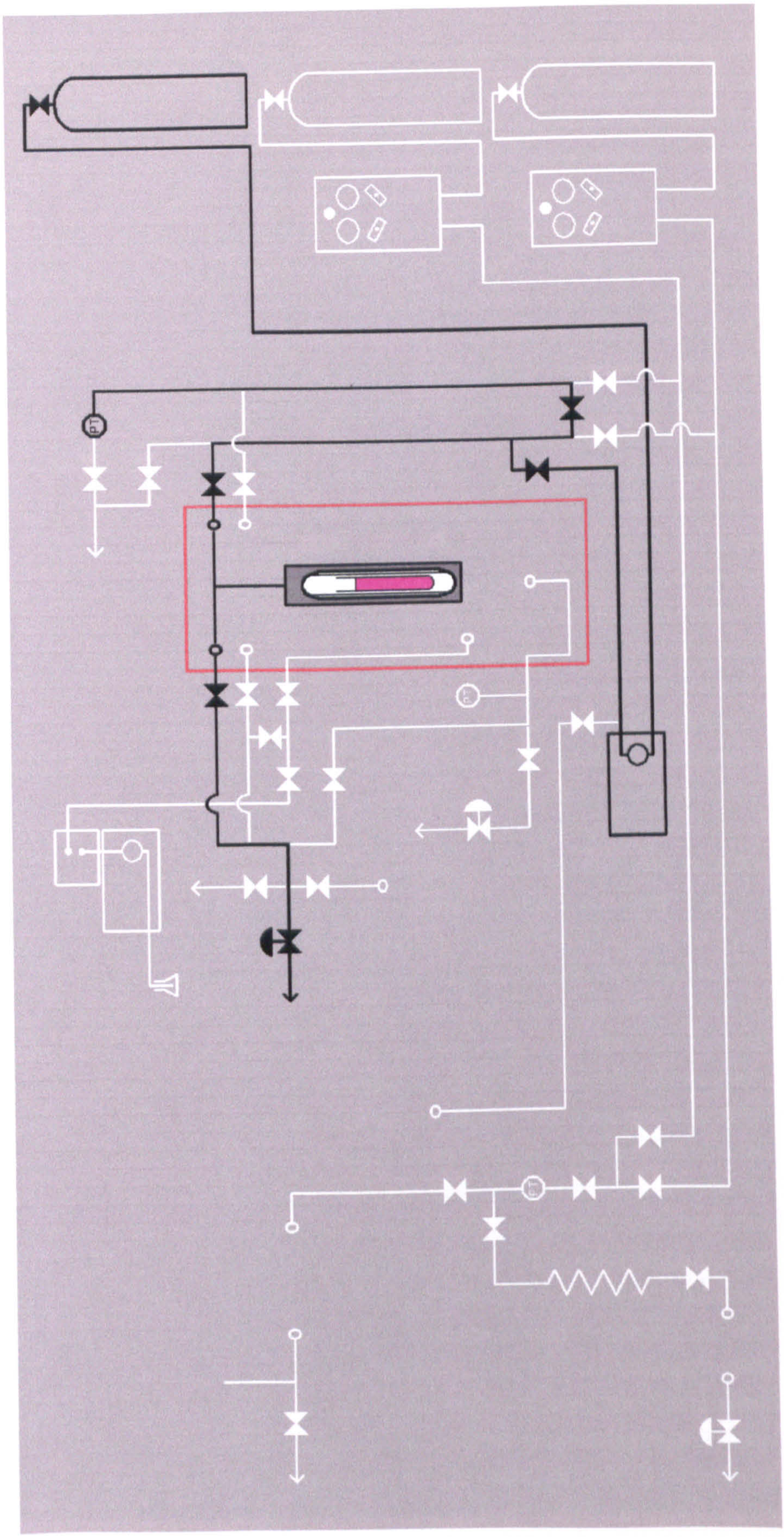


Figure 3-13: The initial diffusion driven precipitation experiment.

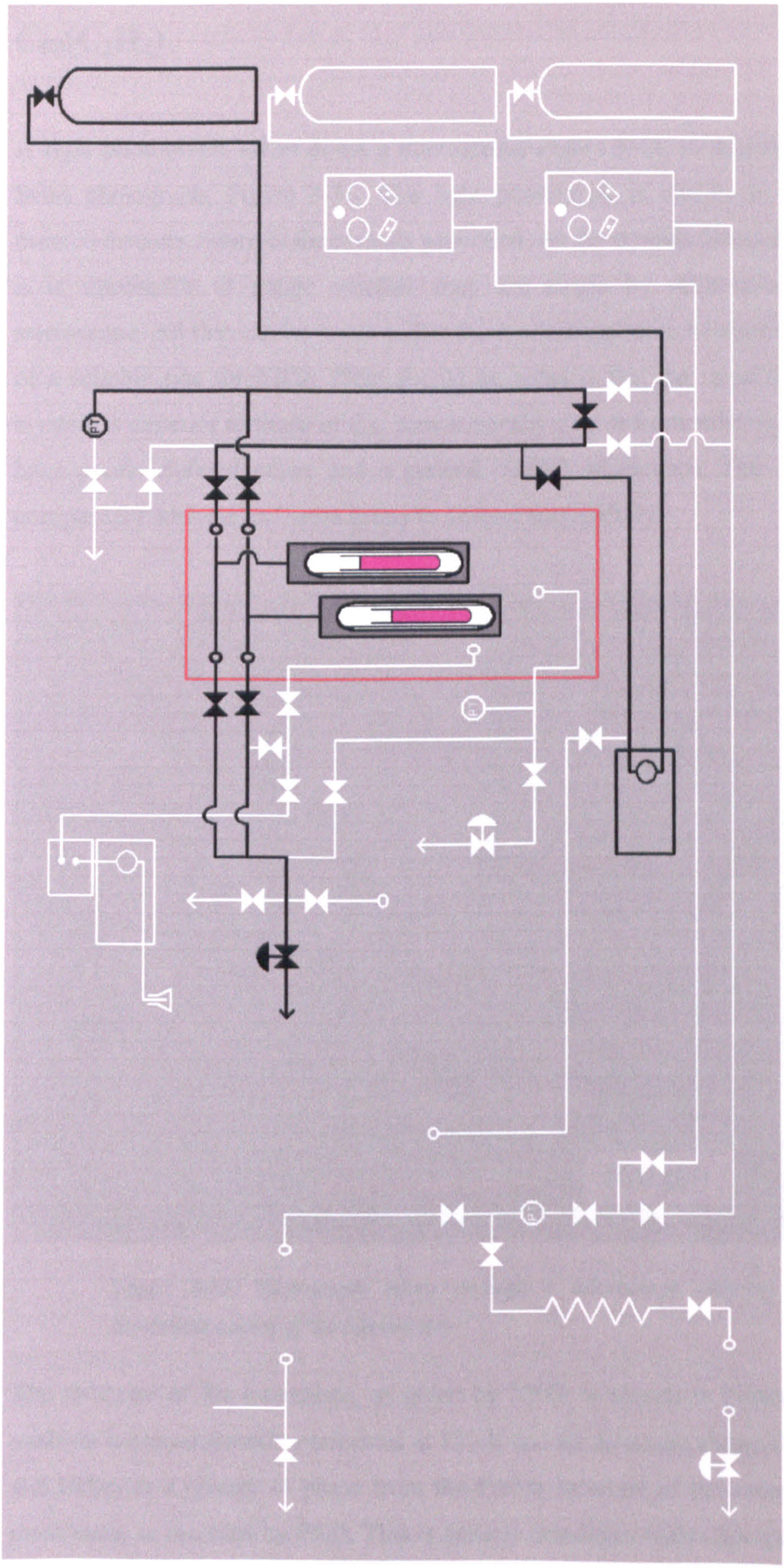


Figure 3-14: The precipitation could be performed in parallel with different solutions and gases.

$C_{60}(C_2H_4)$

A light photograph, taken down a microscope, Figure 3-15, is accompanied by an SEM photograph, Figure 3-16. The light photograph is clearer in showing the ordered discrete nature of the crystals generated. As the crystals themselves are black it is impossible to gauge whether they are single by observation through a microscope. All that can be learnt is that the crystals appear to be single and they are of a suitable size for XRD. What should be noted is that the visual quality of the crystals is superior to those of C_{60} conventionally grown from solution, which often have poorly defined edges and a general 'sooty' appearance. The crystals were accepted for analysis and were found to diffract successfully.

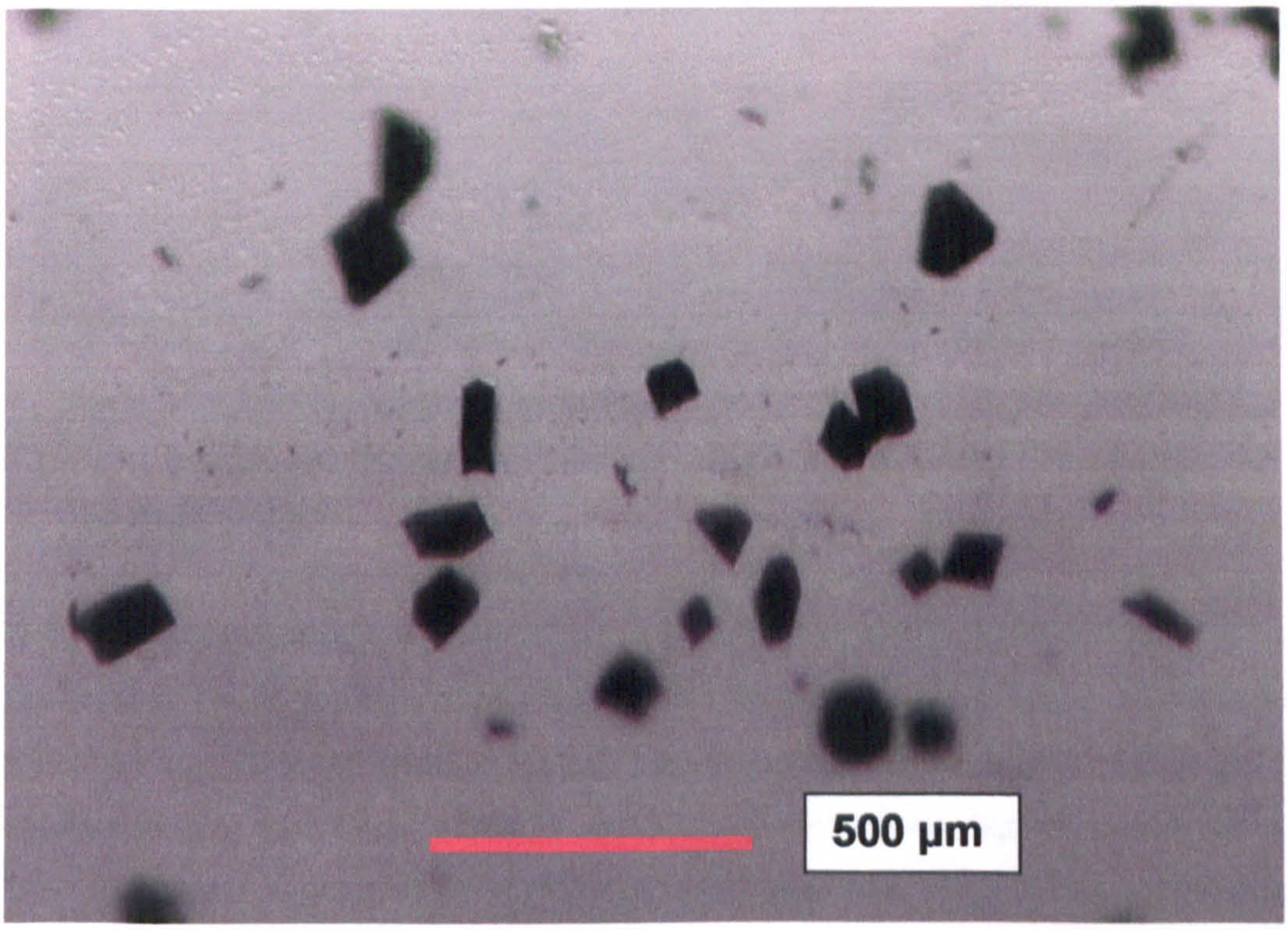


Figure 3-15: Photograph taken through a microscope showing the crystalline nature of the intercalates.

The structure of the intercalate, as given by XRD, is shown in Figure 3-18. XRD analysis is conventionally performed at 150 K and the structure shows Pā3 symmetry and indicates a change of phase from the Fm3m structure of the room temperature intercalate, as revealed by PXD. This is entirely consistent with other gas intercalates

which have been identified at low temperature via PND.[178,189] The unit cell was calculated to be a = 14.1902(12) Å at 150 K.

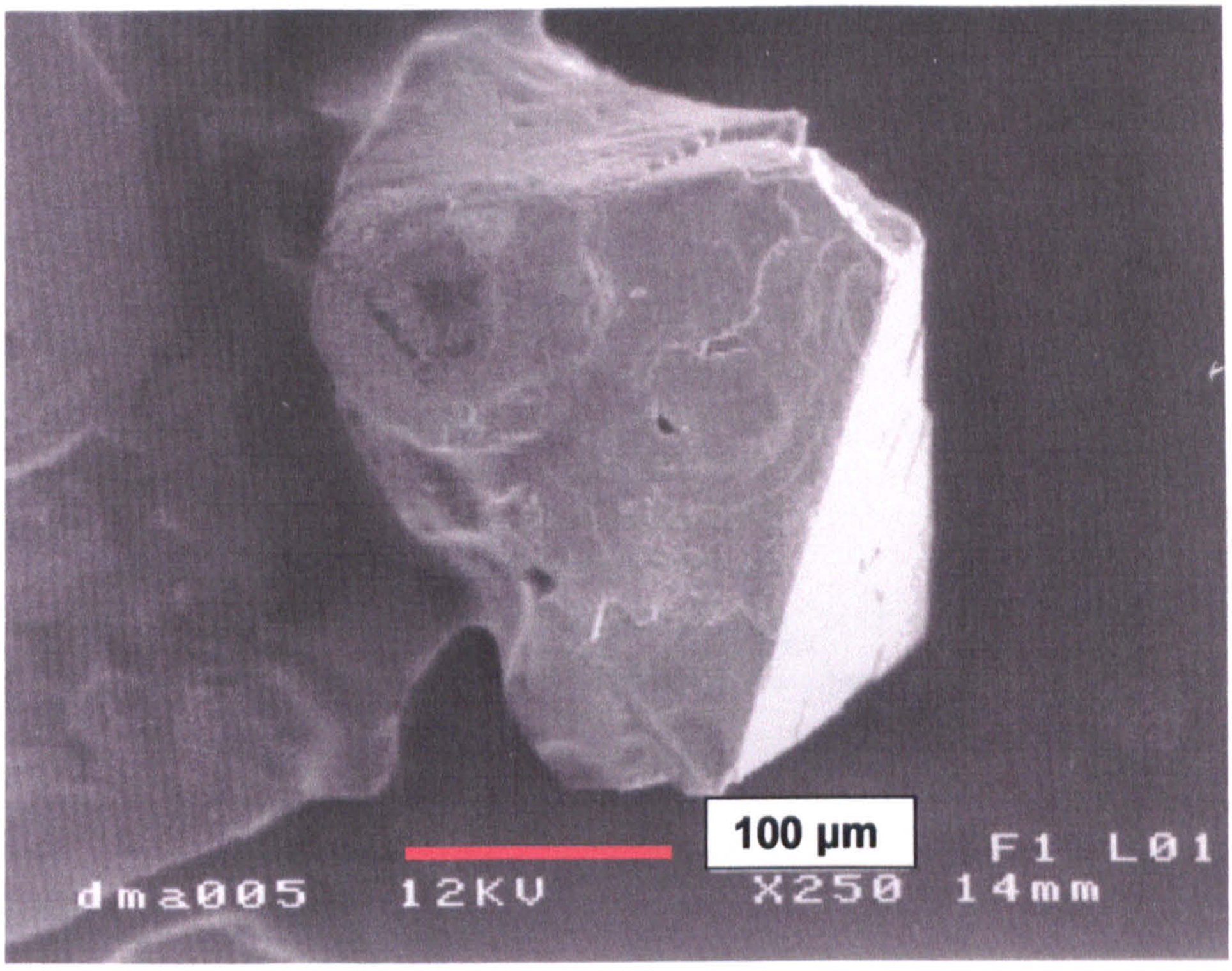
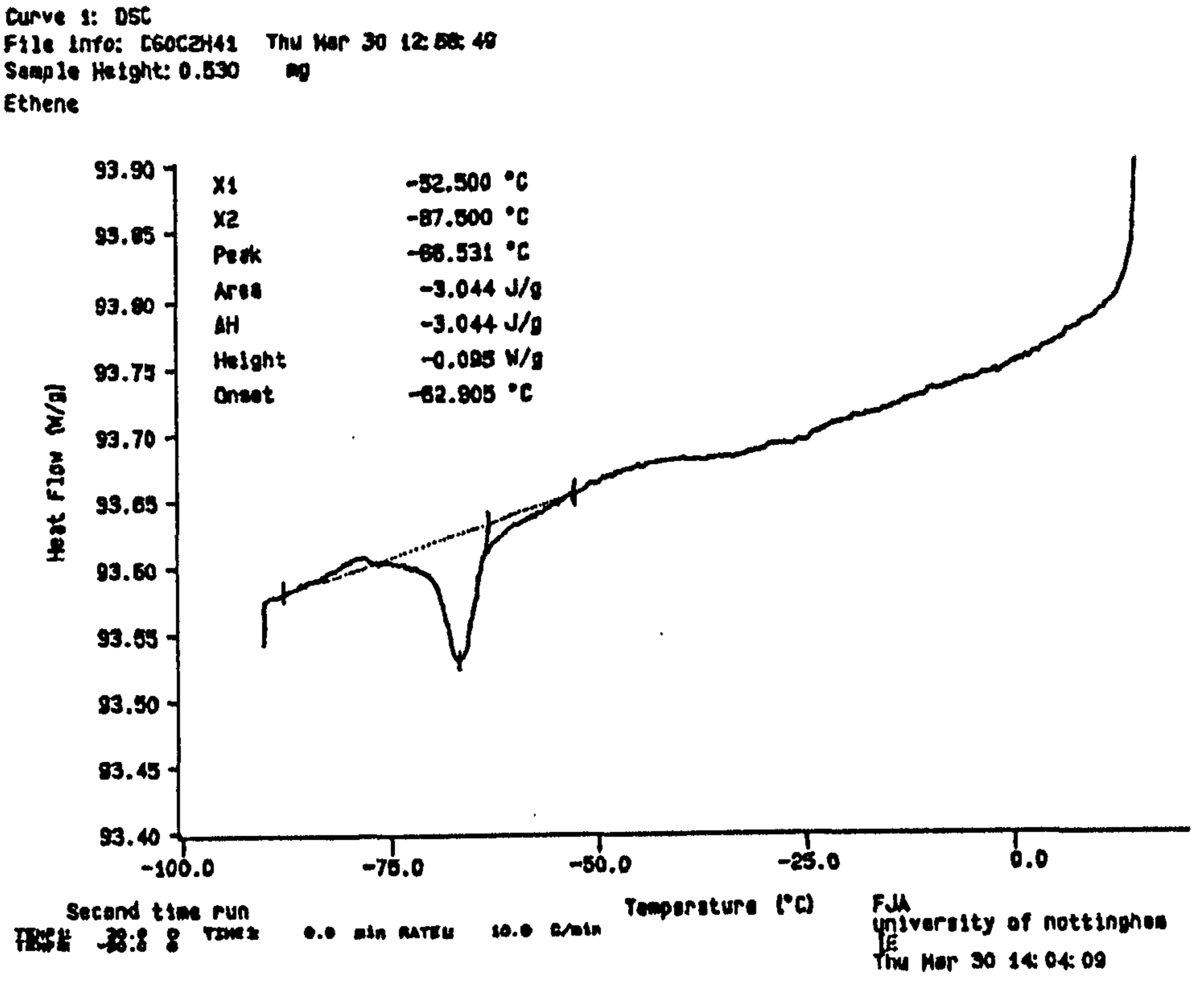


Figure 3-16: SEM photograph of crystalline material generated by the precipitation of C_{60} with ethene. The example appears to be large enough for single crystal XRD. Some surface features are apparent.

A cubic F-centred lattice was found, a = 14.28(3) Å for single crystal data at 290 K. On cooling, a phase change occurs leading to a primitive cubic lattice, as also occurs for pure C_{60}. X-ray results and DSC measurements on $C_{60}(C_2H_4)$ are in good agreement with transitions at 211(2) and 210.1 K respectively, approximately 40 K lower than for pure C_{60} (249 K).[224] This represents one of the lowest transition temperatures reported for C_{60}(gas) compounds, *e.g.* CH_4 241 K, CD_4 235 K and Ar 240.2 K.[189,199] The 210 K transition is reversible and reproducible, Figure 3-17, with no observable deterioration in crystal quality with repeated cycling.



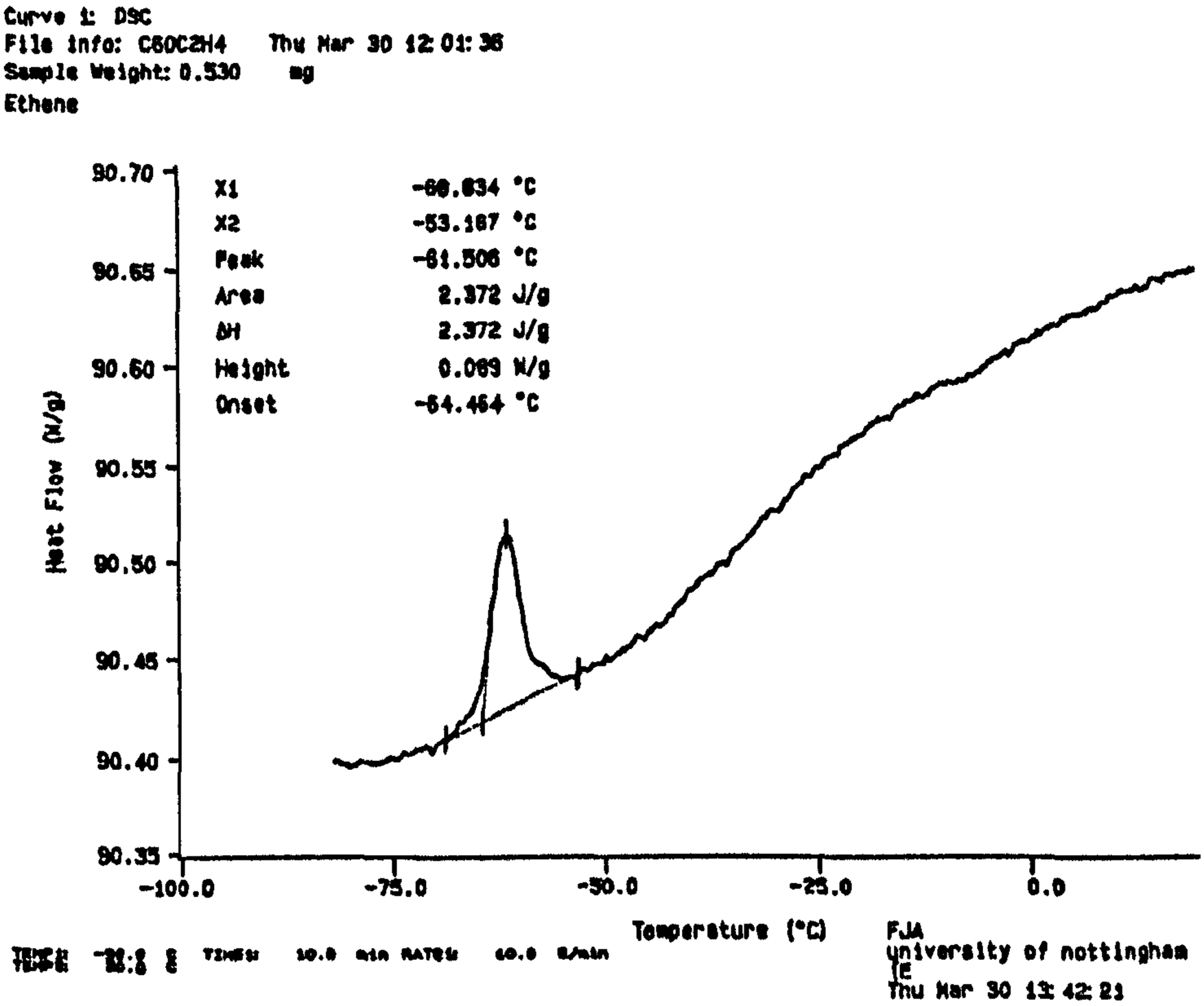


Figure 3-17: DSC traces of $C_{60}(C_2H_4)$ shows a well defined, reversible peak at -66 °C lowering temperature and -61 °C raising temperature.

Full structural refinements were carried out for data collected at 150, 90 and 30 K, with similar results for all three temperatures; all values are quoted for 150 K, further details are given below.[225] The low temperature structure of $C_{60}(C_2H_4)$, space group *Pā3*, is very similar to that of pure C_{60} with the C_2H_4 occupying the octahedral interstitial sites, as found in other gas intercalates.[189,199] Figure 3-18 show the packing structure. Neighbouring C_{60} molecules are orientated as in pure C_{60} [175,226] such that, when viewed along the [110] direction, a bond fusing two hexagons of a neighbouring unit is located above the centre of a pentagonal face[175,226] which optimises the alignment of an electron-rich region (the 6:6 bond) over an electron deficient one (the pentagonal face). These are the shortest intermolecular contacts between C_{60} molecules, 3.252 and 3.338 Å. The bonds in the C_{60} molecule, which were refined freely, fall into two distinct groups, with shorter 6:6 bonds, ranging from 1.386(3) to 1.391(3) Å and longer bonds fusing pentagons and hexagons (6:5 bonds) ranging from 1.442(3) – 1.454(3) Å. No indication of disorder of the C_{60} is observed but the intercalated C_2H_4 shows disorder and was modelled over 3 orientations at this site. As the H-atoms could not be located the discussion of the orientation of the C_2H_4 with respect to the C_{60} is limited; the shortest C...C contact between the C_{60} and C_2H_4 is 3.266 Å.

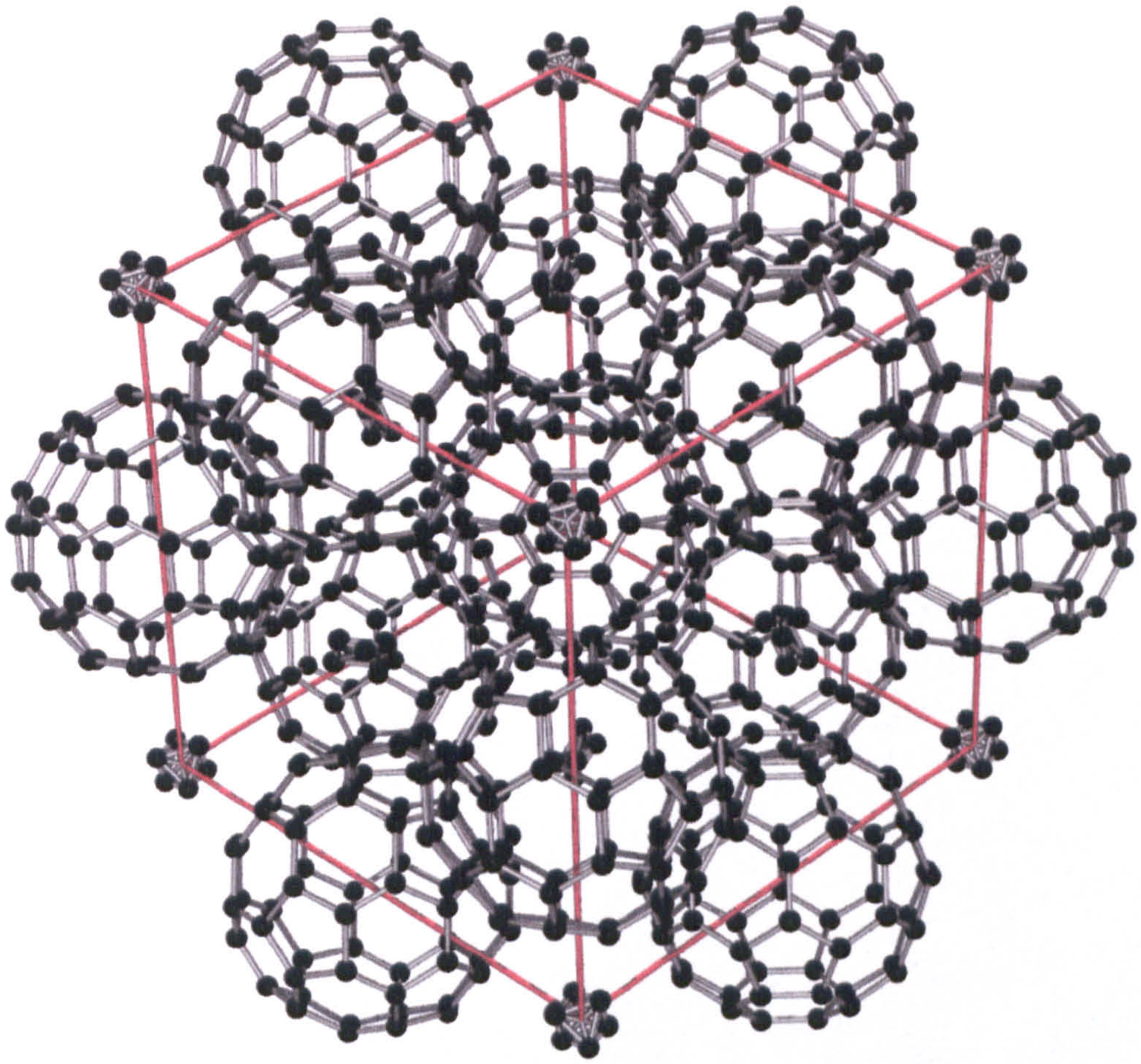


Figure 3-18: The first crystal structure of the $C_{60}(C_2H_4)$ intercalate and the first example of a crystal structure of a C_{60}(gas) intercalate grown from solution. Notice ethene can be roughly seen in the three orientations that would be expected for the octahedral hole.

$C_{60}(C_2H_6)$

In the case of $C_{60}(C_2H_6)$ discrete, crystalline material of an apparent high quality were again achieved. These are shown in Figure 3-19 for light microscopy and Figure 3-20 for SEM.

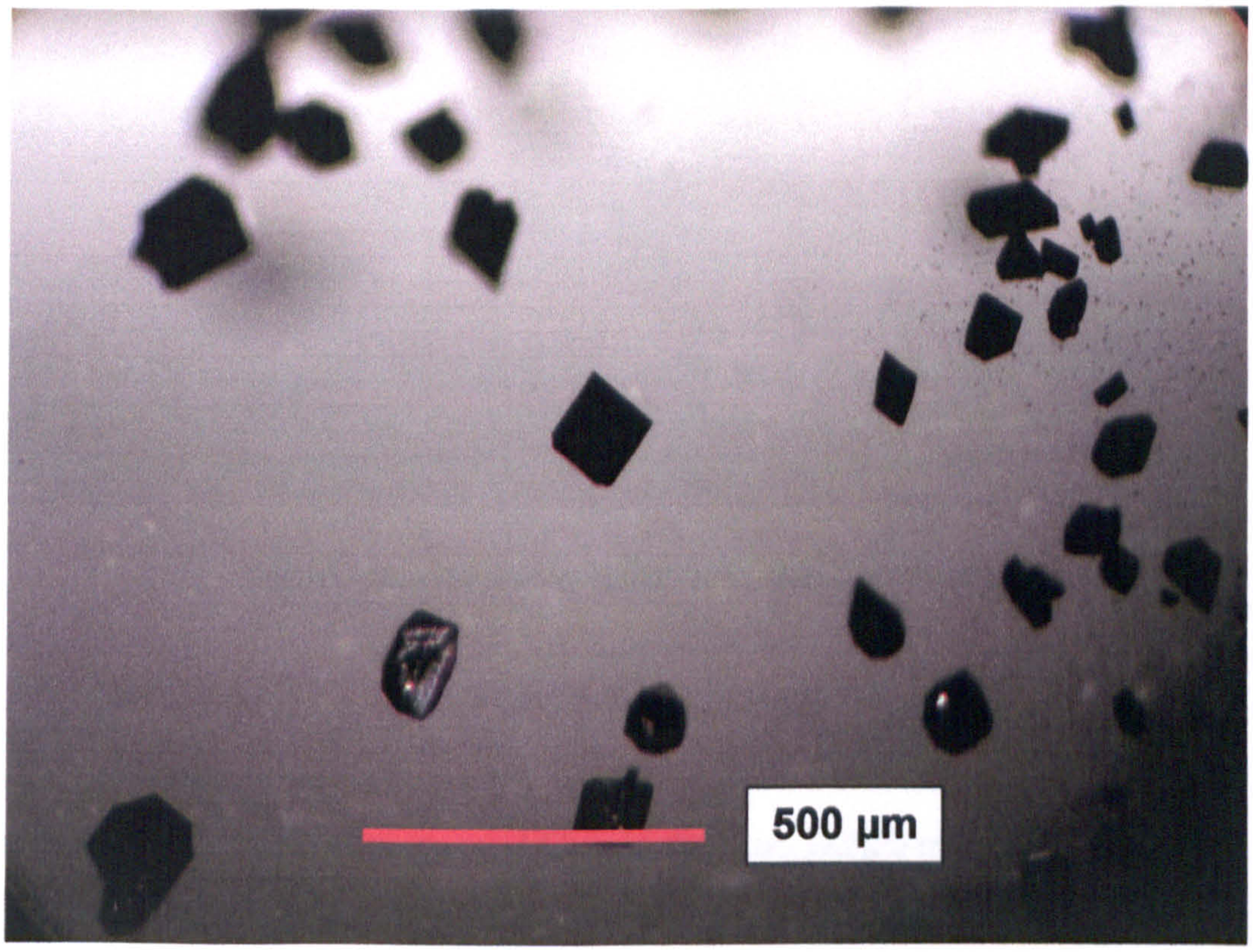


Figure 3-19: Optical photograph of the ethane species, the crystals appear to be ordered.

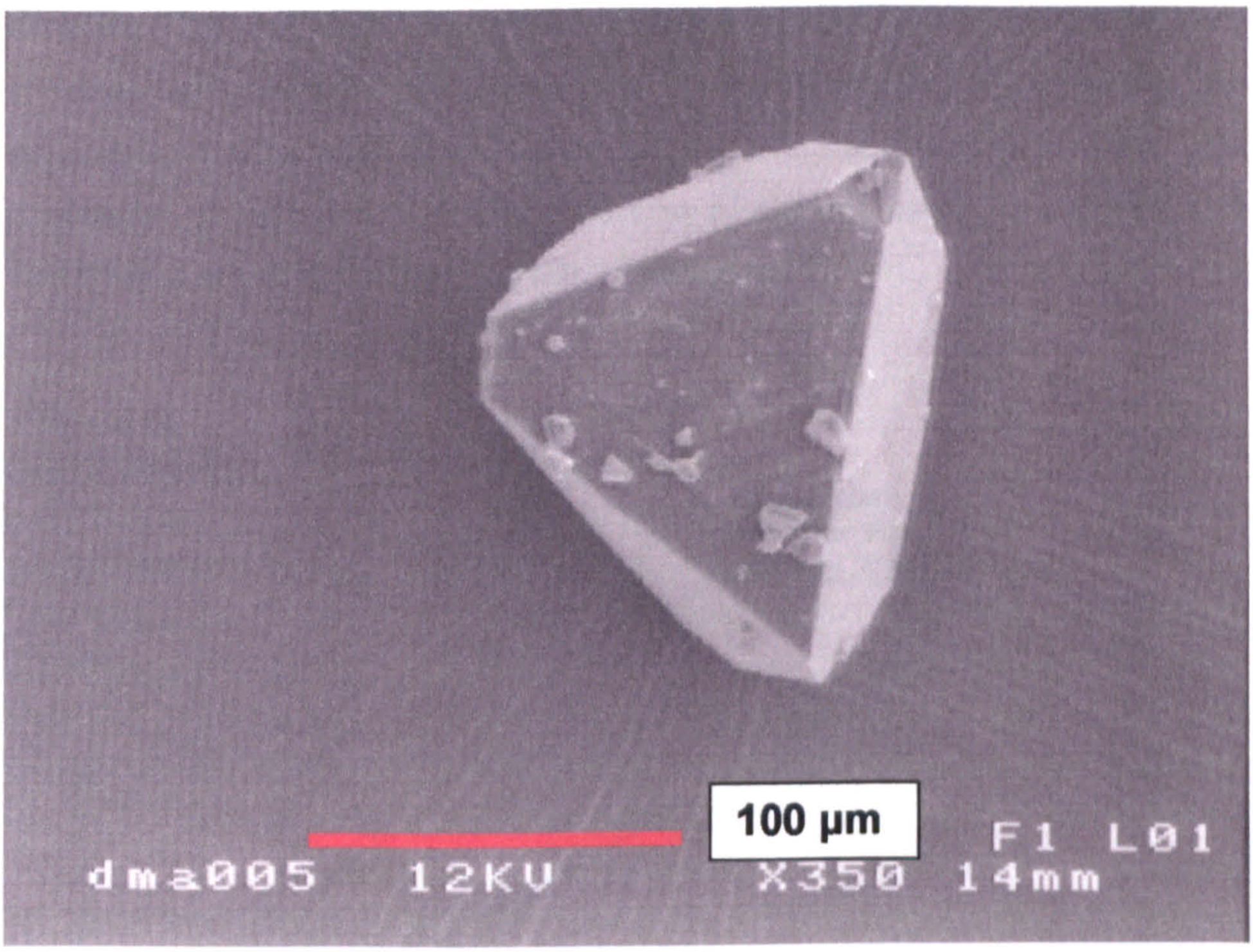


Figure 3-20: SEM photograph of the $C_{60}(C_2H_6)$ intercalate.

The DSC results for $C_{60}(C_2H_6)$, Figure 3-21, suggest a second transition occurring over a wide temperature range in addition to the sharp feature at ~268 K. Below 268 K, the crystals appear to have a primitive tetragonal lattice like $C_{60}(CO_2)$, where $a \approx a_{cubic}/\sqrt{2}$.[201] However, repeated efforts to solve and refine the structure in a number of tetragonal space groups were not successful because tetragonal symmetry constrains the mirror plane of C_{60} molecules to lie in the *ab* plane. These problems could be due to disorder so data were collected at 30 K in an attempt to 'freeze out' the any motion of C_{60}. However, the same problems with the higher symmetry models occurred. This is similar to the neutron powder diffraction study of $C_{60}(CO_2)$ (5-293 K), where a reduction of the symmetry from tetragonal to monoclinic led to a satisfactory model.[201] This same model with C_{60} in the monoclinic space group $P2_1/n$ was used as our starting point, leading to a far more satisfactory result with C_{60} and C_2H_6 both ordered, see Figure 3-22. Although the agreement factors are still high, the model is chemically reasonable. Indeed, all models for $C_{60}(C_2H_6)$ are consistent

in the alignment of the C_2H_6 molecules, in the octahedral interstices in the C_{60} structure. The major difference between $C_{60}(C_2H_6)$ and $C_{60}(CO_2)$ is that the C_2H_6 molecules are almost exactly aligned with the *c*-axis, Figure 3-22, while the CO_2 molecules lie at an angle of 21° to the *bc* plane and ~5° from the *ac* plane. This orientation is consistent with the expansion of the cell in the *c*-direction, c = 14.829(2) Å at 150 K, *c.f.* pure C_{60} with 14.061(5) Å.[175]

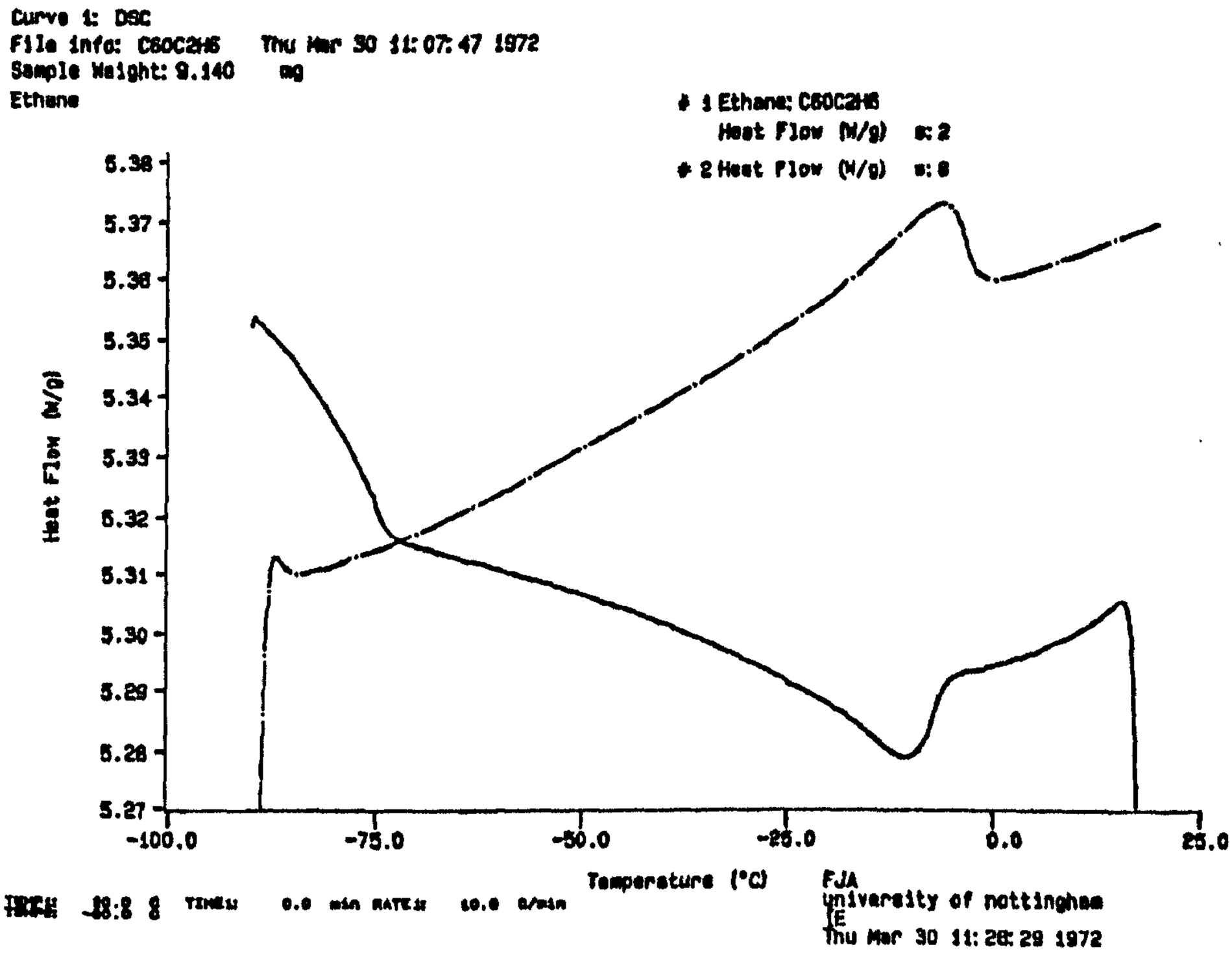


Figure 3-21: DSC traces of the C_{60} ethane intercalate which show a very broad reversible phase transition, initiating at -5 °C. The change shows the transition between two tetragonal phases.

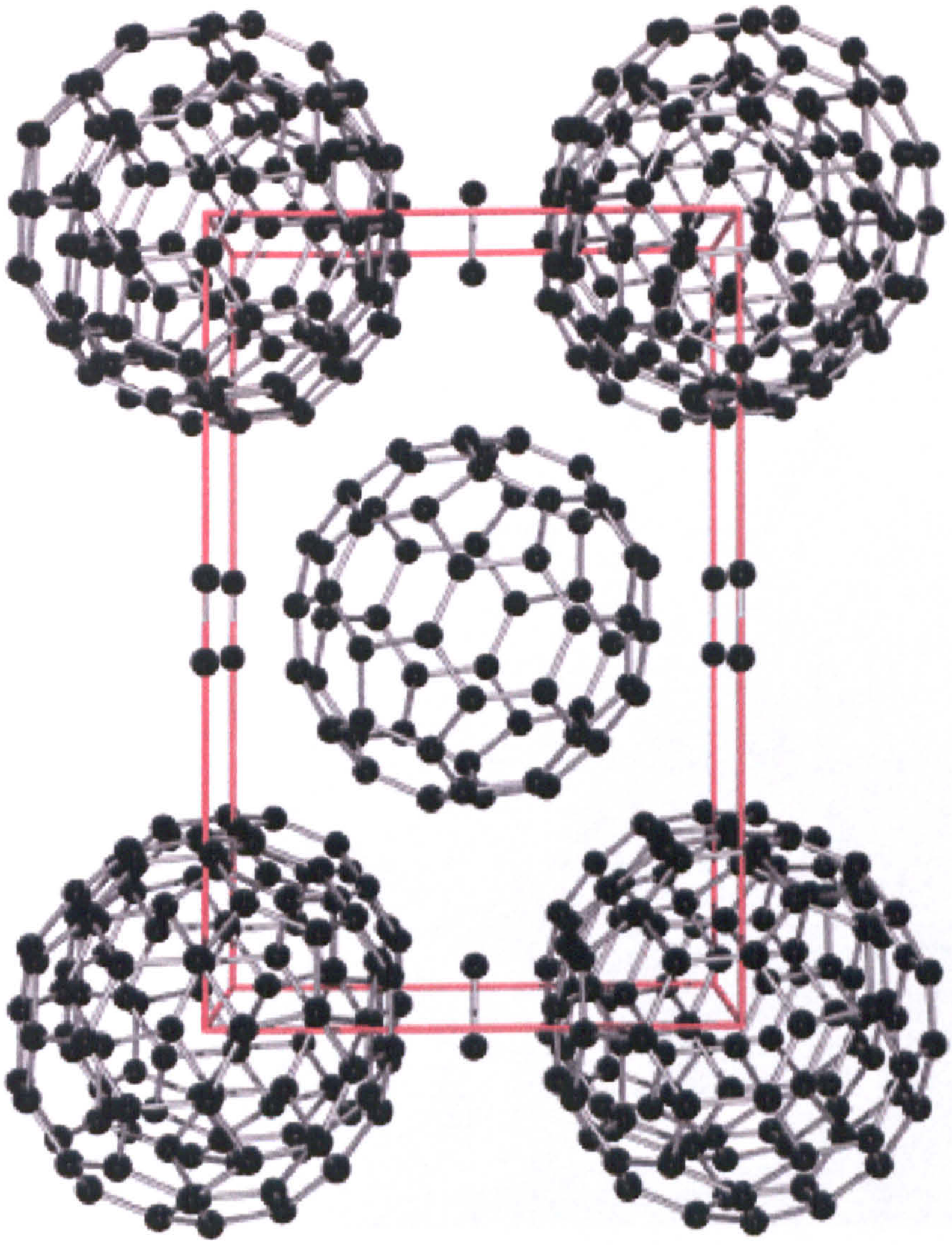


Figure 3-22: Tetragonal lattice of $C_{60}(C_2H_6)$, shows evidence of the first gas intercalate initiating a phase change in the C_{60} lattice.

$C_{60}(C_3H_6)$

On first inspection the crystals grown of the propene intercalate appear to be superior to those from ethene and ethane. Optical and SEM photographs are given in Figure 3-23 and Figure 3-24.

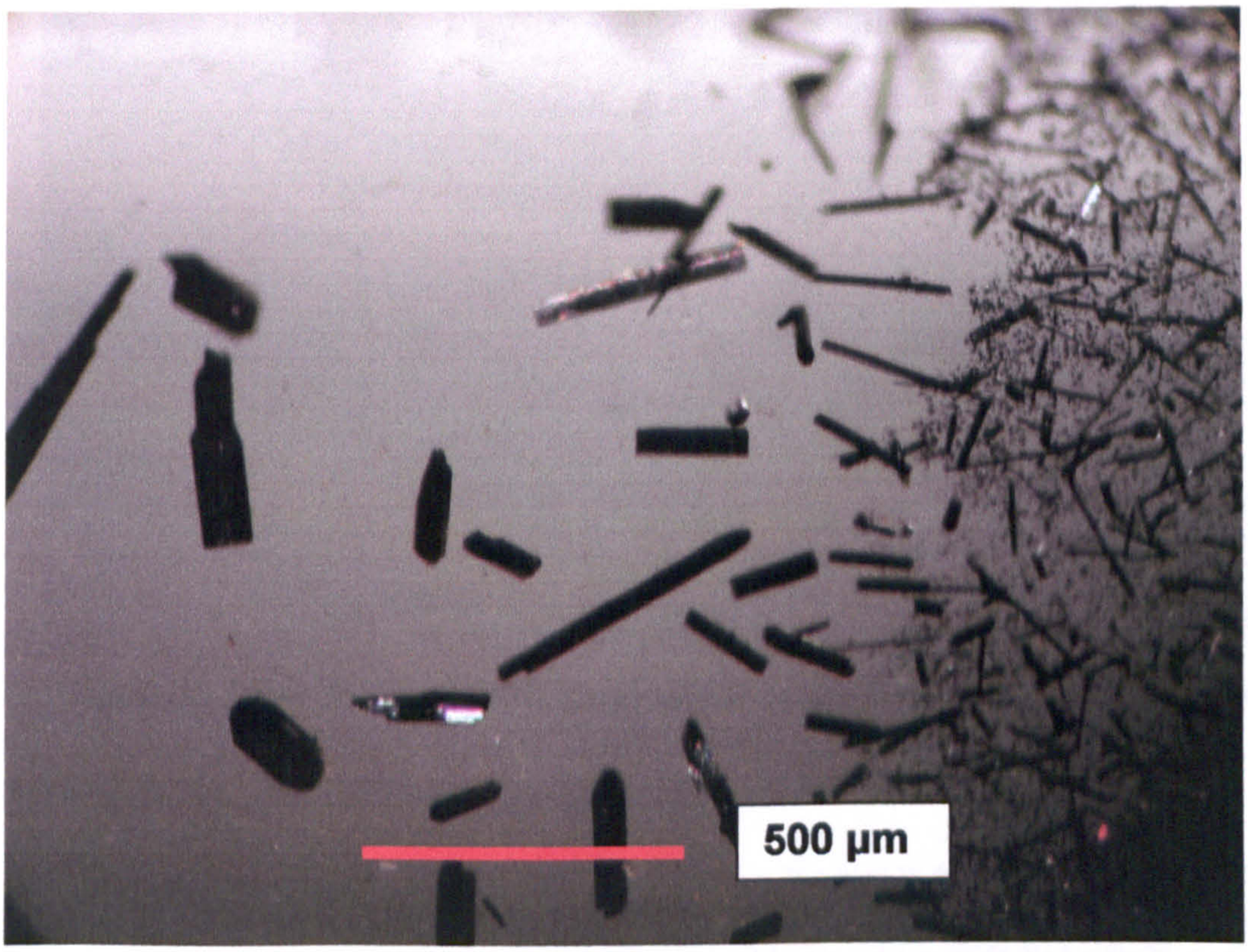


Figure 3-23: Crystals of $C_{60}(C_3H_6)$ appear highly ordered and refract light well.

Unfortunately all attempts at XRD failed and either no or poor diffraction was recorded. This is not surprising considering the poor PXD patterns recorded for the GAS grown intercalates in Chapter 2. Indeed on closer examination it is possible to see flaws in the crystal. An example is shown in Figure 3-25 which is a zoomed version of the bottom right hand corner of Figure 3-24. Here we see the crystal appears to be a series of needles which have grown together. This 'ragged' end to the crystal indicates aggregation. Also in the top right hand corner of this photograph we see a series of crystals running at right angles to the main crystal indicating twinning and further disorder.

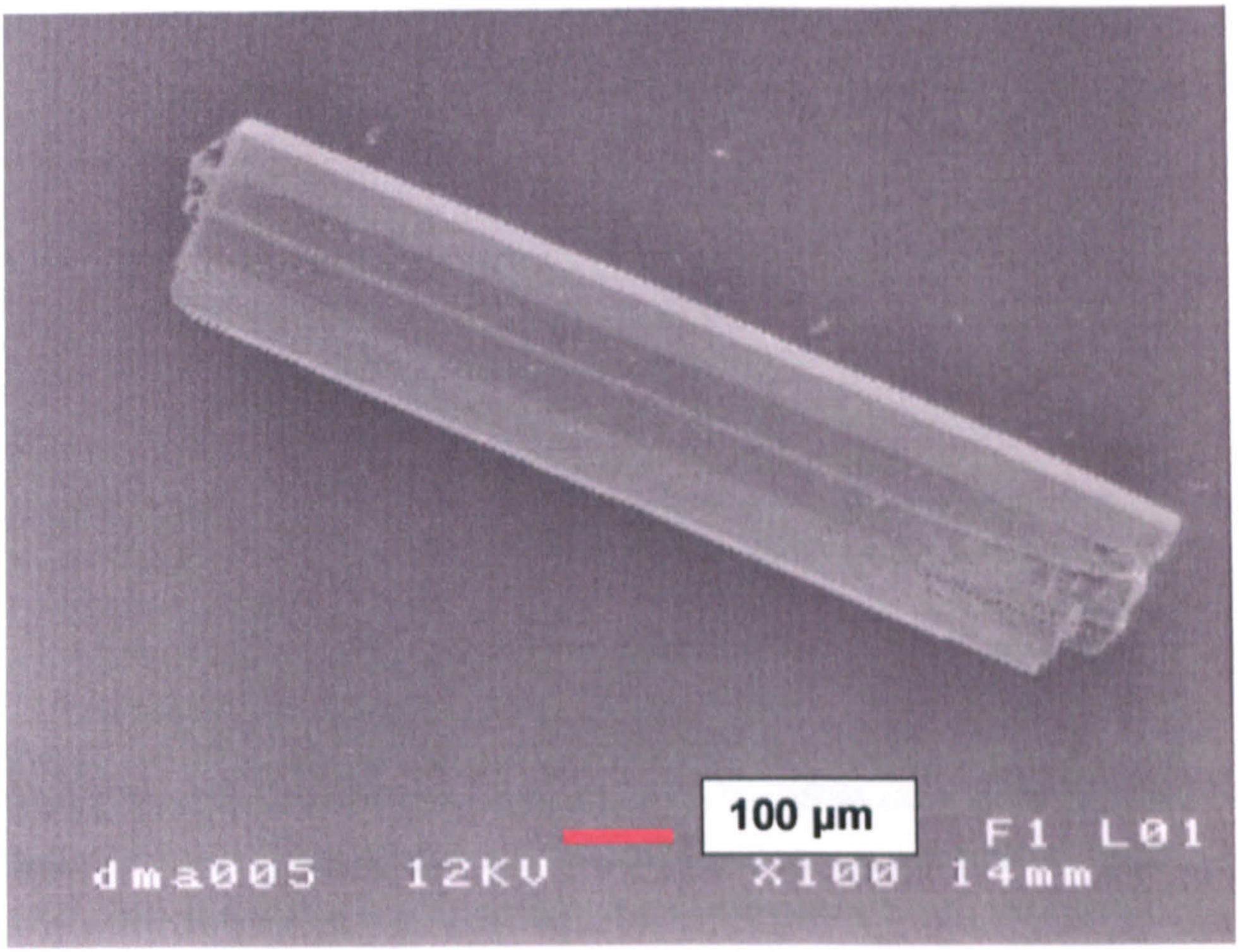


Figure 3-24: SEM photograph of $C_{60}(C_3H_6)$ appears very crystalline. An expanded view of the bottom right hand corner is shown in Figure 3-25.

Further evidence for the aggregation is given in Figure 3-26. This is an SEM photograph taken of a sample produced by the GAS technique used in Chapter 2. It was not included in Chapter 2 at it is in no way representative of the products of that technique. It was believed to be formed during the filling step of the GAS experiment by a similar mechanism to the DDP experiments. It does, however, show how a crystal of the propene intercalate may appear crystalline to the eye but in fact be highly twinned and hence useless for XRD. The storage of propene in C_{60} can be shown therefore by the NMR, IR and TGA data of Chapter 2, the XRD data that it was hoped that this Chapter would show appears unavailable through this route.

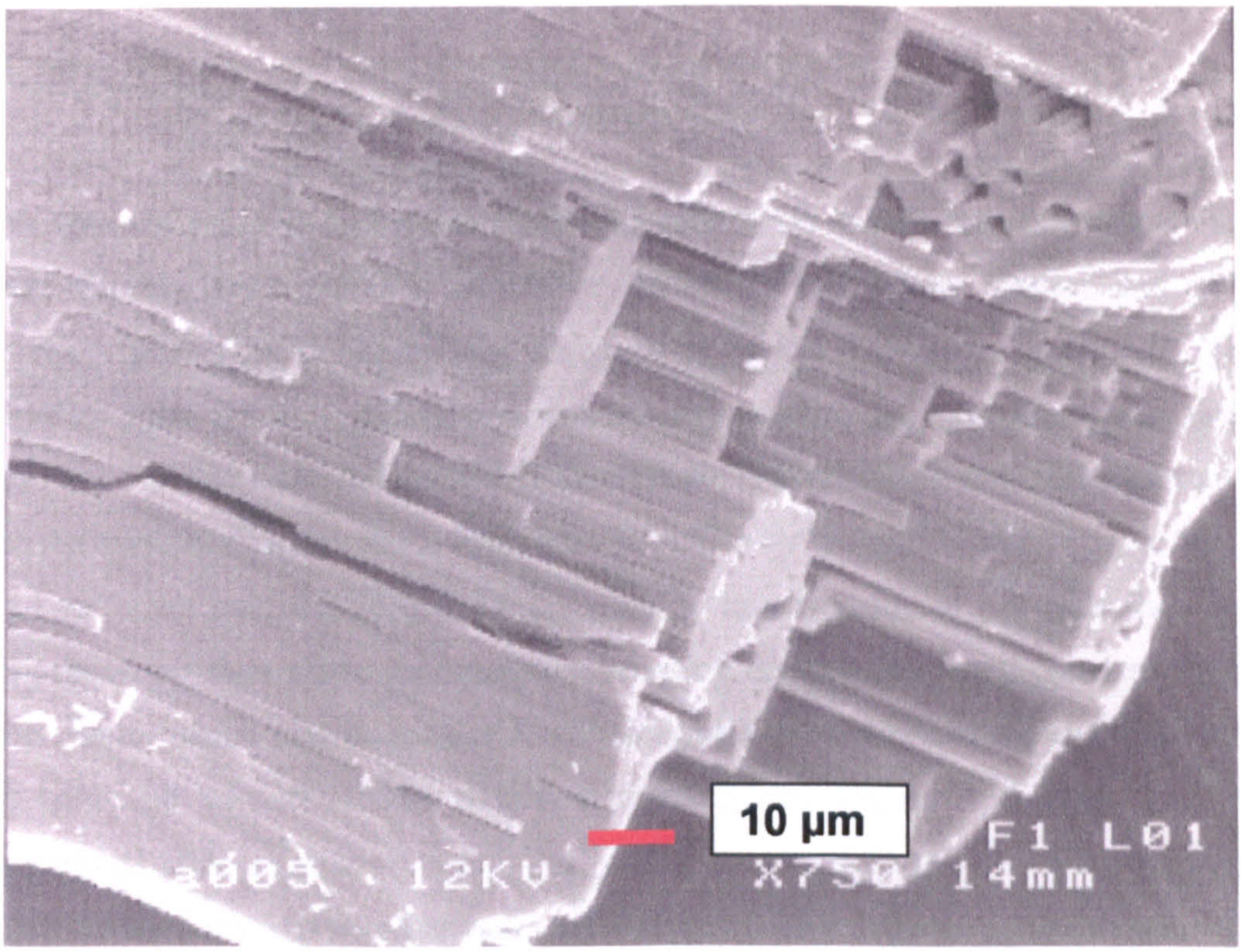


Figure 3-25: Zoomed view of Figure 3-24, shows the crystal is not as well defined as it first appear. Instead it appears to be an aggregation of smaller crystals lying in one direction. Some evidence of another phase is visible in the top right hand corner at right angles to the main direction.

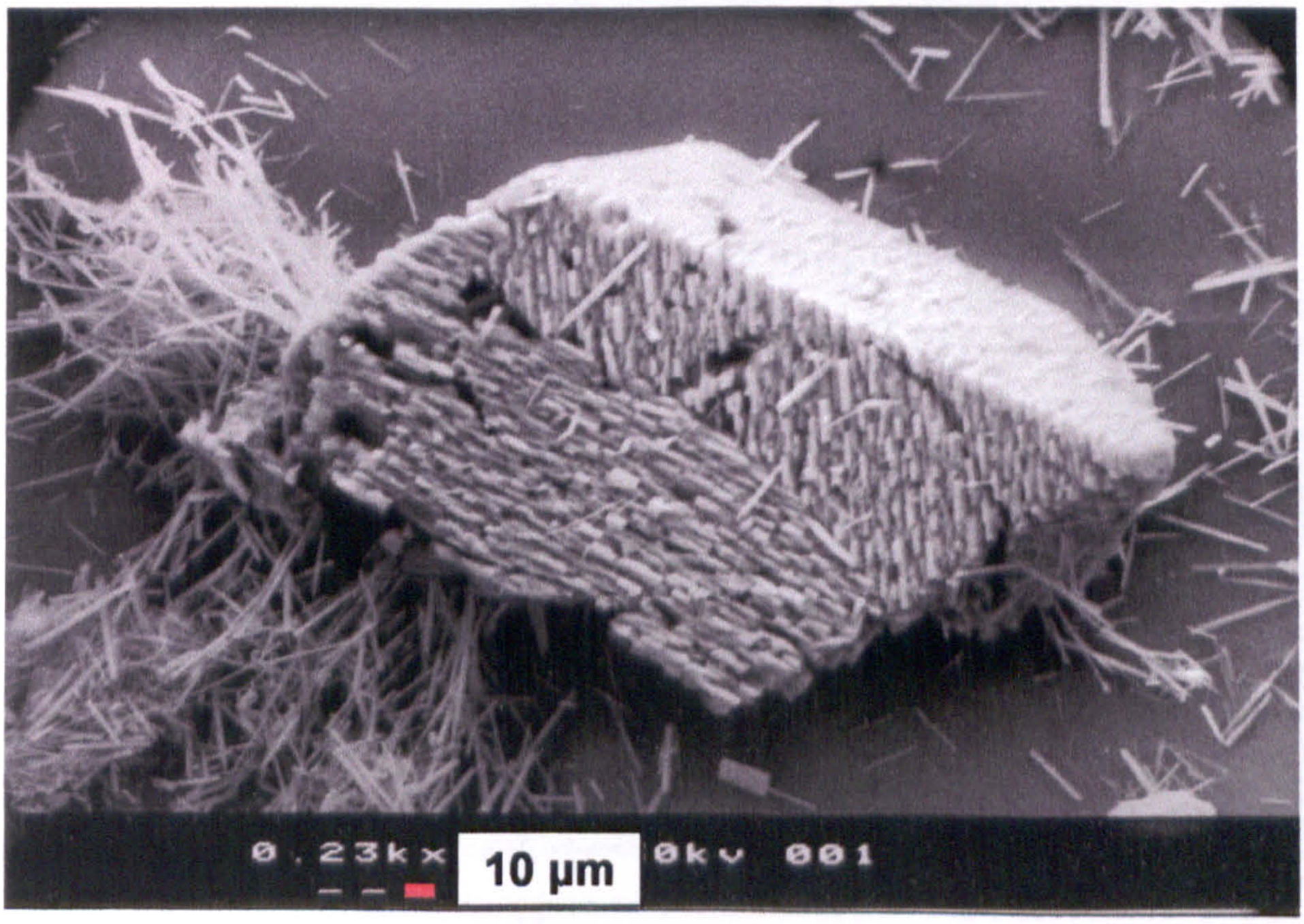


Figure 3-26: Aggregated crystal of $C_{60}(C_3H_6)$ shows how a non singular crystal can give the appearance of a more ordered structure.

$C_{60}(C_3H_8)$

As with the propene intercalate $C_{60}(C_3H_8)$ gave larger regular crystals which were considerably larger than for the ethene and ethane intercalates. Optical and SEM photographs of these intercalates are given in Figure 3-27 and Figure 3-28. The crystals again failed to diffract or diffracted very weakly, and again this is supported by poor PXD patterns. No further SEM evidence is available to show the true nature of the crystals although some roughness is visible by the optical microscope, this is not sufficient evidence to dismiss the crystals, however and in this state they still appear better than many successfully diffracting crystals generated conventionally. One factor which may be present is the decagonal twinning reported by Pauwels.[227] A truncated version of this observed twinning may explain the highly ordered decagonal cross section of the crystal needle and the difficulty in collecting data. This remains speculation at present and a simple poorly ordered crystal remains the most likely explanation for the lack of access to XRD data.

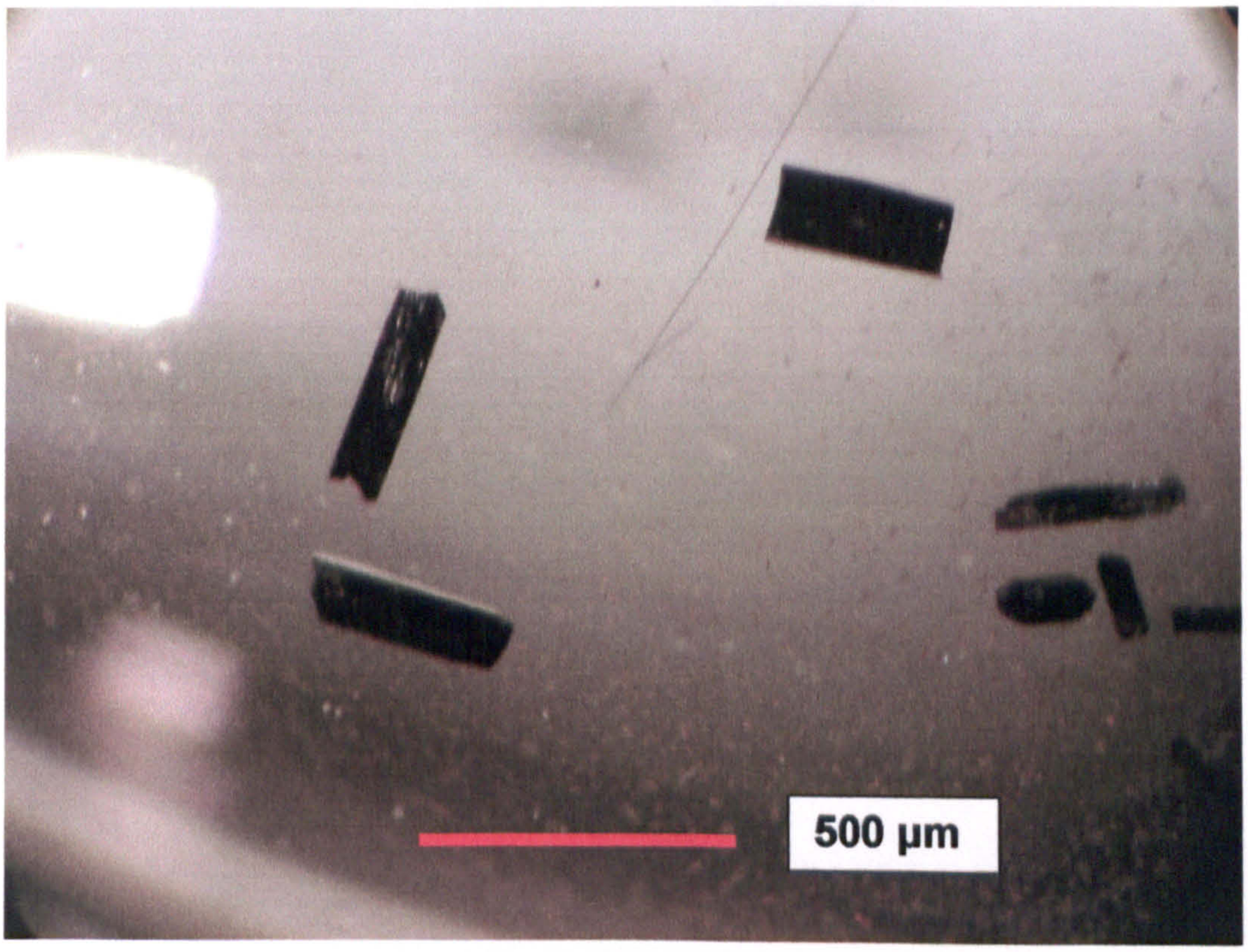


Figure 3-27: Highly crystalline in appearance, the propane intercalate was hoped to diffract.

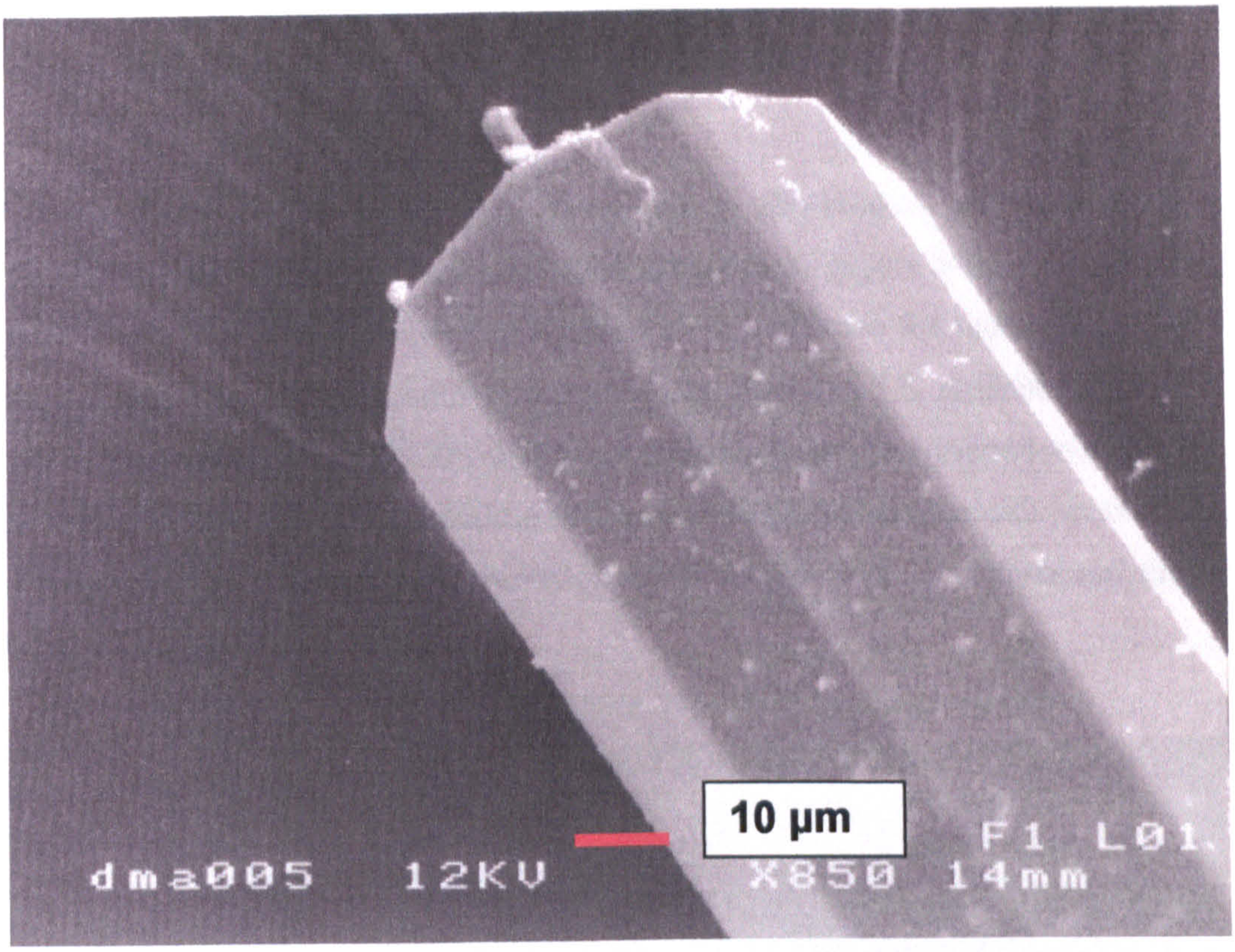


Figure 3-28: SEM photograph of $C_{60}(C_3H_8)$ shows a decagonal cylinder.

$C_{60}(CO_2)$

Crystal of the CO_2 intercalate were also grown by this method and produced high quality crystals. This is shown by optical microscopy in Figure 3-29. These crystals were shown to diffract X-rays and a data set was collected for them. The species itself is well known with data at room temperature down to 5 K available from PND and PXD studies.[178,200,201,206] The data does not immediately correspond to the lattice structures attributed to the intercalate and the structure currently remains unsolved. It is suggested that a complicated twinning system is present in the crystals and this is what is causing the problems.

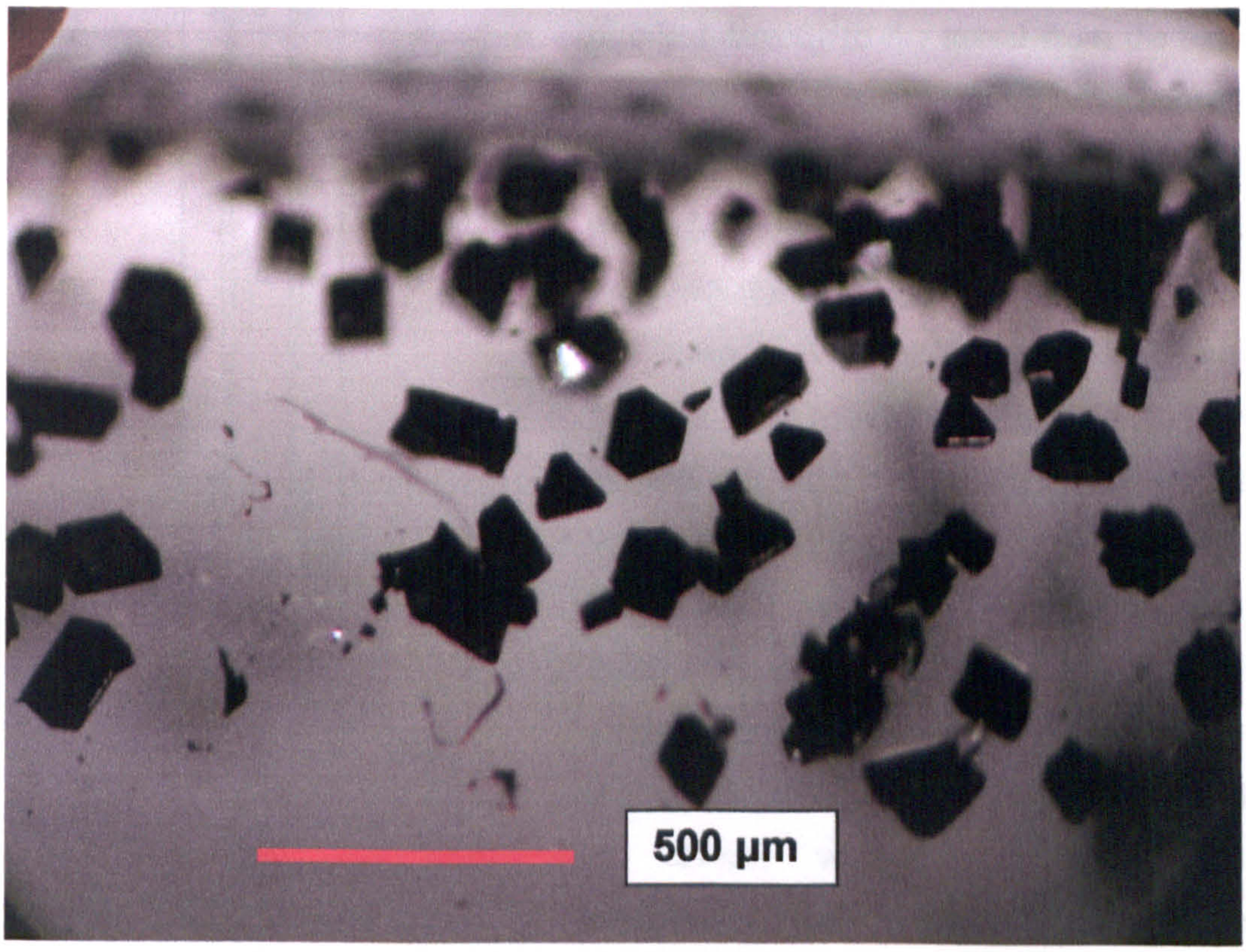


Figure 3-29: Optical microscope photograph of $C_{60}(CO_2)$ crystals, shows well ordered, non-aggregated systems.

Continuous Diffusion Driven Precipitation

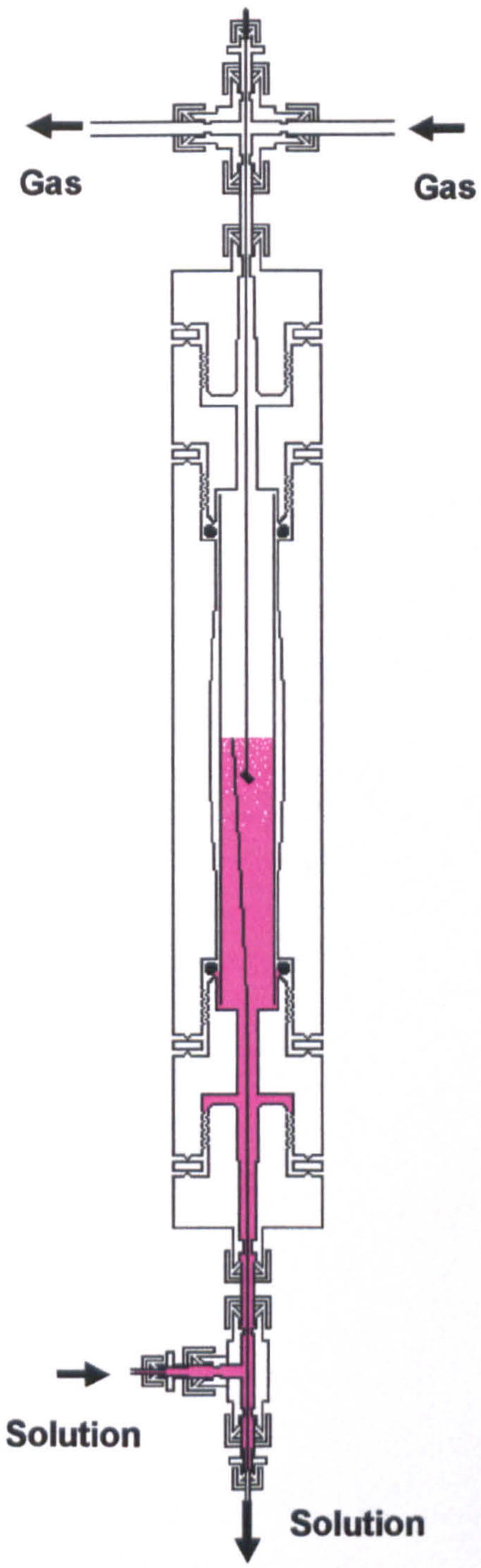


Figure 3-30: Diffusion experiment designed to grow larger crystal by allowing the growing region of the solution to be moved and replaced. A seed crystal was used to attempt controlled growth of a larger sample

The experiments were extended to attempt to increase the maximum crystal size by extending the time available for crystal growth. This was done by using a seed crystal from a previous experiment. This crystal was glued onto a highly polished steel needle suspended from the top of the vessel. The gas was supplied to the top of the vessel with the ability to send gas directly to the back pressure regulator. The solution was supplied directly to the vessel from the base of the vessel and waste solvent was removed from the vessel by a highly polished steel tube which rose from the base of the vessel to a point approximately 1 cm above the base of the needle. This setup is shown in Figure 3-30 and is plumbed as in Figure 3-31. The experiments were carried out at 150 bar as with the standard original experiments. Experiments could theoretically be run indefinitely with the solution being replaced when needed. This also had the advantage that crystal could be more effectively rinsed of solvent when crystallisation was completed Attempts were made to run the apparatus constantly by matching the diffusion rate of the gas with the flow rate of the pump. This proved impossible as the slowest flow rate was still much faster than the progress of the gas. This could be remedied if a slower pump was available.

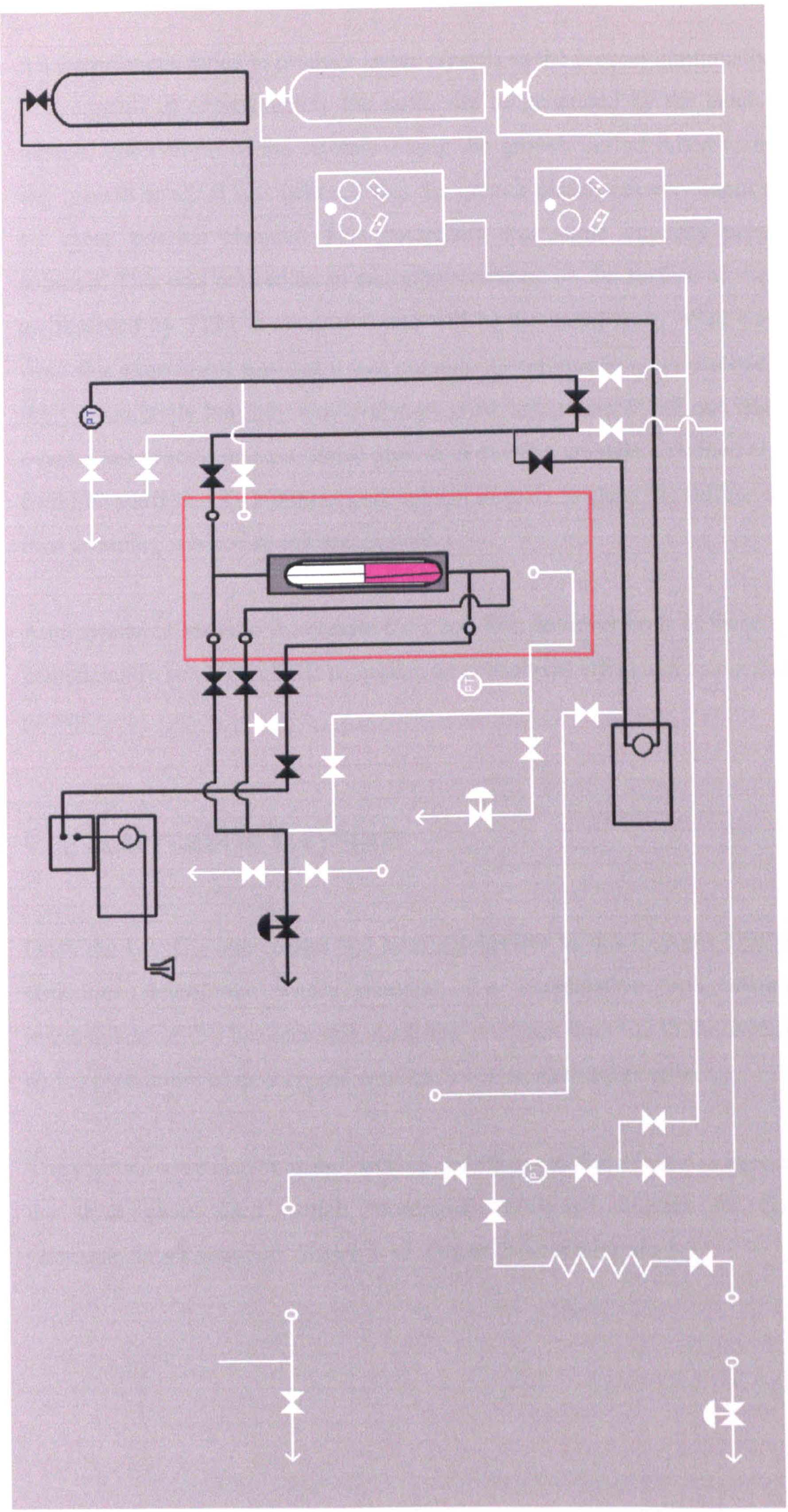


Figure 3-31: Position of the crystallisation vessel in the main experimental design.

All experiments failed to produce larger crystals as the process continually generated new crystals of approximately the same size as generated by the batch technique. Indeed, observation of the crystals during the growth period failed to demonstrate any growth at all. It was believed that the growth phase was very rapid then halted by some external element. This potentially was some impurity present in the solution. This was noticed as an amorphous coating on the surface of the nanotubes as observed by TEM in Chapter 4 and will be discussed later. What was observed from this experiment was that it was possible to continue to grow discrete crystals of the C_{60} materials but they would always grow independently of one another as an overlapped process and continued growth of existing crystals remained elusive. This could be addressed by pumping pure solvent initially to clean the surface of the seed, then pumping solution to initiate growth.

Attempts were made to intercalate C_2F_6 and SF_6, however both of these gases were insufficiently soluble in DCB to initiate an antisolvent effect and so no crystals were grown.

C_{70} Intercalate Crystals

Once the five C_{60} intercalates had been synthesised as macroscopic crystals and the structures determined where possible, C_{70} intercalation was attempted. The intercalation of C_{70} has received much less attention than C_{60} in the literature[203] and so the production of new crystal structures was an exciting possibility.

The crystals were grown using identical conditions to that of the C_{60} intercalates with the three gases used, which successfully collected datasets for C_{60}. Optical photographs are shown in Figure 3-32, Figure 3-33 and Figure 3-34.

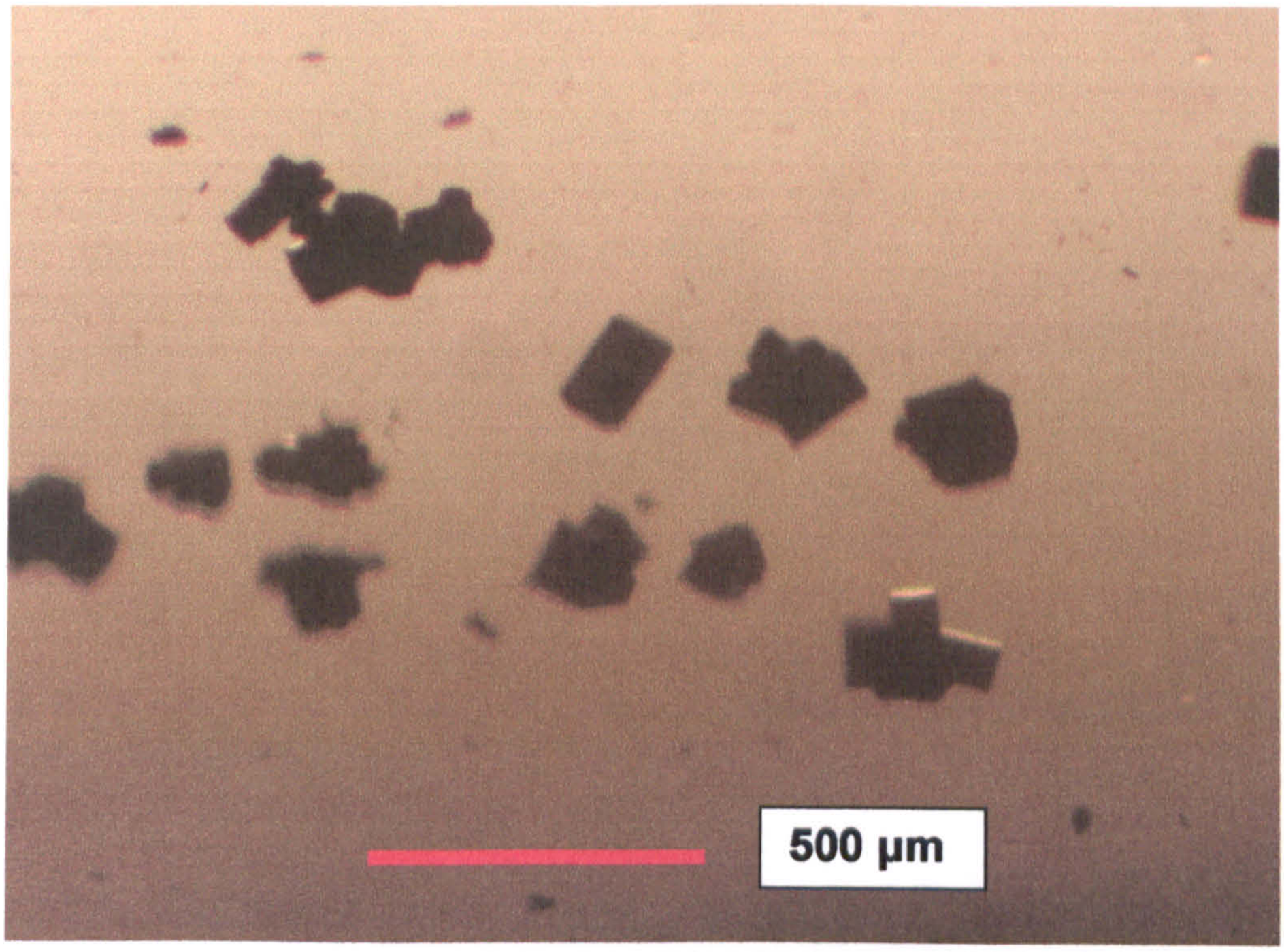


Figure 3-32: Optical photograph of what is believed to be $C_{70}(C_2H_4)$.

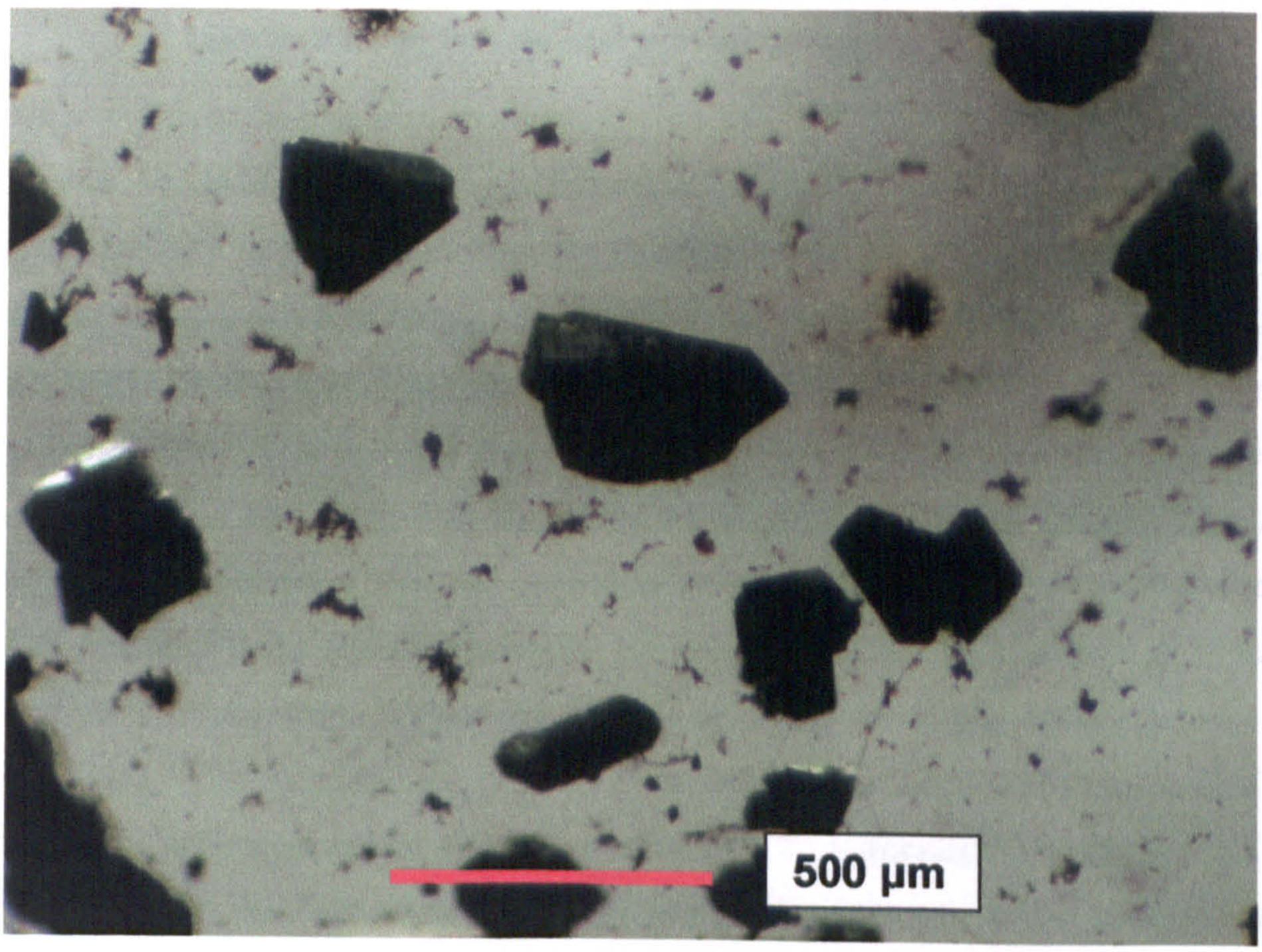


Figure 3-33: Crystals of the expected $C_{70}(C_2H_6)$ intercalate

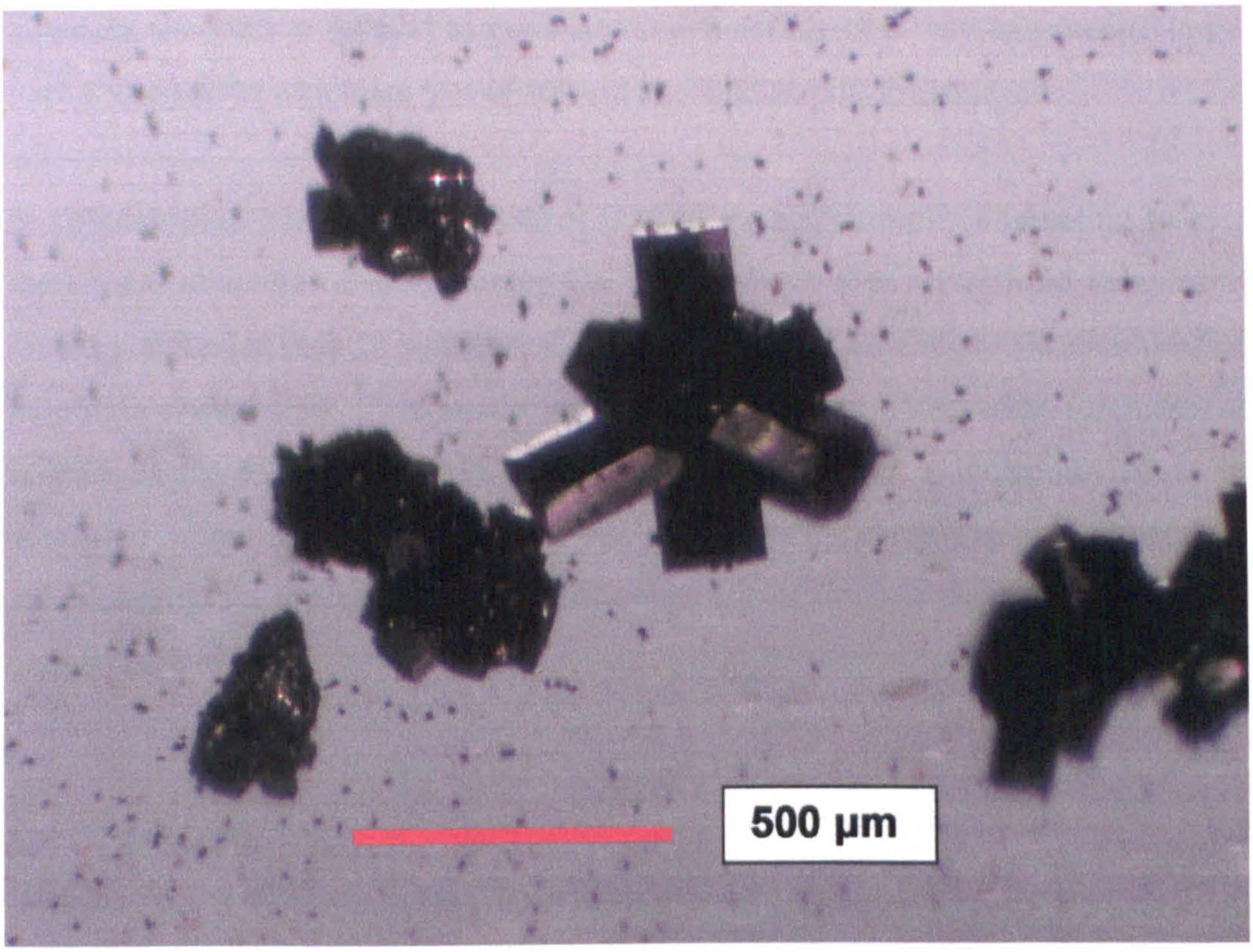


Figure 3-34: Evidence of the $C_{70}(CO_2)$, this sample showed more apparent twinning than the other two intercalates.

In work by Gadd on the noble gas intercalates of C_{70} he showed that they displayed lower stability to temperature than the C_{60} equivalents.[203] This caused concern that the intercalates of much larger species may be even less stable. In fact this proved not to be the case and X-ray data were collected for the intercalates of ethane and carbon dioxide. It is believed that the ethene sample failed to diffract due to poor sample quality and fresh data should be collected soon. Of the samples that did diffract, both diffracted well and gave clear patterns. Unfortunately, at present, these data have yet to be solved. However, the cell parameters are available. A simple hexagonal arrangement is observed for both systems with a = 21.501(4) Å and c = 16.691(5) Å for the C_2H_6 sample and a = 21.545(4) Å and c = 16.703(4) Å. This is similar to data reported for pure C_{70} systems. [228-231] Difficulties in solving the C_{70} structure have also been encountered by other groups who are also yet to provide an adequate complete solution to the pure C_{70} structure. At present it is not certain if the intercalation has been achieved, either way would be a significant discovery,

however, as either a method to generate new materials or a way to generate large, pure C_{70} crystals, which are free of solvent and antisolvent, is displayed.

In collaboration with the University of Oxford we are currently attempting to gain the crystal structure of the fullerene C_{78} and we have also crystallized samples of mixed endohedral $N@C_{70}$ and pure C_{70}. This mixture should allow the examination by single crystal ESR. This would be a highly important observation for fullerene science as the magnetic moment effect of individual $N@C_{70}$ molecules could be measured in the lattice. The technique has recently been adapted to only require 0.5 mg of sample for this reason it is ideally suited for analysis of these highly precious materials.

Discussion

The generation of the crystals shown above can be compared to the theoretical equations at the beginning of this Chapter. The slow action of an antisolvent is shown in Figure 3-35, a figure similar to Figure 3-1 at the beginning of this Chapter. Here we see that action of an antisolvent on a solution. As stated earlier the decrease in solvation follows a cubic equation. Without experimentation there is no way of knowing the actual form of this equation but it is still possible to ascribe a basic parabolic curve to it as shown in Figure 3-35. This diagram shows the action of two antisolvent processes. The first is shown in red and represents a schematic depiction at rapid precipitation. The solution, in this case, is thrust very rapidly into a supersaturated state (Y) and hence nucleation can spontaneously occur and generates nanoparticles. The key to this is that the solution remains in the supersaturated state for as long as possible to allow the maximum amount of nucleation before concentrations drop the solution back into the metastable state (Z) and growth mechanisms will control the system. In our crystallisations, however, we are attempting to grow crystals more slowly and so we wish to have the solution in the supersaturated state for the minimum amount of time (A). This will generate a small number of nuclei which will grow rapidly (B) and leave the solution along the equilibrium concentration. This will continue with slow growth of the crystal and no

further nucleation as the antisolvent concentration increases (C). This could be seen in the crystallisation photographs shown in Figure 3-10. This showed that initial addition of the antisolvent instigated the growth of many crystals but this was followed by a period of slow growth in only a few points. Some further nucleation was observed during this period but only at a very small number of places.

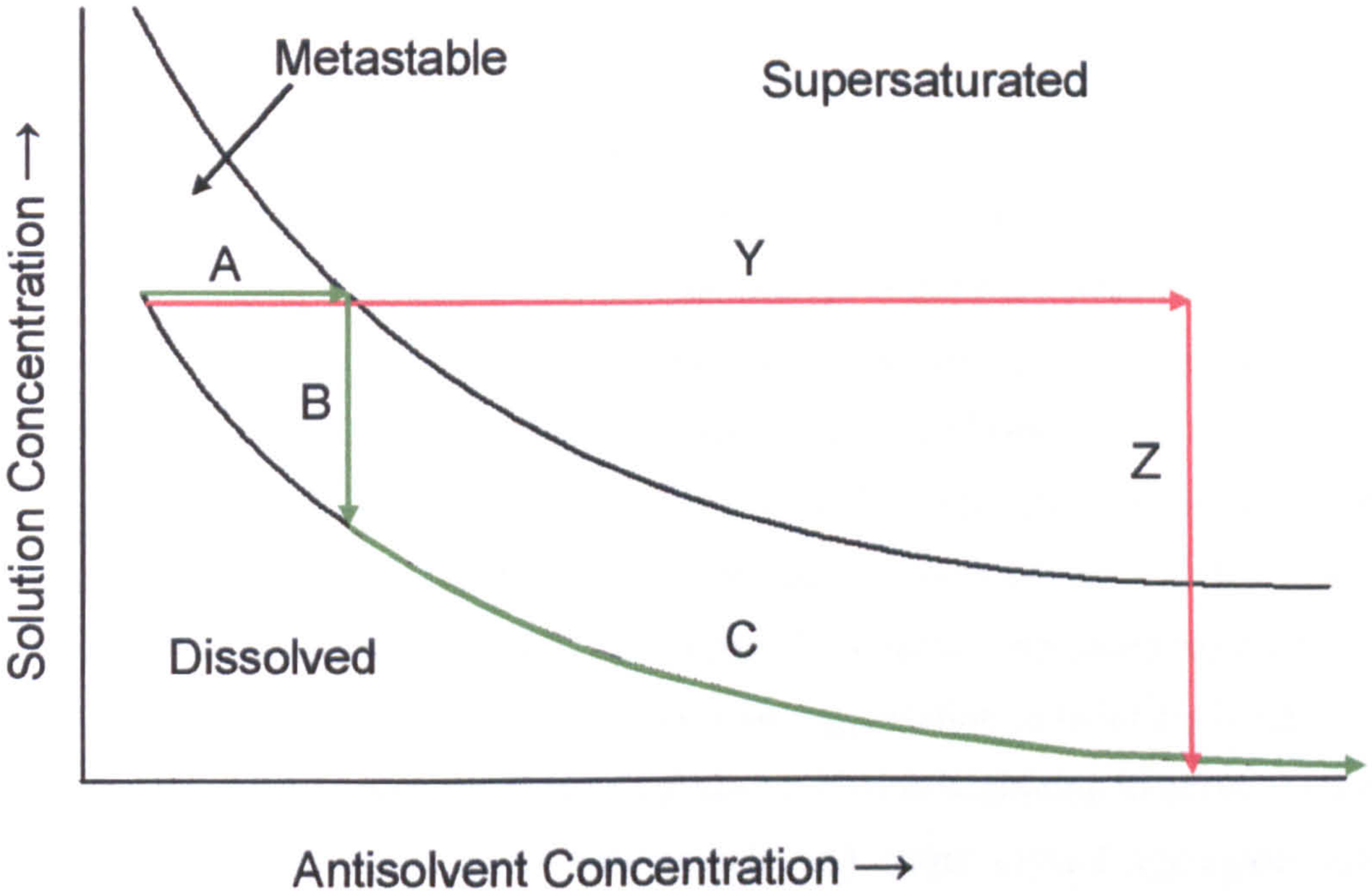


Figure 3-35: Diagram to explain the effect of antisolvent concentration on solutions, including a model for nanoparticulate and macroscopic crystallisations.

In examining the system it appears there is little control over our crystallisation. Constant pressure is used and so the flow of the antisolvent into the solution is constant throughout the experiment. If the pressure was varied it may be possible to initiate a more precise crystallisation. For example if low pressure was used at the beginning of the experiment to allow for a very slow nucleation rate to occur, this would allow only a very small number of crystals to be formed. If this pressure was maintained then the growth of the subsequent crystals would be very slow, relying on the reduced diffusion of the antisolvent. The pressure could be raised, however, on completion of the nucleation and the rate of growth increased. This would potentially allow the generation of larger crystals in a similar time period to the

previous experiments. Care would have to be taken to not increase the pressure too greatly or a new supersaturated system would be established. This would need careful observation. A simpler system would use a more dilute solution. This could be pressurised with antisolvent and potentially exist purely in the metastable region. This would mean that any nucleation which did occur would produce a relatively large crystal. A possible drawback being that nucleation might not occur at all and since the solution is less concentrated there will be less solute available to form the crystal, this could lead to smaller crystals.

The mechanisms of crystal growth have not been examined thoroughly so it is not possible to determine the methods by which the crystal grows. It can be seen, however, that the morphology of the crystals change at different points of the tube, Figure 3-36. At the top of the tube the crystals are tiny as the antisolvent perturbs the surface in a manner similar to the GAS experiments of Chapter 2. If the tube is examined lower down, the crystal sizes grow, while still retaining the discrete appearance. The even growth indicates a continuous growth system. Further down the tube the crystals again appear to be larger. This section provided most of the crystals for analysis, although in this section some aggregation or twinning is starting to appear. This may be an indication of surface nucleation beginning to occur. At the bottom of the tube this is even more evident and larger crystal aggregates are formed. It may be that secondary nucleation would be favoured for this system. Alternatively it might simply be the forced combination of crystals because of precipitation by antisolvent without any immediate mechanism to drop out of solution. The Damköhler number would be expected to be high as the system seems likely to be integration controlled rather than mass transport controlled, due to the expansion of these properties by the SCF. This would mean that the concentration at the interface, c_i, would be close to the solution concentration, c_∞, and as such it might favour a surface nucleation growth mechanism due to the higher concentrations of solute at the surface being able to form small nuclear bundles. This is simply speculation, however and no firm statement can be made until the process has been observed more thoroughly.

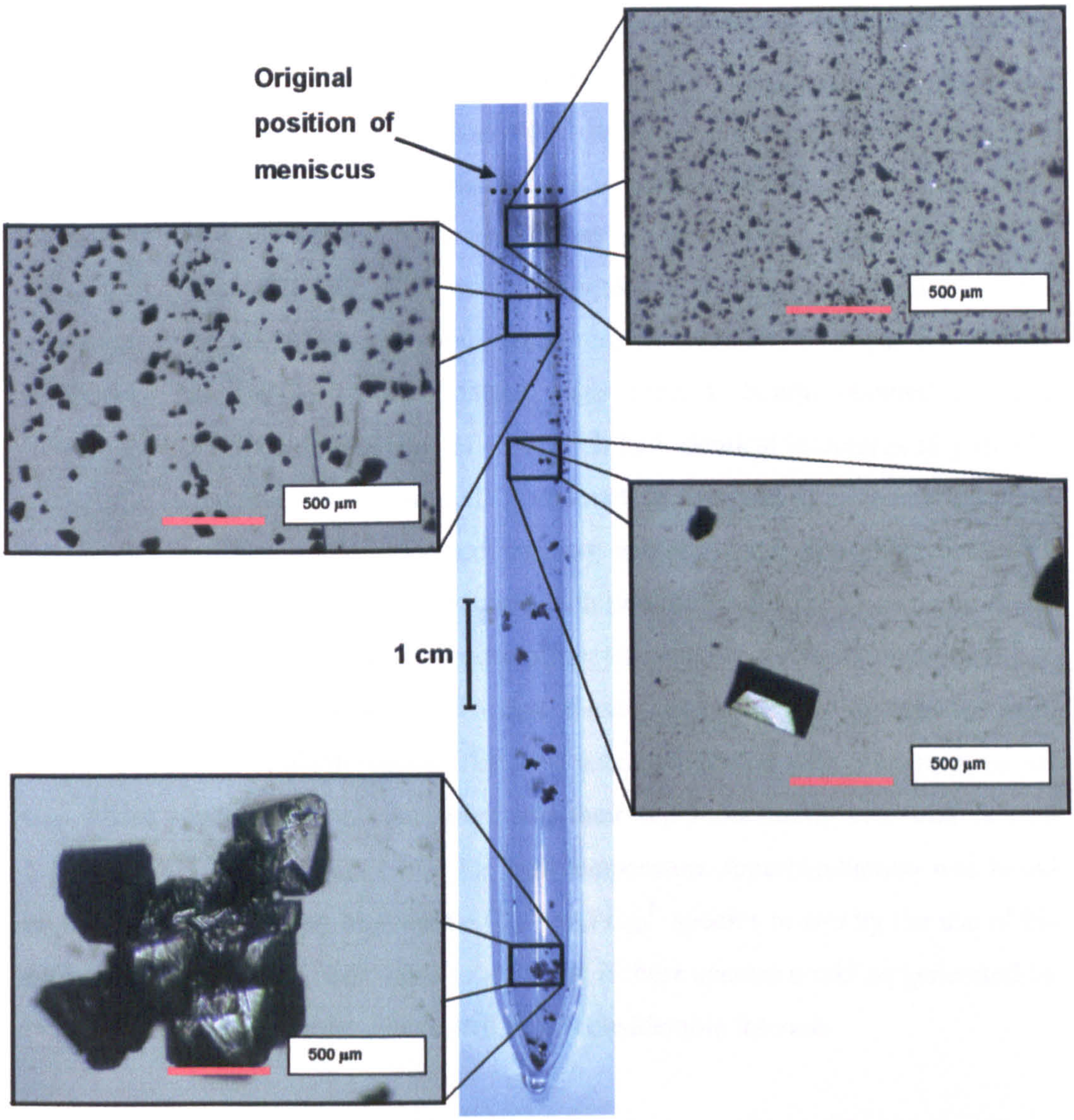


Figure 3-36: The morphology of the crystals at different parts of the glass tube can give clues as to the conditions for growth.

The experiments so far have generated crystalline material of all samples examined and in five cases of sufficient quality to gather X-ray data. This represents real progress in the science of fullerene gas intercalates but it has an even wider potential for fullerene chemistry in general. One suggested use of these compounds was as superconductors, similar to the alkali metal containing fullerite. This was suggested by Schön but was later retracted by the Bell Laboratories after a rare scientific scandal over allegations of data duplication and manipulation. The work of Schön was shown to be highly improbable and a full hearing summary has been published.[232] The part of Schön's work which relates to this thesis was in the area of high temperature fullerene superconductors and solvent intercalates of them. These were said to be remarkably high temperature superconductors when doped with holes from a gate electrode. This work was shown to not have taken place and the existence of the gate electrode, which could remove three electrons per C_{60} without destroying the sample or the contacts, was refuted. Schön claimed to have investigated haloform intercalates of C_{60} which had identical structures to pure C_{60} except the atoms were further spaced. This structure was said to have one haloform atom per C_{60}. The structure seemed unlikely and was later proved incorrect by Dinnebier,[233] where a hexagonal structure with two molecules per C_{60} was given. In truly superconducting C_{60}, the superconducting temperature can be related linearly to the separation of the C_{60} atoms. To date these species are C_{60} intercalated with different numbers of alkali metals. The most successful being with 3 intercalates per C_{60}. These species are ionic in nature and their superconducting character is well established.[234] Schön's false claim for high temperature superconduction was based on this premise, claiming to generate C_{60}^{3+} and C_{60}^{3-} species *in situ* by the use of his gate electrode. It is still reasonable to state that if these species could be generated by other means their properties would still be of considerable interest.

The technique detailed in this Chapter answers two specific problems which have blocked advancement in this field, firstly that of obtaining crystalline samples and secondly of being able to vary the C_{60} separation. While Schön claimed to use a gate electrode to create C_{60}^{3+} and C_{60}^{3-} this can be done by creating an endohedral species where a charged species is contained within the C_{60} sphere. These are difficult but not impossible to synthesis. The materials behave identically to pure fullerene in terms of solution chemistry but are formally charged. These have failed to be

crystallized except through the use of complex co-crystallites.[235] When carried out, these crystallizations were performed from solution and even if the co-crystallite was not present the lattice would be changed by the solvent which would be incorporated into the structure. In this Chapter, SCF crystallization has been shown to produce single crystals of material with varied separation between the molecules. It is hoped that this phenomenon can be investigated further in the future with our collaboration with the University of Oxford. If successful we would be able to generate materials for superconductor examination without the need for a gate electrode.

Conclusion

From this Chapter, the principles used in Chapter 2 have been applied in conjunction with theory on the formation of crystals to devise a new technique for growing single crystals using SCFs. The technique was used initially for crystallising plain fullerenes and in this capacity two new structures have been discovered. The technique is currently being put to use crystallising very rare fullerenes and endohedral fullerenes. In this capacity the work within this Chapter has considerable potential to influence the study of fullerene materials, allowing the generation of single crystals of very small quantities of material without a major alteration of the crystal lattice and only requiring very small quantities of sample.

Chapter 4 Nano-Peapods

This Chapter moves away from the use of supercritical fluids as antisolvents and introduces their use as a solvent, while maintaining a link to fullerene chemistry. We begin with a description of fullerene nanotubes and then discuss preliminary work performed on placing C_{60} spheres inside them. A brief description of the possible uses of these systems will be given and, finally, the results acquired to date on a new synthesis of these materials with a great potential for the future of nanotechnology. Only a very small amount of data are currently available on this topic, although the potential implications of these data are enough that they warrant reporting.

Introduction to Nanotubes

Fullerene nanotubes represent an exciting new area of chemistry which grew out of research into fullerenes.[236] A carbon nanotube consists of a single- or multi-walled cylinder of carbon with hemispheres enclosing the ends. They are commonly synthesised by electric arc with graphite electrodes and a metal catalyst, often iron, under a low pressure of Ne.[153,237,238] They possess a narrow distribution of widths with an average value of approximately 14 Å.[239,240] Techniques have become sufficiently advanced that, by careful manipulation of conditions and catalyst, it is now possible to have a relatively high degree of control over the synthesis. Recently work by Dai displayed an novel synthesis of nanotubes from ethene gas.[241] This technique produced growth from an individual particle of catalyst mounted on a silica surface. This technique should be very important in the future of fullerene chemistry, however it is not yet widely available and all material used in this Chapter were synthesised using the conventional arc method. Once the tubes are generated they must be cleaned by annealing at 450 °C to remove amorphous carbon. The catalyst must be removed and the ends opened up. This is performed by treatment of the tubes with strong acid which accomplishes both tasks simultaneously.[242,243] Samples are then annealed at 450 – 500 °C to remove and waste products.

The existence of C_{60} inside of carbon nanotubes is well documented, with the name "nano-peapods" given to the product material.[244-248] These peapods are currently solely produced under low pressures and at high temperatures where sublimed C_{60} is free to enter the tubes. Due to the similarity in size between the interior of the tube and the fullerene an extremely neat fit is achieved. The positive mutual interactions between the two fullerenes is believed to introduce a large stabilising energy.[249-251] As Qian states, "the C_{60} ... is "sucked" into the (10, 10) or (9, 9) tubes" from data collected by his computational studies. This is supported by the fact that partially filled tubes are relatively rare, while the majority of a product sample will be either completely filled or completely empty. A rare example of a partially filled tube is given in Figure 4-1, this shows real-time movement of the C_{60} spheres inside the tube, as measured by TEM by Khlobystov.[252] Completely empty tubes are believed to possess end-caps which have not been completely removed by the acid treatment.[251] The production of peapods has the exciting possibility that, if a fullerene possessing a magnetic moment, for example endohedral C_{60}, where the endohedral atom possesses an unpaired electron, then a code or pattern of magnetic moments can be stored inside the tube.[253-255] This could be potentially the beginning of data storage on a molecular level. However, this information is lost when the product is heated above 150 °C. To achieve successful peapod production, a temperature of 600 °C is currently required under low pressure to sublime the fullerene. Therefore a low temperature route to these peapod materials is needed. Attempts have been made by researchers in Japan, under Shinohara, to use toluene solvent to introduce C_{60} to the nanotube.[256] All current attempts in this manner have failed to produce the peapods.

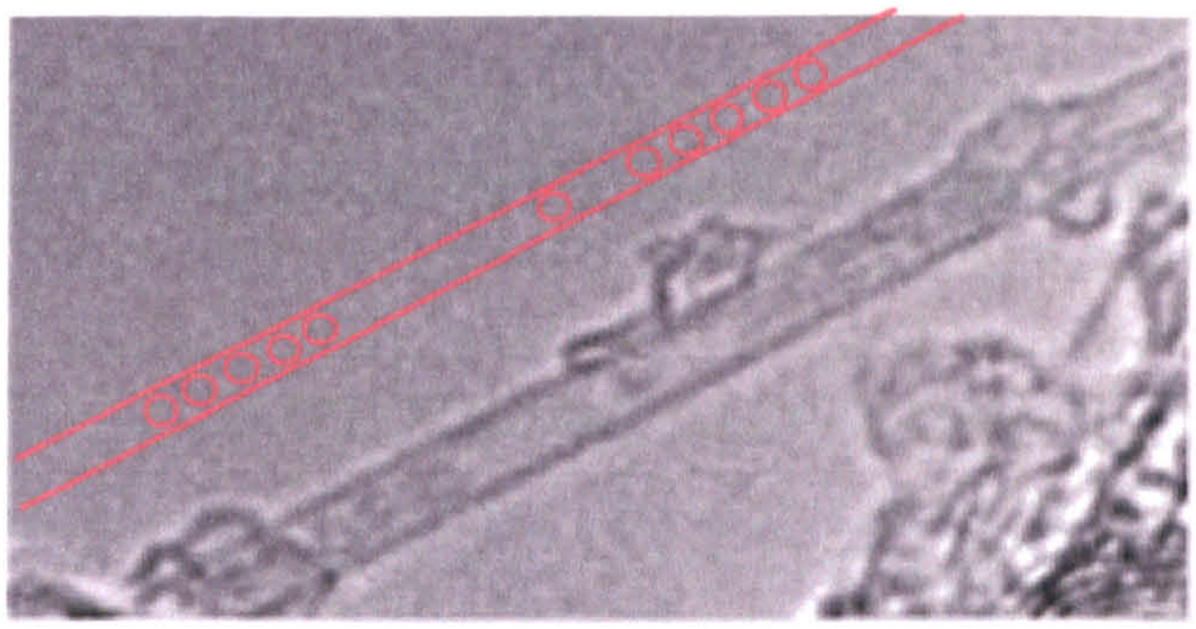


Figure 4-1: On rare occasions a partially filled tube can be found, here real-time movement of the C_{60} inside the nanotube can be seen.[252]

Filling of Nanotubes with C_{60} Using SCF

In this Chapter, we discuss preliminary findings using supercritical fluids as solvents to transport C_{60} into a nanotube structure. Two experimental setups were used; the first was an arrangement similar to the crystallisation experiments in Chapter 3. This was attempted as it was believed the solvent might allow the C_{60} access to a fluid phase which might permit greater movement, and in this way provide a route to the end of the nanotube. This would also provide an extra imperative to the insertion as the antisolvent would act to continually precipitate the material out of solution. Also, the fact that the experiment is carried out in solution would mean that the nanotubes were more evenly dispersed and so able to interact well with the C_{60} solution. A solution of 5 mg of C_{60} in 1 ml of DCB was placed in a sapphire tube view cell as in Chapter 2. The vessel was taken to 150 bar and the precipitation was allowed to occur over 5 days. It became immediately obvious that the experiment was unlikely to succeed as the nanotubes, which due to their size, only made up a suspension, sank to the bottom of the tube over the course of the first day. This meant that the position where the precipitation was occurring was well away from the nanotube and so a conventional crystallisation was taking place. Towards the end of the experiment the C_{60} was precipitating near to the nanotubes; however by this time most of the C_{60} had already crystallised. This meant that, even if the supposition was true that the C_{60} could be driven into the nanotubes, by the time this became a possibility there was relatively little C_{60} remaining in solution to enter the tubes. Analysis on this experiment and all subsequent experiments was carried out by TEM in Oxford. This showed that < 1 % of the sample is filled. This was identical to an untreated sample of nanotubes and indicated that the insertion had failed. What was most likely observed in this case is a crystallisation as in the previous Chapter with the nanotubes playing little or no role.

It was then decided to attempt a simpler experiment where a mixture of the nanotubes and C_{60} were to be exposed to SCF directly in the hope that the fluid might be potent enough to encourage the C_{60} to enter the tubes. This seems unlikely as was described in Chapter 3 the strong antisolvent effects of SCFs on C_{60} solutions.

However, although the solvent effect would be very low, the stabilisation energy for the formation of the "nano-peapods" is believed to be large and so, the presence of the SCF may be enough to allow sufficient movement.

A tube containing a mixture of nanotubes and C_{60} (5 mg, 1:1 by weight) was placed inside a sapphire tube this was sealed and placed under 150 bar of C_2H_4 for 1 week at room temperature. When the sample had been removed, it was analysed by TEM several times and the results showed an intercalation of 5 %. This was a highly encouraging result, as no incorporation of C_{60} has been previously observed at room temperature. An example TEM image is shown in Figure 4-2. An unknown amorphous layer was noticed on the sample, this was removed by annealing the sample at 450 °C. This was likely to be an impurity from the gas and may have influenced the successful filling of the tubes.

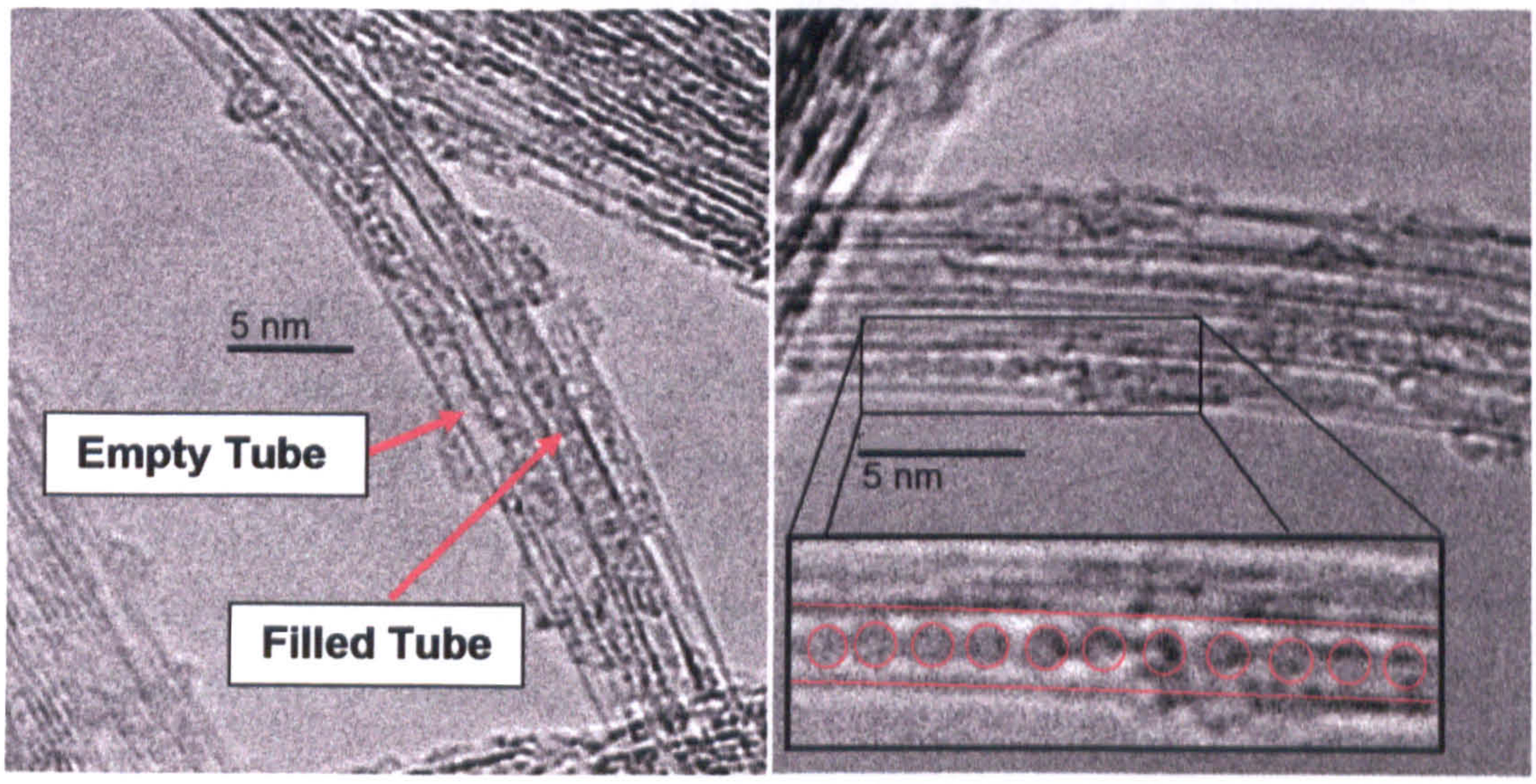


Figure 4-2: TEM data on the filling of nanotubes using scC_2H_4, most tubes in the sample are not filled, however several are filled completely.

The next experiment used CO_2, with the same quantity of sample and pressure, the vessel was left for 10 days in this instance at room temperature. After 10 days the pressure inside the vessel was observed to have dropped by approximately 40 bar. The experiment resulted in an incorporation of approximately 30 %. This was hugely encouraging, suggesting that the CO_2 was exhibiting a real effect on the nanotubes

and C_{60} mixture. TEM is given in Figure 4-3. No amorphous material was observed coating this sample.

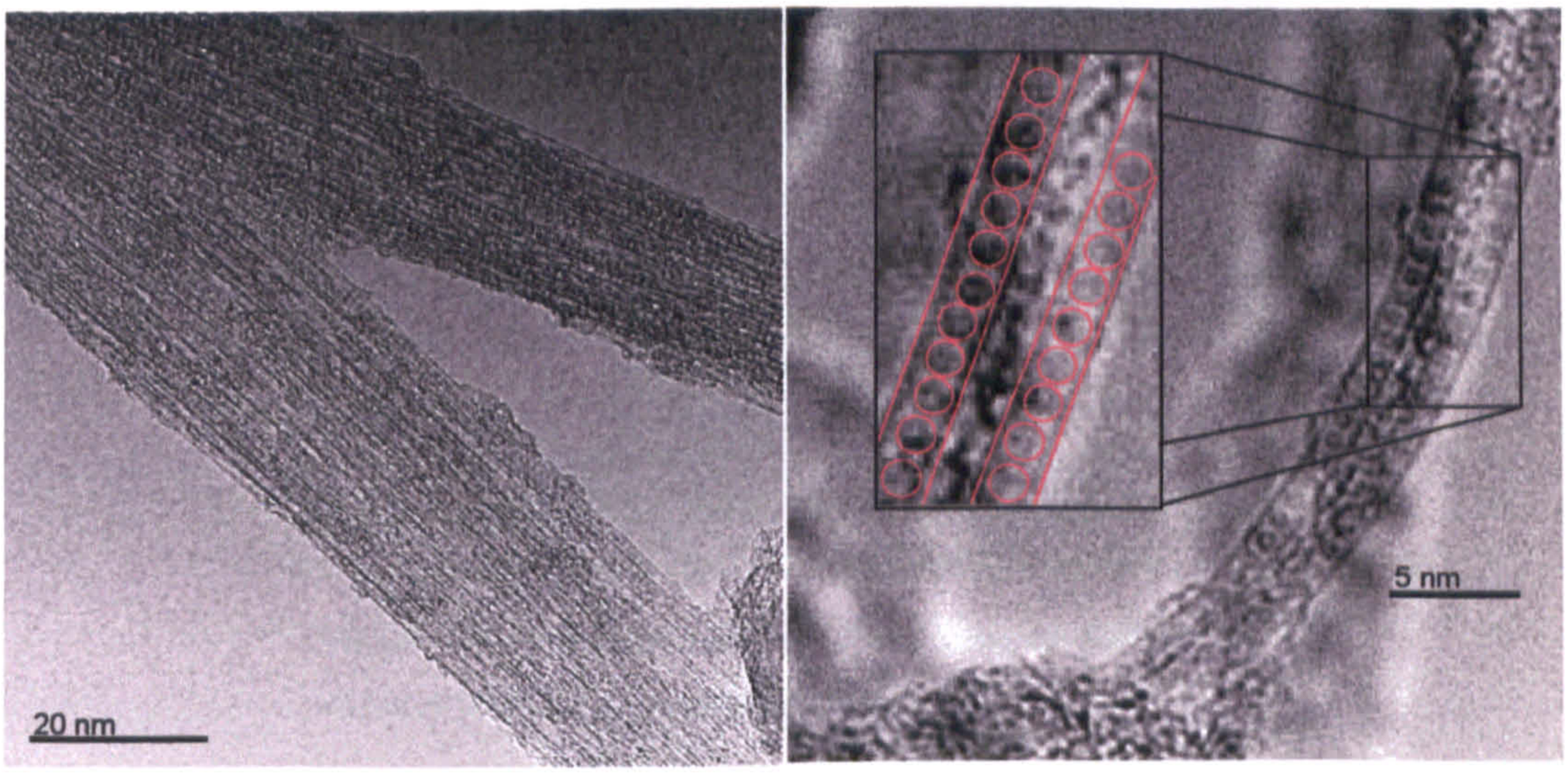


Figure 4-3: TEM analysis shows filling of ~30% for the sample treated with CO_2 for 10 days. The sample is also observed to be free from amorphous material, which was present in the ethene sample.

Since the nanotube/C_{60} mixture arrived from Oxford pre-combined it was wondered if the sample itself might form peapods spontaneously. Therefore a sample of this mixture was sent back for analysis, after it had been left at room temperature and pressure under air for three weeks. This showed the < 1 % filling associated with untreated samples and indicated that the CO_2 was definitely effecting the incorporation of the C_{60}.

On analysis of these data, we attempted the final experiment to date, which involved the establishment of two experiments to be carried out simultaneously. One repeated the successful filling experiment at 150 bar while the other was performed with just 1 bar of CO_2. In this way it was possible to check that it is actually the pressure which is instigating the effect on the filling stage. These tubes were setup side-by-side and both left at room temperature for 10 days. A photograph of the two tubes is given in Figure 4-4, showing that except for pressure the conditions were identical. During this experiment the gas inside the 150 bar vessel was topped up daily to ensure no significant pressure loss.

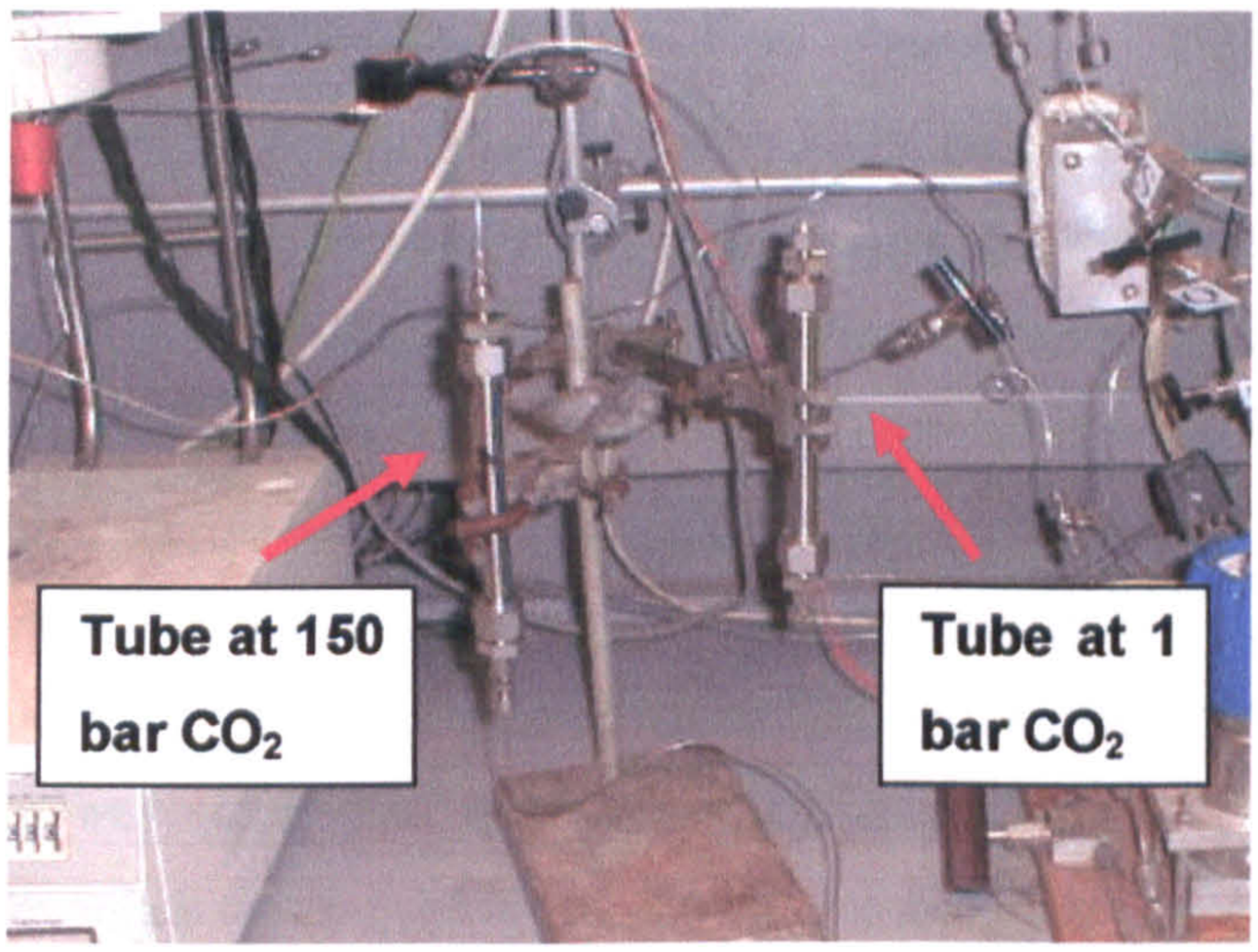


Figure 4-4: Two tubes used to create used to analyse the effect of pressure on nanotubes filling.

The samples were sent to Oxford for TEM analysis as before. This showed a 25 % filling of the 1 bar sample and a 60 % filling of the 150 bar sample. The results are summarised in Table 4-1. The incorporation of 60 % is a very positive result. A limiting factor, which stops this being higher, is believed to be incompletely removed end caps on the nanotubes. High temperature experiments are believed to give the C_{60} enough kinetic energy to break through these ends, while for low temperature samples this would not be possible.

Table 4-1: Summary of available on the five filling experiments.

SCF	Time (days)	Pressure bar	Filling %	Comment
C_2H_4	7	150	5	Gas topped up daily
CO_2	10	150	30	Gas left, ~40 bar loss over 10 day period
Air	21	1	<1	Control sample, left untreated in air
CO_2	10	1	25	Gas left, high pressure fittings assumed to be 100 % effective for such low pressure
CO_2	10	150	60	Gas topped up daily

In examining the summary of the data, Table 4-1 there are several points to be discussed. Firstly the use of CO_2 as the solvent is superior to C_2H_4. This is not surprising as the density of CO_2 is greater than C_2H_4 under identical conditions. This is particularly important as the carbon dioxide is present as a liquid while the ethane is present as a SCF. It would seem reasonable that the ethene would have less influence than the CO_2. This is less reasonable when compared to the sample treated with CO_2 at only 1 bar. Here it would be expected that a significantly higher filling by the ethene fluid would be observed, however, the reverse is seen. The most obvious observation was the presence of an amorphous material coating the nanotubes. This was unidentified but was present only in the C_2H_4 sample. This could potentially block the ends of the tubes and thus make incorporation of the C_{60} more problematic. Another possible explanation of this is that as the CO_2 had to be added as a liquid at ~50 bar that some may have condensed on the inside of the tube. When the vessel was sealed this could have equilibrated and generated a pressure inside the vessel. No pressure release was observed on opening of this vessel, however, so this seams unlikely. An alternative argument might be that CO_2 simply interacts much more favourably with the fullerenes than the ethene and this is enough to drive the greater degree of filling. The filling may be rapid and since the 1 bar sample was exposed to 50 bar when the CO_2 was added, if only for a few minutes, this may have been long enough to produce an effect. Also, since it was only possible to complete so few experiments, it may be simple irreproducibility leading to a seemingly unlikely result.

This theory may help to explain the difference in two almost identical experiments where the mixtures are treated with CO_2 at 150 bar. Two possible factors are suggested, which may have influenced the filling. (1) the slow loss of pressure in the first tube would be expected to have an impact on result, although perhaps not as extreme an effect as was observed. (2) the temperature was not controlled during the experiments and as such was dependent on the laboratory temperature. This fluctuated between 22-26 °C in the first experiment and 24-28 °C in the second experiment. This may provide an explanation to the increased loading, although again this small difference does not seem sufficient to explain such a large difference in the product.

In comparing the two results of the final experiment it can be seen that the low pressure sample incorporated half as much as the high pressure sample. This is much higher than we would expect. What may be happening is on addition of the CO_2 an adsorption process could occur on the fullerenes, assuming favourable interactions. This initial contact with ~50 bar of CO_2 may be enough to initiate adsorption onto the surface. This might give the ability of the C_{60} spheres to move, which then may continue over the 10 day period. This is highly speculative and not adequately understood at this time.

Another interesting feature of the high pressure filling is linked to the effect of the nanotubes themselves on the CO_2. This was shown recently by Tarumagnanam, who calculated that when the free path of a substance is limited by an enclosed space (in this case the nanotubes) then the critical parameters would be reduced.[257] This is interesting as in our case the parameters would be lowered sufficiently so that, although the CO_2 is liquid in the vessel, there would be a $scCO_2$ inside the nanotubes. This would suggest a lower density and so when C_{60} spheres are to enter the tube fewer CO_2 molecules will need to be displaced. This can be added to a list of possible factors, including size of molecules and compressibility, which allows the process to occur in CO_2 where it fails in toluene.

Conclusion

This Chapter has introduced the possibility of filling carbon nanotubes at low temperature. This has not been possible previously and so represents a step forward in nanotube science. If the C_{60} test molecules are replaced with endohedral fullerenes then it should be possible to establish a fixed array of magnetic moments. This would allow data to be read from a molecular source and would represent a significant advancement of fullerene based nanotechnology. However, due to limited data, it is not possible to provide much information on the factors influencing the filling. This Chapter also represents a link between the fullerenes of Chapters 2 and 3, and the impregnation work of Chapter 5, which also involves the addition of a molecule to an existing structure using SCF to facilitate transport.

Chapter 5 Mesoporous Silica Impregnation

This Chapter concerns the generation of solid acid catalysts. Supercritical fluids are used as solvents to transport aluminium containing molecular species into a silica structure. This work relates to the nano-peapods of Chapter 4 because the fluid is used as a solvent to facilitate entry into an existing structure. The Chapter begins with an introduction to mesoporous silica and progresses to a description of why the impregnation of these materials is beneficial. Results gathered to date on how the impregnations proceeded, using both supercritical carbon dioxide and propane are then presented. Data is also given on the success of impregnations with grafting time and aluminium source varied.

An Introduction to Mesoporous Silica

"Mesoporous" is a term given to ordered porous structures containing pores within a 2-50 nm size range.[258-260] IUPAC classifies porous materials into 3 groups depending on pore size, micro-porous (< 2 nm), mesoporous (2-50 nm) and macroporous (> 50 nm).[261] Microporous silica, or "zeolites", have been known for decades and comprise of microporous alumina and silica structures. Zeolites are used on vast scales in the petrochemical industry as cracking catalysts.[262] They are generated by the construction of a negatively charged alumininosilicate framework around a positively charged template molecules. Zeolites work well as catalysts for smaller molecules as only smaller molecules are capable of fitting inside the micropores of the zeolite structures. These systems allow easy access to highly stable aluminium groups. However, an expansion of the pores is required for chemistry to be performed on larger molecules such as benzene. Attempts to expand the zeolite pore size by using larger templates failed until, in 1996, a Cobalt complex was used to produce a larger stable zeolite. [263] Removal of the Cobalt from the structure is problematic, however, and this fails to provide an economically viable route to mesoporous materials.

Two different mesoporous silica materials were discovered simultaneously in the early 1990's by a collaboration between Mobil and Princeton University lead by Beck[264,265] and a group of researchers in Japan lead by Kuroda.[266,267] The subsequent work on these compounds has mainly followed Beck and his work with Mobil on MCM (Mobil Composition of Matter) materials.[260] The work by Kuroda was based on forming the mesoporous materials from existing sheets of Kanemite silica with a surfactant template. These both produced mesoporous silica, however, they exhibit different physical properties. The work described in this Chapter and the next centre around investigation of the MCM materials designed by Beck. These, unlike Kuroda's, are formed in situ from a molecular source of silica.

MCM silica is generated by the formation of a silica structure around a self organised surfactant support. Evidence for this was presented by Beck[268] who conducted an investigation on the effect on chain length of surfactant. This showed that when the length was shortened to C_6 and C_8 mesoporous material was not produced. This is explained by the fact that at these chain lengths the surfactants become more soluble in the aqueous environment and the hydrophobic imperative is no longer sufficient do drive the formation of micelles. An overview of the process is given in Figure 5-1.[258] The surfactants used contain a long hydrocarbon chain and a hydrophilic head group, these can be positively or negatively charged or non-polar. A common silica precursor is tetraethyl orthosilicate (TEOS),[269-271] although sodium silicate[272-274] and fumed silica[275] are often used. The reactions are performed in water where surfactants spontaneously self organise into structures depending on their concentration. The hydrophilic head group interacts well with the silica precursor and, in the case of the example, Figure 5-1 (MCM- 41), current understanding states that silica forms a coating around the cylinders of surfactant. The silica coated rods then orientate themselves to form bundles and begin to precipitate where they can then be collected by filtration. Once the structure is stable the sample is calcined to strengthen it by increasing the number of quaternary (Q4) silicon atoms and to remove the surfactant. This will be discussed more in Chapter 6 with an alternative to this calcinations step. The synthesis leaves a porous one dimensional structure comprising of aggregated cylinders which are capable of allowing large molecules to enter.

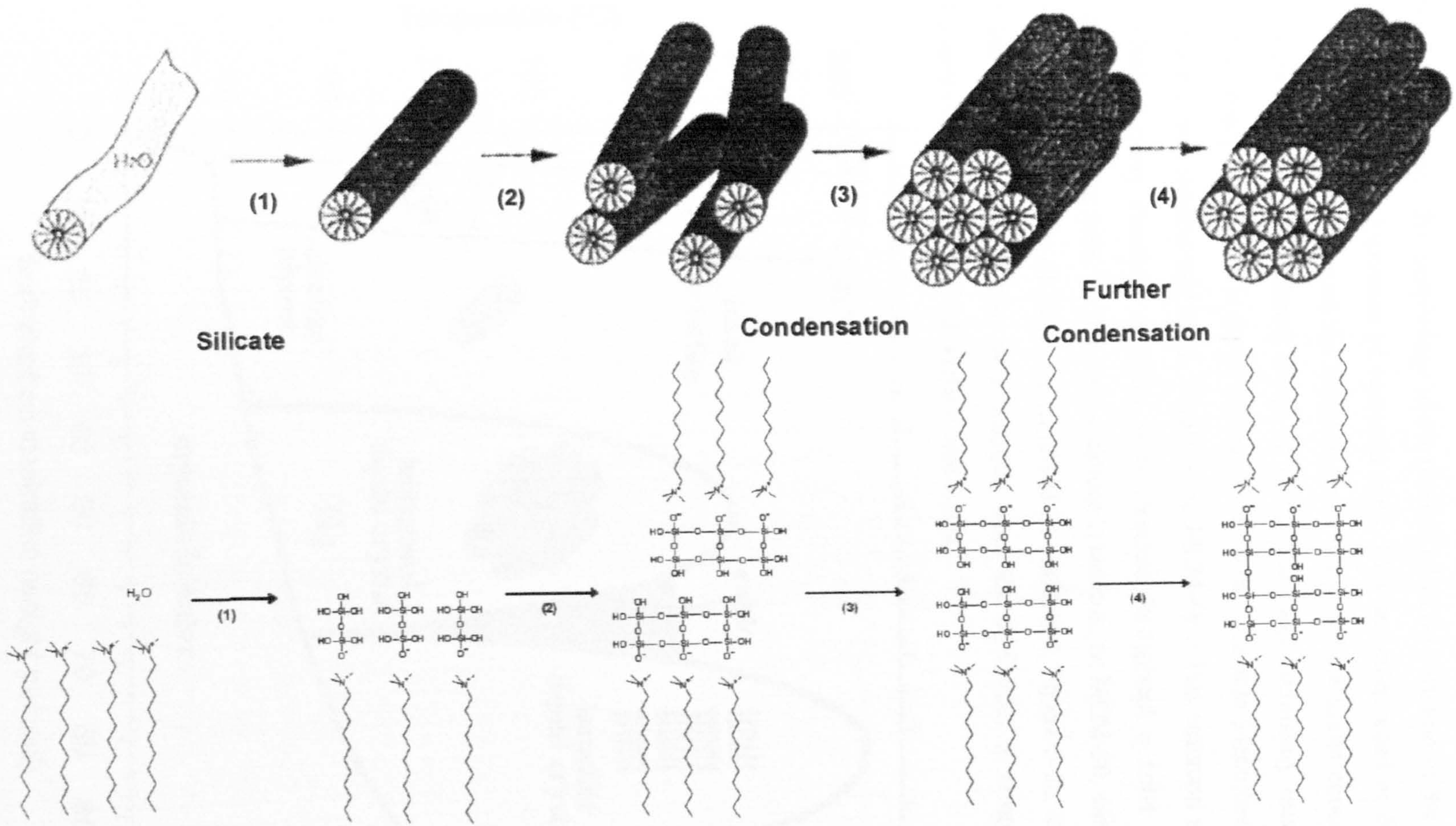


Figure 5-1: A mesoporous silica system is established by organisation of surfactant followed by hardening of the system by calcinations, which increases the number of siloxane bonds supporting the structure.

Much work has been carried out on varying the conditions of the synthesis in attempts to control the morphology of the product silica by variation of the reaction conditions and concentrations of reactants used. This has culminated in the graph given in Figure 5-2,[276] where the synthesis temperature and surfactant concentration are varied to produce different forms of silica. The most commonly investigated form of mesoporous silica is the hexagonal or MCM-41 structure (described above), which is a one dimensional solid, Figure 5-3a. MCM-48 is less common and is an interlinked cubic structure of silica with channels throughout a solid in three dimensions, Figure 5-3b.[277] The third structure is laminar, or MCM-50, where large two dimensional sheets of silica are separated by surfactant, Figure 5-3c. This form is less useful than the other two because, once the surfactant is removed, the structure collapses and the high surface area is lost.

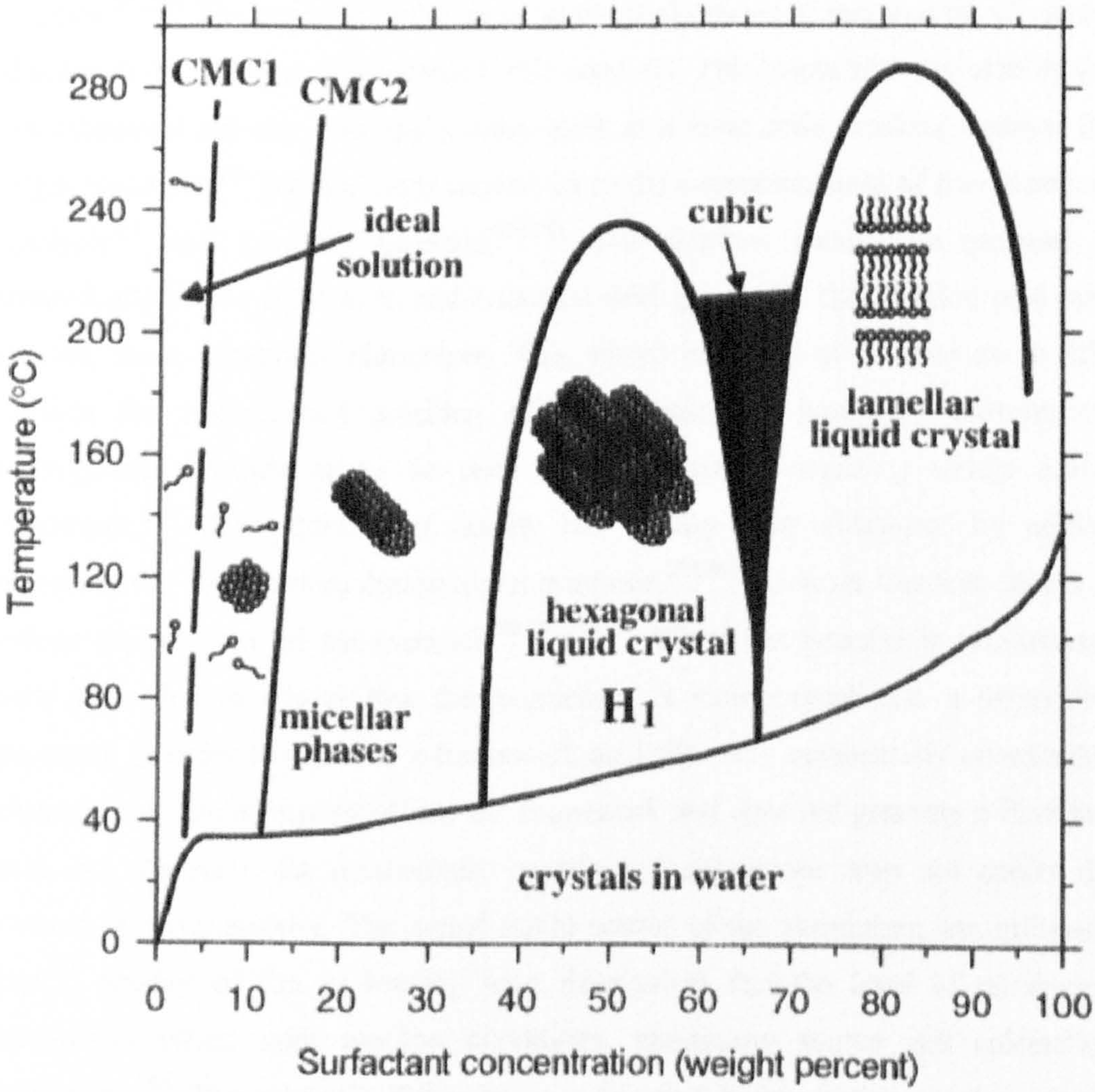


Figure 5-2: This commonly used figure shows how the form of the synthesised silica changes with variation of the temperature and the surfactant concentration.[276]

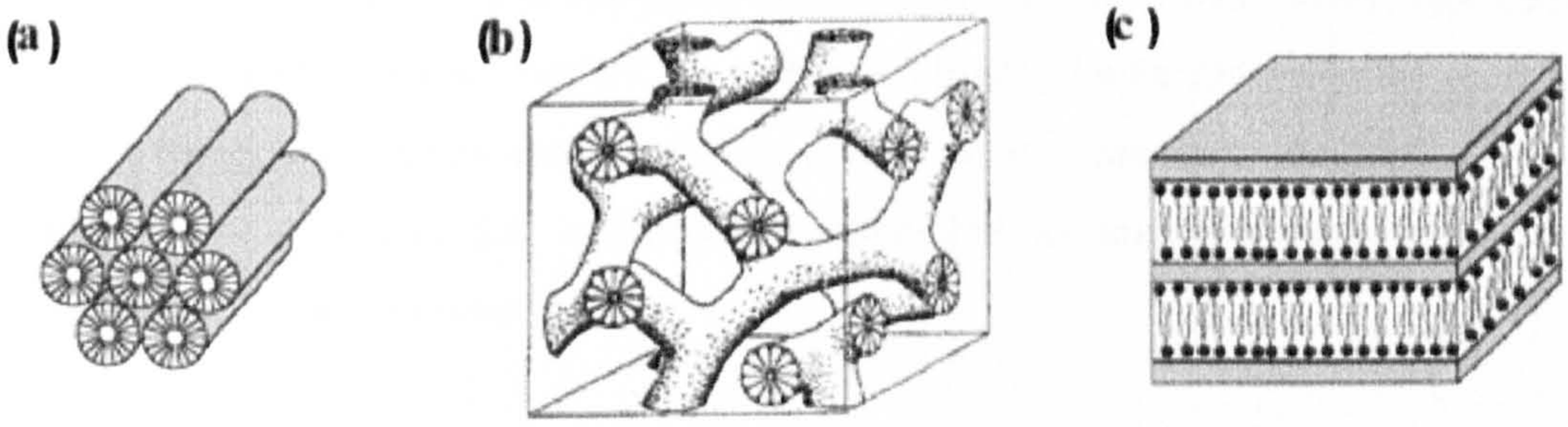


Figure 5-3: Three types of mesoporous silica can be produced by varying the experimental conditions as shown in Figure 5-2. These are shown here as hexagonal MCM-41 (a), cubic MCM-48 (b), and lamellar MCM-50.[276]

There have been many suggested uses of mesoporous silica including separation of bulk molecules,[278] chromatography,[279] electron transfer materials[280] and the sorption of gases.[281,282] The majority of the work on the applications of mesoporous silica and aluminosilica, however, is concerned with catalysis. This began with research by the petrochemical industry into applications such as a large scale cracking catalyst for larger molecules[258] but has since moved on to the expanding field of fine chemical catalysis[283] and catalytic supports.[284,285] The simplest method to generate a catalytically active solid is to add Brønsted acid groups by the addition of a new species, most commonly aluminium. This would enable it to be used as an acid catalyst for hydrocarbon cracking of compounds too large for conventional microporous zeolites or to be used in any reaction requiring mildly acidic conditions.[286] This addition of acidity has mainly been attempted by adding aluminium to the structure during direct synthesis.[287,288] However this was shown to reduce the ordering of the material.[283,286,289,290] When the material is synthesised, care is needed to ensure that the aluminium is incorporated into a tetrahedral geometry in order to generate a framework acid site. Any octahedrally coordinated aluminium is not incorporated into the framework and does not generate a Brønsted acid site. As such, the octahedrally coordinated aluminium does not confer the desired catalytic activity. The actual initial source of the aluminium can influence this.[283] Studies of the Al loading have determined that the level of tetrahedral aluminium varied with reaction conditions, aluminium source and calcination conditions.[258] The essential difficulty in achieving highly active catalysts is in obtaining maximum possible loading of active (tetrahedral) aluminium without loss of structural order or hydrothermal stability. This is highly important when the

cracking of hydrocarbons is compared between zeolites and Al-MCM-41. However, although the mesoporous catalyst is capable of allowing larger molecules to enter its pores, its acidity, activity and stability are always greatly inferior to those of zeolites. It is for this reason that research has attempted to improve these factors in mesoporous silica systems.

Some work on the impregnation of silica with transition elements during an extraction process has recently been suggested by Lu.[291] This involved and ion exchange step during the removal of surfactant template to replace surfactant with a metal complex. This allows a direct transfer to catalytic species in one step from initially formed silica. However, incomplete removal of the template and low loading of the support mean that this is currently an unsatisfactory route to these materials.

The study undertaken in this Chapter uses the post-synthesis grafting technique, first attempted by Mokaya in 1997, who used hexane as a medium to transport aluminium alkoxide into a silica structure.[292] This work involves the solvent transporting and depositing aluminium on the surface of the silica without disturbing the silica itself. In this way, aluminosilicate material is produced with a larger concentration of active aluminium and greater structural ordering with less penetration of aluminium into the interior of the walls of the structure. This work led to a new way of generating mesoporous aluminosilicate material which possessed superior hydrothermal strength to previous direct methods.[293-298] A problem exists, however, concerning uneven distribution of the aluminium inside the silica as prepared by post-synthesis grafting. Not unreasonably, when aluminium is added to the silica it will encounter the outside of the sample first. In the case of one-dimensional materials such as MCM-41, the aluminium will be required to travel relatively long distances before it reaches the centre of the sample. This is shown in Figure 5-4b. The aluminium is not believed to be sufficiently mobile to cover the whole internal surface evenly and give the desired product, Figure 5-4c.

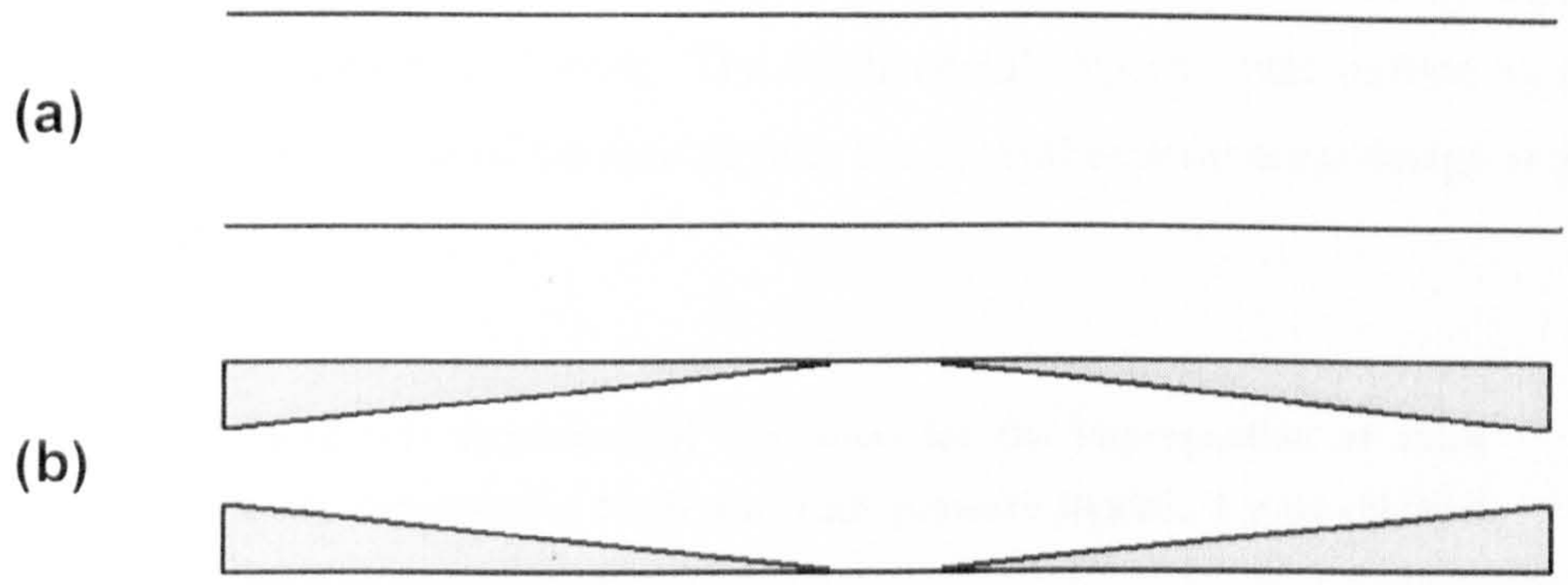


Figure 5-4: Diagram to show the filling of an empty mesoporous silica tube (a). This is believed to result in uneven coverage (b) when a liquid solvent is used. Here the centre of the sample has exposed silica and so is not afforded resistance to steaming. The desired even filling of the tube is shown (c). It was hoped that improved mass transport properties of SCF would provide a route to this type of coverage.

This Chapter extends this type of impregnation by using supercritical and liquefied gases as the medium for adding an aluminium source to the silica. The goal of this work, therefore, is to use improved mass transport properties of SCF to achieve a more uniform distribution of aluminium inside the silica. It was also hoped that the SCF would exhibit less interaction with the silica that hexane. In this way the, SCF grafting would reduce even further the damage to the silica and hence, generate samples with higher structural ordering following calcination.

Silica Impregnation with Aluminium

The experiments were carried out in the 60 ml stirred autoclave, see Appendix II, and carbon dioxide and propane were used as liquids or supercritical fluids as the solvents. The majority of the work was carried out with aluminium isopropoxide as

Al source. However additional minor investigation was made using aluminium chloride and aluminium lactate. The fundamental experimental outline is detailed below and the position of the autoclave in the general experimental design is given in Figure 5-5.

Table 5-1: Experimental conditions for the impregnation of silica using supercritical fluids and high pressure liquids. 2 g of calcined silica were used in all cases.

Expt	Solvent	Aluminium Source (g)	Si/Al	Time hr	Temp °C	Pressure bar
1	CO_2	-	-	19	40	150
2	CO_2	Aluminium isopropoxide 0.68	10	19	40	150
3	Propane	Aluminium isopropoxide 0.68	10	19	110	150
4	Propane	Aluminium isopropoxide 0.68	10	19	40	150
5	CO_2	Aluminium isopropoxide 0.68	10	19	110	150
6	CO_2	Aluminium isopropoxide 0.68	10	3	40	150
7	CO_2	Aluminium isopropoxide 1.36	5	19	40	150
8	CO_2	Aluminium chloride 0.44	10	19	40	150
9	CO_2	Aluminium lactate 0.98	10	19	40	150

Mesoporous MCM-41 silica (2.0 g) was added to the stirred autoclave with a quantity of the aluminium precursor, see Table 5-1. The substrate was then mixed thoroughly and the vessel sealed. The vessel was then connected to the high pressure

system and stirring of the sample was commenced, see Figure 5-5. The vessel was heated to the required operating temperature, filled with gas and maintained for 19 hours. The pressure was lifted and the samples were then, calcined at 600 °C for 4 hour. Two hydrothermal tests were carried out on the new materials. The first was steaming of the sample at 900 °C for 4 hour under a flow of nitrogen saturated with water. This allowed a measure of the aluminium stability as damage will only occur at points where the aluminium is not well integrated into the surface. A second treatment was used, where the samples were boiled in water for 48 hours. This will provide information on how resistant the silica is to harsh capillary forces and how well it is protected from hydrolysis. Both techniques are harsh treatments of the silica but are commonly used to assess a mesoporous material. Data on the pore size, surface area and acidity were gathered for post-synthesis material and after hydrothermal treatments by nitrogen adsorption and PXD.

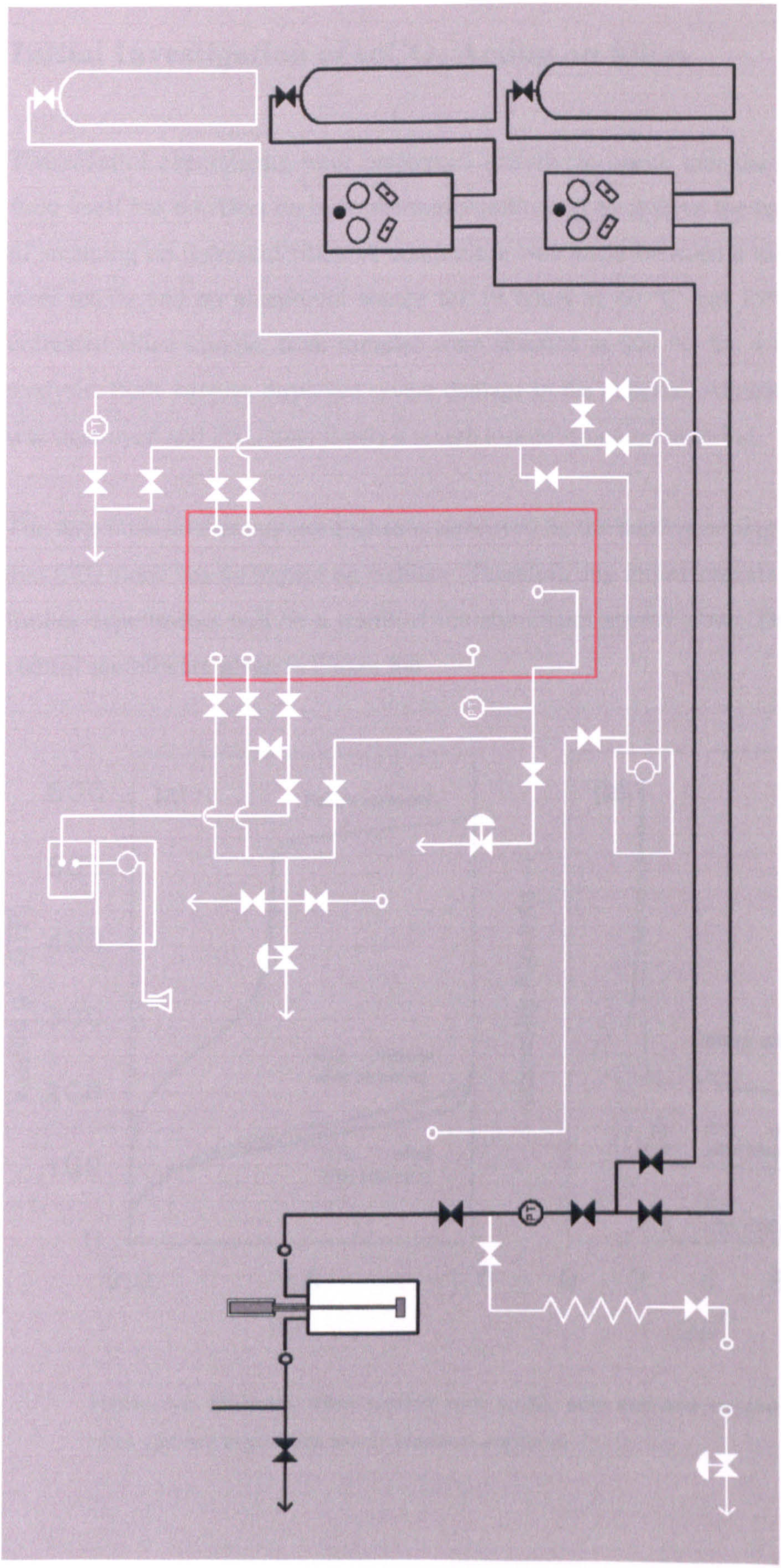


Figure 5-5: Position of 60 ml stirred autoclave for silica impregnation experiments inside the general experimental arrangement.

Initial Investigation of $scCO_2$ Acting on Silica

Two control experiments were performed initially to check that the supercritical fluid itself has no effect on hydrothermal stability and to observe the baseline effect of steaming on untreated silica. A comparison was made between a sample treated with $scCO_2$ and no aluminium source for 19 hours at 40 °C and 150 bar and an untreated silica sample. Both samples were steamed at 900 °C for 4 hours before analysis. Both samples displayed severe damage to the material. Almost all porosity was destroyed and PXD data shows a severe loss of structural ordering.

The data indicate that untreated silica is destroyed by the harsh steaming process and that CO_2 alone has no impact on stability. Therefore any improvements observed in further experiments will be a result of the aluminium source alone. Data on these control samples are given in Figure 5-6

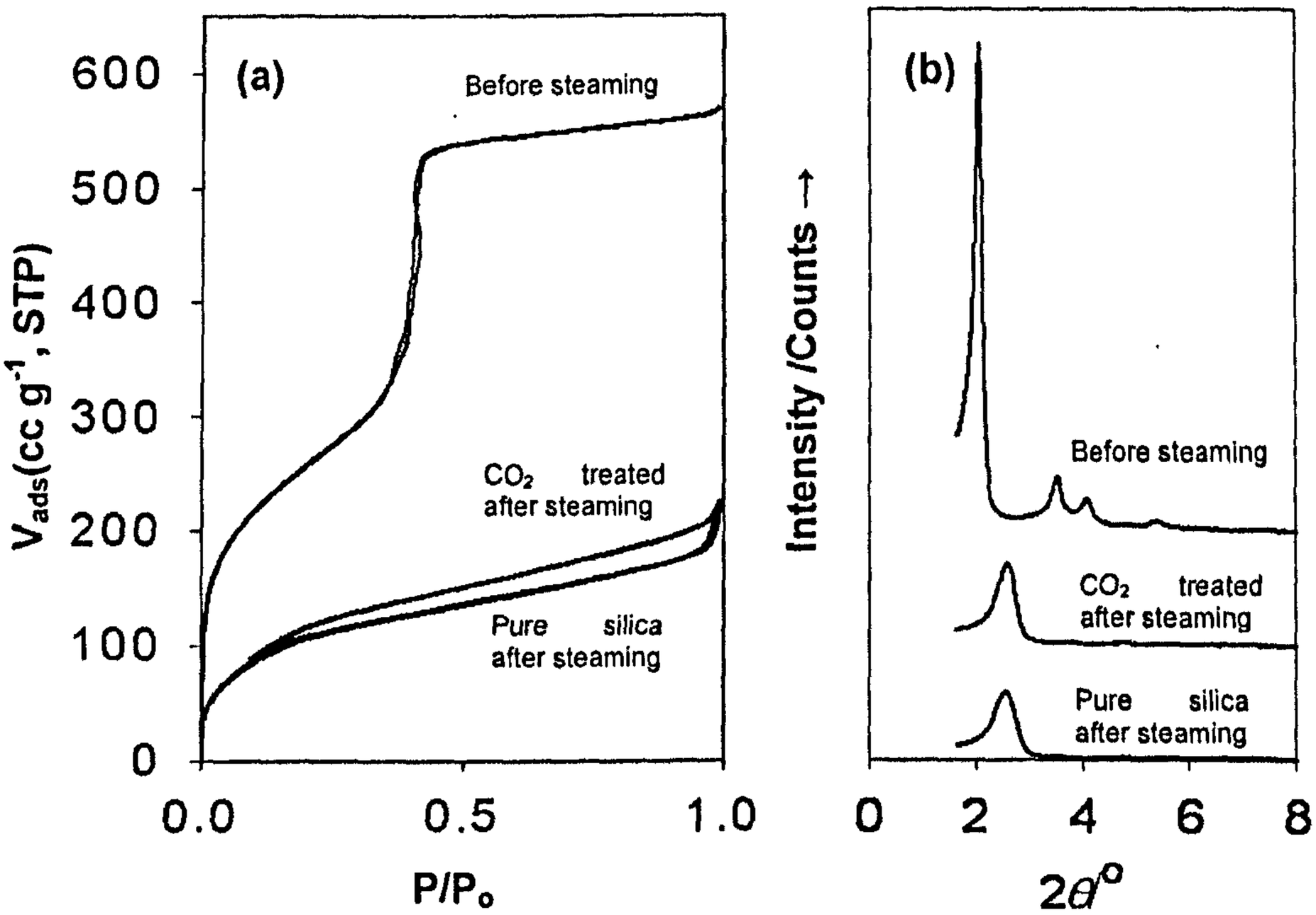


Figure 5-6: Steaming silica treated with $scCO_2$ only and non treated silica appears to produce nearly identical products.

Table 5-2: Data on steaming of pure silica and silica treated with only $scCO_2$.

Status	d_{100} (Å)	S_{BET} (m^2g^{-1})	Pore vol (ccg^{-1})
Pure silica	42.1	958	0.97
CO_2 treated, after steaming	36.1	44	0.11
Pure silica, after steaming	36.4	69	0.12

Table 1-1 shows us that damage to the silica without treatment, or with supercritical fluid but no Al source, is enough to virtually destroy the structure.

Supercritical CO_2 and Propane Impregnation

The initial examination of alumination shows the effect of supercritical propane and CO_2 on the impregnation process. ^{27}Al MAS NMR was used to analyse tetrahedrally coordinated aluminium. This showed that 40 % of the aluminium in the initial sample was tetrahedral and this was converted to at least 60 % on calcination. Measurements of acidity (*ca.* 0.75 mmol H^+/g) were consistent with this proportion of tetrahedrally coordinated Al.

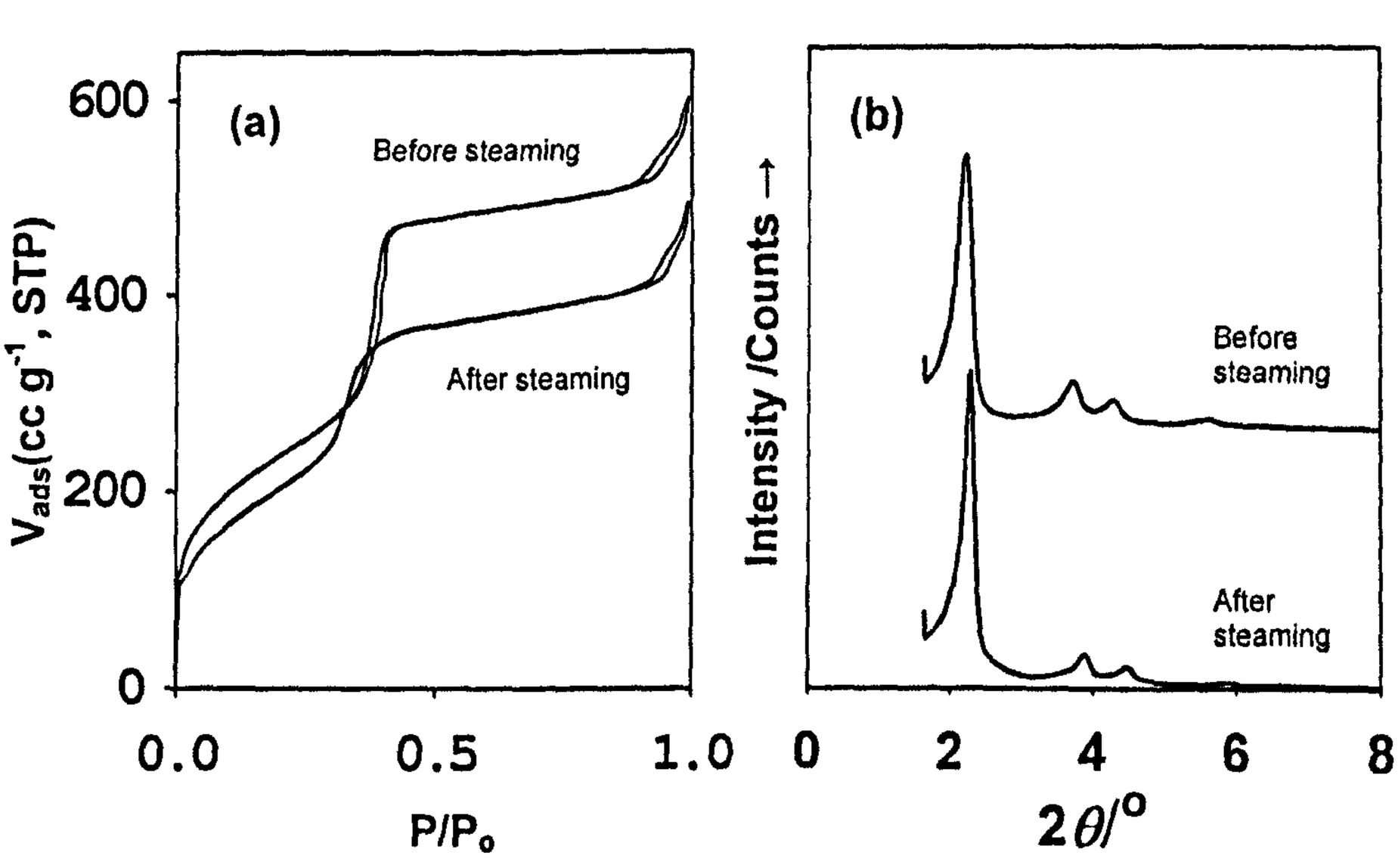


Figure 5-7: Nitrogen adsorption trace (a) and PXD pattern (b) for silica samples treated in supercritical CO_2 at 40 °C and 150 bar for 19 hours before and after the 900 °C steaming process.

Figure 5-7a shows the nitrogen sorption isotherms of the sample treated in CO_2. It can be seen that the sample retains much of its surface area after the high temperature steaming process. This shows that the materials exhibit very high steam stability as both the parent and the steamed samples give a sharp mesopore filling step characteristic of well-ordered MCM-41 materials. The sample itself retains 86 % of its surface area and so provides a highly positive result for the supercritical impregnation process. An overview of the post steaming data is given in Table 5-3. The PXD data is given in Figure 5-7b. This shows that the structure contracts slightly on steaming. However it remains highly ordered. These samples were prepared out with a Si/Al ratio of 10. On steaming some of the aluminium was lost from the sample, however at least 80 % remained. The level of stability for these samples with this degree of alumination is unprecedented.

Table 5-3: Data showing the effect of steaming on the $scCO_2$ treated sample.

Status	d_{100} (Å)	S_{BET} (m^2g^{-1})	Pore vol (ccg^{-1})
After grafting	39.8	864	0.91
After steaming	38.7	744	0.74
After boiling	41.0	771	0.80

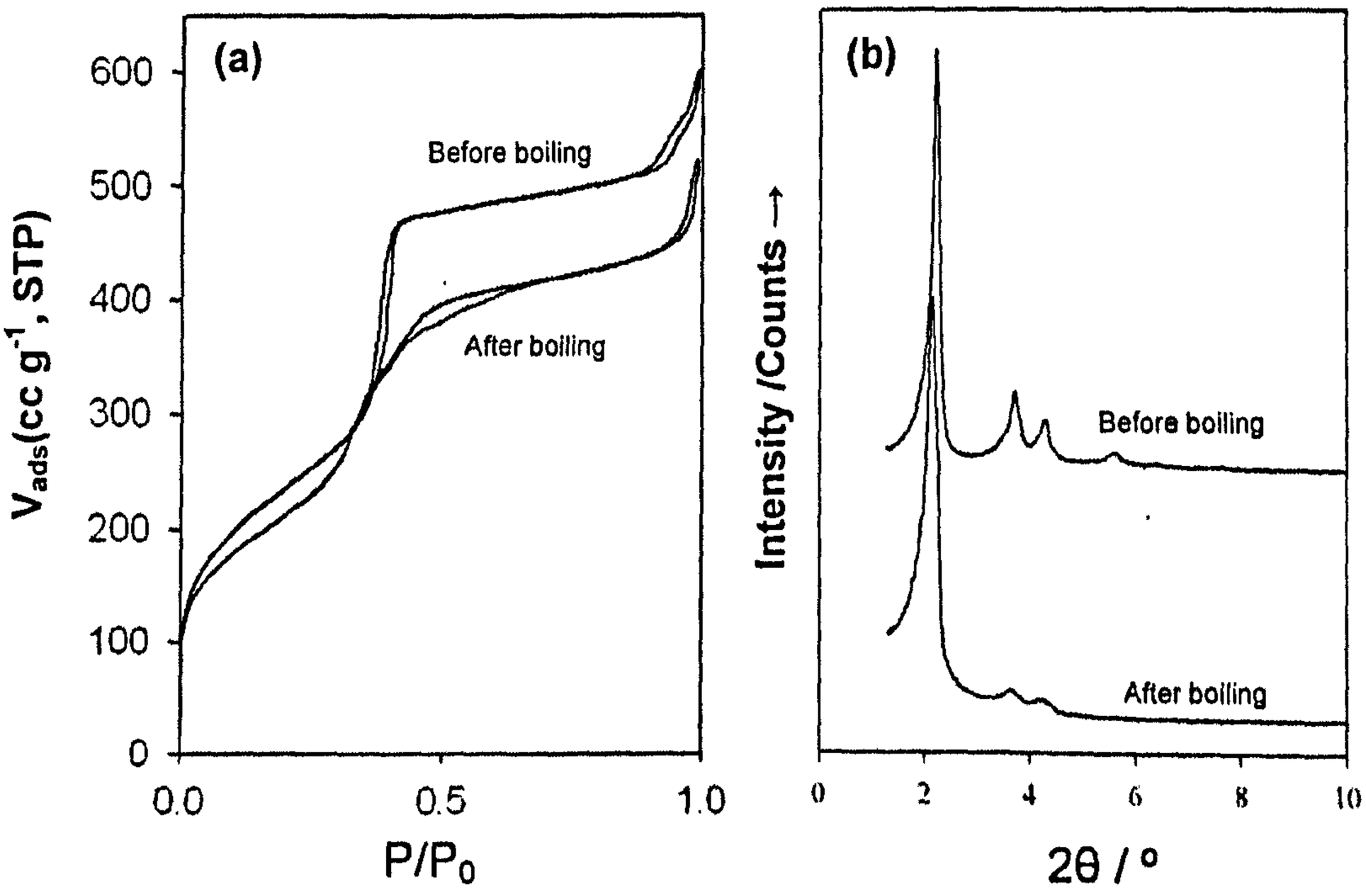


Figure 5-8: Data on the silica material treated under $scCO_2$ for 19 hours before and after boiling.

Investigation of the boiling of the sample showed a drop of 14 and 12 % in surface area and pore volume, respectively. This shows less damage to the structure than the high temperature steaming. However, the PXD pattern indicates a severe disruption of the mesostructure. This is common for similar aluminated samples prepared by conventional means and indicates that the silica is being mechanically broken up by the water, so that one long mesoporous tube might produce several smaller ones, while maintaining its surface area. The high retention of this surface area suggests that the silica is well covered and few silanol groups or siloxane bonds are free to react with the water.

Data on the sample using supercritical propane as a solvent were very similar to those of the carbon dioxide. The nitrogen adsorption data is given in Figure 5-9a.

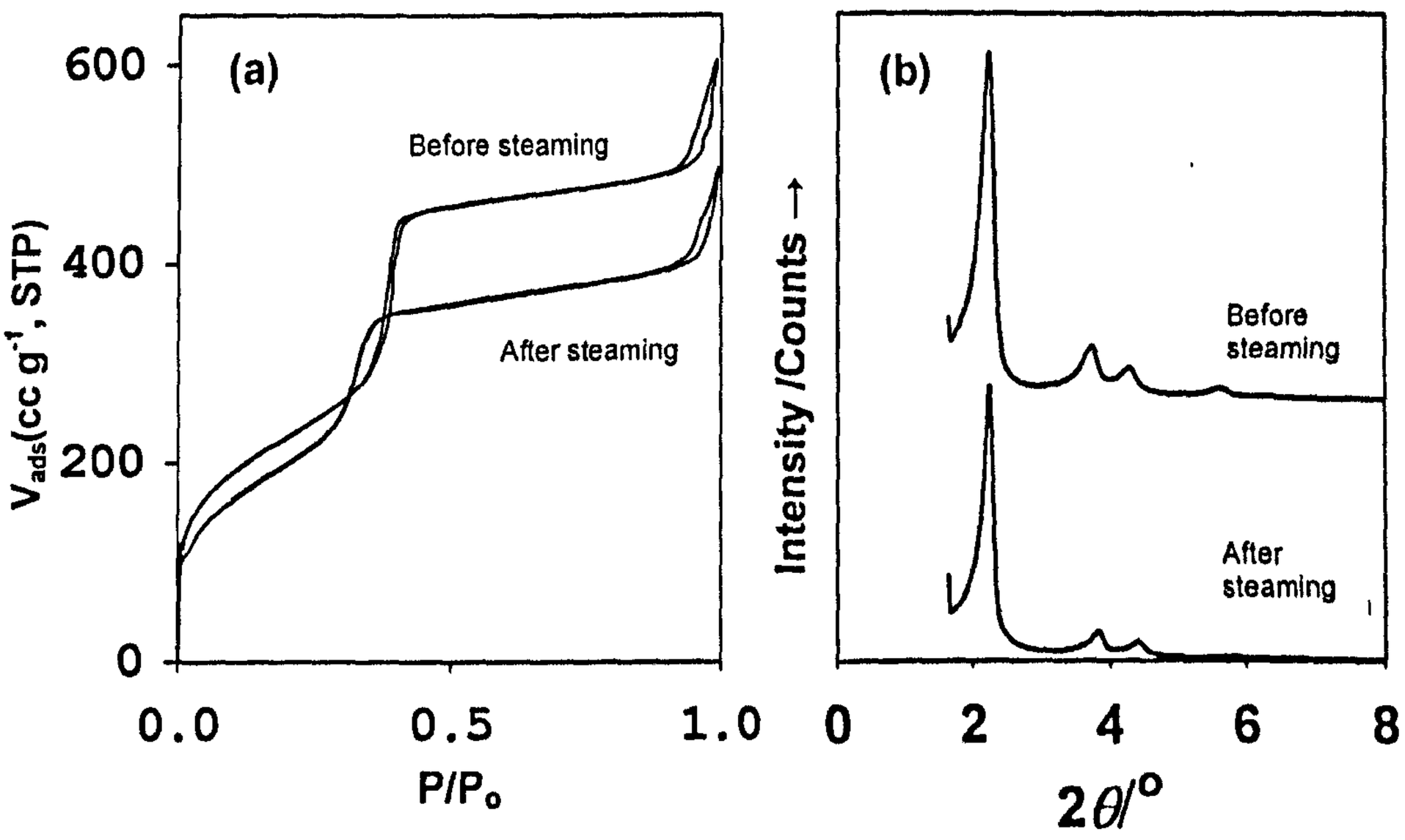


Figure 5-9: Nitrogen adsorption (a) and PXD patterns (b) of the silica sample impregnated using supercritical propane 110 °C and 150 bar for 19 hours.

Here we have a very similar adsorption to that of CO_2 where the material is retaining a highly ordered structure after the steaming process. Quantitative data for this stability is given in Table 5-4. This shows retention of 87 % of the original surface area and 79 % of the original pore volume after the steaming process. PXD data support this and is given in Figure 5-9b.

Table 5-4: Use of scPropane is very similar to $scCO_2$ in terms of hydrothermal stability.

Status	d_{100} (Å)	S_{BET} (m^2g^{-1})	Pore vol (ccg^{-1})
After grafting	39.6	833	0.92
After steaming	39.4	729	0.73
After boiling	39.3	762	0.77

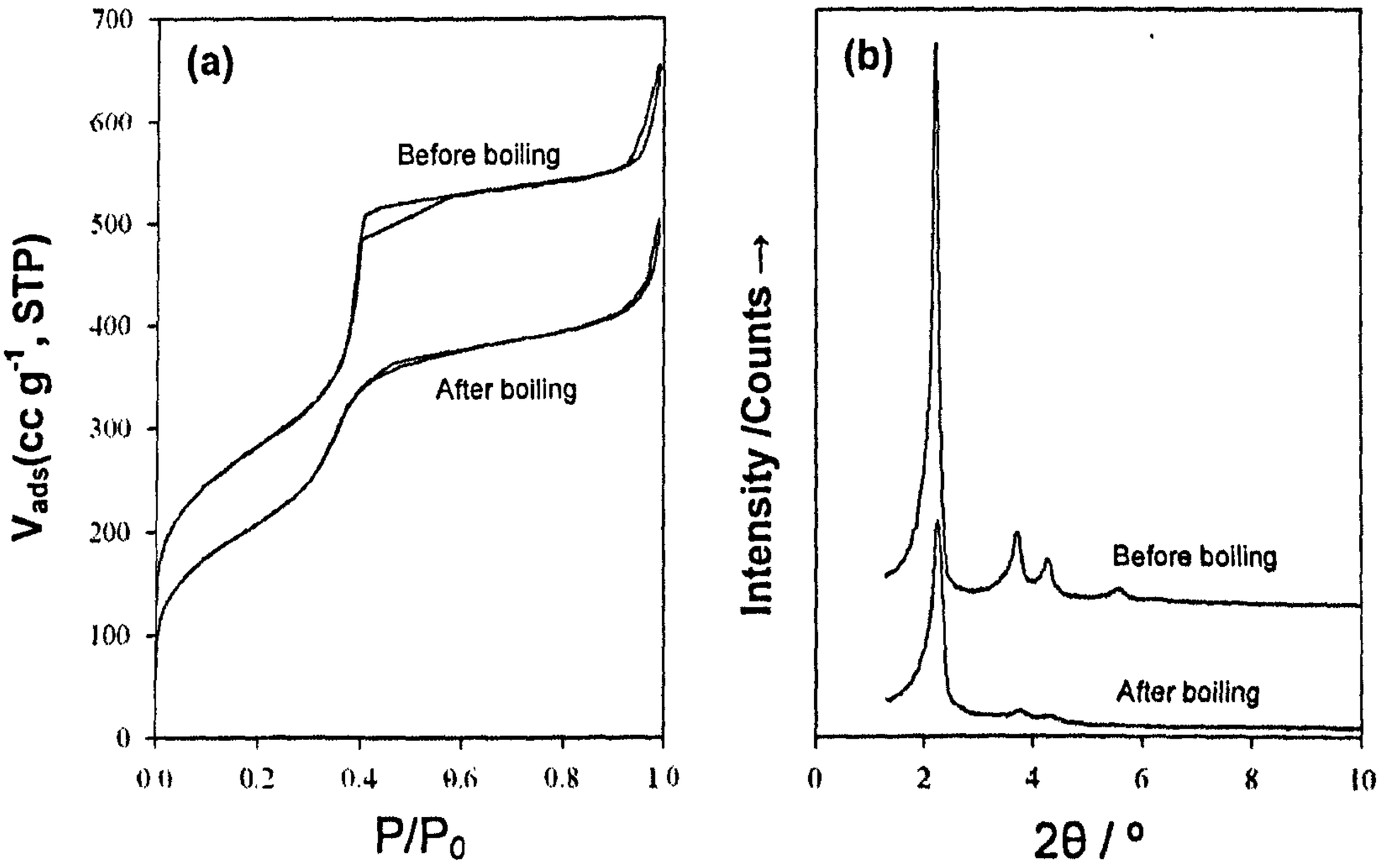


Figure 5-10: Boiling data for the silica sample treated under scPropane.

Boiling data is again similar to the $scCO_2$ sample with losses in surface area of 9 % and pore volume of 16 %. The dissruption of the PXD pattern is again present, indicating a physical breakup of the structure without a severe loss of porosity.

Materials with this level of hydrothermal stability have currently only been reported at levels of Si/Al of about 40.[298] That work, used grafting with a hexane solvent, however, stability dropped when at lower Si/Al ratios. Therefore a uniquely

aluminated and stable structure at high temperatures is created. The reflux stability of the samples remains similar to those prepared by other techniques, however.

Liquid Propane Impregnation

In the experiments, there was the option of directly comparing supercritical and liquid propane to see if the process was influenced by the phase of the solvent. An experiment was therefore performed in liquid propane at 40 °C and 150 bar over 19 hours. After steaming at 900 °C a significant reduction in surface area was observed for the sample treated in liquid propane, see Figure 5-11a. Here an extreme reduction in the mesoporous filling step of the nitrogen adsorption is seen, indicating a large loss of the structural order. This is supported by the PXD data, Figure 5-11b.

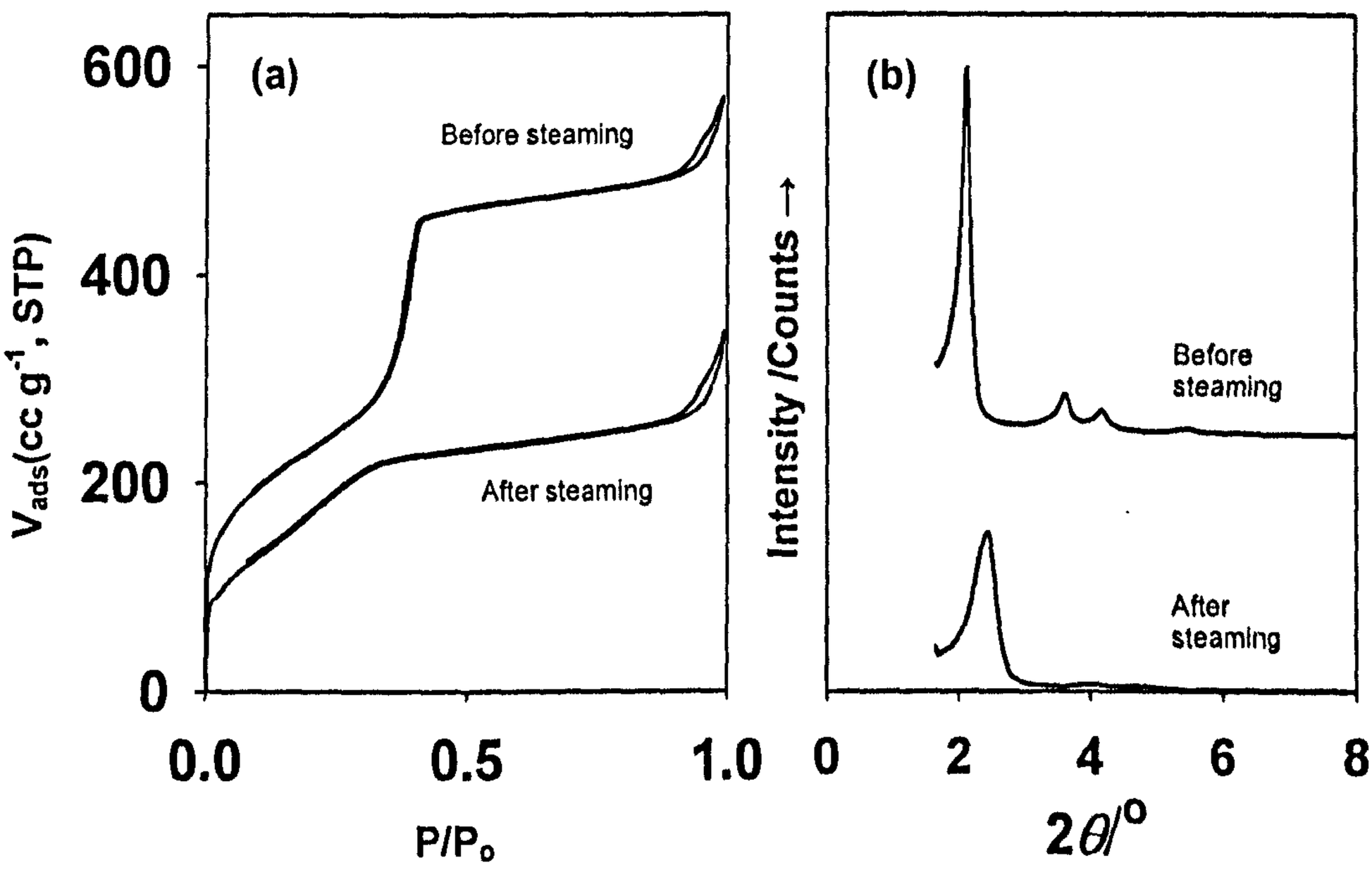


Figure 5-11: The nitrogen adsorption diagram (a) and PXD pattern (b) shows loss of the sharp mesoporous filling phase for the sample treated with liquid propane at 40 °C and 150 bar for 19 hours. This sample exhibits behaviour similar to one treated with hexane as solvent.

The data show the reductuion of the surface area to approximately 76 % and the pore volume to 57 % of the original values. This compares to a reduction to 78 % and 53 % respectively in the examination of grafting using hexane.[298] It was noticed that the pore volume is similar to that of silicas which has been grafted under supercritical conditions. This suggests that a similar quantity of aluminium is entering both samples. The much greater drop in pore volume on steaming and loss of mesostructure indicate a hydrothermally less stable sample. This is potentially an indicator that there is also an incomplete coverage in the sample as we might expect that high incorporation at the surface gives the decrease in pore volume before steaming while uncovered silica in the centre gives the reduction in structural strength. Alternatively the supercritical nature of the previous solvents may be offering some intrinsic benefit to the grafting process.

Table 5-5: Data on the damage of hydrothermal treatment of the liquid propane impregnated sample.

Status	d_{100} (Å)	S_{BET} (m^2g^{-1})	Pore vol (ccg^{-1})
After grafting	42.0	846	0.88
After steaming	36.6	643	0.51
After boiling	40.6	753	0.68

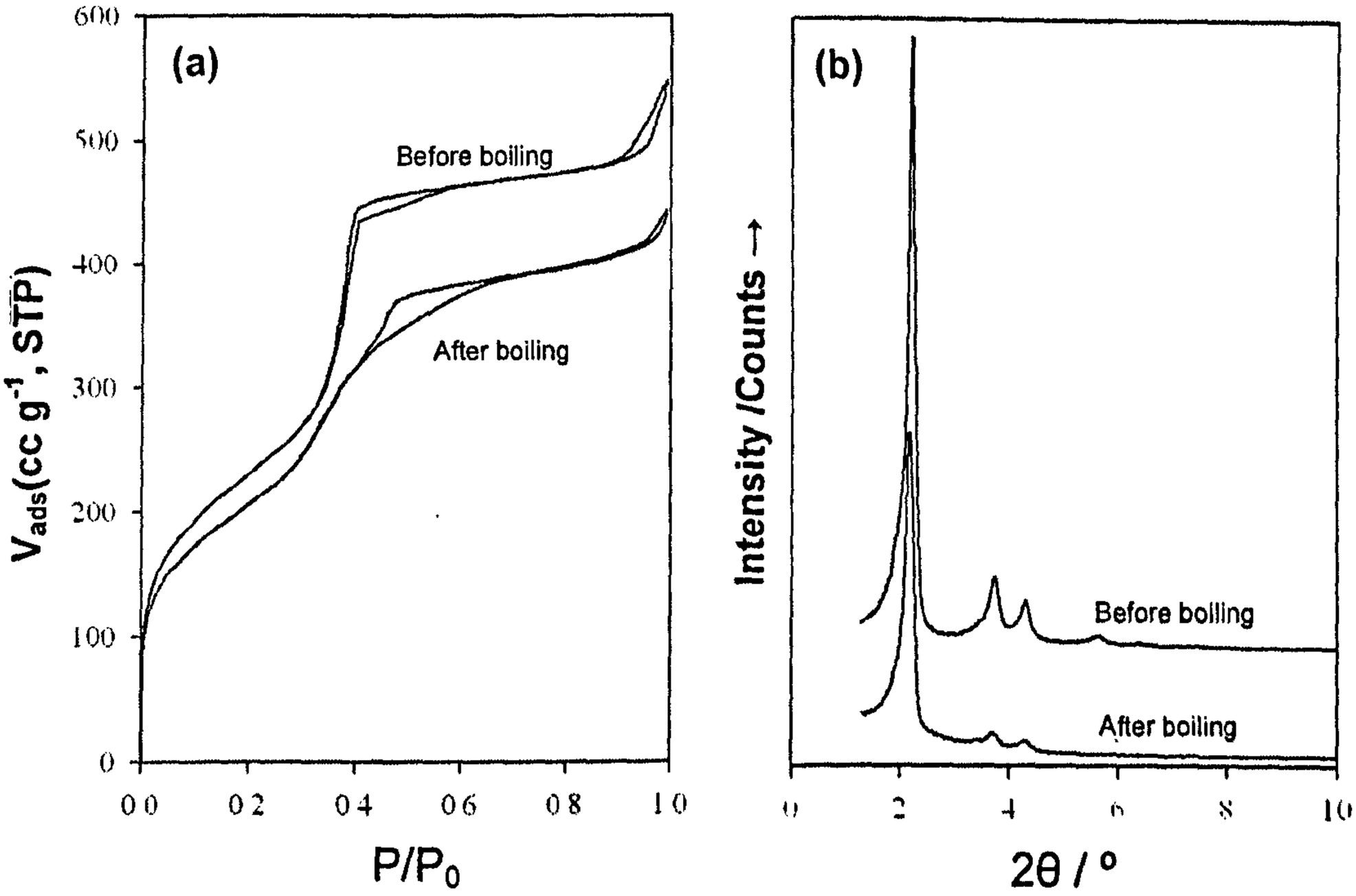


Figure 5-12: Data showing the effect of boiling on the sample which had been treated under liquid propane.

Again, the boiled samples were less stable than the supercritically impregnated samples with a reduction of 11 and 23 % for surface and pore volume. The reduction in structural ordering is again shown in the PXD pattern. The reduction in pore volume indicates a poorer coverage than in the above examples which is consistent with the steaming data.

Effect of Impregnation Time

An experiment was carried out to observe the effect of time on the impregnation. The experiments were carried out over 3 hours rather than the 19 hours used in the previous experiments. This was to observe whether the 19 hour impregnation time was necessary to achieve the highly stable samples. Nitrogen adsorption data for the steaming are given in Figure 5-13a.

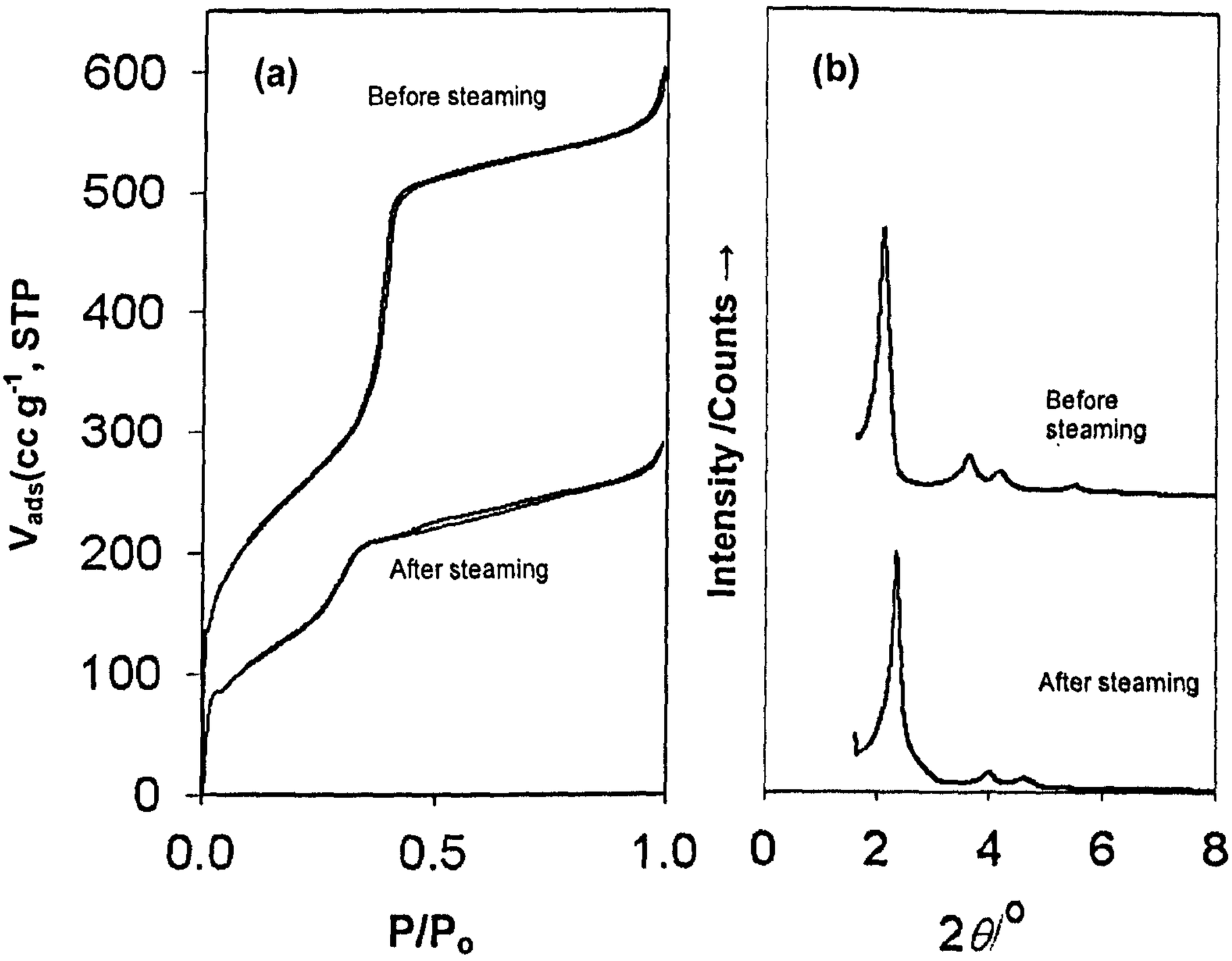


Figure 5-13: Nitrogen adsorption (a) and PXD (b) data of a silica sample treated with supercritical CO_2 at 40 °C and 150 bar but only for 3 hours.

The data for the 3 hour experiments shows significantly lower stability than the 19 hour equivalent result. Quantitative data are given in Table 5-6. Here we see an initial surface area and pore volume higher than the previous examples. This suggests that less aluminium has been incorporated which is reasonable considering that there has been less time for the molecules to enter the structure. This lower concentration is then coupled with a significant loss of ordering on steaming as shown by both data sources, Figure 5-13. A loss of 20 % surface and 33 % pore volume is accompanied by a loss of some structural ordering. The sample is, however, superior to that formed in liquid propane and, as we saw in the control experiment, greatly superior to that of pure silica, Figure 5-6. We can therefore conclude that a time period longer than 3 hours is required to achieve the maximum strengthening benefit, although a great deal of structural advantage is afforded in the shorter time.

Table 5-6: Analysis of data for the 3 hour impregnation with $scCO_2$ solvent.

Status	d_{100} (Å)	S_{BET} (m^2g^{-1})	Pore vol (ccg^{-1})
After grafting	41.8	921	0.90
After steaming	37.6	743	0.60
After boiling	41.3	545	0.59

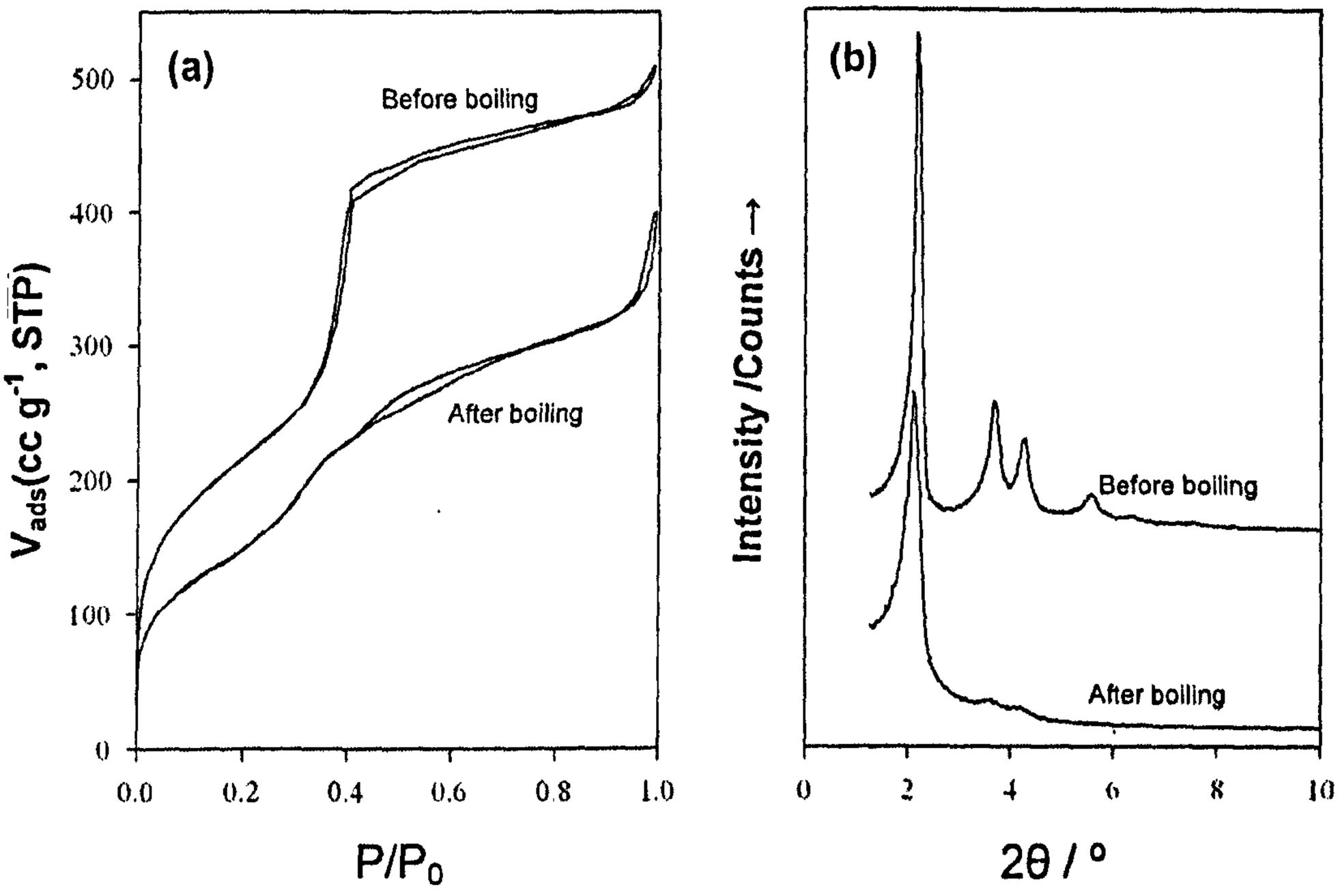


Figure 5-14: Boiling data for the sample treated in $scCO_2$ for only 3 hours shows a great deal of damage to the silica structure.

Boiling data for the 3 hour sample is significantly different from the other samples as this is the only sample where the effect of boiling is more damaging than of steaming. The surface area is reduced to 59 % of its original value and the pore volume to 65 %. The loss of structural ordering seems to be as severe as for the other samples. This loss of surface area and porosity is likely to be because silanol groups and siloxane bonds are being left unprotected as the aluminium is not given enough time to adequately penetrate and cover the sample. This is similar to the sample prepared in liquid propane although there is an increased amount of damage in this case.

Increased Aluminium Content

Another source of interest was the potential maximum loading of aluminium onto the silica structure. This was investigated by an attempt to double the quantity of aluminium available for impregnation. This is of particular interest as, already, the materials produced are of very high stability. As mentioned earlier, in all mesoporous silicas the availability of aluminium groups is inferior to zeolites. It was hoped that this impregnation technique might allow production of even more heavily laden aluminosilicates than previously possible. To this end a sample containing twice the aluminium isopropoxide was impregnated in CO_2 over 19 hours at 40 °C and 150 bar. This will provide an Si:Al ratio of 5 if all aluminium is incorporated. The nitrogen adsorption and PXD data for this are given in Figure 5-15.

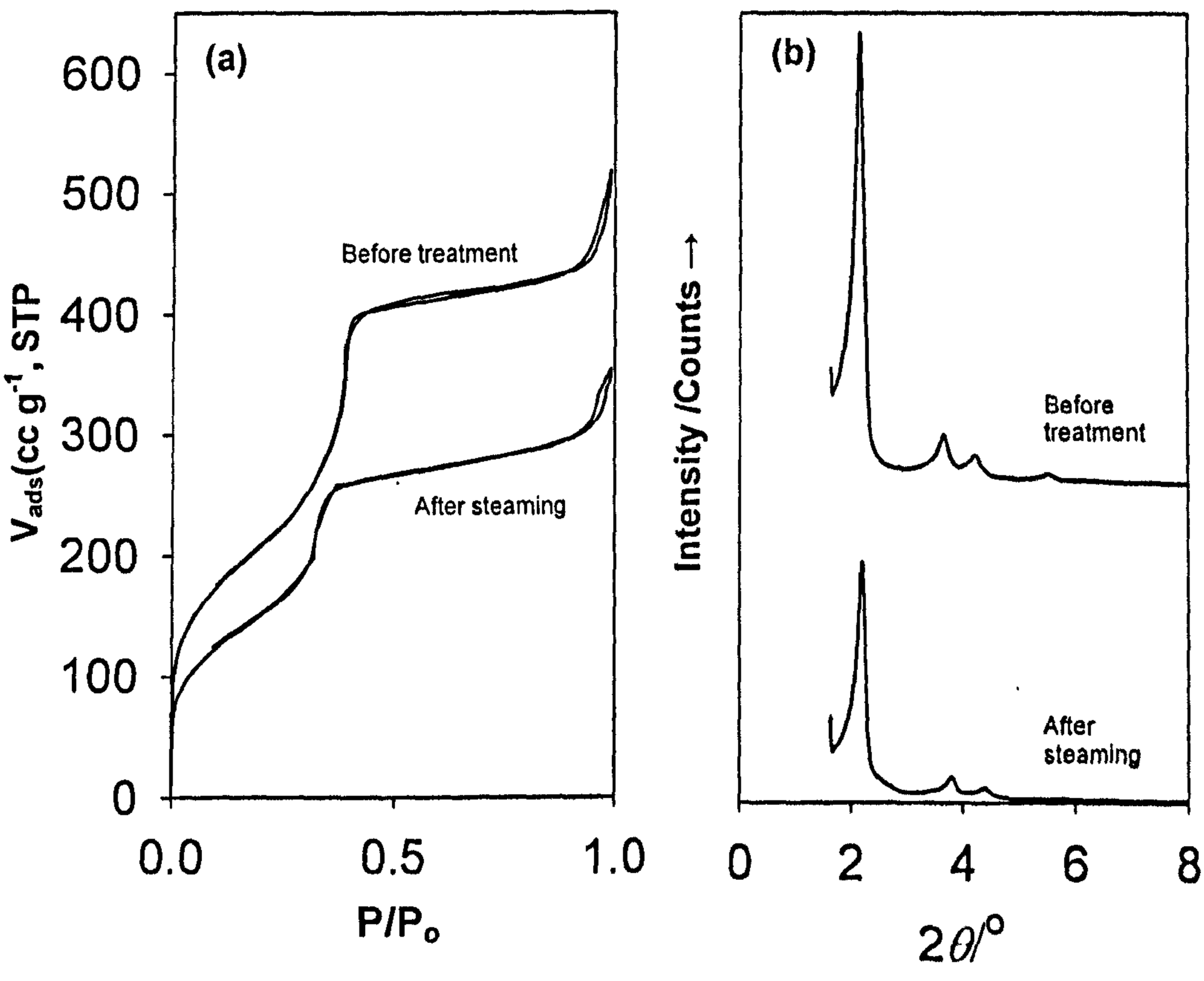


Figure 5-15: Nitrogen adsorption (a) and PXD (b) data for high aluminium experiment, carried out in $scCO_2$ at 40 °C and 150 bar for 19 hours.

The results show a much lower initial surface area and pore volume. This indicates that there is more aluminium deposited on the surface. This would indicate the successful creation of a higher aluminium content structure. The loss of surface area and pore volume, 27% in both cases (Table 5-7), coupled with the good retention of structural ordering shown by the PXD pattern indicate a strong, highly aluminated sample. It is interesting that the reduction of the surface area is larger than at higher Si:Al ratios but the pore volume reduction is smaller. What this might suggest is that increased dosing with aluminium is actually causing portions of the silica tube to be sealed. This would be a reasonable assumption as this would reduce the surface area available during nitrogen adsorption experiments, while X-rays, which are able to penetrate the sample, show an only slightly damaged structure. The decrease in d spacing of the silica is actually less than that observed for the initial $scCO_2$ sample, possibly indicating a slightly stronger structure. This experiment has shown the highly exciting potential of the supercritical impregnation technique, suggesting that it may be possible to generate mesoporous aluminosilicate materials of very high structural strength and aluminium loading levels.

Table 5-7: Data on the high aluminium containing species indicates a stable structure but with an unexpectedly low surface area.

Status	d_{100} (Å)	S_{BET} (m^2g^{-1})	Pore vol (ccg^{-1})
After grafting	41.3	759	0.75
After steaming	40.4	556	0.55
After boiling	40.3	742	0.70

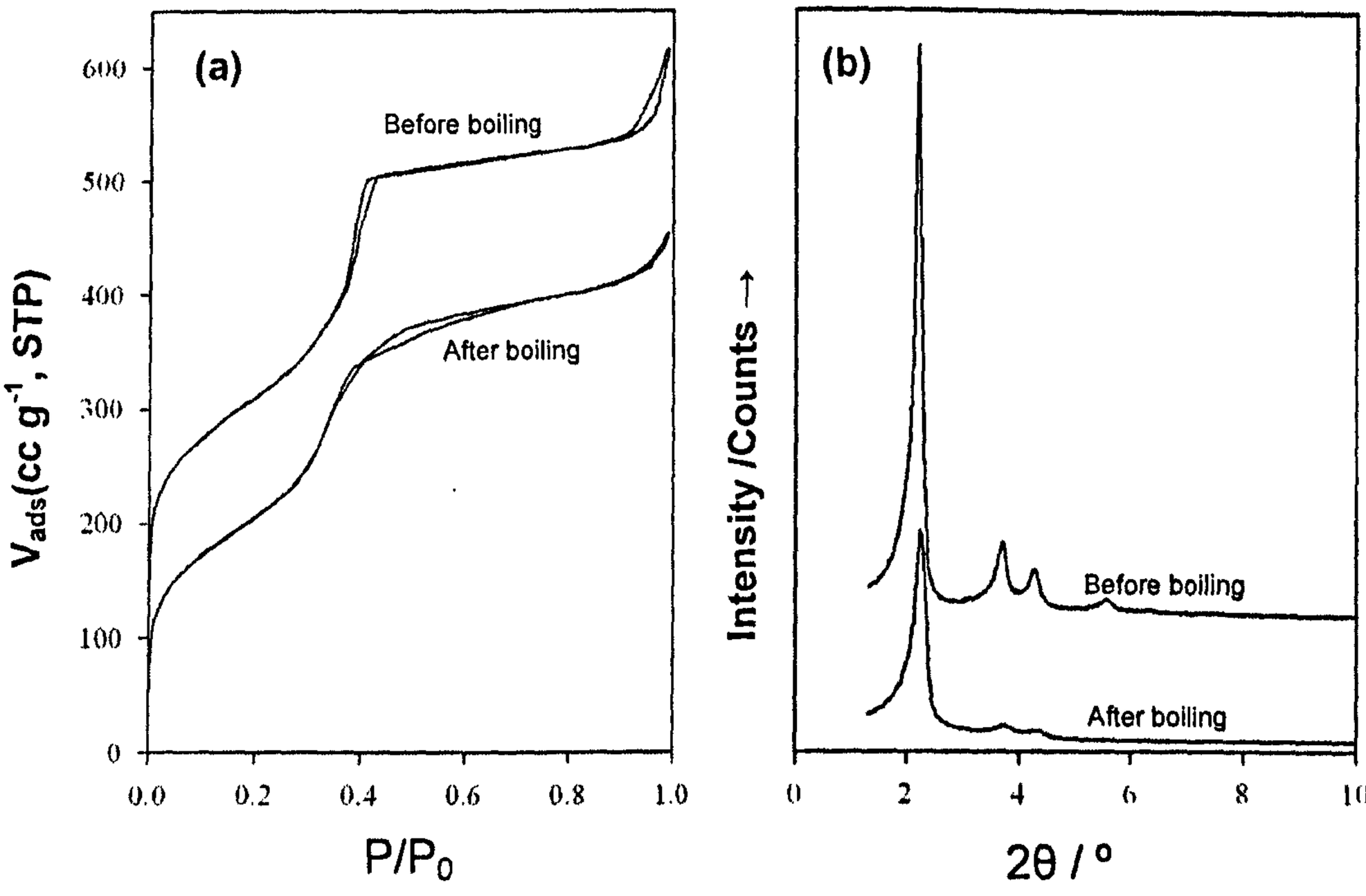


Figure 5-16: Boiling data for the Si/Al = 5 sample treated under $scCO_2$ for 19 hours.

Data on boiling of the high aluminium content sample showed that this was the most resistant to surface area and pore volume change. The surface decreased by only 2 % and the pore volume by only 7 %. This is interesting as the PXD pattern again shows a significant loss of structural ordering after refluxing. It seems likely in this case that the increased aluminium is forming a thicker protective layer than in the other cases and so is able to protect the silica framework more effectively from hydrolysis.

Repeated Steaming

An experiment was setup to observe the effects of repeated steaming on the stability of treated silica. This is important for any future use as a cracking catalyst as repeated exposure to harsh conditions will be unavoidable. The chosen silica had been treated with aluminium isopropoxide and $scCO_2$ for 19 hours at 40 °C and 150 bar. The sample was then steamed at 750 °C for 4 hours and then analysed. The

remaining sample was then subjected to steaming at 900 °C for a further 4 hours. The results of these experiments are given in Figure 5-17.

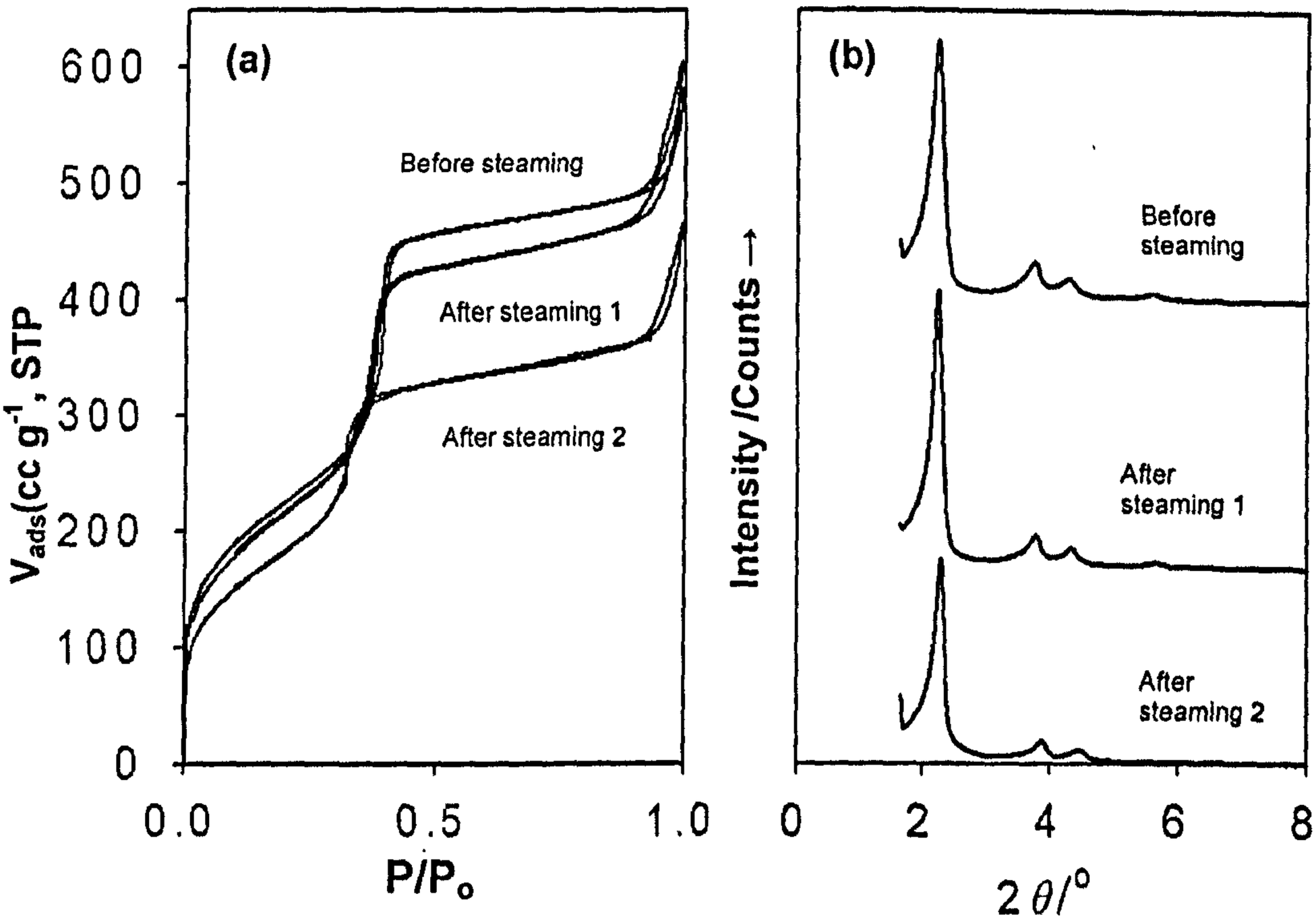


Figure 5-17: Data from the scPropane experiment shows the initial sample then after steaming for 4 hours at 750 °C then steamed for a second time at 900 °C for 4 hours.

The results we observe from subjecting the samples to repeated steaming are encouraging. The initial steaming, which is carried out at a lower temperature than previous experiments, shows milder effects than that of those examined after steaming at 900 °C. Only a relatively small loss of surface area and pore volume is observed which correspond to retention of 95 % of original structure in both cases, Table 5-8. When the sample is re-treated with 900 °C steaming; the parameters drop but by a more pronounced amount. The reductions equate to drops to 81% and 58% of original values for surface area and pore volume. The d-spacing remains roughly constant and PXD patterns indicate the retention of much of the structure. This represents the beginning of a large number of potential experiments to characterise the relative stability of the new aluminosilicate. Initial results are very positive regarding repeat usage of the catalyst, particularly at lower temperatures.

Table 5-8: Data on the repeat steaming of a sample treated with aluminium isopropoxide under $scCO_2$.

Status	d_{100} (Å)	S_{BET} (m^2g^{-1})	Pore vol (ccg^{-1})
After grafting	39.2	833	0.92
After steaming 1	39.8	794	0.87
After steaming 2	39.1	675	0.53

Alternative Sources of Aluminium

Finally, experiments were also carried out to observe the effect of the aluminium source on the impregnation and silica stability. Experiments were carried out under identical conditions to the first sample prepared in $scCO_2$, but using aluminium chloride and aluminium lactate in the quantities needed to achieve a Si:Al ratio of 10. These experiments were carried out at 40 °C, 150 bar and over 19 hours. Nitrogen adsorption and PXD data are given in Figure 5-18 for aluminium chloride and Figure 5-19 for aluminium lactate.

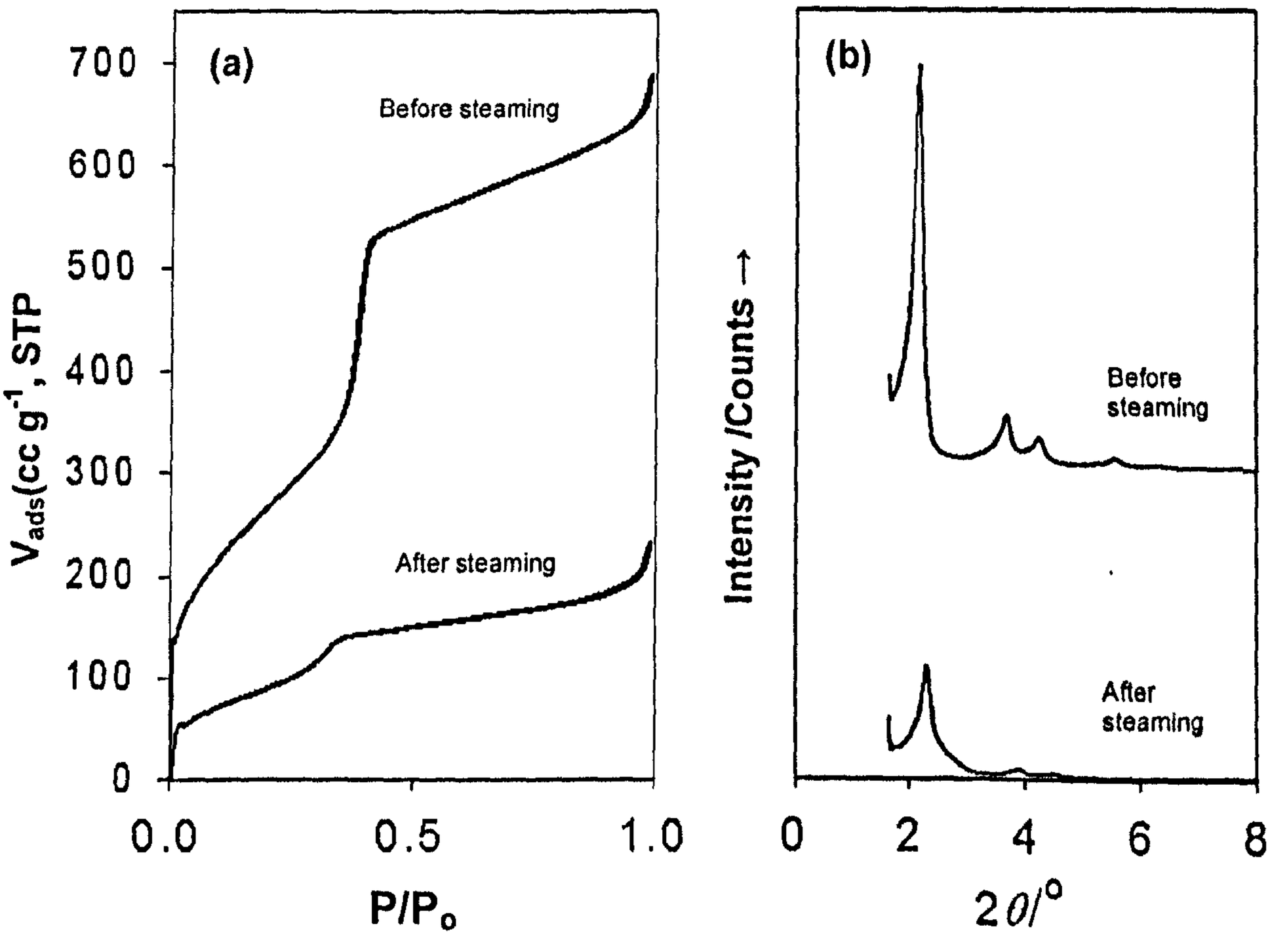


Figure 5-18: Aluminium chloride can be seen to be a much poorer molecule for delivery of aluminium.

It is clear form Figure 5-18 that the aluminium source plays a key role in the efficiency of aluminium incorporation. This is supported by Table 5-9 which shows that the initial pore volume and surface area are substantially higher than with original aluminium isopropoxide experiments. This indicates a low quantity of aluminium inside the silica structure. This is supported by the similarity between this sample and the pure silica sample after steaming. An improvement in stability is observed over the pure silica example, although this is vastly inferior to that of the aluminium isopropoxide sample. Analysis of data given in Table 5-9 shows a drop to 33 % initial surface area and 30 % initial pore volume on steaming, indicating severe damage to the structure.

Table 5-9: Data on the effect of steaming on a sample treated with aluminium chloride.

Status	d_{100} (Å)	S_{BET} (m^2g^{-1})	Pore vol (ccg^{-1})
After grafting	41.3	993	1.05
After steaming	38.7	332	0.32

The final experiment carried out in this section involves the use of aluminium lactate. This provided a new aluminium source but unfortunately proved again to be less successful than the isopropoxide experiments. Data is shown in Figure 5-19.

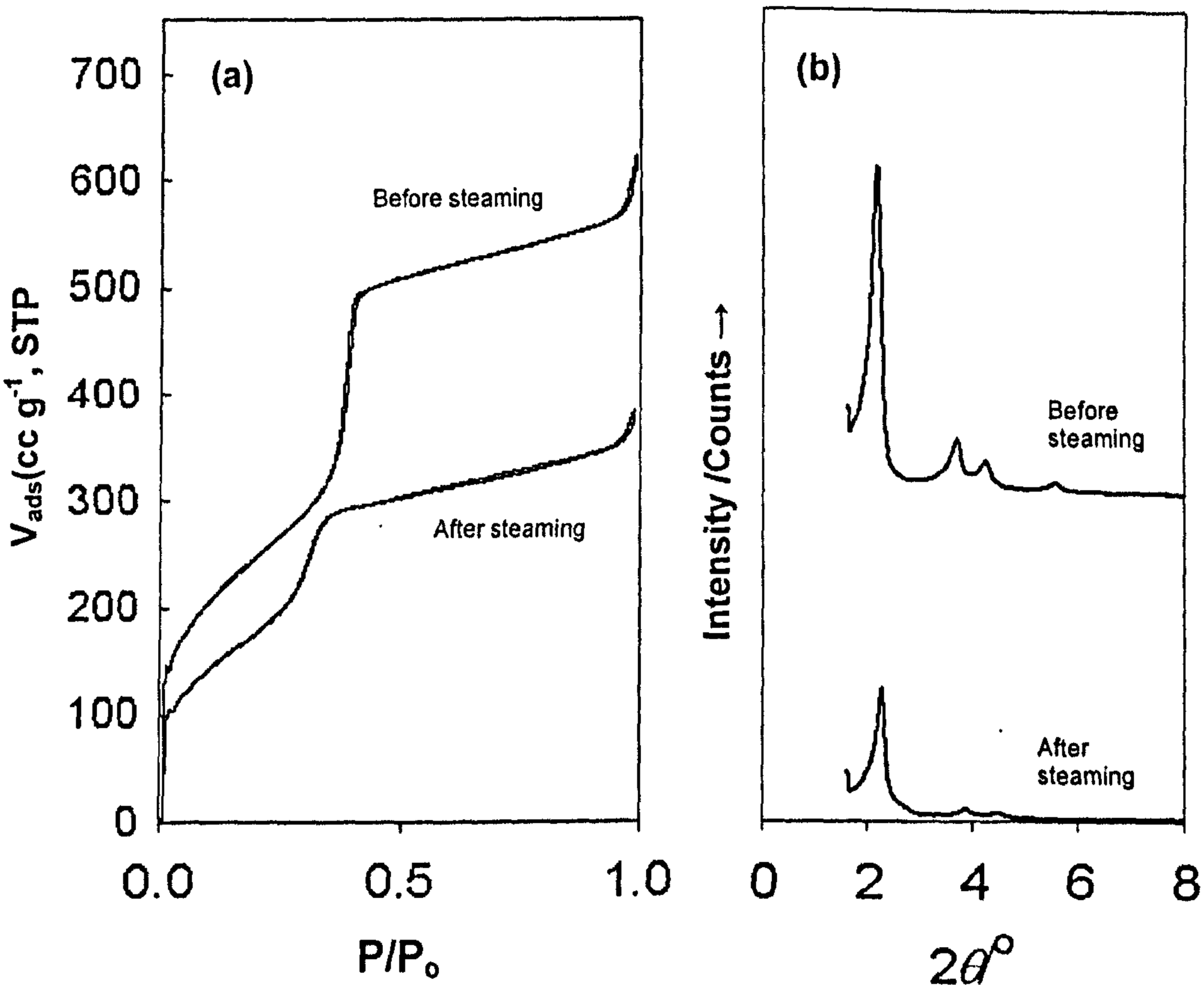


Figure 5-19: As with aluminium chloride, aluminium lactate produces silica with a lower stability than that impregnated with aluminium isopropoxide.

The aluminium lactate experiment was similar to the aluminium chloride result although was superior with a surface area reduction to only 72 % and pore volume to 62 % on steaming, Table 5-10. The initial surface area and pore volume is lower than in the aluminium chloride experiment. This indicates a larger quantity of aluminium being adsorbed during the grafting process. This is supported by the increased stability afforded to the structure, although this is still weaker than the aluminium isopropoxide. This effect will be discussed later.

Table 5-10: Data on the effect of steaming on a silica sample treated with *aluminium lactate*.

Status	d_{100} (Å)	S_{BET} (m^2g^{-1})	Pore vol (ccg^{-1})
After grafting	40.7	914	0.94
After steaming	38.9	654	0.58

Discussion

Three possible factors to explain the advantageous behaviour of the SCF on the hydrothermal stability of the materials are suggested. (1) the mass transport properties of the fluid as described in the Introduction are superior to those of a liquid even though the ability to dissolve material is reduced. This is one suggestion to explain the improved coverage of the silica, that the fluid is simply able to carry the aluminium further into the silica before it is deposited on the surface. (2) the fluid is certainly a weaker solvent for the aluminium source and it is believed that the aluminium will more effectively partition itself into the silica in a greater concentration than in the liquid. (3) the relative weakness of the solvent will mean fewer interactions with the silica itself and this is believed to be a very important factor in depositing the aluminium onto the surface of the silica rather than allowing the aluminium to enter into the structure. This is important in determining hydrothermal stability[298] as aluminium which is evenly distributed on the surface of the silica will act to protect the silanol groups and silioxane bonds from hydrolysis.[295] This method of depositing aluminium onto the surface probably exists as the SCF is too weakly interacting to cause any hydrolysis of the silica itself. This has the effect that, when aluminium is lost from the sample on calcination, the aluminium is removed from surface sites rather than from deeper in the structure and so damage to the core silica structure is minimised. This type of damage is particularly evident when samples have been prepared under aqueous conditions.[299] These samples exhibit low stability under steam. Boiling data has shown that the silica is effectively protected from hydrolysis by the aluminium, although this is not substantially different from other samples prepared using liquid solvent.

One explanation for the phenomenon observed when aluminium sources is changed is related to the solubilities of these compounds in CO_2. The model for the impregnation experiments involves dissolution, transport and deposition. If any of these factors are restricted then our system is weakened. We would expect that, since the solvent remains constant, transport should remain unchanged. The variable factors are therefore the dissolution and the deposition. We know that aluminium isopropoxide is sparingly soluble in $scCO_2$. This information is only derived,

however, from polymerisation studies which use aluminium isopropoxide as a catalyst.[300] Information indicating that $AlCl_3$ is soluble comes from Friedel Crafts reactions performed in $scCO_2$, with $AlCl_3$ as catalyst. [301,302] Reference to the use of aluminium lactate in SCFs is yet to be found. Also, no specific solubility data has been found for this or the other aluminium containing compounds. If the fact that aluminium isopropoxide grafts simply and effectively to the silica is examined, it can be concluded that the process of solubility and deposition are working well (although not necessarily optimally). Although no data is available at present on relative solubilities of the three aluminium sources, it can be stated that the solubility of $AlCl_3$ and aluminium lactate are either higher or lower than that of aluminium isopropoxide. This leads to poorer stability either by low solubility resulting in low quantities being moved or high solubility leading to retention of aluminium in the fluid. This is supported by the fact that, regardless of the solubility, we might well expect the solubility of aluminium isopropoxide to be closer to that of aluminium lactate than to $AlCl_3$ and this is indeed the case as the data shows the lactate system to be stronger and, therefore, closer the isopropoxide system than samples with $AlCl_3$. This requires further study to fully understand the effect solubility has on the impregnation. It does suggest, however, that an investigation of varied pressure, which is linked closely to solvating power, would be highly interesting in determining optimal conditions for a specific aluminium source.

Some progress has also been made towards understanding the system. While experiments already produce materials with a combination of alumination level and high temperature stability not seen before, the refluxing stability remains comparable to existing systems.[298] We have shown that much of the high temperature stability of the structure is retained when the impregnation time is reduced. This severely decreases the reflux stability, however, indicating that a complete cover of the sample had not been achieved. It has been shown that the aluminium content can be extend to even achieve higher loading levels (Si:Al = 5) while still retaining stability. This in itself could have potentially major implications as increasing aluminium content while retaining stability is of vital importance in generating solid acid catalysts. This sample also proved to be the most resistant to refluxing conditions. Further study should reveal how high loading can be achieved while retaining a working catalyst. In examining the long term stability of the silica species we also

determined that they remain relatively stable to a modest number of repeat steaming experiments. Many more experiments will be required, however, before the data are useful in an industrial context. The initial investigation is, however, very promising.

Conclusion

This work has shown the possibility of using supercritical fluids to impregnate mesoporous silica in a manner which produces solid acid catalysts with a high hydrothermal stability. Catalysts produced have been of an exceptionally high acidity for these types of materials while retaining most of its original ordering. It has been shown that this process is heavily influenced by the fact the solvents used are supercritical rather than liquid and that aluminium source plays a key role in achieving desired loading. Initial investigation of the effect of increased loading and of repeat steaming was made and afforded positive results. This Chapter introduced mesoporous silica and was reliant on the weakly solvating power of SCFs. In the next Chapter we will look at the use of SCFs to extract the surfactant template molecules from uncalcined silica samples, using SCFs solvating powers more directly.

Chapter 6 Mesoporous Silica Extraction

This Chapter continues the description of the work on the action of supercritical fluids on mesoporous silicas. However this study is on the use of SCFs as an extraction medium. In this Chapter, mesoporous silica is discussed with a greater focus on of the removal of the surfactant template. Data collected in collaboration with The University of York on the extraction of amine template is present.

As mentioned in Chapter 5, mesoporous silica is prepared by the self-organisation of either silica sheets[266,267] or molecular silica[264,265] around a surfactant template. Once this structure is formed, the surfactant must be removed to allow access to the mesopores. This is performed routinely by calcination, where the surfactant is simply destroyed by extreme temperature.[258] This is an inefficient process, particularly if the silicas are to be made on an industrial scale, requiring large amounts of energy to heat and loss of the surfactant at the end. For these reasons, several attempts have been made to remove the surfactant template in a benign manner.[303-305] A study into the effects of conventional solvent extraction on the product silica has been made.[306]

Several extraction attempts have been made using supercritical CO_2 as the solvent medium.[307,308] These attempts have also included methods to impregnate materials with transition metal ions during this process.[291] However, the CO_2 was insufficiently polar to produce efficient extraction so in all cases a methanol or dichloromethane modifier was added to the $scCO_2$. This is a common method in SCF technology to increase the polarity and hence the ability of CO_2 to dissolve polar molecules. It does, however, risk damaging the silica in a manner similar to the use of conventional solvent extractants. This was shown to be the case recently by Kawi.[309] In all cases, complete removal of the template was not possible using these systems. However, there were encouraging data to suggest that samples treated with CO_2 maintained a higher degree of ordering than purely calcined materials, suggesting further benefits for the technique.[307] The surfactant used in the formation

of silica can take several forms, polar or non-polar, provided that the interaction between the hydrophilic group and the silica and water is sufficient to achieve ordering. These surfactants usually take the form of a quaternary ammonium ion or sometimes a primary amine group. There is concern over the extraction of amines using CO_2, however, as a reaction between the two is known to result in the formation of solid carbamic acids rapidly.[310]

Extraction of Dodecylamine: Design 1

In this study a primary amine templated silica is used. This was obtained from The University of York. The collaboration was intended initially to test a milder extraction technique on a specially made sample of silica containing organically modified groups.[284] This was designed to provide anchor points in the structure for catalyst molecules to be grafted to later. Due to the thermally unstable organic element in the silica, it was not possible to calcine the samples after synthesis. Instead, the samples were refluxed in ethanol for 18 hours to remove the template. This is believed to have caused damage to the silica, although, unlike calcinations, did allow the surfactant to be potentially recovered after refluxing. It was suggested that the use of supercritical extraction might allow a more satisfactory method for surfactant removal. To this end, experiments were devised to extract these silicas, although a set of pure, unmodified silica was analysed as a test of the theory. Propene was used as the extraction gas rather than CO_2 due to concern over the production of carbamic acid. Initial experiments were carried out in the Keystone extraction vessel, see Appendix II. This was set up as shown in Figure 6-1 with a glass tube inside it to contain the silica sample. This arrangement was very similar to that of the PCA experiments in Chapter 2. In this SFE experiment, silica was placed inside the glass tube which was then placed inside the vessel. The diameter of the glass tube was less than that of the vessel. In this way, the propene was allowed to pass through the sample but was not forced through it. It was therefore supposed that surfactant was removed in this experiment due to solubility, albeit very low, in the propene fluid. These experiments were performed before the general experimental setup shown in Appendix II was designed. The vessel itself was housed inside a GC

oven and this provided the heating for the experiments. Gas was supplied using a Pickel Pump and a Tescom back pressure regulator was used. An overview of the experiments carried out using this setup is given in Table 6-1. A silica sample (3 g) was placed inside the Keystone vessel. This was sealed and connected to the pump and back pressure regulator. The oven was set to the correct temperature which was verified by thermometer. The flow was started at the correct pressure, once the temperature was reached and continued for the allotted time. On completion, the vessel was depressurised and the sample collected. Extraction efficiency measurements were made by our collaborators in York by TGA analysis.

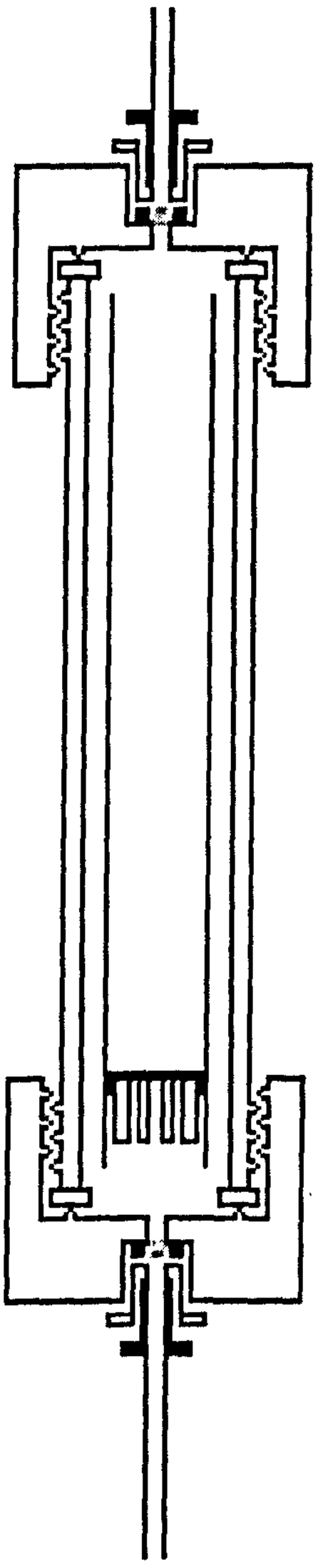


Figure 6-1: Keystone extraction vessel used for the first set of surfactant template extractions. Sample is placed inside a glass tube with a perforated Teflon stopper. This is very similar to that used on the PCA experiments of Chapter 2. As opposed to the PCA experiments only one inlet of SCF is admitted from the top of the vessel to instigate a downward flow of gas.

Table 6-1: Experimental details and extraction efficiencies of the initial set of experiments performed in the Keystone extraction vessel. Propene is used as the extractant and a constant mass of 3 g of silica is used throughout.

Expt	Temperature °C	Pressure bar	Time min	Extraction %
1	50	150	30	17.1
2	50	250	30	13.8
3	75	80	30	27.6
4	75	100	30	37.6
5	75	150	30	29.8
6	75	150	60	47.5
7	75	150	90	59.7
8	75	150	120	65.2
9	75	200	30	29.8
10	75	250	30	21.0
11	100	100	30	46.7
12	100	150	30	49.0
13	100	250	30	73.5
14	150	150	30	92.3
15	150	150	60	98.1
16	150	150	90	100.0
17	150	150	120	100.0
18	150	200	30	90.2
19	150	250	30	94.9

From these data, a picture of the important factors which are influencing the process can be developed. Firstly, if the effect of temperature on the extractions is compared, it is possible to plot a graph of change with temperature at several pressures. This is shown in Figure 6-2. Unsurprisingly, a trend of increased efficiency with increasing temperature is observed in all cases.

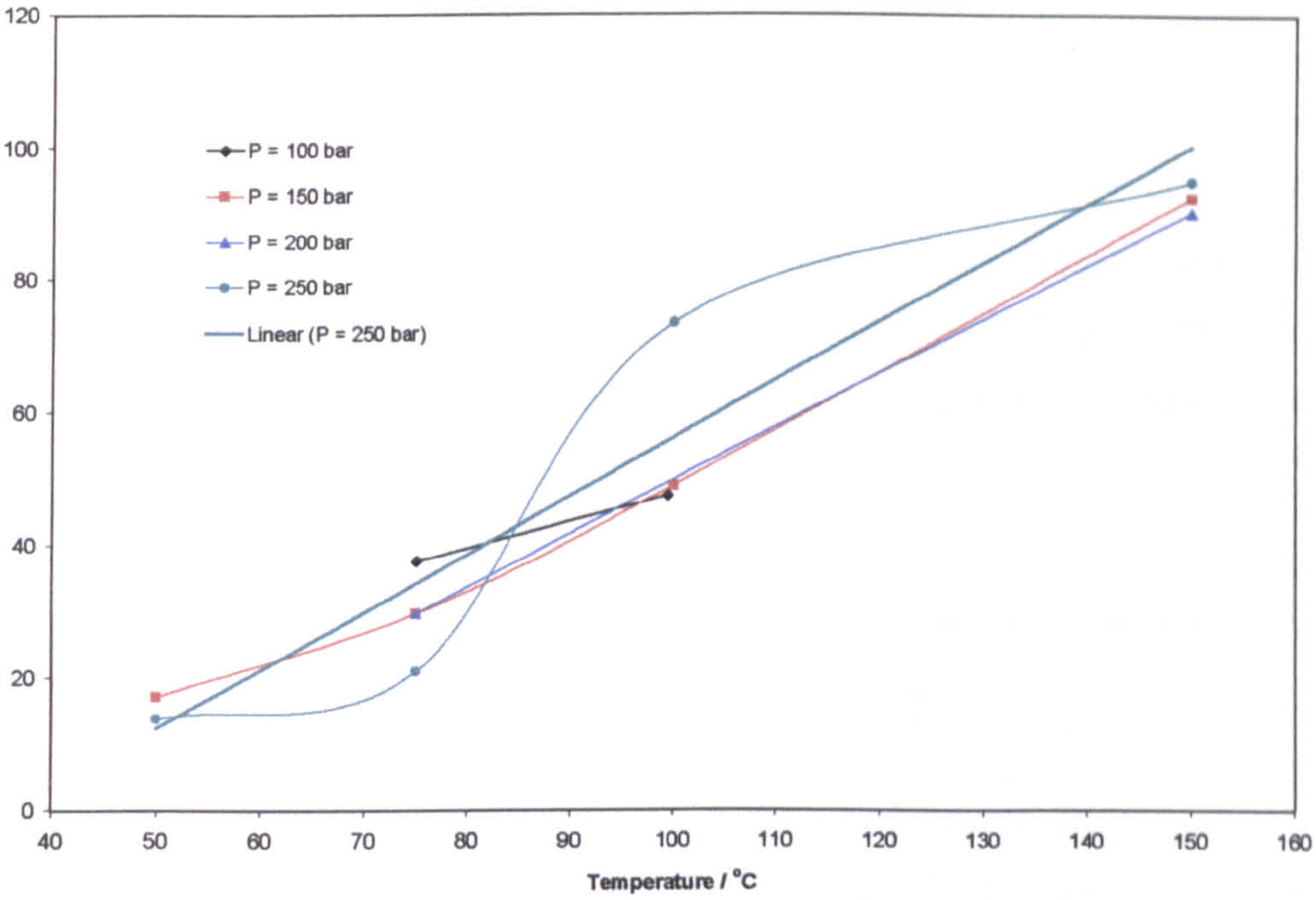


Figure 6-2: Data on how the extraction efficiency varies with temperature. Each data line corresponds to a specific pressure. All experiments were carried out for 30 minutes. Data at 250 bar does not fit the linear behaviour exhibited by the other pressures, for this reason a linear plot is superimposed on the graph, this suggests the discrepancy may simply be experimental error.

Interestingly, the lines for temperature change for 100, 150 and 200 bar are very similar, suggesting that pressure has less influence over the extraction process. The result for 250 bar appears to deviate from this linear relationship. It is an interesting phenomenon where the greatest rise in the extraction efficiency occurs when the solvent changes from liquid to supercritical. This may be significant but it is clearly not observed in the 100, 150 and 200 bar cases. This would be unexpected as density, which is believed to have the greatest influence on solubility, is less affected by the critical temperature at 250 bar than at the lower pressures. Hence, if a transitional effect was to be observed, it would be expected to be seen more prominently at the lower pressures. If a linear trend line is plotted to account for the 250 bar result a similar result is obtained to the 100, 150 and 200 bar results. In this case, all results are very similar supporting the idea that pressure has little impact on extraction efficiency. This can be further see in Figure 6-3, which shows lines that are close to horizontal, and hence apparently unaffected by pressure. This is contrary

to the work published with CO_2 as the extractant where under identical temperatures a pressure of 350 bar was shown to be far superior to 250 bar.[307] Kawi's result is perhaps better explained by the presence of a greater amount of methanol in the higher pressure experiment and it could be this extra methanol which is allowing the increased extraction, independent of the fluid pressure. The methanol would also allow local density augmentation as mentioned in the Introduction. It is unfortunate that this cannot be tested as the pressure rating of the equipment is limited to 300 bar.

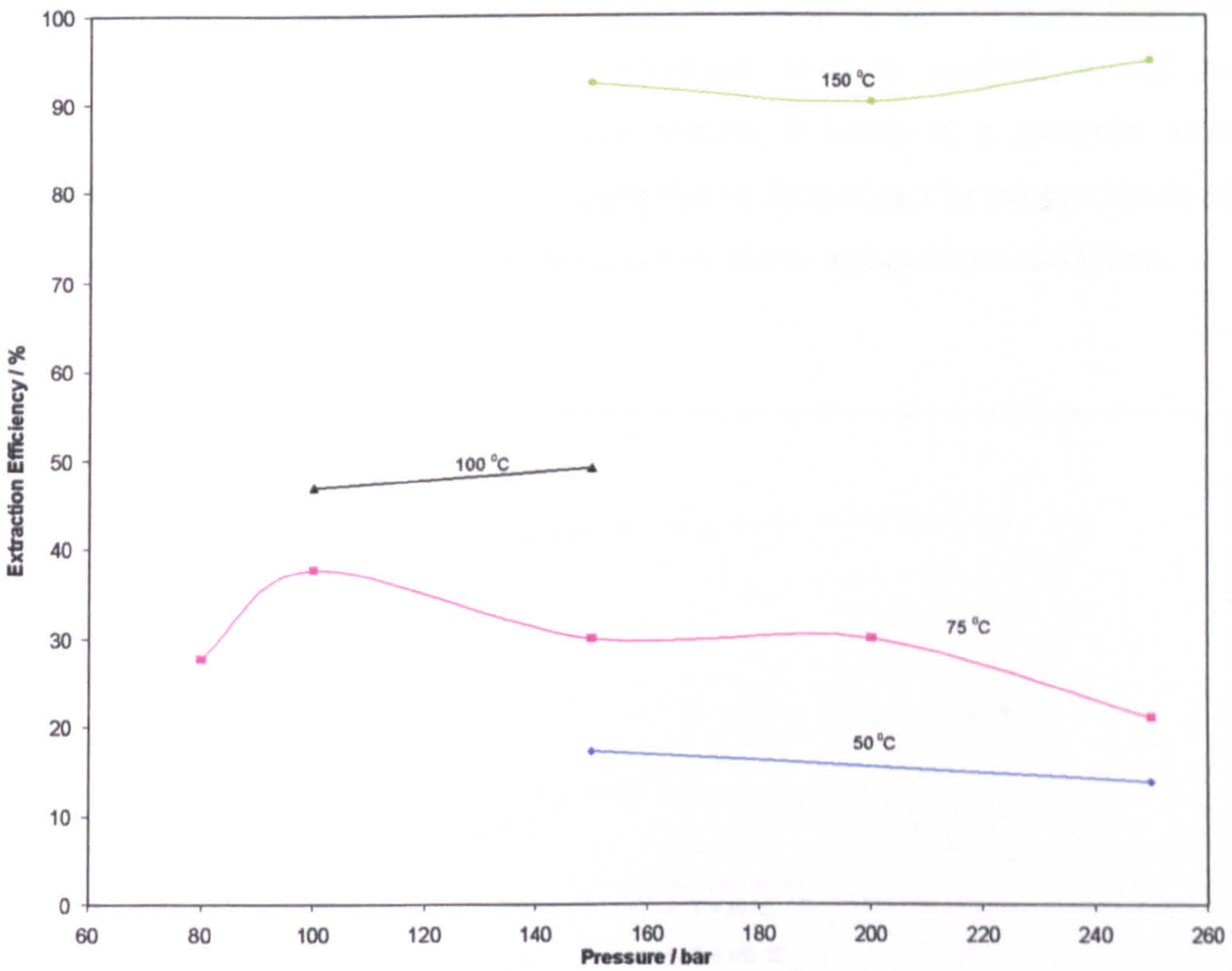


Figure 6-3: Variation of extraction efficiency with pressure, where each line represents a specific temperature. This shows that the extraction seems independent of pressure with all lines showing relatively little change with pressure.

Having observed temperature and pressure effects, extraction time was then examined. Two conditions were used to compare a system where almost all the surfactant is removed with a system where there is surfactant remaining. This was done at 150 bar and 150 °C where almost complete removal of the template had

already been observed and 150 bar and 75 °C where the removal would be significantly less. This is shown in Figure 6-4. Here, in both cases, it can be seen that the rate of extraction slows with time. In the case of the 150 bar sample the template has been completely removed after 90 minutes of extraction. This is an important factor, as previous work using supercritical fluids only achieved a maximum removal of 92.3 %.[307] This observed trend of the extraction slowing as time progresses is repeated in the result for 75 °C. What is learnt from this is that it is possible to remove all template from the silica using scPropene. The fact that temperature is the most important factor in this experiment is also reiterated. Also it can be seen that in the investigation of 30 min maximum extraction for a given system is not achieved. However, even when that maximum extraction level is reached, it will not necessarily proceed to 100 % extraction; instead, it levels at a particular point dependent on the temperature. This suggests that surfactant can be trapped inside the structure in some manner and is only removed by higher temperature conditions.

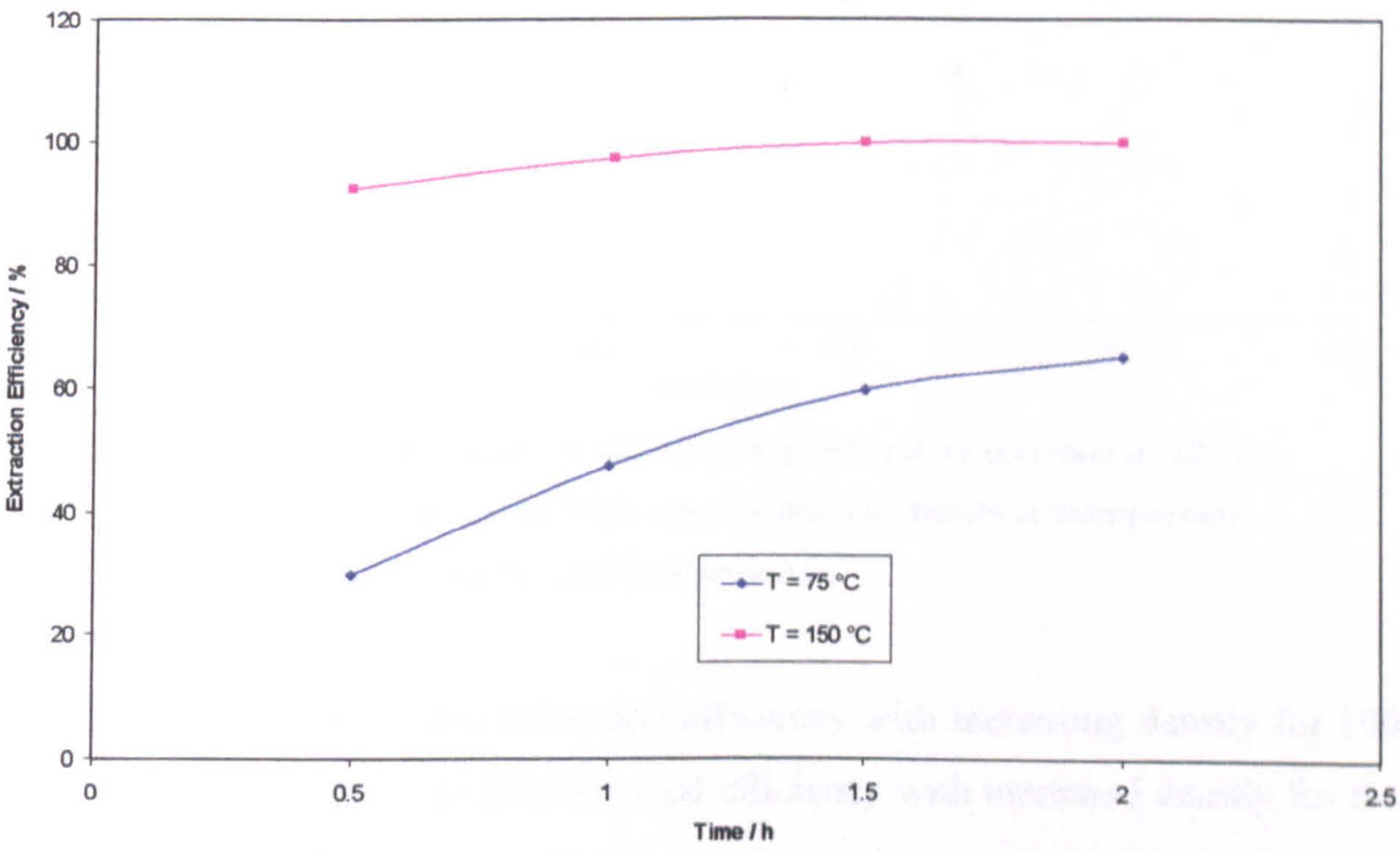


Figure 6-4: This graph shows the extraction efficiencies of two sets of experiments, one at 150 bar and 75 °C and the other at 150 bar and 150 °C. We see the progression of the extraction over two hours as the amount being extracted lowers with time. This also shows us that it is possible to achieve 100 % extraction of the template using this system.

It was believed that the density of the fluid may be an important factor as this is closely linked to the solubility of materials in supercritical fluids. Since the density is controlled by temperature and pressure, a graph can be plotted directly relating density with extraction. This is given in Figure 6-5. Here no obvious correlation with density is seen. This suggests that the solubility of the dodecylamine in the fluid is unimportant. A raised temperature is required only to lower the viscosity of the fluid. This is highlighted in Figure 6-6 where the temperature data are added to Figure 6-5.

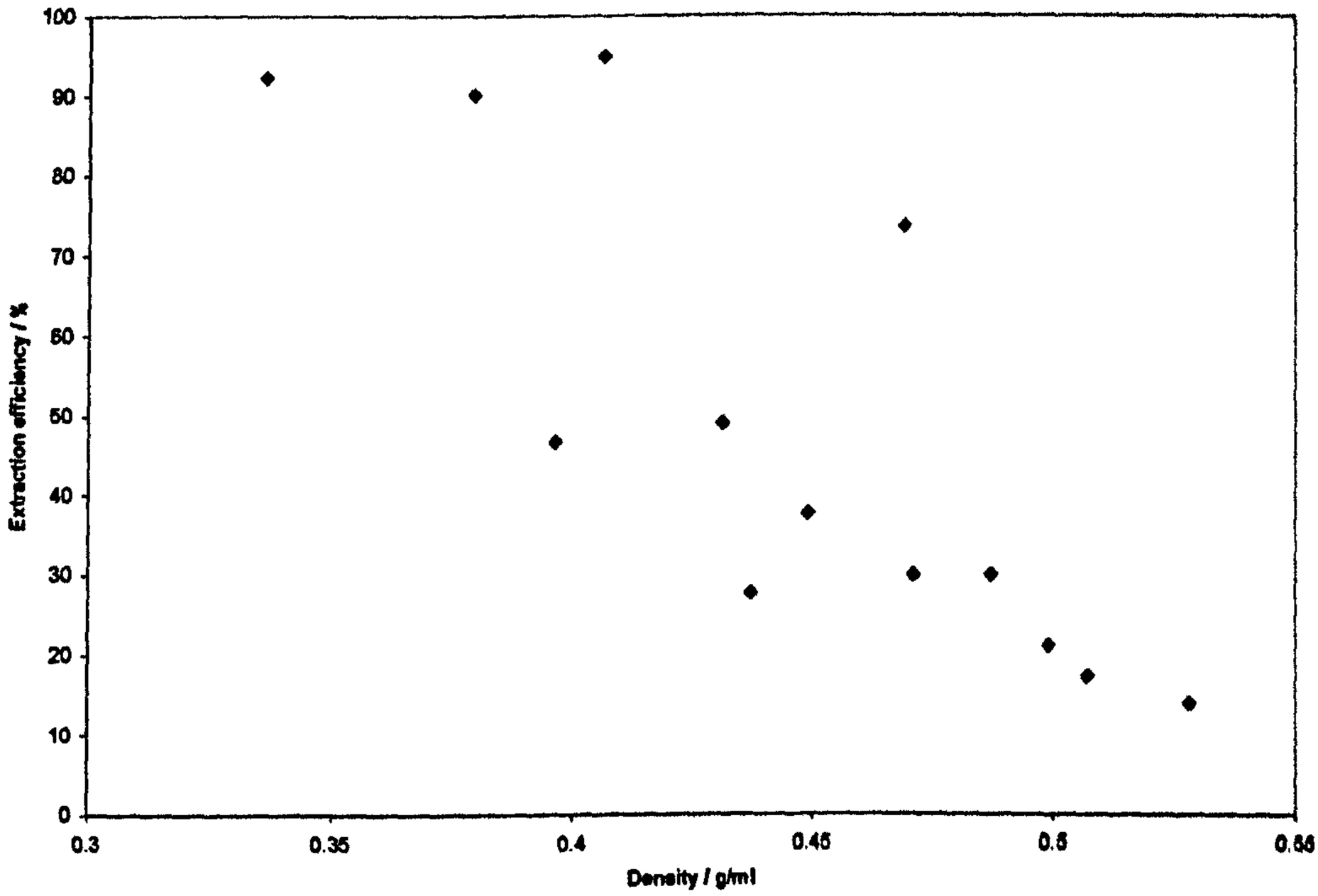


Figure 6-5: The extraction efficiency appears not to correlate at all to the density of the system. This suggests that the density is unimportant, or much less important, than another factor.

In Figure 6-6 a slightly raised extraction efficiency with increasing density for 100 and 150 °C samples, and a slightly lowered efficiency with increased density for the 50 and 75 °C samples can be seen. Although no clear result is observed, this is interesting as this distinction is also noted to be where the liquid/fluid boundary occurs. It is possible that the increased density, which also corresponds to an increased viscosity, in the liquid case makes the propene less able to penetrate the sample. Instead the liquid may be forced around the sample and hence extraction efficiency is lowered. Conversely the SCF examples show a slight increase with density. In these examples it might be the case that the increased temperature is

enough to allow the surfactant to be moved more easily, in these cases the increase in density may be observed to improve the extraction simply by either a slight increase in solubility or by an increase in the number of molecules available to push out the surfactant. Currently there is too little data to adequately determine the exact influences in this case. However, the very strong relationship with temperature, with the solvent moving in a downward direction, indicates that a facilitated diffusion mechanism is operating on the surfactant.

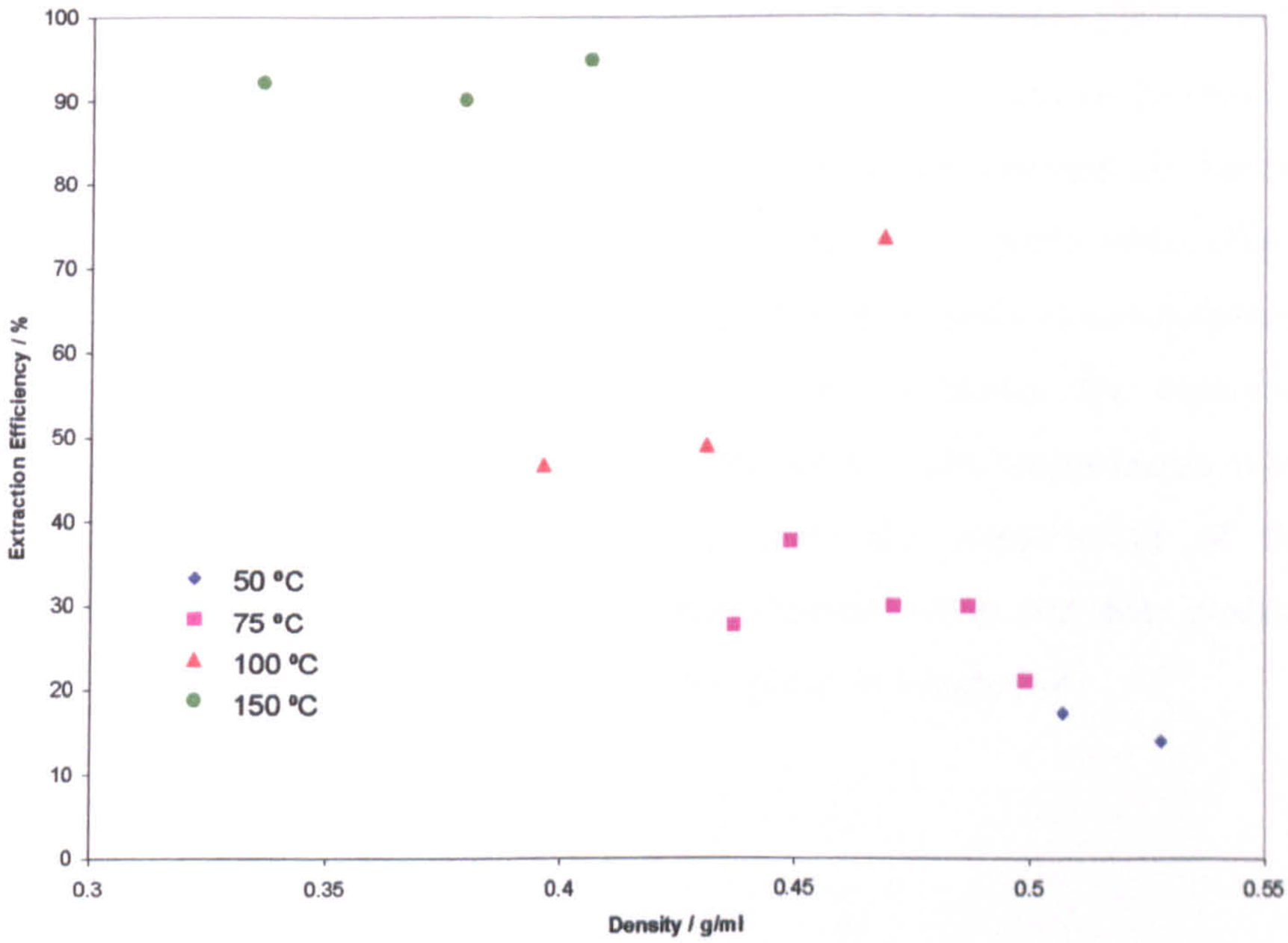


Figure 6-6: When temperature data is included in the density plot it becomes immediately apparent that this is a much more important factor in determining extraction efficiency. A possible divergence between experiments at super- and sub-critical condition is also noticed.

Extraction of Dodecylamine: Design 2

The previous set of experiments was limited by the maximum temperature rating of the Keystone vessel. Temperatures in excess of 150 °C could not be used due to the PEEK seals on the vessel. It was considered desirable to attempt experiments at a higher temperature to observe any increased activity of the solvent. A new set of experiments was therefore established using a steel tube reactor, see Appendix II and Figure 6-7. This would allow higher temperatures to be reached but would be limited to a maximum pressure of 200 bar because of the rating of the steel piping. Since pressure had appeared to have little effect on the extraction efficiency, it was assumed that this would not influence the outcome of the extractions. These experiments were carried out after the construction of the larger experimental setup and their position within it is given in Figure 6-8.

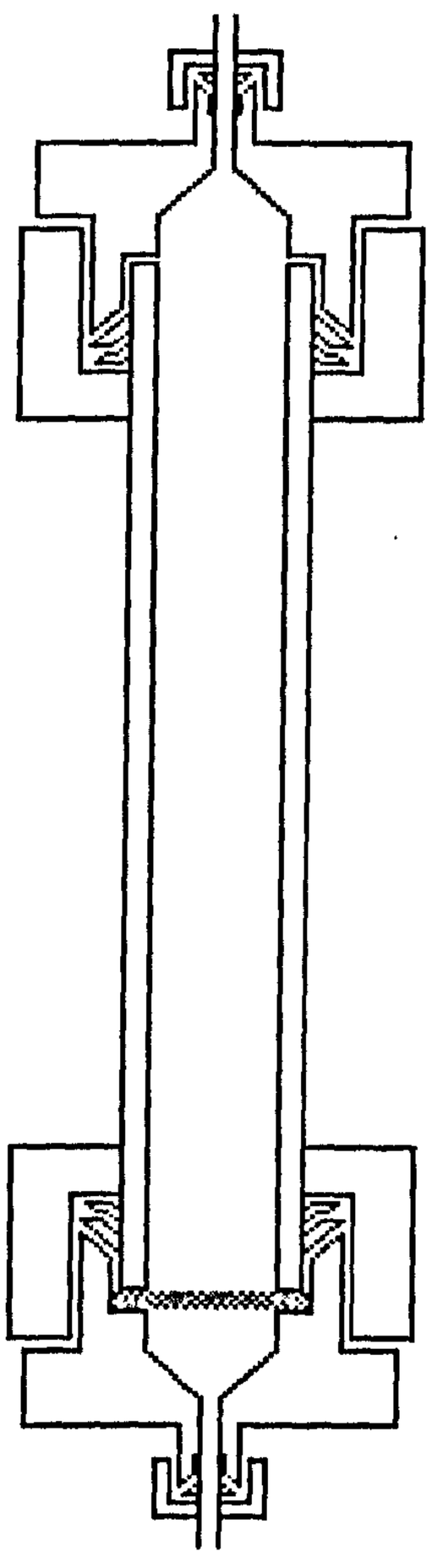


Figure 6-7: Steel tube extraction vessel for high temperature extraction. This allows higher temperatures to be used for the extraction, although limits the maximum pressure to 200 bar.

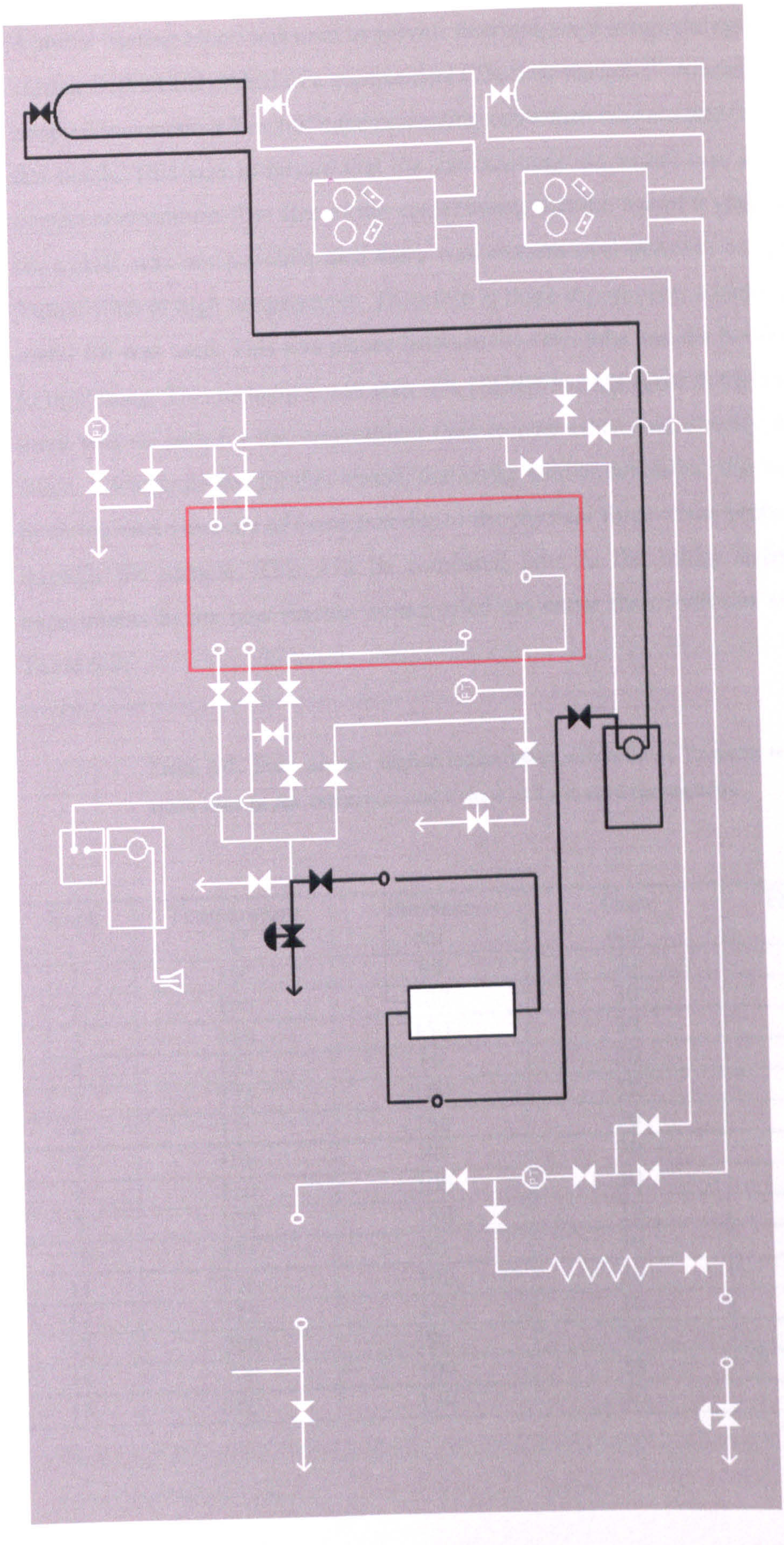


Figure 6-8: Apparatus for high temperature extraction of silica.

A metal heating block was used to provide heat and, once setup, the system was very similar to the catalyst bed of a supercritical CO_2 flow reactor.[311] A heating block was adapted to contain a 2 m 1/8" tube preheating coil which was mounted to the back of the block. This was to ensure that the gas reaching the vessel was already at the correct temperature. The size of the vessel meant that the use of a glass tube inside the vessel was not possible; also there was concern over possible creeping of the Teflon filter at high temperatures. Therefore in these experiments a plain tube with a metal frit was used. This was placed between the steel tube and the bottom nut prior to tightening. This technique was seen as a slightly harsher route to the extraction as there was no path for the supercritical fluid to take other than directly through the silica. It was expected for this reason, that under similar conditions this would result in an increased amount of extraction due to the physical force of the propene moving through the sample. This will be compared later to the initial technique. The experiments in the new reactor were carried out under the conditions as shown in Table 6-2.

Table 6-2: Data for the higher temperature extractions. Propene is again used as the extractant and a mass of 2 g is used throughout.

Expt.	Temperature °C	Pressure bar	Time min	Extraction %
1	100	80	30	69.0
2	100	100	30	67.0
3	100	150	30	80.0
4	125	80	30	75.1
5	125	100	30	85.0
6	125	150	30	89.0
7	150	80	30	79.6
8	150	100	30	89.0
9	150	150	30	93.5
10	175	80	30	87.6
11	175	100	30	90.4
12	175	150	30	97.9
13	200	80	30	90.4
14	200	100	30	98.0
15	200	150	30	99.0

Samples were placed inside the vessel and the vessel sealed. This was then plumbed into the experimental setup as in Figure 6-8. The heating block was switched on and the correct temperature reached before gas was added to the system. The flow was then started at the correct pressure and maintained for 30 minute. No subcritical conditions were used in this case and 100 % extraction was not observed in this series of experiments. This is attributed to the fact that all experiments were run over only 30 minutes.

Data shown in Figure 6-9 shows the effect of temperature on the extractions. The three lines all agree on rising extraction efficiency between 100 and 200 °C. This might be explained by increasing temperature thus raising the solubility of the surfactant or simply ensuring it is less viscous and hence more easily moved. Experiments at 80 and 150 bar show a steady rise in extraction with temperature while experiments at 100 bar appear more erratic this may be ascribed to experimental error. Ultimately the results point towards the same trend with temperature as seen in the previous data set.

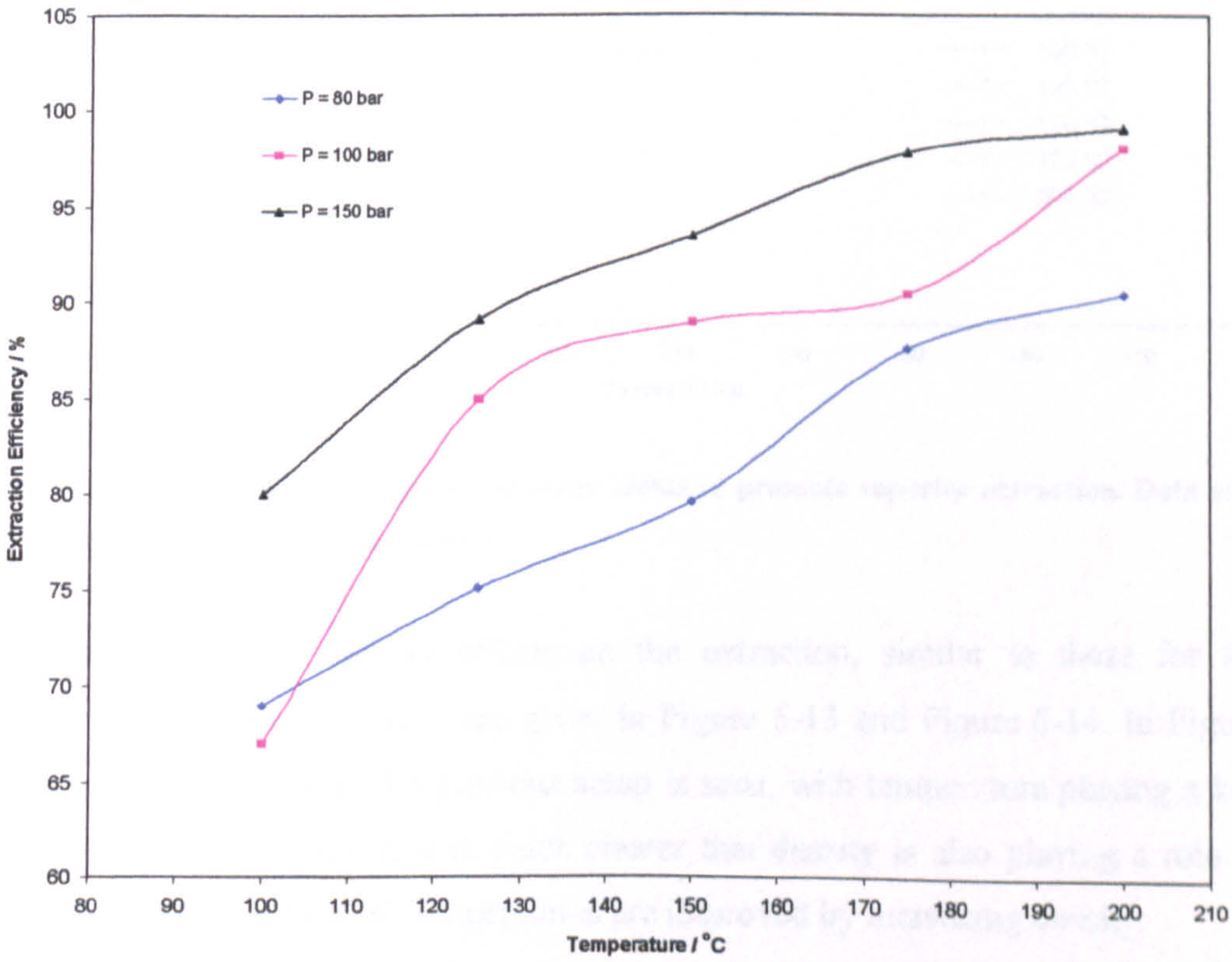


Figure 6-9: Extraction efficiency displays a positive change with increasing temperature for three different pressures.

If the pressure dependence of the system is examined, Figure 6-10, the data show an increase in extraction in all cases with pressure. This was not observed in the previous experiments. It is suggested that this increase is due to the denser solvent physically forcing the surfactant out of the silica system. Density is likely to have a greater effect in the new technique as there is no way for the solvent to go except through the silica.

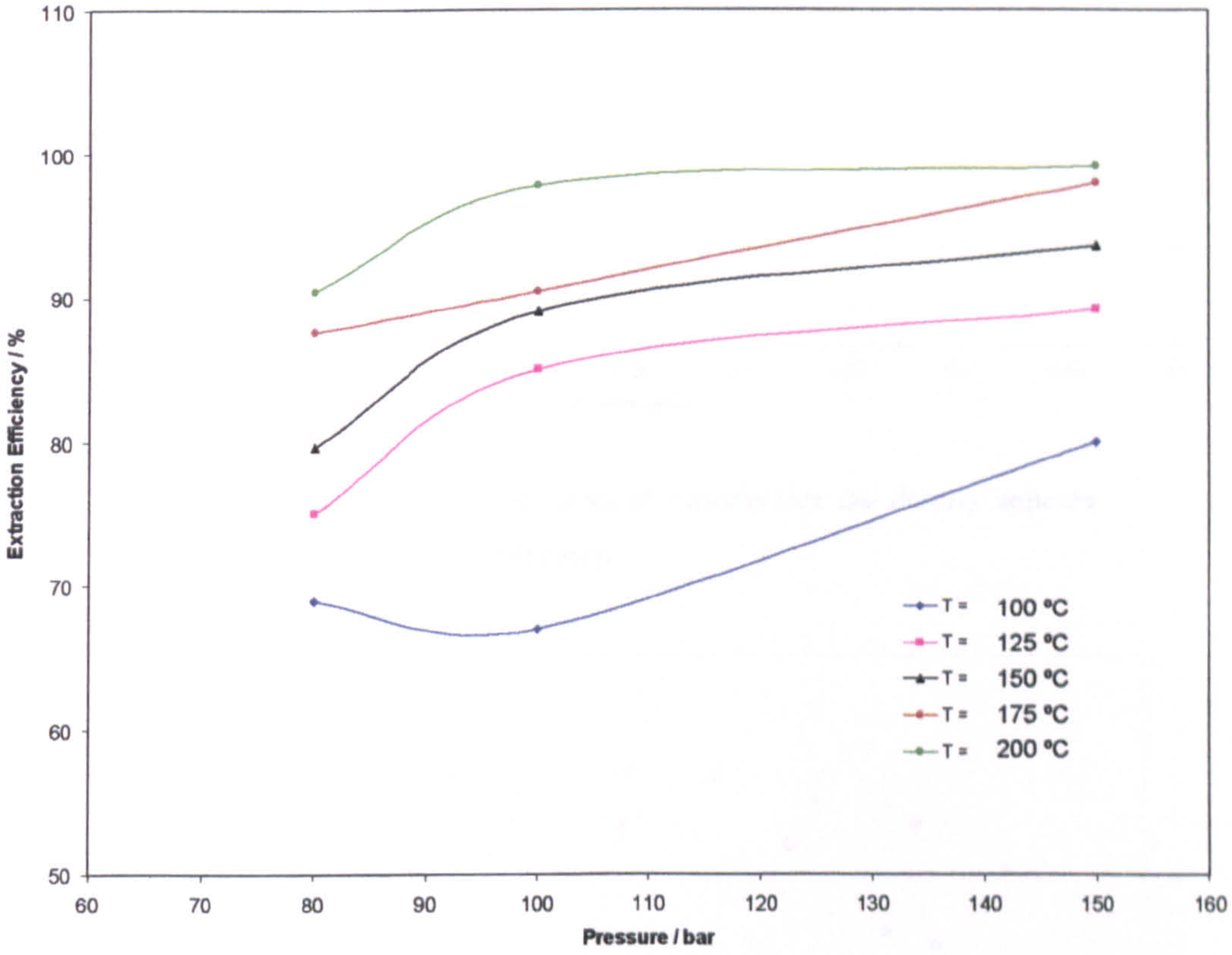


Figure 6-10: Increased system pressure seems to promote superior extraction. Data at several temperatures are shown.

Examinations of the density effects on the extraction, similar to those for the previous experimental section, are given in Figure 6-13 and Figure 6-14. In Figure 6-14, a similar pattern to the previous setup is seen, with temperature playing a key role. In this case, however, it is much clearer that density is also playing a role as extraction efficiencies at all temperatures are improved by increasing density.

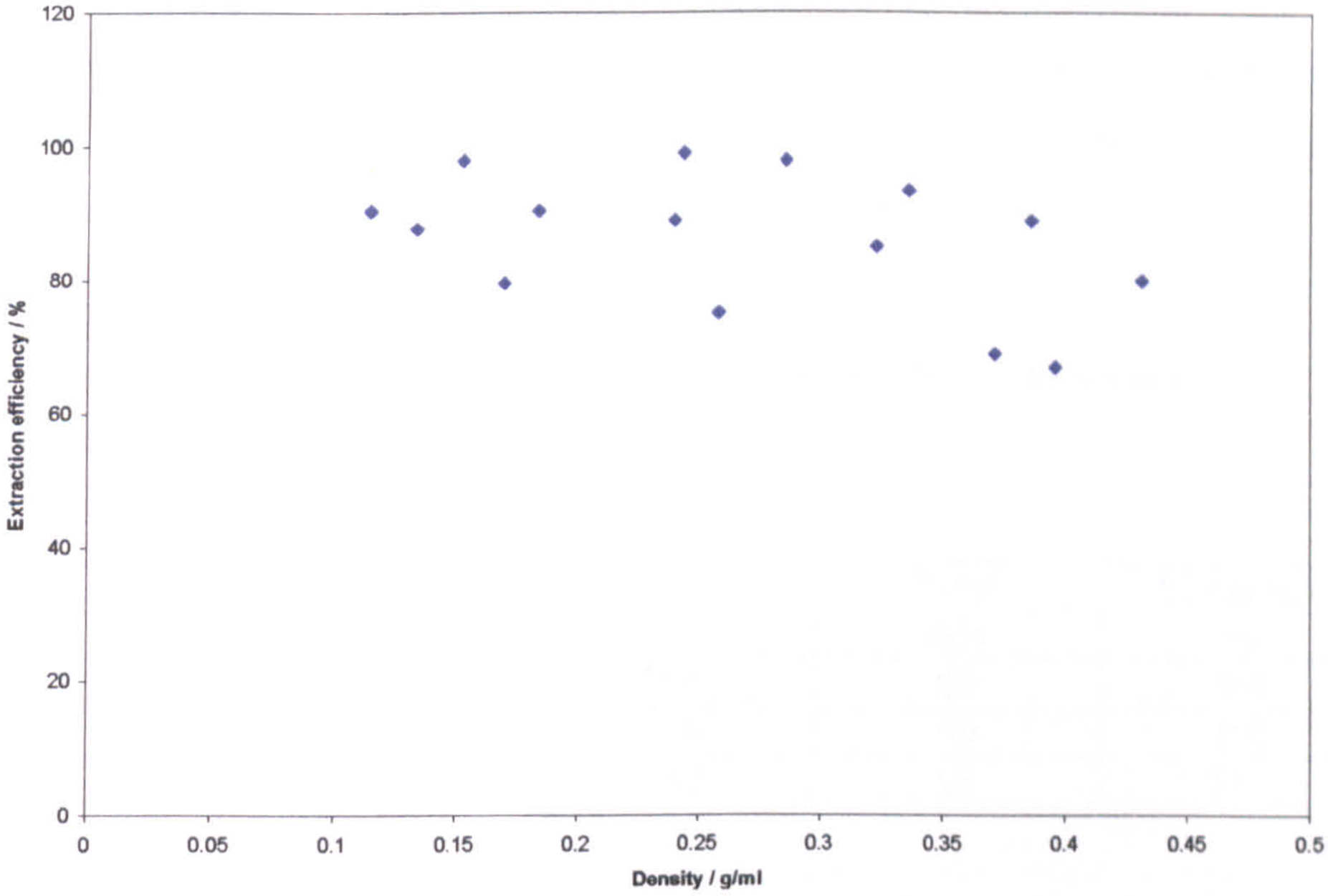


Figure 6-11: As with the first series of experiments the density appears unrelated to the extraction efficiency.

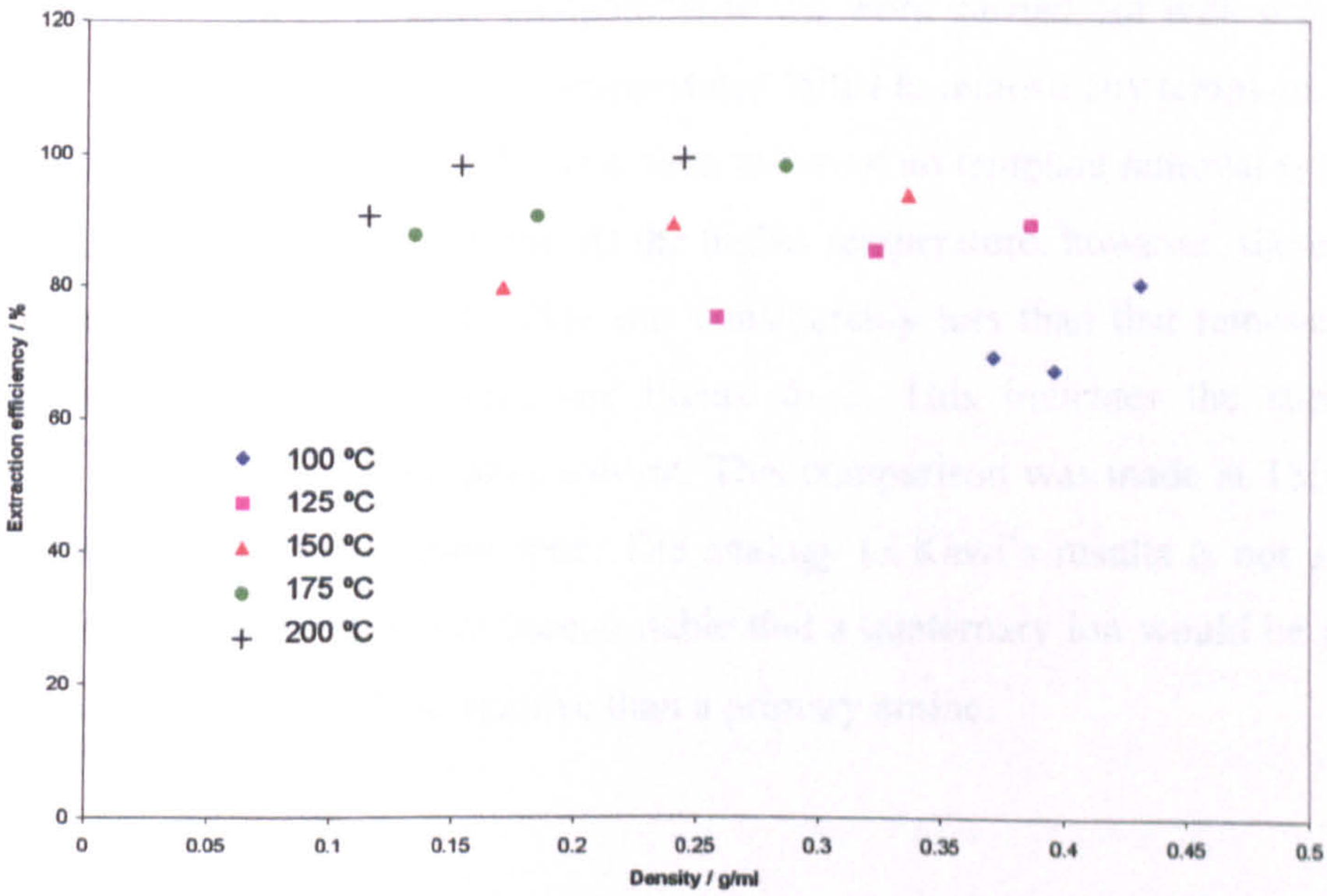


Figure 6-12: Addition of temperature data reveals temperature is very important, but density does play a key role as well. This is contrary to data from the previous experimental setup.

Some extractions were also made with CO_2 as the solvent extractant. This was performed in the second extraction apparatus and was designed to investigate whether the use of a non-flammable gas might provide a suitable alternative to propene. The experiments carried out are detailed below in Table 6-3.

Table 6-3: CO_2 is used as an extractant and is shown to be a much poorer extractant that propene.

Expt	Temperature °C	Pressure bar	Time min	Extraction %
1	35	80	60	0.0
2	85	150	60	0.0
3	150	150	60	24.7

These experiments looked at CO_2 just above the critical point, at conditions comparable to the work with the extraction of quaternary ammonium ions[308] and a sample which would be directly comparable to the work carried out with propene. The initial experiments at the lower temperatures failed to remove any template. This is not surprising and agreed with Kawi's observation of no template removal without the methanol modifier being present. At the higher temperature, however, there was some template removed by CO_2. This was considerably less than that removed by propene under similar conditions, see Figure 6-13. This indicates the superior extraction properties of the propene solvent. This comparison was made at 150 bar, 150 °C with a 60 min extraction time. The analogy to Kawi's results is not a true comparison, however as it is not unreasonable that a quaternary ion would be more difficult for a non-polar SCF to remove than a primary amine.

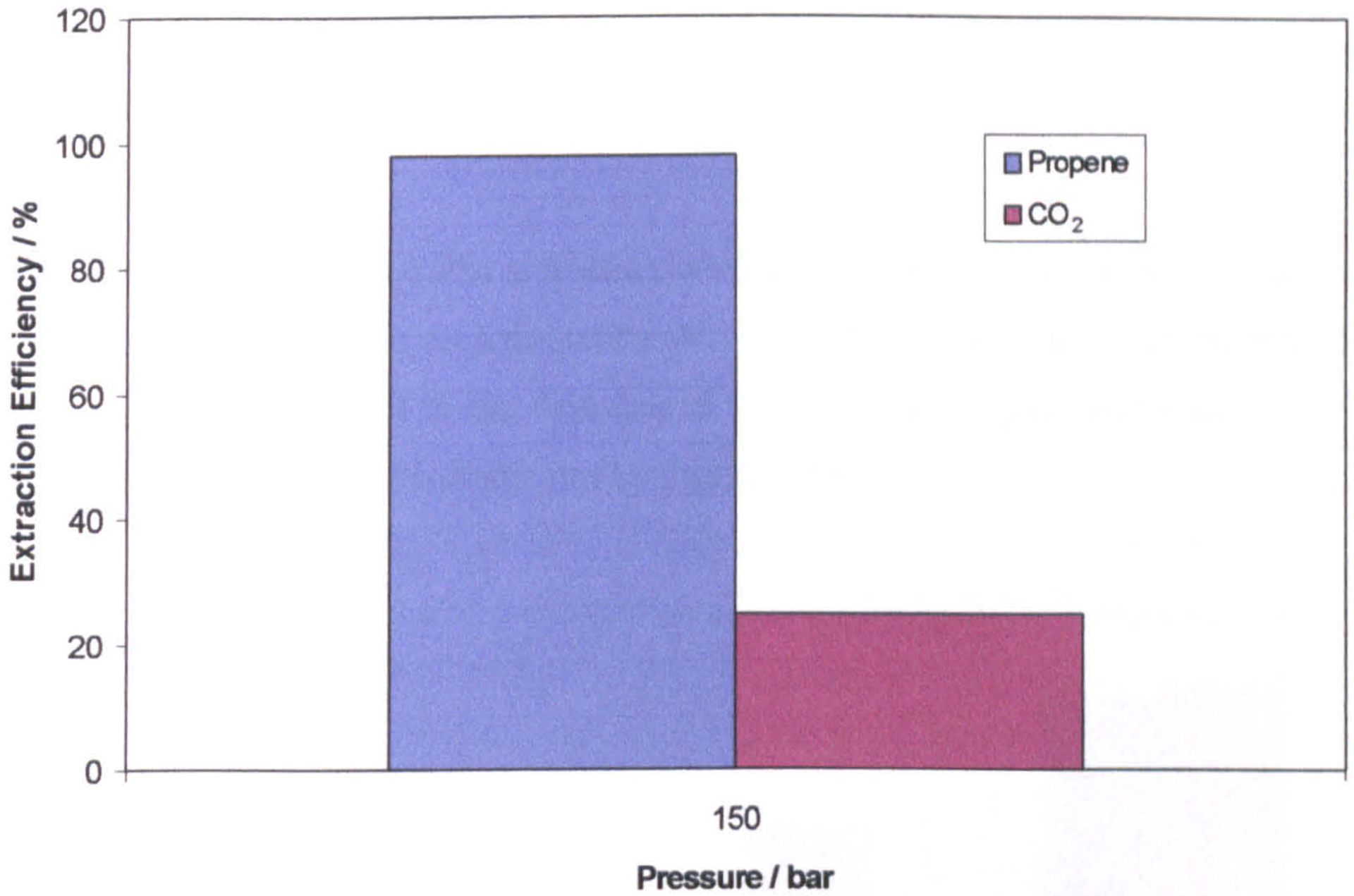


Figure 6-13: Comparison of propene to CO_2 at 150 bar and 150 °C shows propene as a much more successful extraction medium.

It is immediately evident that under these conditions propene is a much better extraction fluid than CO_2. It was suggested earlier, with regards to the temperature effects of the extractions, that the removal of the template might be affected by the fluidity of the surfactant itself at a given temperature. If this were the case, then to achieve efficient extraction a specific temperature would have to be reached. Our work to date suggests that this would be around 150 °C. This temperature would dramatically affect the density of the fluid used and hence the ability of the fluid to either solubilise the surfactant or simple push it through the system. At 150 °C and 150 bar the density of CO_2 is 0.234 g ml^{-1} and the density of propene is 0.336 g ml^{-1}. [15] This could act to explain the obvious success of the propene extraction. CO_2 would gain the density of 0.336 g ml^{-1} at 205 bar at 150 °C. This would be an interesting comparison to the data; however it takes our equipment beyond their maximum working pressures and as such an alternative system would be required before work could be carried out. This would pose an interesting question if successful as to which gas would be preferable to use: propene could be used at lower pressures so the process could be carried out less expensively, while CO_2 use would eliminate the risk of using a flammable gas.

Assessment of the Two Designs

As a final examination of this extraction work a comparison was made between the two experimental setups. As was mentioned earlier the second setup was believed to offer superior extraction to the first due to the fact that all gas must pass directly through the sample. This is borne out by Figure 6-14.

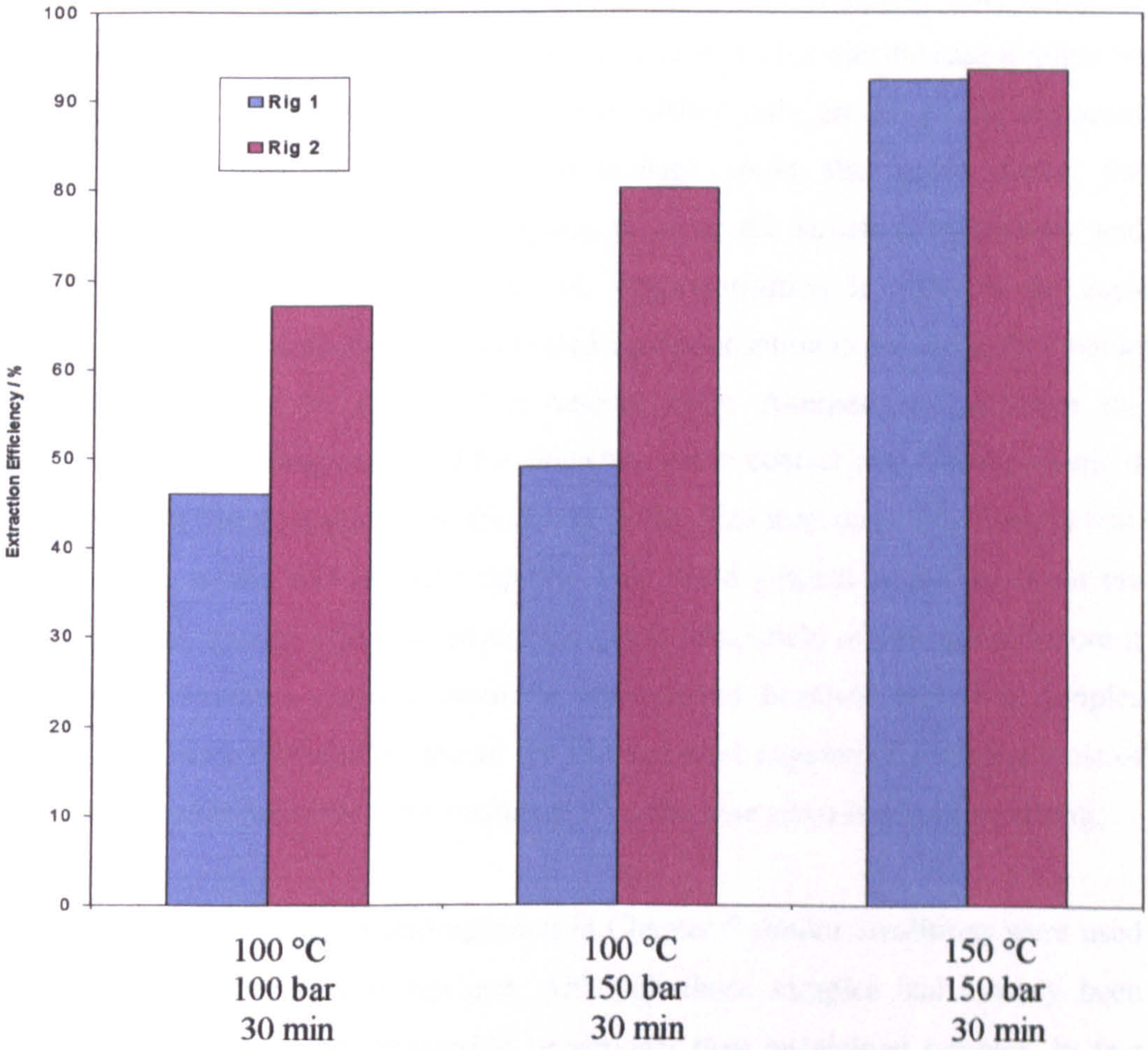


Figure 6-14: Comparison for identical experiments carried out using the different experimental setups. The second xperimental design is consistently better, although this difference is reduced at higher temperature.

Here in all three cases it is seen that the second apparatus is superior to the first in terms of extraction, with the effect being more pronounced at lower extraction efficiency and temperatures. One problem with this is that it may cause damage to the silica as the flow of the gas compresses the sample more in the second experimental setup. Only very tentative data on the structural order of the samples is available at present, which suggests that during the extraction process the silica structure is being damaged to very different extents with no discernable pattern. An explanation of this is that possibly, since most samples are incompletely extracted at the end of the experiment, surfactant blocks the ends of the silica tubes and an internal overpressure is allowed to build up inside the structure. This could be sufficient to damage the structure on depressurisation. If this was the case it might be expected that the severest damage would be visible only on the poorly extracted samples but this does not occur. The damage could also occur during the depressurisation stage with gas attempting to leave the structure too rapidly and creating an internal overpressure. As the depressurisation is different for each sample, because no automatically controlled depressurisation is available, this would be expected to be the source of a random error. Alternatively, although the experiments were designed so that the silica was not in contact with liquid propene if the heating of the system was insufficient then the silica may come into contact with liquid which would boil off very rapidly. This could potentially put stress on the sample and so greater efforts to ensure the gas is adequately of pre-heated before it reaches the extraction vessel. It should be remembered, however, that these samples traditionally were refluxed in ethanol for 18h and were capable of retaining most of their structure through this harsh treatment,[284] so the base silica is relatively strong.

Also during the work using impregnation in Chapter 5 similar conditions were used and structural ordering was retained. Although those samples had already been calcined and so might be expected to be stronger than uncalcined samples. In fact remarkably little damage was recorded. Indeed, retention of structural order was seen as one of the advantages of performing the experiments using supercritical fluids. This area requires more study to properly answer these questions over the suitability of the process. However, if the silica was damaged by too rapid depressurisation, this could be remedied very simply by addition of a computer controlled BPR capable of reducing the pressure very slowly over a set period of time. In a final examination, a

sample of the extracted amine was analysed by ^{1}H NMR. This was shown to not contain any impurities, indicating the recovered surfactant was not damaged by the process. This will need further examination, with the ideal goal of generating a new batch of silica using a collected sample of surfactant.

Conclusion

In this Chapter primary amine surfactant has been successfully extracted from as synthesised mesoporous silica at significantly lower temperatures than used during calcinations. A route is therefore suggested to remove template from thermally unstable species which would normally be damaged by the extreme heat of calcination. A route has also been provided to potentially recycle template, which could have a large impact on the cost of mesoporous silica generation. Reliable structural data as to the post extraction stability of the samples is not currently available and should be the next step in determining the usefulness of the technique. Two reactor designs have also been demonstrated and comparisons given between them.

Chapter 7 Conclusion

Through this thesis, the use of supercritical fluids acting as antisolvents and as fluids to facilitate the transport of substances either into or away from a solid structure has been observed.

Given the task of continuing work on C_{60} intercalation compounds proof of the existence of $C_{60}(C_2H_4)$ and $C_{60}(C_2H_6)$ has been obtained. These were characterised by MAS ^{13}C NMR, IR and PXD data. The first evidence of the existence of $C_{60}(C_3H_6)$ and $C_{60}(C_3H_8)$ with MAS ^{13}C NMR and IR data has also been given. This leaves the possibility of new intercalation compounds which may be possible to synthesis. These potentially include HCl, NH_3 and halogen analogues of the gases. The inclusion of HCl would be interesting as is would give a compound with a well established quantity of acid inside it which is not chemically bound. This might provide a method to dose reactions with a specific quantity of HCl, a task which is currently difficult on a small scale.

In studying the intercalation compounds a new antisolvent technique to maximise their production and generate the first macroscopic single crystals of the fullerene materials has been developed. This represents a new way in which SCF antisolvents have been harnessed. This has allowed us to publish the first X-ray diffraction data on the C_{60}(gas) compounds.[312] The technique was then extended to look at C_{70} compounds; X-ray data, collected so far, has failed to yield a satisfactory solution, however. This is nevertheless consistent with other C_{70} data sets which also only yield a rough simple hexagonal structure. This technique has the potential to allow crystallisation of very precious fullerene materials, particularly endohedral fullerenes, which can only be prepared on a very small scale. This will potentially allow access to crystal data on these compounds as the technique has been demonstrated to work on samples as small as 0.5 mg in 0.1 ml and potentially can even require even less material. A collaboration now exists with The University of Oxford to grow crystals of rare fullerenes synthesised by the Department of Materials.

Links with the University of Oxford also allowed preliminary results of the generation of nano-peapods to be presented. The synthesis of nano-peapods creates a molecule which might record magnetic data in a linear array. The conventional route to this array requires high temperatures where samples are homogenised and all information is lost. The use of SCF as a medium to allow transport of fullerenes into nanotubes has provided the first example of a low temperature route to nano-peapods in high concentration. Although data on these materials is only preliminary they represent a definite advancement in the field of nanotechnology. This will be developed further and the C_{60} test molecules replaced by endohedral fullerenes to attempt a readable molecular array in the near future.

In an investigation to observe if it was possible to graft Al to a mesoporous silica support, much improved stability features of the resultant solid was demonstrated. SCF improved mass transport properties are used to create an even coverage of aluminium. This has led to the production of samples of unparalleled stability at very high aluminium content.[313] This represents an important achievement in the field of solid acid catalysts and research is continuing into the stability of the materials over many repeat steaming experiments to imitate industrial use. Investigation will also be made into catalysis of test reactions using the products.

Finally the use of scPropene as a potential extractant for the surfactant template following the formation of mesoporous silica has been investigated. This has been shown to achieve complete removal of surfactant which is then recoverable, without noticeable damage. This provides a low temperature alternative to the calcination process and the prospect of recycling amine on completion. However, problems resulting in the damage of some of the silica samples by treatment with the fluids raise the question of the future potential of this technique. There are plans to examine a similar extraction of a quaternary amine template molecule, although there are no plans to continue the primary amine extraction at this time.

Chapter 8 References

(1) McHugh, M. A.; Krukonis, V. J. *Supercritical Fluid Extraction*; Butterworth-Heinmann, Boston, MA., 1994; Vol. 2nd Ed.

(2) Clifford, T. *Fundamentals of Supercritical Fluids*; Oxford University Press: Oxford, 1999.

(3) Noyori, R. *Chem. Rev.* **1999**, *99*, 353.

(4) Jessop, P. G.; Leitner, W., Eds. *Chemical Synthesis Using Supercritical Fluids*; Wiley-VCH: Weinheim, 1999.

(5) Darr, J. A.; Poliakoff, M. *Chem. Rev.* **1999**, *99*, 495.

(6) Anastas, P. T.; Williamson, T. C., Eds. *Green Chemistry: Frontiers in Benign Chemical Synthesis*; Oxford University Press, 1998.

(7) Lancaster, M. *Green Chemistry: An Introductory Text*; RSC: Cambridge, 2002.

(8) Ke, J., **2002**, PhD Thesis Nottingham, UK

(9) Teja, A. S.; Eckert, C. A. *Ind. Eng. Chem. Res.* **2000**, *39*, 4442.

(10) Crette, S. A.; DeSimone, J. M. *Nachr. Chem.* **2001**, *49*, 462.

(11) Young, J. L.; DeSimone, J. M. *Pure Appl. Chem.* **2000**, *72*, 1357.

(12) Hauthal, W. H. *Chemosphere* **2001**, *43*, 123.

(13) Atkins, P. W. *Physical Chemistry*; 5th ed.; Oxford University Press: Oxford, 1994.

(14) Shinoda, K. *Principles of Solution and Solubility*; Marcel Dekker, Inc.: New York, 1966.

(15) Lemmon, E. W.; McLinden, M. O.; Friend, D. G. In *NIST Chemistry WebBook, NIST Standard Reference Database Number 69*; Linstrom, P. J., Mallard, W. G., Eds.; National Institute of Standards and Technology: Gaithersburg MD, 20899 (http://webbook.nist.gov), 2001.

(16) Webster, J. M., **2000**, PhD Thesis University of Nottingham, UK

(17) Cansell, F.; Chevalier, B.; Demourgues, A.; Etourneau, J.; Even, C.; Garrabos, Y.; Pessey, V.; Petit, S.; Tressaud, A.; Weill, F. *J. Mater. Chem.* **1999**, *9*, 67.

(18) Sandler, S. I., Ed. *Models for Thermodynamic and Phase Equilibria Calculations*; Marcel Dekker, Inc.: New York, 1994.

(19) Peng, D. Y.; Robinson, D. B. *Ind. Eng. Chem. Fund.* **1976**, *15*, 59.

(20) Redlich, O.; Kwong, J. N. S. *Chem. Rev.* **1949**, *44*, 233.

(21) Soave, G. *Chem. Eng. Sci.* **1984**, *39*, 357.

(22) Pitzer, K. S. *J. Am. Chem. Soc.* **1955**, *77*, 3433.

(23) Saitow, K.; Otake, K.; Nakayama, H.; Ishii, K.; Nishikawa, K. *Chem. Phys. Lett.* **2003**, *368*, 209.

(24) Ruckenstein, E.; Shulgin, I. L. *Chem. Phys. Lett.* **2000**, *330*, 551.

(25) Egorov, S. A.; Yethiraj, A.; Skinner, J. L. *Chem. Phys. Lett.* **2000**, *317*, 558.

(26) Roberts, C. B.; Chateauneuf, J. E.; Brennecke, J. F. *AIChE J.* **1995**, *41*.

(27) Ellington, J. B.; Park, K. M.; Brennecke, J. F. *Ind. Eng. Chem. Res.* **1994**, *33*, 965.

(28) Ngo, T. T.; Bush, D.; Eckert, C. A.; Liotta, C. L. *AIChE J.* **2001**, *47*, 2566.

(29) http://www.svce.ac.in/~msubbu/LectureNotes/MassTransfer/MT-1.htm

(30) http://www.svce.ac.in/~msubbu/LectureNotes/MassTransfer/MT-2.htm

(31) Scott, R. L.; van Konynenburg, P. B. *Discuss. Faraday Soc.* **1970**, *49*, 87.

(32) Scott, R. L. *Ber. Bunsen-Ges. Phys. Chem. Chem. Phys.* **1972**, *76*, 296.

(33) Streett, W. B. In *Chemical Engineering at Supercritical Fluid Conditions*; Paulaitis, M. E., Penninger, J. M. L., Gray, R. D., Davidson, P., Eds.; Ann Arbor Science: Ann Arbor, 1983.

(34) Hicks, C. P. *A Bibliography of Thermodynamic Quantities for Binary Fluid Mixtures* London, 1978; Vol. 2.

(35) Knapp, H.; Döring, R.; Oellrich, L.; Plöcker, U.; Prausnitz, J. M. *Vapour-Liquid Equilibria for Mixtures of Low-Boiling Substances*; DECHEMA Chemical Data Series VI, 1981.

(36) Fornari, R.; Alessi, P.; Kikic, I. *Fluid Phase Equilib.* **1990**, *57*, 1.

(37) Dohrn, R.; Brunner, G. *Fluid Phase Equilib.* **1995**, *106*, 213.

(38) Christov, M.; Dohrn, R. *Fluid Phase Equilib.* **2002**, *202*, 153.

(39) Jessop, P. G. *Top. Catal.* **1998**, *5*, 95.

(40) Subramaniam, B.; McHugh, M. A. *Ind. Eng. Chem. Res. Proc. Des. Devel.* **1986**, *25*, 1.

(41) Hyde, J. R.; Licence, P.; Carter, D.; Poliakoff, M. *Appl. Catal. A-Gen.* **2001**, *222*, 119.

(42) Leitner, W. In *Modern Solvents in Organic Synthesis*; Springer-Verlag, Berlin: Berlin, 1999; Vol. 206, pp 107.

(43) Jessop, P. G.; Ikariya, T.; Noyori, R. *Chem. Rev.* **1999**, *99*, 475.

(44) Rezaei, K.; Temelli, F. *J. Supercrit. Fluids* **2001**, *19*, 263.

(45) Lang, Q. Y.; Wai, C. M. *Talanta* **2001**, *53*, 771.

(46) Gnayfeed, M. H.; Daood, H. G.; Illes, V.; Biacs, P. A. *J. Agric. Food Chem.* **2001**, *49*, 2761.

(47) Chester, T. L.; Pinkston, J. D.; Raynie, D. E. *Anal. Chem.* **1998**, *70*, 301R.

(48) Terfloth, G. *J. Chromatogr. A* **2001**, *906*, 301.

(49) Smith, R. M. *J. Chromatogr. A* **1999**, *856*, 83.

(50) Hannay, J. B.; Hogarth, J. *Proc. Roy. Soc.* **1879**, *29*, 324.

(51) Smith, R. D., **1986**, U.S. patent 4,582,731

(52) Chang, C. J.; Randolph, A. D. *AIChE J.* **1989**, *35*, 1876.

(53) Debenedetti, P. G.; Tom, J. W.; Kwauk, X.; Yeo, S. D. *Fluid Phase Equilib.* **1993**, *82*, 311.

(54) Matson, D. W.; Fulton, J. L.; Petersen, R. C.; Smith, R. D. *Ind. Eng. Chem. Res.* **1987**, *26*, 2298.

(55) Shim, J. J.; Yates, M. Z.; Johnston, K. P. *Ind. Eng. Chem. Res.* **2001**, *40*, 536.

(56) Matsuyama, K.; Mishima, K.; Umemoto, H.; Yamaguchi, S. *Environ. Sci. Technol.* **2001**, *35*, 4149.

(57) Krukonis, V. In *Aiche Annual Fall Meeting*: San Fransisco, CA, 1984, p 140f.

(58) Gallagher, P. M.; Coffey, M. P.; Krukonis, V. J.; Klasutis, N. In *Supercritical Fluids Science and Technology*; American Chemical Society, 1989, pp 334.

(59) Donsi, G.; Reverchon, E. *Pharm. Acta Helv.* **1991**, *66*, 170.

(60) Reverchon, E. *J. Supercrit. Fluids* **1999**, *15*, 1.

(61) Gallagher, P. M.; Coffey, M. P.; Krukonis, V. J.; Hillstrom, W. W. *J. Supercrit. Fluids* **1992**, *5*, 130.

(62) Loth, H.; Hemgesberg, E. *Int. J. Pharm.* **1986**, *32*, 265.

(63) Yeo, S. D.; Debenedetti, P. G.; Patro, S. Y.; Przybycien, T. M. *J. Pharm. Sci.* **1994**, *83*, 1651.

(64) Bustami, R. T.; Chan, H. K.; Dehghani, F.; Foster, N. R. *Pharm. Res.* **2000**, *17*, 1360.

(65) Winters, M. A.; Knutson, B. L.; Debenedetti, P. G.; Sparks, H. G.; Przybycien, T. M.; Stevenson, C. L.; Prestrelski, S. J. *J. Pharm. Sci.* **1996**, *85*, 586.

(66) Reverchon, E.; Della Porta, C.; Di Trolio, A.; Pace, S. *Ind. Eng. Chem. Res.* **1998**, *37*, 952.

(67) Reverchon, E.; De Marco, I.; Della Porta, G. *J. Supercrit. Fluids* **2002**, *23*, 81.

(68) Reverchon, E.; Celano, C.; Della Porta, G.; Di Trolio, A.; Pace, S. *J. Mater. Res.* **1998**, *13*, 284.

(69) Lele, A. K.; Shine, A. D. *Abstr. Pap. Am. Chem. Soc.* **1990**, *199*, 373.

(70) Mawson, S.; Johnston, K. P.; Betts, D. E.; McClain, J. B.; DeSimone, J. M. *Macromolecules* **1997**, *30*, 71.

(71) Tan, C. S.; Lin, H. Y. *Ind. Eng. Chem. Res.* **1999**, *38*, 3898.

(72) Gallagher, P. M.; Coffey, M. P.; Krukonis, V. J.; Klasutis, N. *ACS Symp. Ser.* **1989**, *406*, 334.

(73) Dixon, D. J.; Johnston, K. P.; Bodmeier, R. A. *AIChE J.* **1993**, *39*, 127.

(74) Schmidt, W. J.; Salada, M. C.; Shook, G. G.; Speaker, S. M. *AIChE J.* **1995**, *41*, 2476.

(75) Gao, Y.; Mulenda, T. K.; Shi, Y. F.; Yuan, W. K. *J. Supercrit. Fluids* **1998**, *13*, 369.

(76) Randolph, T. W.; Randolph, A. D.; Mebes, M.; Yeung, S. *Biotechnol. Prog.* **1993**, *9*, 429.

(77) Robertson, J.; King, M. B.; Seville, J. P. K.; Merrifield, D. R.; Buxton, P. C. In *Proceedings of the 4th International Symposium on Supercritical Fluids*; Arai, K., Ed.: Sendai, Japan, 1997, pp 47.

(78) Werling, J. O.; Debenedetti, P. G. *J. Supercrit. Fluids* **2000**, *18*, 11.

(79) Werling, J. O.; Debenedetti, P. G. *J. Supercrit. Fluids* **1999**, *16*, 167.

(80) Jessop, P. G.; Lough, A. J.; Morris, R. H.; Schlaf, M. *Abstr. Pap. Am. Chem. Soc.* **1993**, *206*, 221.

(81) Tan, C. S.; Chang, W. W. *Ind. Eng. Chem. Res.* **1998**, *37*, 1821.

(82) Warwick, B.; Dehghani, F.; Foster, N. R.; Biffin, J. R.; Regtop, H. L. *Ind. Eng. Chem. Res.* **2002**, *41*, 1993.

(83) Jung, J.; Perrut, M. *J. Supercrit. Fluids* **2001**, *20*, 179.

(84) Marr, R.; Gamse, T. *Chem. Eng. Proc.* **2000**, *39*, 19.

(85) Shekunov, B. Y.; York, P. *J. Cryst. Growth* **2000**, *211*, 122.

(86) Cooper, A. I. *Advanced Materials* **2001**, *13*, 1111.

(87) Kompella, U. B.; Koushik, K. *Crit. Rev. Ther. Drug Carrier. Sys.* **2001**, *18*, 173.

(88) Reverchon, E.; Della Porta, G. *P. Appl. Chem.* **2001**, *73*, 1293.

(89) Tan, H. S.; Borsadia, S. *Exp. Opin. Ther. Patents* **2001**, *11*, 861.

(90) Texter, J. *J. Disp. Sci. Technol.* **2001**, *22*, 499.

(91) Thiering, R.; Dehghani, F.; Foster, N. R. *J. Supercrit. Fluids* **2001**, *21*, 159.

(92) Williams, J. R.; Clifford, A. A.; Al-Saidi, S. H. R. *Molec. Biotechnol.* **2002**, *22*, 263.

(93) DeSimone, J. M. *Science* **2002**, *297*, 799.

(94) Harris, R.; Jureller, S. H.; Kerschner, J. L.; Trzasko, P. T.; Humphreys, R. W. R., **1999**, U.S. patent 5,977,348

(95) Hanna, M.; York, P., **2000**, US patent 6,063,138

(96) Chattopadhyay, P.; Gupta, R. B. *Aiche J.* **2002**, *48*, 235.

(97) Chattopadhyay, P.; Gupta, R. B. *Ind. Eng. Chem. Res.* **2001**, *40*, 3530.

(98) Chattopadhyay, P.; Gupta, R. B. *Int. J. Pharm.* **2001**, *228*, 19.

(99) Chattopadhyay, P.; Gupta, R. B. *Ind. Eng. Chem. Res.* **2002**, *41*, 6049.

(100) Snavely, W. K.; Subramaniam, B.; Rajewski, R. A.; Defelippis, M. R. *J. Pharm. Sci.* **2002**, *91*, 2026.

(101) Elvassore, N.; Bertucco, A.; Caliceti, P. *Ind. Eng. Chem. Res.* **2001**, *40*, 795.

(102) Taki, S.; Badens, E.; Charbit, G. *J. Supercrit. Fluids* **2001**, *21*, 61.

(103) Tu, L. S.; Dehghani, F.; Foster, N. R. *Powder Technol.* **2002**, *126*, 134.

(104) Reverchon, E.; Della Porta, G.; De Rosa, I.; Subra, P.; Letourneur, D. *J. Supercrit. Fluids* **2000**, *18*, 239.

(105) Sarkari, M.; Darrat, I.; Knutson, B. L. *Aiche J.* **2000**, *46*, 1850.

(106) Elvassore, N.; Baggio, M.; Pallado, P.; Bertucco, A. *Biotechnol. Bioeng.* **2001**, *73*, 449.

(107) Song, K. H.; Lee, C. H.; Lim, J. S.; Lee, Y. W. *Kor. J. Chem. Eng.* **2002**, *19*, 139.

(108) Rantakyla, M.; Jantti, M.; Aaltonen, O.; Hurme, M. *J. Supercrit. Fluids* **2002**, *24*, 251.

(109) Velaga, S. P.; Ghaderi, R.; Carlfors, J. *Int. J. Pharm.* **2002**, *231*, 155.

(110) Reverchon, E.; Della Porta, G.; Falivene, M. G. *J. Supercrit. Fluids* **2000**, *17*, 239.

(111) Reverchon, E.; De Marco, I.; Della Porta, G. *Int. J. Pharm.* **2002**, *243*, 83.

(112) Reverchon, E.; Della Porta, G.; Pallado, P. *Powder Technol.* **2001**, *114*, 17.

(113) Shekunov, B. Y.; Baldyga, J.; York, P. *Chem. Eng. Sci.* **2001**, *56*, 2421.

(114) Edwards, A. D.; Shekunov, B. Y.; Kordikowski, A.; Forbes, R. T.; York, P. *J. Pharm. Sci.* **2001**, *90*, 1115.

(115) Teipel, U.; Krober, H.; Krause, H. H. *Propel. Explos. Pyrotech.* **2001**, *26*, 168.

(116) Krober, H.; Teipel, U. *J. Supercrit. Fluids* **2002**, *22*, 229.

(117) Rehman, M.; Shekunov, B. Y.; York, P.; Colthorpe, P. *J. Pharm. Sci.* **2001**, *90*, 1570.

(118) Badens, E.; Magnan, C.; Charbit, G. *Biotechnol. Bioeng.* **2001**, *72*, 194.

(119) Hong, L.; Guo, J. Z.; Gao, Y.; Yuan, W. K. *Ind. Eng. Chem. Res.* **2000**, *39*, 4882.

(120) Hsu, R. Y.; Tan, C. S.; Chen, J. M. *J. Appl. Poly. Sci.* **2002**, *84*, 1657.

(121) Yeo, S. D.; Choi, J. H.; Lee, T. J. *J. Supercrit. Fluids* **2000**, *16*, 235.

(122) Lopez-Sanchez, J. A.; Bartley, J. K.; Burrows, A.; Kiely, C. J.; Havecker, M.; Schlogl, R.; Volta, J. C.; Poliakoff, M.; Hutchings, G. J. *New J. Chem.* **2002**, *26*, 1811.

(123) Hutchings, G. J.; Bartley, J. K.; Webster, J. M.; Lopez-Sanchez, J. A.; Gilbert, D. J.; Kiely, C. J.; Carley, A. F.; Howdle, S. M.; Sajip, S.; Caldarelli, S.; Rhodes, C.; Volta, J. C.; Poliakoff, M. *J. Catal.* **2001**, *197*, 232.

(124) Hutchings, G. J.; Lopez-Sanchez, J. A.; Bartley, J. K.; Webster, J. M.; Burrows, A.; Kiely, C. J.; Carley, A. F.; Rhodes, C.; Havecker, M.; Knop-Gericke, A.; Mayer, R. W.; Schlogl, R.; Volta, J. C.; Poliakoff, M. *J. Catal.* **2002**, *208*, 197.

(125) Kordikowski, A.; Shekunov, T.; York, P. *Pharm. Res.* **2001**, *18*, 682.

(126) Subra, P.; Jestin, P. *Ind. Eng. Chem. Res.* **2000**, *39*, 4178.

(127) Reverchon, E. *Ind. Eng. Chem. Res.* **2002**, *41*, 2405.

(128) Muhrer, G.; Lin, C.; Mazzotti, M. *Ind. Eng. Chem. Res.* **2002**, *41*, 3566.

(129) Elvassore, N.; Bertucco, A.; Di Noto, V. *J. Chem. Eng. Data* **2002**, *47*, 223.

(130) Badilla, J.; Peters, C. J.; Arons, J. D. *J. Supercrit. Fluids* **2000**, *17*, 13.

(131) Ke, J. H.; Tan, C. S. *J. Chin. Inst. Chem. Eng.* **2002**, *33*, 491.

(132) Bristow, S.; Shekunov, T.; Shekunov, B. Y.; York, P. *J. Supercrit. Fluids* **2001**, *21*, 257.

(133) Cocero, M. J.; Ferrero, S. *J. Supercrit. Fluids* **2002**, *22*, 237.

(134) Corrigan, O. I.; Crean, A. M. *Int. J. Pharm.* **2002**, *245*, 75.

(135) Cai, J. G.; Zhou, Z. Y.; Deng, X. *Chin. J. Chem. Eng.* **2001**, *9*, 258.

(136) Thiering, R.; Dehghani, F.; Dillow, A.; Foster, N. R. *J. Chem. Technol. Biotechnol* **2000**, *75*, 42.

(137) Thiering, R.; Dehghani, F.; Dillow, A.; Foster, N. R. *J. Chem. Technol. Biotechnol.* **2000**, *75*, 29.

(138) Warwick, B.; Dehghani, F.; Foster, N. R.; Biffin, J. R.; Regtop, H. L. *Ind. Eng. Chem. Res.* **2000**, *39*, 4571.

(139) Elvassore, N.; Bertucco, A.; Caliceti, P. *J. Pharm. Sci.* **2001**, *90*, 1628.

(140) Moneghini, M.; Kikic, I.; Voinovich, D.; Perissutti, B.; Filipovic-Grcic, J. *Int. J. Pharm.s* **2001**, *222*, 129.

(141) Zhang, H. F.; Han, B. X.; Yang, G. Y.; Yan, H. K. *J. Colloid Interface Sci.* **2000**, *232*, 269.

(142) Zhang, H. F.; Han, B. X.; Yang, G. Y.; Liu, F. F. *Acta Chimica Sinica* **2000**, *58*, 958.

(143) Zhang, H. F.; Lu, J.; Han, B. X. *J. Supercrit. Fluids* **2001**, *20*, 65.

(144) Zhang, J. L.; Han, B. X.; Liu, J. C.; Zhang, X. G.; Liu, Z. M.; He, J. *Chem. Commun.* **2001**, 2724.

(145) Zhang, J. L.; Han, B. X.; Liu, J. C.; Zhang, X. G.; He, J.; Liu, Z. M.; Jiang, T.; Yang, G. Y. *Chem. Europ. J.* **2002**, *8*, 3879.

(146) Kroto, H. W.; Heath, J. R.; Obrien, S. C.; Curl, R. F.; Smalley, R. E. *Nature* **1985**, *318*, 162.

(147) Pawley, M. *Buckminster Fuller*; Trefoil Publications: London, 1990.

(148) Kratschmer, W.; Lamb, L. D.; Fostiropoulos, K.; Huffman, D. R. *Nature* **1990**, *347*, 354.

(149) http://sbchem.sunysb.edu/msl/fullerene.html

(150) Fujita, M.; Kurita, N.; Nakao, K. *Synth. Met.* **1995**, *70*, 1509.

(151) Braun, T.; Schubert, A. P.; Kostoff, R. N. *Chem. Rev.* **2000**, *100*, 23.

(152) Tsang, S. C.; Harris, P. J. F.; Green, M. L. H. *Nature* **1993**, *362*, 520.

(153) Hiura, H.; Ebbesen, T. W.; Tanigaki, K. *Adv. Mater.* **1995**, *7*, 275.

(154) Satishkumar, B. C.; Govindaraj, A.; Mofokeng, J.; Subbanna, G. N.; Rao, C. N. R. *J. Phys. B-At. Mol. Opt. Phys.* **1996**, *29*, 4925.

(155) Chang, J.-Y.; Ghule, A.; Chang, J.-J.; Tzing, S.-H.; Ling, Y.-C. *Chem. Phys. Lett.* **2002**, *363*, 583.

(156) Ikeda, A.; Hatano, T.; Kawaguchi, M.; Suenaga, H.; Shinkai, S. *Chem. Commun.* **1999**, 1403.

(157) Friedman, S. H.; Ganapathi, P. S.; Rubin, Y.; Kenyon, G. L. *J. Med. Chem.* **1998**, *41*, 2424.

(158) Sijbesma, R.; Srdanov, G.; Wudl, F.; Castoro, J. A.; Wilkins, C.; Friedman, S. H.; Decamp, D. L.; Kenyon, G. L. *J. Am. Chem. Soc.* **1993**, *115*, 6510.

(159) Da Ros, T.; Prato, M. *Chem. Commun.* **1999**, 663.

(160) Friedman, S. H.; Decamp, D. L.; Sijbesma, R. P.; Srdanov, G.; Wudl, F.; Kenyon, G. L. *J. Am. Chem. Soc.* **1993**, *115*, 6506.

(161) Fungo, F.; Otero, L. A.; Sereno, L.; Silber, J. J.; Durantini, E. N. *Dyes Pigment.* **2001**, *50*, 163.

(162) Yoo, J. W.; Park, T. H.; Choi, H. Y. *Physica C* **2001**, *364*, 66.

(163) Iwasa, Y. *New Diam. Front. Carbon Technol.* **2001**, *11*, 415.

(164) Fischer, J. E. *J. Phys. Chem. Solids* **1997**, *58*, 1939.

(165) Hebard, A. F.; Rosseinsky, M. J.; Haddon, R. C.; Murphy, D. W.; Glarum, S. H.; Palstra, T. T. M.; Ramirez, A. P.; Kortan, A. R. *Nature* **1991**, *350*, 600.

(166) Dahlke, P.; Denning, M. S.; Henry, P. F.; Rosseinsky, M. J. *J. Am. Chem. Soc.* **2000**, *122*, 12352.

(167) Schon, J. H.; Kloc, C.; Batlogg, B. *Nature* **2000**, *406*, 702.

(168) Schon, J. H.; Kloc, C.; Siegrist, T.; Steigerwald, M.; Svensson, C.; Batlogg, B. *Nature* **2001**, *413*, 831.

(169) Fujiki, S.; Kubozono, Y.; Takabayashi, Y.; Kashino, S.; Emura, S. *J. Synchrot. Radiat.* **2001**, *8*, 725.

(170) Ruoff, R. S.; Tse, D. S.; Malhotra, R.; Lorents, D. C. *J. Phys. Chem.* **1993**, *97*, 3379.

(171) Marcus, Y.; Smith, A. L.; Korobov, M. V.; Mirakyan, A. L.; Avramenko, N. V.; Stukalin, E. B. *J. Phys. Chem. B* **2001**, *105*, 2499.

(172) Marcus, Y. *J. Phys. Chem. B* **1997**, *101*, 8617.

(173) Roth, M.; Maag, K.; Schneider, G. M.; Tuma, D. *J. Phys. Chem. B* **2001**, *105*, 10373.

(174) Ruoff, R. S.; Malhotra, R.; Huestis, D. L.; Tse, D. S.; Lorents, D. C. *Nature* **1993**, *362*, 140.

(175) Burgi, H. B.; Blanc, E.; Schwarzenbach, D.; Liu, S. Z.; Lu, Y. J.; Kappes, M. M.; Ibers, J. A. *Angew. Chem.-Int. Edit. Engl.* **1992**, *31*, 640.

(176) Yannoni, C. S.; Wendt, H. R.; Devries, M. S.; Siemens, R. L.; Salem, J. R.; Lyerla, J.; Johnson, R. D.; Hoinkis, M.; Crowder, M. S.; Brown, C. A.; Bethune, D. S.; Taylor, L.; Nguyen, D.; Jedrzejewski, P.; Dorn, H. C. *Synth. Met.* **1993**, *59*, 279.

(177) Dworkin, A.; et; al *Acad. Sci. Paris* **1991**, *313*, 1017.

(178) Gadd, G. E.; Evans, P. J.; Kennedy, S.; James, M.; Elcombe, M.; Cassidy, D.; Moricca, S.; Holmes, J.; Webb, N.; Dixon, A.; Prasad, P. *Fullerene Sci. Technol.* **1999**, *7*, 1043.

(179) Assink, R. A.; Schirber, J. E.; Loy, D. A.; Morosin, B.; Carlson, G. A. *J. Mater. Res.* **1992**, *7*, 2136.

(180) Belahmer, Z.; Bernier, P.; Firlej, L.; Lambert, J. M.; Ribet, M. *Phys. Rev. B* **1993**, *47*, 15980.

(181) Schirber, J. E.; Kwei, G. H.; Jorgensen, J. D.; Hitterman, R. L.; Morosin, B. *Phys. Rev. B* **1995**, *51*, 12014.

(182) Kwei, G. H.; Jorgensen, J. D.; Schirber, J. E.; Morosin, B. *Fullerene Sci. Technol.* **1997**, *5*, 243.

(183) Morosin, B.; Hu, Z. B.; Jorgensen, J. D.; Short, S.; Schirber, J. E.; Kwei, G. H. *Phys. Rev. B* **1999**, *59*, 6051.

(184) Morosin, B.; Jorgensen, J. D.; Short, S.; Kwei, G. H.; Schirber, J. E. *Phys. Rev. B* **1996**, *53*, 1675.

(185) Gadd, G. E.; James, M.; Moricca, S.; Evans, P. J.; Davis, R. L. *Fullerene Sci. Technol.* **1996**, *4*, 853.

(186) Gadd, G. E.; Evans, P. J.; Moricca, S.; James, M. *J. Mater. Res.* **1997**, *12*, 1.

(187) Gadd, G. E.; Kennedy, S. J.; Moricca, S.; Howard, C. J.; Elcombe, M. M.; Evans, P. J.; James, M. *Phys. Rev. B* **1997**, *55*, 14794.

(188) Tang, T. B.; Gu, M. *Phys. Sol. State* **2001**, *44*, 631.

(189) Gadd, G. E.; Moricca, S.; Kennedy, S. J.; Elcombe, M. M.; Evans, P. J.; Blackford, M.; Cassidy, D.; Howard, C. J.; Prasad, P.; Hanna, J. V.; Burchwood, A.; Levy, D. *J. Phys. Chem. Solids* **1997**, *58*, 1823.

(190) Gadd, G. E.; Schmidt, P.; Bowles, C.; McOrist, G.; Evans, P. J.; Wood, J.; Smith, L.; Dixon, A.; Easey, J. *J. Am. Chem. Soc.* **1998**, *120*, 10322.

(191) Itoh, T.; Nitta, S.; Nonomura, S. *Appl. Surf. Sci.* **1997**, *114*, 282.

(192) van Smaalen, S.; Dinnebier, R.; Holleman, I.; von Helden, G.; Meijer, G. *Phys. Rev. B* **1998**, *57*, 6321.

(193) van Smaalen, S.; Dinnebier, R. E.; Schnelle, W.; Holleman, I.; von Helden, G.; Meijer, G. *Europhys. Lett.* **1998**, *43*, 302.

(194) Renker, B.; Roth, G.; Schober, H.; Nagel, P.; Lortz, R.; Meingast, C.; Ernst, D.; Fernandez-Diaz, M. T.; Koza, M. *Phys. Rev. B* **2001**, *64*.

(195) Kolesnikov, A. I.; Antonov, V. E.; Bashkin, I. O.; Grosse, G.; Moravsky, A. P.; Muzychka, A. Y.; Ponyatovsky, E. G.; Wagner, F. E. *J. Phys.: Con. Mat.* **1997**, *9*, 2831.

(196) Holleman, I.; Robyr, P.; Kentgens, A. P. M.; Meier, B. H.; Meijer, G. *J. Am. Chem. Soc.* **1999**, *121*, 199.

(197) Holleman, I.; von Helden, G.; van der Avoird, A.; Meijer, G. *Phys. Rev. Lett.* **1998**, *80*, 4899.

(198) Holleman, I.; vonHelden, G.; Olthof, E. H. T.; vanBentum, P. J. M.; Engeln, R.; Nachtegaal, G. H.; Kentgens, A. P. M.; Meier, B. H.; vanderAvoird, A.; Meijer, G. *Phys. Rev. Lett.* **1997**, *79*, 1138.

(199) Morosin, B.; Assink, R. A.; Dunn, R. G.; Massis, T. M.; Schirber, J. E.; Kwei, G. H. *Phys. Rev. B* **1997**, *56*, 13611.

(200) Gadd, G. E.; James, M.; Moricca, S.; Cassidy, D.; Evans, P. J.; Collins, B.; Armstrong, R. S. *J. Phys. Chem. Solids* **1998**, *59*, 1383.

(201) James, M.; Kennedy, S. J.; Elcombe, M. M.; Gadd, G. E. *Phys. Rev. B* **1998**, *58*, 14780.

(202) James, M.; Gadd, G. E. *Physica B* **2000**, *276*, 242.

(203) Gadd, G. E.; Elcombe, M. M.; Dennis, J.; Moricca, S.; Webb, N.; Cassidy, D.; Evans, P. J. *J. Phys. Chem. Solids* **1998**, *59*, 937.

(204) Nagano, Y.; Kiyobayashi, T.; Nitta, T. *Chem. Phys. Lett.* **1994**, *217*, 186.

(205) Dyachenko, O. A.; Graja, A. *Fullerene Sci. Technol.* **1999**, *7*, 317.

(206) Field, C. N.; Hamley, P. A.; Webster, J. M.; Gregory, D. H.; Titman, J. J.; Poliakoff, M. *J. Am. Chem. Soc.* **2000**, *122*, 2480.

(207) Chattopadhyay, P.; Gupta, R. B. *Ind. Eng. Chem. Res.* **2000**, *39*, 2281.

(208) Mawson, S.; Kanakia, S.; Johnston, K. P. *J. Appl. Polym. Sci.* **1997**, *64*, 2105.

(209) Hertzberg, G. *Molecular Spectra and Molecular Structure*; Macmillan and Company, Ltd: London, 1945.

(210) Hare, J. P.; Dennis, T. J.; Kroto, H. W.; Taylor, R.; Allaf, A. W.; Balm, S.; Walton, D. R. M. *J. Chem. Soc.-Chem. Commun.* **1991**, 412.

(211) Taylor, R.; Hare, J. P.; Abdulsada, A. K.; Kroto, H. W. *J. Chem. Soc.-Chem. Commun.* **1990**, 1423.

(212) Kratschmer, W.; Fostiropoulos, K.; Huffman, D. R. *Chem. Phys. Lett.* **1990**, *170*, 167.

(213) Wang, K. A.; Rao, A. M.; Eklund, P. C.; Dresselhaus, M. S.; Dresselhaus, G. *Phys. Rev. B* **1993**, *48*, 11375.

(214) Martin, M. C.; Du, X. Q.; Kwon, J.; Mihaly, L. *Phys. Rev. B* **1994**, *50*, 173.

(215) Boultif, A.; Louer, D. *J. Appl. Crystallogr.* **1991**, *24*, 987.

(216) Tan, M. Q.; Xu, B.; Li, H. N.; Qi, Z. F.; Xu, Y. *J. Cryst. Growth* **1997**, *182*, 375.

(217) Davey, R. J.; Garside, J. *From Molecules to Crystallizers*; Oxford University Press: Oxford, 2000.

(218) Hartman, P., Ed. *Crystal Growth: An Introduction*; North Holland: Amsterdam, 1973.

(219) Temkin, D. E. *Crystallisation Processes*; Consultants Bureau: New York, 1966.

(220) Frank, F. C. *Discuss. Faraday. Soc.* **1949**, *5*, 48.

(221) Butron, W. K.; Cabrera, N.; Frank, F. C. *Philos. Trans. Roy. Soc.* **1951**, *243*, 299.

(222) Davey, R. J.; Ristic, R. I.; Zizic, B. *J. Cryst. Growth* **1979**, *47*, 1.

(223) Garside, J. In *Advances in Industrial Crystallisation*; Garside, J., et, al, Eds.; Butterworth-Heinemann: Oxford, 1991, p 92.

(224) Heiney, P. A.; Fischer, J. E.; McGhie, A. R.; Romanow, W. J.; Denenstein, A. M.; McCauley, J. P.; Smith, A. B.; Cox, D. E. *Phys. Rev. Lett.* **1991**, *66*, 2911.

(225) Single crystal diffraction data were collected for C_{60} (C_2H_4) at 3 temperatures, 150, 90 and 30 K and for C_{60}(C_2H_6) at 2 temperatures, 150

and 30 K.In all cases, X-ray diffraction data were collected using graphite monochromated Mo-Ka radiation (l = 0.71073Å) on a Bruker CCD area detector diffractometer. Integrated intensities, corrected for Lorentz and polarization effects, were obtained using SAINT v6.02a. [Bruker] For data collected at 150 and 90 K the crystals were cooled using an Oxford Cryosystems Cryostream N_2-flow and for the 30 K datasets an Oxford Cryosystems HELIX open flow He gas cryostat was used.[20] The ethene structure was solved by direct methods (SHELXS-97) and all refinements were made against F2 using full matrix least-squares (SHELXTL-97). [Bruker refs] All ordered carbon atoms were refined with anistropic atomic displacement parameters (adps). Hydrogen atoms were not located.

C_{60} (C_2H_4)

A different crystal was used for each of the temperatures; all were mounted in perfluoropolyether oil on dual stage fibres and flash frozen. The 150 and 90 K data were collected on a Bruker SMART1000 diffractometer, the 30 K data on a SMART 1K diffractometer. The model from the 150 K refinement was used as a starting point for the refinements against data at the other 2 temperatures. All crystals examined showed merohedral twinning. The ethane was modelled as 0.333 occupied site after refinement of the occupancy gave 0.333 within 2 esds i.e. 1:1 C_{60}:C_2H_4 , with an isotropic adp and 3 orientations of ethane are generated by symmetry.

C_{60} (C_2H_4), M = 748.65, cubic, a = 14.1902(12)Å, U = 2857.4(7) $Å^3$, T = 150 K, space group P a-3 (no. 205), Z = 4, rcalcd = 1.740 gcm^{-3}, m(Mo-Ka) = 0.10 mm^{-1}, 25297 reflections measured, 1340 unique (Rint = 0.072) to 2qmax = 58°. The final wR(F2) was 0.103 for all 1261 data, R1(F) was

0.046 for 916 observed data where I> 2s(I) for 96 parameters. Black tablet shaped crystal of dimensions 0.22 x 0.20 x 0.11 mm.

At 90 K as above except, a = 14.178(4) Å, rcalcd = 1.745 gcm^{-3}, 20646 reflections measured, 891 unique (Rint = 0.10) to 2qmax = 50°. The final wR(F2) was 0.218 for all 891 data, R1(F) was 0.072 for 816 observed data where I> 2s(I) for 96 parameters. Black block shaped crystal of dimensions 0.24 x 0.12 x 0.08 mm.

At 30 K as above except, a = 14.181(2) Å, rcalcd = 1.744 gcm^{-3}, 14971 reflections measured, 892 unique (Rint = 0.17) to 2qmax = 50°. The final wR(F2) was 0.288 for all 892 data, R1(F) was 0.091 for 734 observed data where I> 2s(I) for 96 parameters. Black triangular tablet shaped crystal of dimensions 0.14 x 0.14 x 0.08 mm.

C_{60} (C_2H_6)

A different crystal was used at each temperature; the crystal used for the 150 K data collection was glued to a glass fibre using araldite and that used for the 30 K data collection was mounted in perfluoropolyether oil on dual stage fibre and flash frozen. The 150 data were collected on a Bruker APEX diffractometer, the 30 K data on a SMART 1K diffractometer. The following twin law was applied (-1 0 0, 0 1 0, 0 0 1) and ratio of components refined to 0.415(6) and 0.395(6) at 150 and 30 K respectively. C_{60} (C_2H_6), M = 750.67, monoclinic, a = 9.8467(12), b = 9.8465(12), c = 14.829(2) Å, b = 90.038(2)°, U = 1437.8(3) $Å^3$, T = 150 K, space group P 21/*n* (no. 14, non-standard setting of P21/c), Z = 2, rcalcd = 1.734 gcm^{-3}, m(Mo-Ka) = 0.10 mm^{-1}, 7375 reflections measured, 2523 unique (Rint = 0.057) to 2qmax = 50°. The final wR(F2) was 0.338 for all 2523 data,

R1(F) was 0.133 for 2497 observed data where I> 2s(I) for 281 parameters.

Black plate like crystal of dimensions 0.15 x 0.08 x 0.02 mm.

At 30 K as above except, monoclinic, a = 9.796(2), b = 9.803(2), c = 14.808(3) Å, b = 90.095(3)°, U = 1422.0(5) $Å^3$, rcalcd = 1.753 gcm^{-3}, m(Mo-Ka) = 0.10 mm-1, 6141 reflections measured, 3072 unique (Rint = 0.043) to 2qmax=50°. The final wR(F2) was 0.380 for all 2441 data, R1(F) was 0.144 for 2433 observed data where I> 2s(I) for 281 parameters. Black polyhedral crystal of dimensions 0.38 x 0.24 x 0.22 mm.

CCDC 187490 - 187494 contain the supplementary crystallographic data for this paper. These data can be obtained free of charge via www.ccdc.cam.ac.uk/conts/retriving.html (or from Cambridge Crystallographic Data Centre (CCDC) 12 Union Road, Cambridge, CB2 1EZ, UK;fax:(+44) 1223-336-033; or deposit@ccdc.cam.ac.uk).

(226) David, W. I. F.; Ibberson, R. M.; Matthewman, J. C.; Prassides, K.; Dennis, T. J. S.; Hare, J. P.; Kroto, H. W.; Taylor, R.; Walton, D. R. M. *Nature* **1991**, *353*, 147.

(227) Pauwels, B.; Bertnaerts, D.; Amelinckx, S.; Van Tendeloo, G.; Joutsensaari, J.; Kauppinen, E. I. *J. Cryst. Growth* **1999**, *200*, 126.

(228) Vaughan, G. B. M.; Heiney, P. A.; Cox, D. E.; Fischer, J. E.; McGhie, A. R.; Smith, A. L.; Strongin, R. M.; Cichy, M. A.; Smith, A. B. *Chem. Phys.* **1993**, *178*, 599.

(229) Blanc, E.; Burgi, H. B.; Restori, R.; Schwarzenbach, D.; Ochsenbein, P. *Europhys. Lett.* **1996**, *33*, 205.

(230) Vantendeloo, G.; Amelinckx, S.; Deboer, J. L.; Vansmaalen, S.; Verheijen, M. A.; Meekes, H.; Meijer, G. *Europhys. Lett.* **1993**, *21*, 329.

(231) Verheijen, M. A.; Meekes, H.; Meijer, G.; Bennema, P.; Deboer, J. L.; Vansmaalen, S.; Vantendeloo, G.; Amelinckx, S.; Muto, S.; Vanlanduyt, J. *Chem. Phys.* **1992**, *166*, 287.

(232) Beasley, M. R.; Datta, S.; Kogelnik, H.; Kroemer, H.; Monroe, D. "Report of the Investigation Committee on the Possibility of Scientific Misconduct in the Work of Hendrik Schon and Coauthors," Bell Laboratories, 2002.

(233) Dinnebier, R. E.; Gunnarsson, O.; Brumm, H.; Koch, E.; Stephens, P. W.; Huq, A.; Jansen, M. *Science* **2002**, *296*, 109.

(234) Margadonna, S.; Prassides, K. *J. Solid State Chem.* **2002**, *168*, 639.

(235) Lee, H. M.; Olmstead, M. M.; Suetsuna, T.; Shimotani, H.; Dragoe, N.; Cross, R. J.; Kitazawa, K.; Balch, A. L. *Chem. Commun.* **2002**, 1352.

(236) Iijima, S. *Nature* **1991**, *354*, 56.

(237) Rinzler, A. G.; Liu, J.; Dai, H.; Nikolaev, P.; Huffman, C. B.; Rodriguez-Macias, F. J.; Boul, P. J.; Lu, A. H.; Heymann, D.; Colbert, D. T.; Lee, R. S.; Fischer, J. E.; Rao, A. M.; Eklund, P. C.; Smalley, R. E. *Appl. Phys. A-Mater. Sci. Process.* **1998**, *67*, 29.

(238) Ebbesen, T. W.; Ajayan, P. M. *Nature* **1992**, *358*, 220.

(239) Sloan, J.; Dunin-Borkowski, R. E.; Hutchison, J. L.; Coleman, K. S.; Williams, V. C.; Claridge, J. B.; York, A. P. E.; Xu, C. G.; Bailey, S. R.; Brown, G.; Friedrichs, S.; Green, M. L. H. *Chem. Phys. Lett.* **2000**, *316*, 191.

(240) Cheng, H. M.; Li, F.; Sun, X.; Brown, S. D. M.; Pimenta, M. A.; Marucci, A.; Dresselhaus, G.; Dresselhaus, M. S. *Chem. Phys. Lett.* **1998**, *289*, 602.

(241) Dai, H. J. *Acc. Chem. Res.* **2002**, *35*, 1035.

(242) Sloan, J.; Hammer, J.; Zwiefka-Sibley, M.; Green, M. L. H. *Chem. Commun.* **1998**, 347.

(243) Tsang, S. C.; Chen, Y. K.; Harris, P. J. F.; Green, M. L. H. *Nature* **1994**, *372*, 159.

(244) Smith, B. W.; Monthioux, M.; Luzzi, D. E. *Nature* **1998**, *396*, 323.

(245) Luzzi, D. E.; Smith, B. W. *Carbon* **2000**, *38*, 1751.

(246) Monthioux, M. *Carbon* **2002**, *40*, 1809.

(247) Smith, B. W.; Russo, R. M.; Chikkannanavar, S. B.; Luzzi, D. E. *J. Appl. Phys.* **2002**, *91*, 9333.

(248) Smith, B. W.; Monthioux, M.; Luzzi, D. E. *Chem. Phys. Lett.* **1999**, *315*, 31.

(249) Qian, D.; Liu, W. K.; Ruoff, R. S. *J. Phys. Chem. B* **2001**, *105*, 10753.

(250) Okada, S.; Saito, S.; Oshiyama, A. *Phys. Rev. Lett.* **2001**, *86*, 3835.

(251) Berber, S.; Kwon, Y. K.; Tomanek, D. *Phys. Rev. Lett.* **2002**, *88*, art. no.

(252) Khlobystov, A. *Unpublished Data* **2002.**

(253) Jakes, P.; Weiden, N.; Eichel, R.-A.; Gembus, A.; Dinse, K.-P.; Meyer, C.; Harneit, W.; Weidinger, A. *J. Mag. Res.* **2002**, *156*, 303.

(254) Muller, K. H.; Dunsch, L.; Eckert, D.; Wolf, M.; Bartl, A. *Synth. Met.* **1999**, *103*, 2417.

(255) Campbell, E. E. B. *Appl. Phys. A-Mater. Sci. Process.* **1998**, *66*, 241.

(256) Kholbystov, A. *Personal Communication* **2002.**

(257) Tharumagnanam, D.; Manos, G. In *4th International Symposium on High Pressure Process Technology and Chemical Engineering*; Bertucco, A., Ed.: Venice, Italy, 2002.

(258) Corma, A. *Chem. Rev.* **1997**, *97*, 2373.

(259) Selvam, P.; Bhatia, S. K.; Sonwane, C. G. *Ind. Eng. Chem. Res.* **2001**, *40*, 3237.

(260) Ciesla, U.; Schuth, F. *Microporous Mesoporous Mat.* **1999**, *27*, 131.

(261) Rouquerol, J.; Anvir, D.; Fairbridge, C. W.; Everett, D. H.; Haynes, J. H.; Pernicone, N.; Ramsay, J. D.; Sing, K. S. W.; Unger, K. K. *Pure Appl. Chem.* **1994**, *66*, 1739.

(262) Corma, A. *Chem. Rev.* **1995**, *95*, 559.

(263) Freyhardt, C. C.; Tsapatsis, M.; Lobo, R. F.; Balkus, K. J. J.; Davies, M. E. *Nature* **1996**, *381*, 295.

(264) Beck, J. S., **1991**, US patent 5,057,296

(265) Kresge, C. T.; Leonowicz, M. E.; Roth, W. G.; Vartuli, J. C.; Beck, J. S. *Nature* **1992**, *359*, 710.

(266) Yanagisawa, T.; Shimizu, T.; Kuroda, K.; Kato, C. *Bull. Chem. Soc. Jpn.* **1990**, *63*, 988.

(267) Inagaki, S.; Fukushima, Y.; Kuroda, K. *J. Chem. Soc.-Chem. Commun.* **1993**, 680.

(268) Beck, J. S.; Vartuli, J. C.; Kennedy, G. J.; Kresge, C. T.; Roth, W. J.; Schramm, S. E. *Chem. Mat.* **1994**, *6*, 1816.

(269) Grun, M.; Unger, K. K.; Matsumoto, A.; Tsutsumi, K. *Microporous Mesoporous Mat.* **1999**, *27*, 207.

(270) Zhang, Z. R.; Suo, J. H.; Zhang, X. M.; Li, S. B. *Acta Phys.-Chim. Sin.* **1998**, *14*, 243.

(271) Tamon, H.; Kitamura, T.; Okazaki, M. *J. Colloid Interface Sci.* **1998**, *197*, 353.

(272) Ryoo, R.; Joo, S. H.; Kim, J. M. *J. Phys. Chem. B* **1999**, *103*, 7435.

(273) Zana, R.; Frasch, J.; Soulard, M.; Lebeau, B.; Patarin, J. *Langmuir* **1999**, *15*, 2603.

(274) Sierra, L.; Guth, J.-L. *Microporous Mesoporous Mat.* **1999**, *27*, 243.

(275) Chen, L. Y.; Horiuchi, T.; Mori, T.; Maeda, K. *J. Phys. Chem. B* **1999**, *103*, 1216.

(276) Mokaya, R. *Personal Communication* **2002**.

(277) Kumar, D.; Schmacher, K.; du Fresne von Hohenesche, C.; Gurn, M.; Unger, K. K. *Colloid Surf. A-Physicochem. Eng. Asp.* **2001**, *187-188*, 109.

(278) Sano, T.; Doi, K.; Hagimoto, H.; Wang, Z.; Uozumi, T.; Soga, K. *Chem. Commun.* **1999**, *38*, 733.

(279) Raimondo, M.; Sinibaldi, P. M.; De Stefanis, A.; Tomlinson, A. A. G. *Chem. Commun.* **1997**, 1343.

(280) Corma, A.; Fornes, V.; Garcia, H. S.; Miranda, M. A.; Sabater, M. J. *J. Am. Chem. Soc.* **1994**, *116*, 9767.

(281) Menon, V. C.; Komarneni, S. *J. Porous Mater.* **1998**, *5*, 43.

(282) Edler, K. J.; Reynolds, P. R.; Branton, P. J.; Trouw, F. R.; White, J. W. *J. Chem. Soc.-Faraday Trans.* **1997**, *93*, 1667.

(283) Corma, A.; Kumar, D. *Stud. Surf. Sci. Catal.* **1998**, *117*, 201.

(284) Macquarrie, D. J.; Jackson, D. B.; Mdoe, J. E. G.; Clark, J. H. *New J. Chem.* **1999**, *23*, 539.

(285) Choudhary, V. R.; Jana, S. K.; Patil, N. S. *Tetrahedron Lett.* **2002**, *43*, 1105.

(286) Chen, C. Y.; Burkett, S. L.; Li, H. X.; Davis, M. E. *Microporous Materials* **1993**, *2*, 27.

(287) Xiao, F. S.; Han, Y.; Qiu, S. L. *Chem. J. Chin. Univ.-Chin.* **2002**, *23*, 1847.

(288) Mokaya, R. *J. Phys. Chem. B* **2000**, *104*, 8279.

(289) Corma, A.; Fornes, V.; Navarro, M. T.; Perez-Pariente, J. *J. Catal.* **1994**, *148*, 569.

(290) Luan, Z. H.; He, H. Y.; Zhou, W. Z.; Cheng, C. F.; Klinowski, J. *J. Chem. Soc.-Faraday Trans.* **1995**, *91*, 2955.

(291) Lu, X. B.; Zhang, W. H.; He, R. *Chin. Chem. Lett.* **2002**, *13*, 480.

(292) Mokaya, R.; Jones, W. *Chem. Commun.* **1997**, 2185.

(293) Mokaya, R.; Jones, W. *Chem. Commun.* **1998**, 1839.

(294) Mokaya, R. *Chem. Commun.* **2000**, 1891.

(295) Shen, S. C.; Kawi, S. *Chem. Lett.* **1999**, 1293.

(296) Mokaya, R. *Angew. Chem.-Int. Edit. Engl.* **1999**, *38*, 2930.

(297) Mokaya, R.; Jones, W. *J. Mater. Chem.* **1999**, *9*, 555.

(298) Mokaya, R. *ChemPhysChem* **2002**, *3*, 360.

(299) Liu, Y.; Zhang, W. Z.; Pinnavaia, T. J. *J. Am. Chem. Soc.* **2000**, *122*, 8791.

(300) Mingotaud, A. F.; Dargelas, F.; Cansell, F. *Macromol. Symp.* **2000**, *153*, 77.

(301) Olah, G. A.; Torok, A.; Joschek, J. P.; Bucsi, I.; Esteves, P. M.; Rasul, G.; Prakash, G. K. S. *J. Am. Chem. Soc.* **2002**, *124*, 11379.

(302) Klys, A.; Zakrzewski, J. *J. Organomet. Chem.* **2002**, *642*, 143.

(303) Whitehurst, D. D., **1992**, US patent 5,143,879

(304) Schmidt, R.; Akporiaye, D.; Stocker, M.; Ellestad, O. H. *Zeolites and Related microporous Materials: State of the Art 1994*; Elsevier Science B. V.: Amsterdam, 1994.

(305) Kawi, S.; Lai, W. W. *Chemtech* **1998**, *28*, 26.

(306) Mokaya, R.; Jones, W. *J. Mater. Chem.* **1998**, *8*, 2819.

(307) Kawi, S.; Lai, M. W. *Chem. Commun.* **1998**, 1407.

(308) Kawi, S.; Goh, A. H. *Stud. Surf. Sci. Catal.* **2000**, *129*, 131.

(309) Kawi, S.; Lai, M. W. *AIChE J.* **2002**, *48*, 1572.

(310) Furstner, A.; Ackermann, L.; Beck, K.; Hori, H.; Koch, D.; Langemann, K.; Liebl, M.; Six, C.; Leitner, W. *J. Am. Chem. Soc.* **2001**, *123*, 9000.

(311) Hitzler, M. G.; Smail, F. R.; Ross, S. K.; Poliakoff, M. *Org. Process Res. Dev.* **1998**, *2*, 137.

(312) O'Neil, A.; Wilson, C.; Webster, J. M.; Allison, F. J.; Howard, J. A. K.; Poliakoff, M. *Angew. Chem.-Int. Edit. Engl.* **2002**, *41*, 3796.

(313) O'Neil, A. S.; Mokaya, R.; Poliakoff, M. *J. Am. Chem. Soc.* **2002**, *124*, 10636.

(314) Barlow, S. J., **2002**, PhD Thesis University of Nottingham, UK

(315) Nichols, R. W. *Pressure Vessel Codes and Standards*; Elsevier: London, 1987.

Appendix I Equipment

The high pressure equipment used in the following experiments is shown in. This experimental setup is shown schematically in Figure I-2 and components are described below. The specific arrangement of pipes and taps is for individual experiments are given in greater detail in the relevant experimental sections. Different vessels used throughout the course of this PhD are listed with a brief description of each. More details on each of these vessels are available elsewhere.
16,314



Figure I-1: Photograph of experimental setup used for the experiments in this thesis.

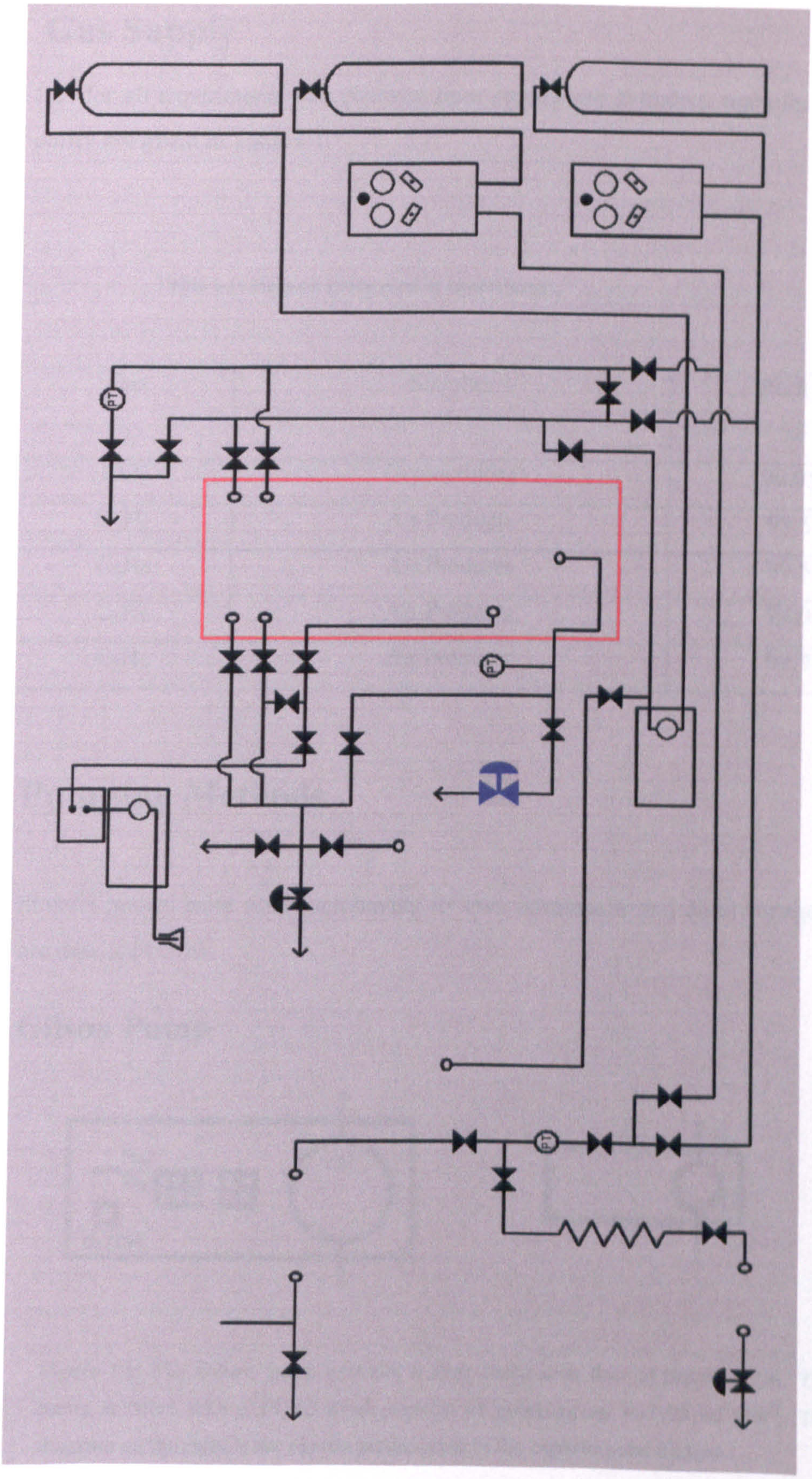


Figure I-2: General overview of the supercritical apparatus used in the experiments in this thesis.

Gas Supply

Gas for all experiments was obtained from pressurised cylinders; manufacturer and purity are given in Table I-1.

.

Table I-1: Data on gases used in experiments.

Gas	Supplier	Purity %
CO_2	Cryoservices	99.95
C_2H_4	Air Products	99.5
C_2H_6	Air Products	99.5
C_3H_6	Air Products	99.0
C_3H_8	Air Products	99.9

Pumping Methods

Several pumps were used each having its own advantages and disadvantages, these are detailed below.

Gilson Pump

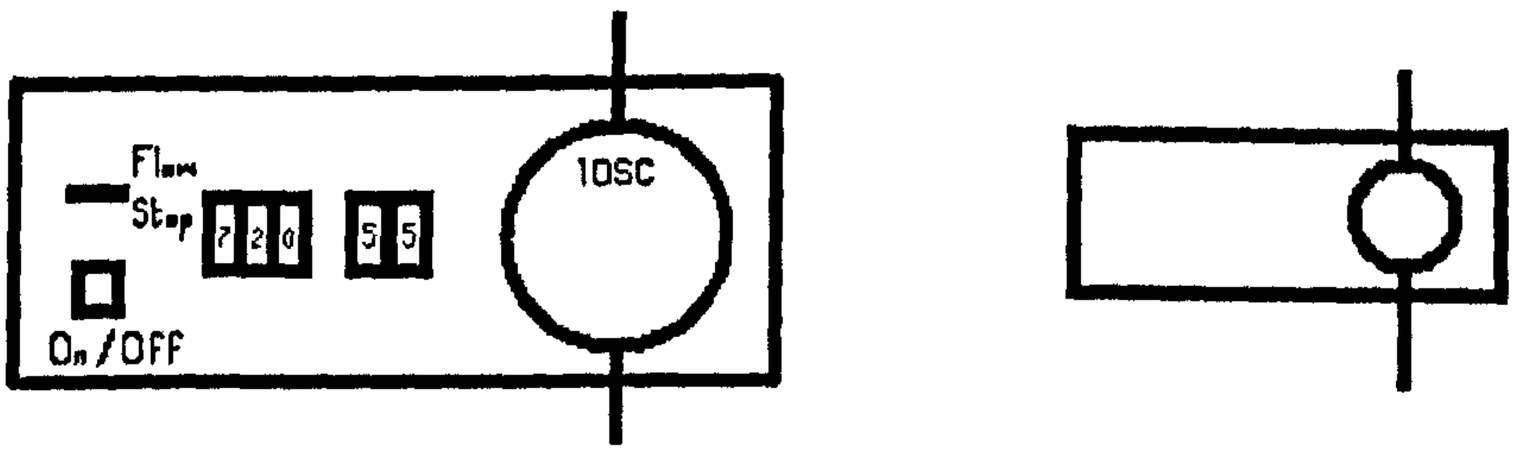


Figure I-3: The Gilson pump provides a near continuous flow of liquefied gas. The pump is fitted with a 10 SC head, capable of pumping up to 9.99 ml min^{-1}. The diagram on the right is the representation used in the experimental designs.

This pump is shown twice in Figure I-2 as, a supercritical fluid dosing unit and, as a solution pump, Figure I-3. The pump relies on a reciprocating sapphire piston to dose a specific volume of liquid into the system. A chiller unit is available to ensure that gas is liquefied at the pump head so pumping efficiency is maximised. Gilson pumps allow a specific flow rate to be set between a minimum of 0.005 ml min^{-1} to a maximum of 25 ml min^{-1} depending on the settings and pump head size. Gilson pumps were the most commonly used pump in this thesis, as they were found to be the most reliable and most easily controlled. Gilson pumps are usually used in conjunction with a manometric module this comprises of a pressure transducer and dampening coil. This allowed a maximum pressure to be set and also gave some control over the smooth flow of the gas or solution.

Pickel Pump

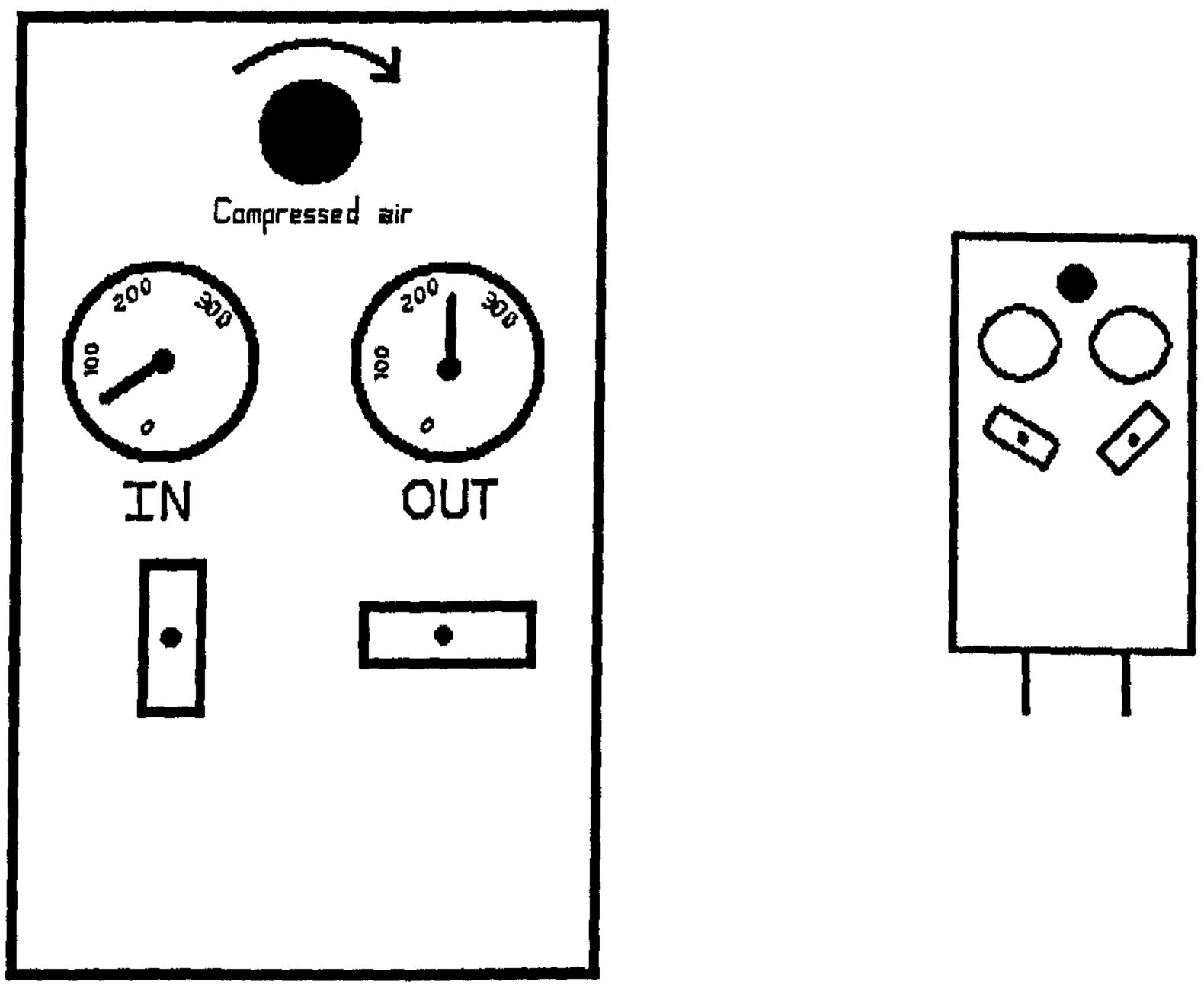


Figure I-4: The Pickel pump PM101 maintains a constant output pressure by pneumatic compression. The pressure is set by control of a lower pressure compressed air supply. This allows more rapid pumping than the Gilson pump (up to 50 ml min^{-1}) but is less accurate in setting and maintaining flow rates.

Pickel pumps, Figure I-4, consist of a Maximator pumping unit combined with an inbuilt refrigeration unit. They rely on a compressed air supply, which is utilised to give a high-pressure output. As with the Gilson pump the Pickel pump relies on dosage by a sapphire needle, in the case of this pump, however the maximum pressure is set and the pump is active until that pressure is met. Pickel pumps are superior to the Gilson in that they can maintain a constant flow of gas at a rate of up to 50 ml min^{-1} and also will not exceed the set pressure without the need for an extra module. They are, however, unreliable at lower flow rates and variation in the compressed air supply pressure can influence the flow rate substantially.

Vessels

32 ml and 10 ml Keystone Extraction Vessels

The basic design of the Keystone vessel is shown in Figure I-5. Sealing is maintained using a PEEK seal between the cell body and the main nut. A top nut fits into the main nut and seals with a frit to avoid blockages. Into this standard Valco fittings may be placed. One top nut was modified to accept a ¼" NPT fitting this allowed direct use of Swagelok manufactured fittings into the vessel. This was an important new feature that facilitated the PCA and GAS experiments detailed later. The Keystone vessels were rated to a temperature of 150 °C and a pressure of 10,000 psi.

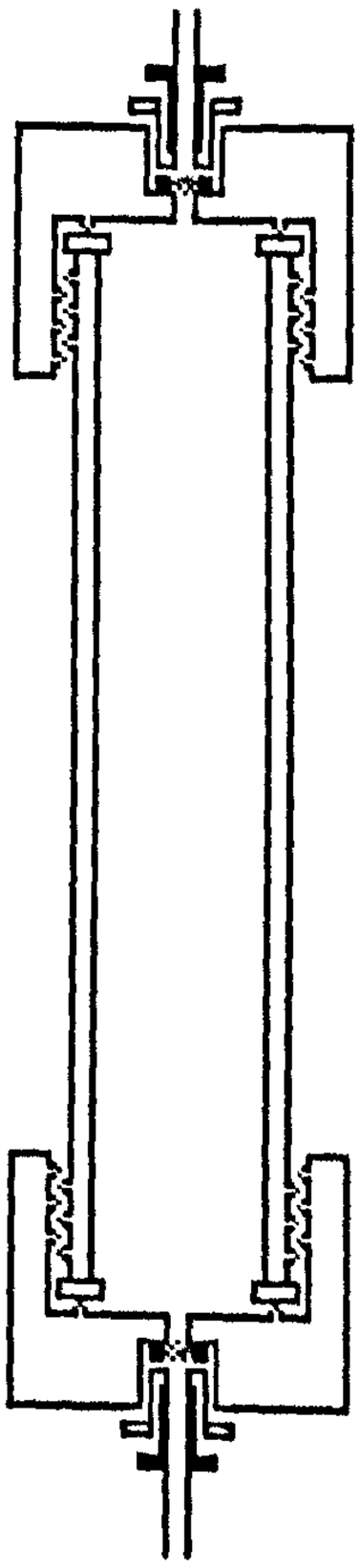


Figure I-5: Keystone extraction vessel.

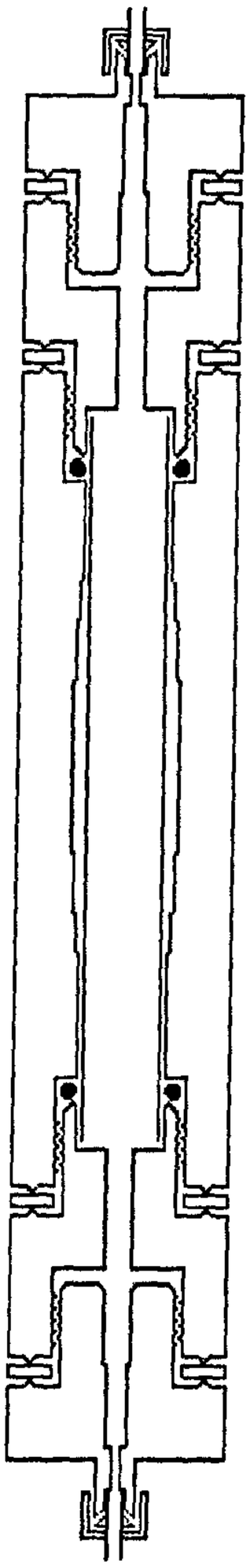


Figure I-6: Sapphire tube view cell.

Sapphire Tube View Cell

The sapphire tube view cell is a view cell based around a tube of sapphire, see Figure I-6. The main body of the vessel and the four nuts (two sets of two) are made from 316 stainless steel. The sapphire tube is held pressure tight by the squeezing action of two Buna N-Nitrile O-rings which grip the tube by the compression of one set of the large nuts. The nuts are all sealed with a Teflon ring and the ends of the vessel are connected with 1/8" Swagelok fittings. The sapphire tube view cell is rated to a pressure of 240 bar and a temperature of (100 °C).[314]

60 ml Stirred Autoclave

The Medimix stirred autoclave has three 1/8" Swagelok fittings, a thermowell and two internal baffles, Figure I-7. The stirring action is induced via a magnet connected to stirring blades. The stirred autoclave in heated with an electronically controlled band heater. This is capable of comfortable heating to up to 400 °C with lagging. The autoclave is rated to a temperature of 400 °C and a pressure of 400 bar. A torque of 120 Nm was required to seal the vessel.

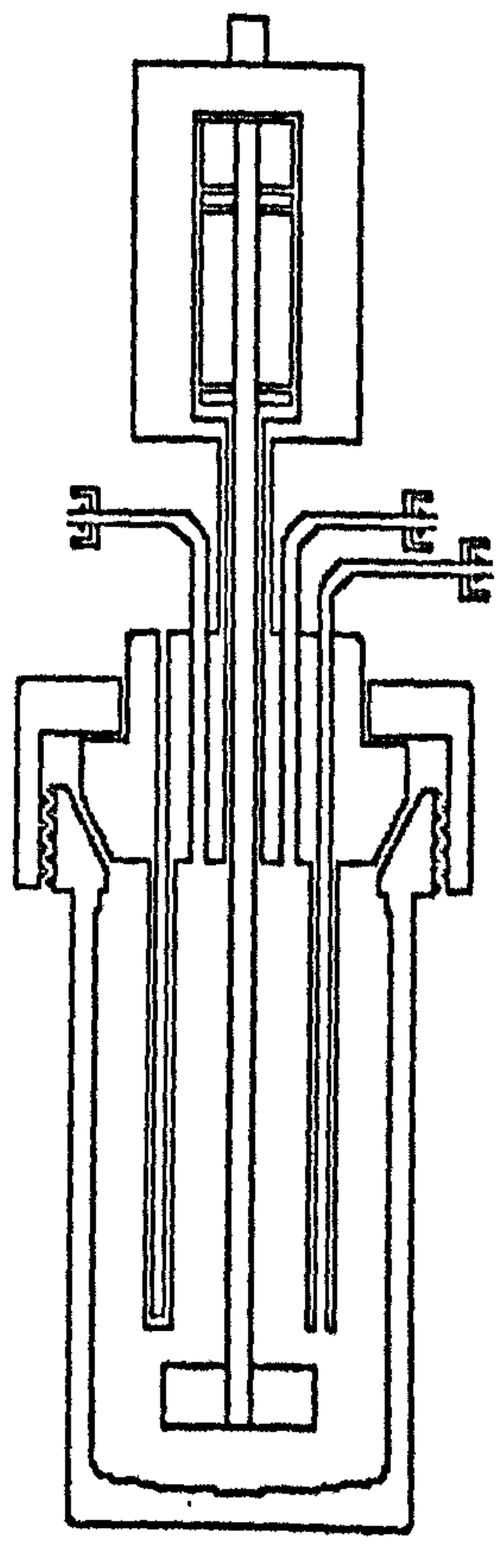


Figure I-7: 60 ml stirred autoclave.

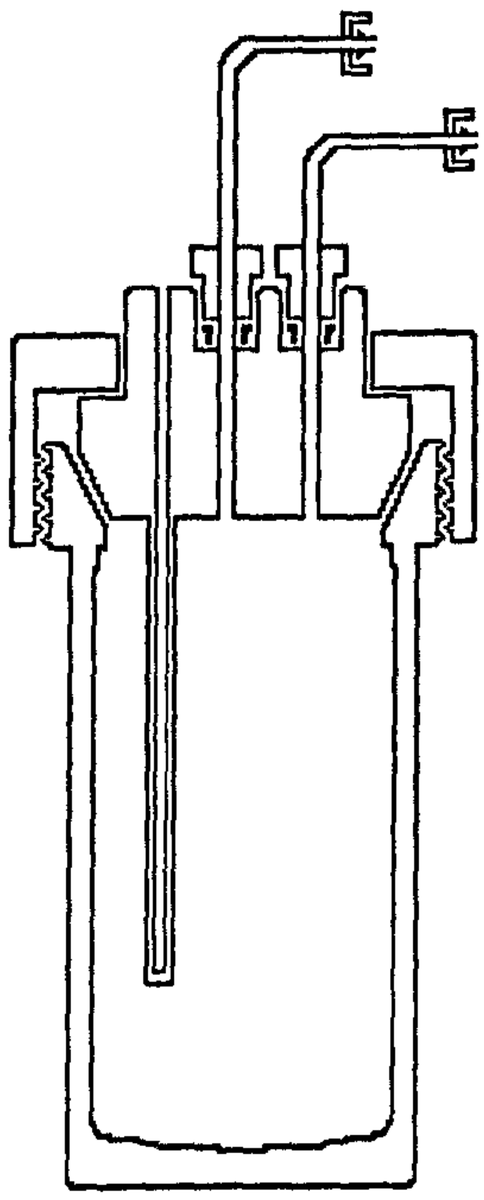


Figure I-8: 60 ml unstirred autoclave.

60 ml Unstirred Autoclave

The unstirred autoclave, Figure I-8, is similar in appearance to the stirred autoclave and is also rated to a temperature of 400 °C and a pressure of 400 bar. The unstirred autoclave is connected by two 1/8" SSI fittings and has a thermowell. The absence of a stirrer or second baffle maximises the space available to the user and was most useful in the DDP experiments.

High Temperature Tube Extraction Vessel

This vessel, Figure I-9, is simply a 15cm length of ½" Swagelok tubing which was held in heating block and used for extractions which were beyond the temperature range of the Keystone vessels. The tubing was of a thinner wall thickness than usual and was rated to 2800 psi with temperature constraints as detailed in Appendix III.

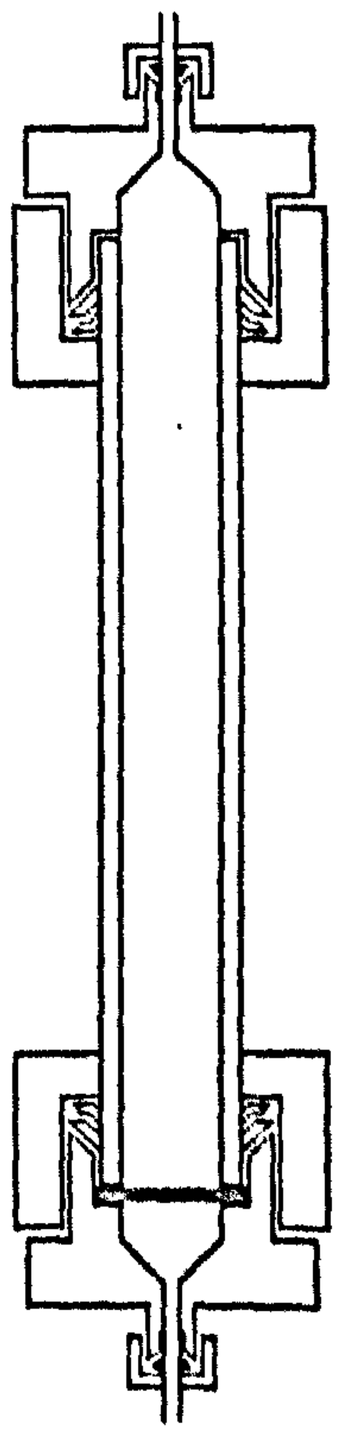


Figure I-9: Steel tube extraction vessel

Large Sapphire View Cell

Large view cell, Figure I-10, as used by Webster and Field[16,206] in preparation of $C_{60}(CO_2)$ and $C_{60}(C_2H_4)$. Maximum pressure 500 bar maximum temperature 150 °C.

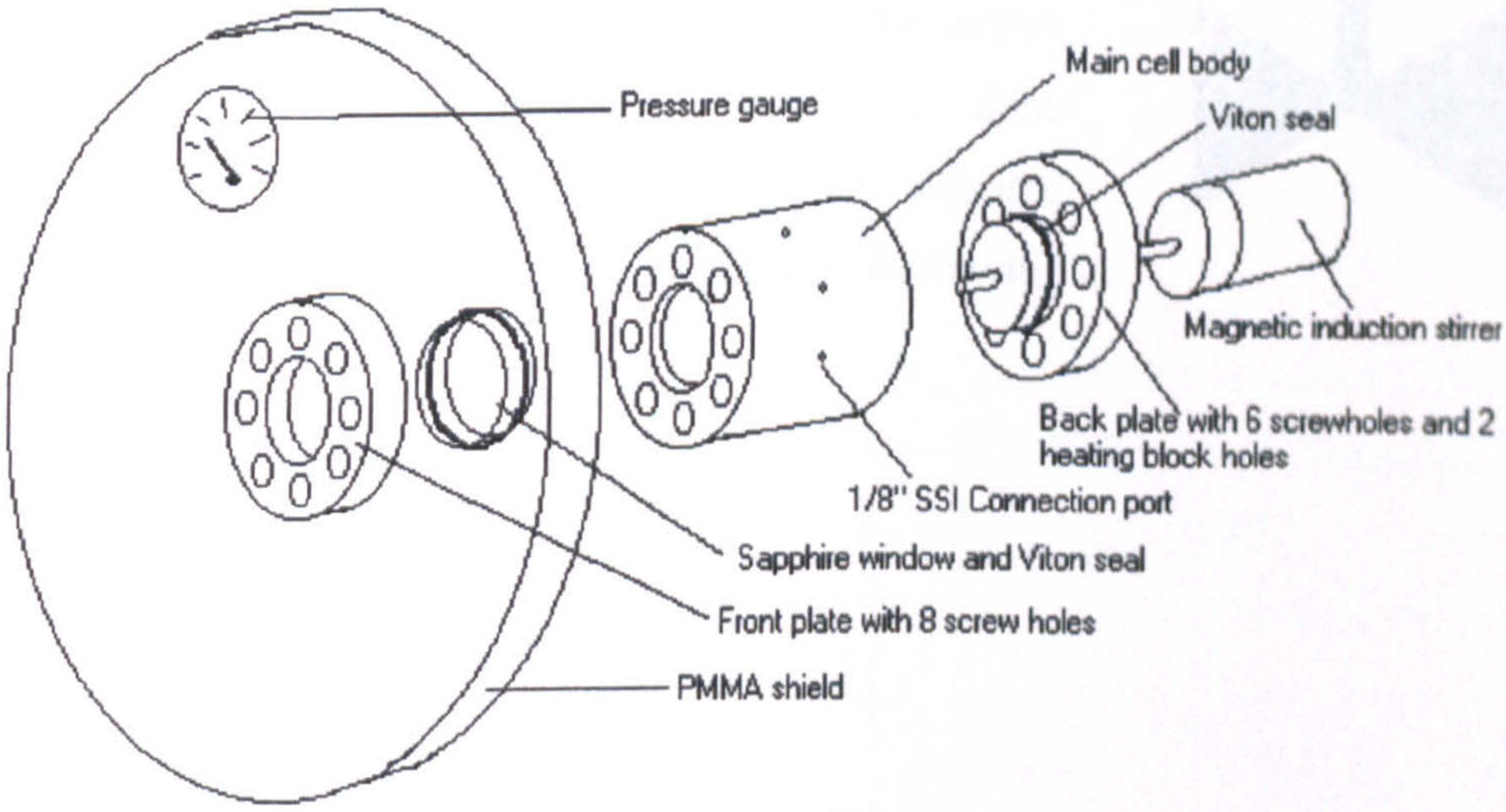


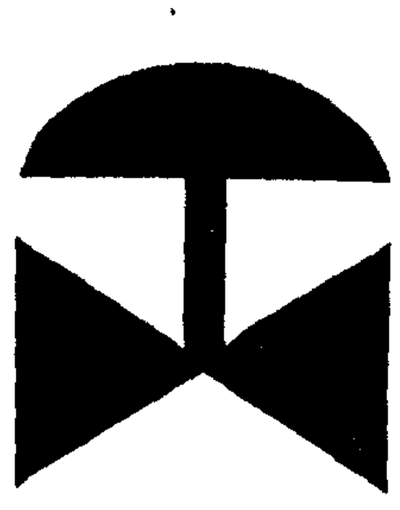
Figure I-10: Large sapphire view cell.

Back Pressure Regulators

Tescom

The Tescom 26-1722-24-043 Back Pressure Regulator was used initially to regulate pressure. This system was less reliable than the Jasco but did allow much higher flow rates of gas to be handled. The regulator works by spring loaded needle fitting onto a PEEK seat. Any scratches on the needle result in sever leakage from the regulator. The pressure setting was controlled by simply altering the compression on the spring.

Jasco



The Jasco 880-81 Back Pressure Regulator provided a more accurate way of maintaining pressure. This worked by a needle vibrating so as to let out gas at the correct rate to maintain the pressure, this was done electronically. The regulator had its own pressure transducer readout for monitoring the pressure before the unit.

Appendix II Analytical Equipment

X-Ray Diffraction XRD

Single crystal data was collected using a Bruker Smart1000 CCD area detector diffractometer equipped with an open flow N_2 cryostat. Crystals were mounted using perfloroether oil on a dual stage fibre before flash freezing to 150 K.

Powder X-Ray Diffraction

Powder X-ray diffraction patterns of all the new materials were taken. A Philips XPERT Θ - 2Θ diffractometer was used with a radiation source of Cu Kα. Diffractograms of the materials were taken over 14 hours and a range of $5° \leq 2\Theta \leq 60°$, although little useful data was obtainable above 40°. Indexing was carried out using the DICVOL91 programme.

MAS ^{13}C NMR

Carbon-13 solid state magic angle spinning (MAS) NMR spectra were measured for all samples at 293K and a resonance frequency of 75.6 MHz. The data was acquired using a 7.5 mm double resonance MAS probe set at spinning rate of 4 kHz ±2 kHz. Parameters of the experiment were: relaxation delay, 60 s; acquisition time 68 ms; carbon-13 $\pi/2$ pulse length, 4 μs; spectral width, 30 kHz. Each spectrum was the combination of between 512 and 1024 scans and 40 kHz exponential line broadening was applied before the FID was transformed.

Scanning Electron Microscopy

Scanning Electron Micrographs (SEM) were taken using a JEOL WinSEM 6400 microscope. The materials were placed on an adhesive carbon layer attached to an aluminium stub and then sputtered with a thin gold film.

Infra Red Spectroscopy

Fourier Transform Infra-red (FT-IR) spectra of the solid material were taken without modification of the sample in any way. A Perkin-Elmer Model I-series IR microscope with a narrow-band MCT detector, cooled with liquid nitrogen. The detector was attached to a PE System 2000 interferometer and a resolution of 4 cm^{-1} was used. Some spectra were also taken as KBr disks using the spectrometer without the microscope attachment.

Differential Scanning Calorimetry

DSC analysis was performed using a power compensated Perkin-Elmer DSC-7 under an Ar, with empty Al pans as reference data prior to collection of the scans. The material was initially cooled to –90 °C and held for 5 min before heating to 20 °C at 10 °C min^{-1}. The sample was then cooled to –90 °C at 200 °C min^{-1} and held for 10 min. prior to ramping from –90 °C to 20 °C at 10 °C min^{-1} to record the data.

Thermal Gravimetric Analysis

Thermogravimetric analysis (TGA) was performed using a Perkin Elmer Pyris 1 analyser with a heating rate of 10°C min^{-1} under nitrogen flow of 30 ml min^{-1}.

MAS ^{27}Al NMR

^{27}Al magic-angle-spinning (MAS) NMR spectra were recorded at 9.4 T with zirconia rotors 7.5 mm in diameter spun at 8 kHz. The spectra were measured at 104.3 MHz with 0.3 s recycle delays and corrected by subtracting the spectrum of the empty MAS rotor. External $Al(H_2O)_6^{3+}$ was used as a reference. To ensure quantitative reliability all calcined samples were fully hydrated and equilibrated with room air prior to the measurements.

N_2 Adsorption

N_2 sorption isotherms and textural properties (surface area and pore volume) were determined at -196 °C using nitrogen in a conventional volumetric technique by a Coulter SA3100 sorptometer. Before analysis the samples were oven dried at 130 °C and evacuated overnight (14 hours) at 200 °C under vacuum. The surface area was calculated using the BET method based on adsorption data in the partial pressure (P/Po) range 0.05 to 0.2 and the total pore volume was determined from the amount of N_2 adsorbed at a P/Po = *ca.* 0.99. The Barrett-Joyner-Halenda (BJH) method and *t*-plot analysis were used to determine the primary (or framework confined) mesopore pore volume.

Acidity Testing

The acid content of the samples before and after hydrothermal treatment was measured using established procedures employing thermal desorption of cyclohexylamine. Samples were exposed to liquid cyclohexylamine at room temperature after which they were kept overnight (at room temperature) and then in an oven at 80 °C for 2 hours so as to allow the base to permeate the samples. TGA curves were obtained for the cyclohexylamine containing samples using a

Polymer Laboratories TG 1500 analyser with a heating rate of 20 °C min^{-1} under nitrogen flow of 25 ml min^{-1}. The weight loss associated with desorption of the base from acid sites was used to calculate the acid content in mmol of cyclohexylamine per gram of sample.

Appendix III Safety Issues

When conducting high pressure experiments it is vital to be always aware of the many safety issues that the relevant procedures require. Below is given a list of several major factors which are relevant to the studies in this thesis and for anybody preparing to take part in supercritical experimentation themselves.

250 bar L Limit

The 250 bar l limit is a control on the size of a vessel in relation the pressure used within it. To adhere to UK law the size of a pressure vessel when multiplied by the working pressure of the experiment must not exceed 250 bar litre. It is possible to conduct experiments over this limit, however the safety legislation is greatly increased and this must all be taken into account before experimentation can begin. During this study the 250 bar L limit was not breached.

Combined Use of High Temperature and Pressure

All high pressure equipment should come from their respective suppliers with a maximum pressure rating. This usually contains a two to three times safety margin. This maximum pressure should not be exceeded at any time. The manufacturer also supplies a maximum temperature rating of the equipment and this also should never be exceeded. The maximum pressure rating, however, is dependent on the operating temperature. This is particularly important when operating at high temperature (*ca.* >350 °C). Depending on the material the equipment is made this can have a greater or lesser effect. Temperature always acts to weaken the vessel and hence lower the maximum pressure rating. A reference table was used from the Swagelok company to assess the effect on maximum operating pressure. This shows the percentage loss in maximum pressure rating with increasing temperature. This percentage is the ratio

to the room temperature pressure rating when operated at a higher temperature. At the higher operating temperature this modified rating should never be exceeded.

Flammable and Non Flammable Gas Supply

The operator should, of course, ensure that flammable gases never come into contact with any possible source of ignition. The cylinders themselves have the following convention; non-flammable gas cylinders require a conventional right-hand threaded cylinder head while flammable gases require a left-handed thread cylinder head. This convention is designed to reduce any chance of mistaken introduction of a flammable gas to a line designed for non-flammable gasses.

Pressure Rating Formulae

These formulae tend to be rather arbitrary although can be useful in ensuring that safe practices are maintained. A two or three times safety margin is often included Nichols[315] suggests a formula to calculate the maximum allowable working pressure of a cell. This is shown in Equation III-1.

$$T = \frac{PD}{2S + D}$$

Equation III-1: Maximum working pressure.

where P is the maximum working pressure, S is the ultimate tensile strength (UTS) divided by 4, D is the outside diameter of the cell and T is the wall thickness. All vessels except view cells used 316 stainless steel which has a UTS of 84000

Seal Types and Suitability

Careful checks must be made when designing any new sets of experiments to ensure that any seals used are appropriate for the experiments. This includes both mechanical and chemical compatibilities. For example Teflon is known to creep severely when exposed to temperatures higher than 100 °C. At this point the actual structural design of the vessel plays an important role as a vessel which holds the Teflon ring in place firmly can be raised successfully to the maximum operating temperature of 260 °C. If there is room for the Teflon to move then it will creep and potentially leak at a much lower temperature. The seals must also be chemically compatible with any materials they will come into contact with. Lists are published by o-ring manufacturers to reference given systems. Checks should be made of o-ring suitability and integrity before starting a new experiment.